The ONIOM Method and Its Applications

Lung Wa Chung,[†] W. M. C. Sameera,[‡] Romain Ramozzi,[‡] Alister J. Page,[§] Miho Hatanaka,[‡] Galina P. Petrova,[∥] Travis V. Harris,[‡,⊥] Xin Li,[#] Zhuofeng Ke,[∇] Fengyi Liu,[○] Hai-Bei Li,[■] Lina Ding,[▲] and Keiji Morokuma*,[‡]

[†]Department of Chemistry, South University of Science and Technology of China, Shenzhen 518055, China

[‡]Fukui Institute for Fundamental Chemistry, Kyoto University, 34-4 Takano Nishihiraki-cho, Sakyo, Kyoto 606-8103, Japan

[§]Newcastle Institute for Energy and Resources, The University of Newcastle, Callaghan 2308, Australia

[∥]Faculty of Chemistry and Pharmacy, University of Sofia, Bulgaria Boulevard James Bourchier 1, 1164 Sofia, Bulgaria

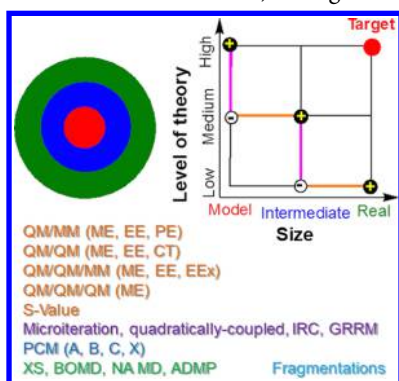[⊥]Department of Chemistry, State University of New York at Oswego, Oswego, New York 13126, United States

[#]State Key Laboratory of Molecular Reaction Dynamics, Dalian Institute of Chemical Physics, Chinese Academy of Sciences, Dalian 116023, China

[∇]School of Chemistry and Chemical Engineering, Sun Yat-sen University, Guangzhou 510275, China

[○]Key Laboratory of Macromolecular Science of Shaanxi Province, School of Chemistry and Chemical Engineering, Shaanxi Normal University, Xi'an, Shaanxi 710119, China

[■]School of Ocean, Shandong University, Weihai 264209, China

[▲]School of Pharmaceutical Sciences, Zhengzhou University, 100 Kexue Avenue, Zhengzhou, Henan 450001, China

CONTENTS

1. INTRODUCTION

The fields of theoretical and computational chemistry have come a long way since their inception in the mid-20th century. Fifty years ago, only rudimentary approximations for very simple molecules could be performed. Thanks in part to the ongoing development of very fast computers, and the efforts of theoretical chemists in developing fast and accurate quantum mechanical (QM) methods for calculating electronic energies of atoms and molecules, theoretical and computational

chemistry can now give reliable geometries, energies, reactivities, and electronic properties for molecules. Such information has become indispensable in understanding and explaining experimental results that would be otherwise difficult to interpret.

Despite these advances, it is still difficult and extremely time-consuming (as well as disk/memory-consuming) to calculate accurately the structure and properties of large and complex molecular systems using purely QM methods. Many efforts have been made to make such calculations feasible. One such effort is the hybrid method, otherwise known as a multiscale method. In a hybrid method, a large molecule is divided into multiple fragments. Different theoretical methods, ranging from very expensive and accurate methods to less expensive and accurate methods, are then applied to the different fragments. Such a method to combine expensive QM and inexpensive classical molecular mechanics (MM) force field was initiated by Honig and Karplus in 1971.[1] They adopted a Hückel QM method for π electrons energy (E_π) and a simple MM force field for nonbonded van der Waals interactions energy involving σ-electron framework (E_{nb}) to describe the torsional potential energy surface (PES) ($E_\pi + E_{nb}$) of a retinal molecule. A Pariser−Parr−Pople (PPP) SCF-CI method[2] was used to calculate excitation energies of the retinal molecule with different conformations. This hybrid method was further developed and extended by Warshel and Karplus (to describe ground and excited-state PESs by combining a PPP method[2] and an empirical function for π and σ electrons, respectively)[3] and was formalized in a "generic" QM/MM scheme by Warshel and Levitt.[4] Karplus, Levitt, and Warshel were awarded the 2013 Nobel Prize in Chemistry, for the "Development of Multiscale Models for Complex Chemical Systems".[5]

In this formalism, nowadays called "QM/MM", the entire molecular system is divided into two parts: the model system and the environment system. The small "model" part, the key chemically important layer, is treated with the accurate and expensive QM method. The remaining environment ("env") part is treated with the less accurate, but more efficient MM method (which cannot describe well bond breaking/formation or complex electronic state). In this scheme, as shown in eq 1, the total energy of the whole system, $E_{QM/MM}$, is a sum of the energy of the model system by the QM method (E_{QM}), the energy of the environment system by the MM method (E_{MM}), and the interactions ($E_{QM−MM}$) between the QM model system and the MM environment system.

$$E_{QM/MM} = E_{QM} + E_{MM} + E_{QM−MM} \tag{1}$$

This scheme is sometimes called an "additive" scheme,[6] in which the energies of the two systems and the interactions between the two systems are added to obtain the total energy of the whole system. The QM/MM coupling Hamiltonian ($E_{QM−MM}$), the interactions between the "model" and "env" systems, generally includes (1) bonded interactions for covalent bond(s) bisecting the QM/MM boundary (i.e., stretching, bending, and torsional contributions), and (2) nonbonded interactions (i.e., van der Waals and electrostatic interactions).[7] All QM−MM interactions are classically evaluated, although the electrostatic interactions can be computed "semi-classically". The QM/MM method has been developed widely by many researchers, with many different adaptations, and has been reviewed extensively.[6,8]

On the other hand, the ONIOM method (that includes the IMOMM and IMOMO methods) is a "subtractive" or "extrapolative" scheme, as will be shown in detail later.[8f,9] ONIOM can be considered as a hybrid method based on a somewhat different concept from the above-mentioned "generic" two-layer QM/MM method. Although ONIOM can be used as a two-layer QM/MM method, it can also, uniquely, combine different QM and QM methods, and can easily be extended to multiple layers (i.e., more than 2).

In this Review, we will introduce the details of the original ONIOM method developed by the Morokuma group, as well as discuss and compare more recent improvements of the ONIOM method and alternative approaches (section 2). We then overview applications of the ONIOM method to seven important chemical, biological, and material systems: organic systems (section 3), inorganic compounds and homogeneous catalysis (section 4), heterogeneous catalysis (section 5), nanomaterials (section 6), excited states (section 7), solution chemistry (section 8), and biological macromolecules (section 9).

2. THE ONIOM METHOD AND RELATED METHOD DEVELOPMENTS

To clearly present the original ideas and concepts of the IMOMM, IMOMO, and ONIOM methods, we will first discuss mainly the methods originally developed by Morokuma and co-workers in section 2.1. These original method developments have triggered many recent ONIOM method improvements, as well as some alternatives for the multilayer multilevel approaches. These ONIOM method improvements and alternative approaches will be discussed and compared in section 2.2. Advanced ONIOM simulation methods and guidelines will be outlined in section 2.3.

2.1. Original IMOMM, IMOMO, and ONIOM Methods and Formulation

2.1.1. Extrapolative IMOMM, IMOMO, and ONIOM Schemes. In 1995, Maseras et al. proposed and developed an alternative QM/MM scheme, so-called Integrated Molecular Orbital (MO) + Molecular Mechanics (IMOMM, eq 2).[10] The IMOMM method can be considered as the first generation of the ONIOM methods developed by Morokuma and co-workers. As opposed to the additive QM/MM schemes that evaluate $E_{QM−MM}$ (eq 1), IMOMM is a "subtractive" or "extrapolative" method: the total energy of the whole ("real") system is evaluated as the MO (or QM) energy of the model system ($E_{QM,model}$) plus the MM energy of the real system ($E_{MM,real}$), and minus the MM energy of the model system ($E_{MM,model}$):

$$E_{IMOMM} = E_{ONIOM2(QM:MM)} = E_{QM,model} + E_{MM,real}$$
$$- E_{MM,model} \tag{2}$$

The subtractive operation removes the "double-counted" MM contributions.[10,11] The IMOMM method was first applied to study several simple systems (the equilibrium geometry of cyclopropene and S_N2 reactions of alkyl chloride complexes),[10] conformations of ethane/butane, as well as oxidative addition of $Pt(PR_3)_2$ (R = H, Me, t-Bu, and Ph) complexes with H_2.[11,12]

As shown in Figure 1a, subtraction of the MM energy of the real system from that of the model system (i.e., $E_{MM,real} − E_{MM,model}$) is used to obtain the effect of the environment on the model system with an inexpensive MM method. Therefore, the IMOMM method can be considered as a size extrapolation[13] from the accurate QM calculation of the small
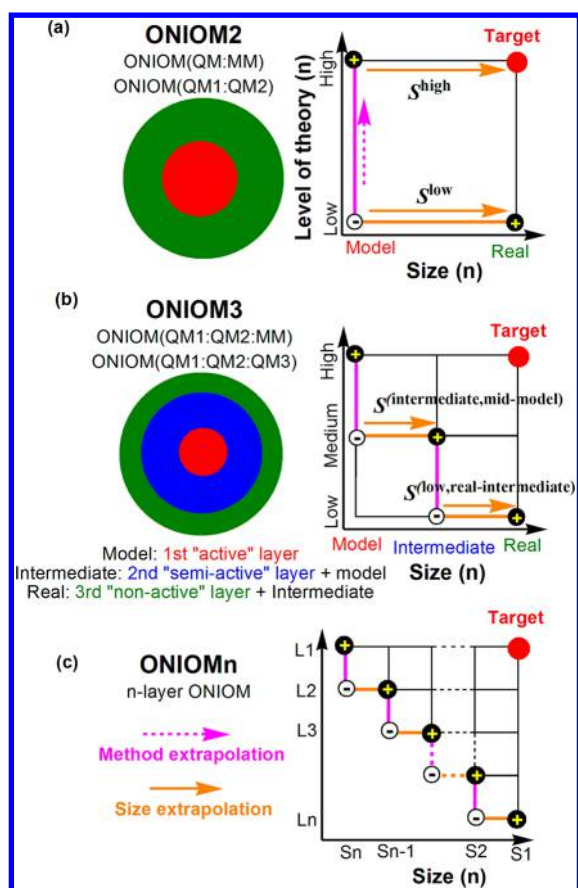
Figure 1. Schematic partitions of the whole system by the ONIOM methods: (a) two-layer ONIOM, (b) three-layer ONIOM, and (c) *n*-layer ONIOM.

model system ($E_{\text{QM,model}}$) to the large real system (E_{real}), by adding the approximate environmental effect evaluated by the inexpensive MM method. From an alternative viewpoint, the IMOMM method can also be considered as the extrapolation of the method (i.e., $E_{\text{QM,model}} - E_{\text{MM,model}}$) from the MM level to the high accuracy QM level starting from the MM energy of the real system, $E_{\text{MM,real}}$.

As compared to the additive QM/MM scheme (eq 1), the absence of the additional QM−MM coupling Hamiltonian ($E_{\text{QM−MM}}$) in the extrapolative IMOMM method makes its implementation easier, and avoids under- or overcounting the QM−MM interactions. Different from the additive scheme, MM calculations of the model system are required in the IMOMM (or subsequently ONIOM2(QM:MM)) method. Therefore, a good set of MM force field parameters for the model system is needed. Nevertheless, due to cancellation of additive MM terms,[8f] only nonbonded parameters for the model system such as van der Waals parameters and atomic charges (for the case of the mechanic embedding, to be discussed later), as well as bonded parameters for the QM/MM boundary, are important.[8f,9b] They should also be required in the additive QM/MM scheme.

Soon after the IMOMM method development, Humbel et al. extended the philosophy of the extrapolation step to a new hybrid method of combining two different QM (or MO) methods, so-called Integrated Molecular Orbital + Molecular Orbital (denoted as IMOMO or ONIOM2(QM1:QM2)).[13] The energy function for the IMOMO method is the sum of the high-level QM (QM1) energy of the model system ($E_{\text{QM1,model}}$)

and the low-level QM (QM2) energy of the real system (i.e., $E_{\text{QM2,real}}$) with subtraction of the low-level QM energy of the model system ($E_{\text{QM2,model}}$) (eq 3 and Figure 1a).

$$E_{\text{IMOMO}} = E_{\text{ONIOM2(QM1:QM2)}} = E_{\text{QM1,model}} + E_{\text{QM2,real}}$$
$$- E_{\text{QM2,model}} \qquad (3)$$

In both IMOMM and IMOMO, or in general in the two-layer ONIOM2 method, the high-level energy of the real system, $E_{\text{high,real}}$, that is the target energy, could be approximated by

$$E_{\text{high,real}} \approx E_{\text{ONIOM2(high:low)}} = E_{\text{high,model}} + E_{\text{low,real}}$$
$$- E_{\text{low,model}} \qquad (4)$$

Both ONIOM and generic QM/MM methods are applied to obtain a reliable relative energy difference (between structures or states), which are chemically and physically more important than the absolute energy of the system (fragmentation methods focus on, see section 2.3.2). The ONIOM2 method can be considered to approximate the expensive high-level "$100" calculation, for the large real system, $E_{\text{high,real}}$, by three less expensive calculations, a "$10" calculation for the high-level small model system, $E_{\text{high,model}}$, another "$10" calculation for the low-level real system, $E_{\text{low,real}}$, and a "$1" calculation for the low-level model system, $E_{\text{low,model}}$.

2.1.2. Estimating Error in the ONIOM2 Method and S-Value Test. Now let us pay attention to the error caused by the ONIOM2 approximation. The error (Err) is the energy difference between the ONIOM2 energy $E_{\text{ONIOM2(high:low)}}$ and the target energy, $E_{\text{high,real}}$:

$$\text{Err} = E_{\text{ONIOM2(high:low)}} - E_{\text{high,real}} \qquad (5)$$

Using eq 4, this can be rewritten as

$$\text{Err} = E_{\text{ONIOM2(high:low)}} - E_{\text{high,real}}$$
$$= (E_{\text{high,model}} + E_{\text{low,real}} - E_{\text{low,model}}) - E_{\text{high,real}}$$
$$= (E_{\text{low,real}} - E_{\text{low,model}}) - (E_{\text{high,real}} - E_{\text{high,model}}) \qquad (6)$$

The S-values (substituent-values)[14−16] for high- and low-level methods are defined as follows:

$$S_{\text{low}} = E_{\text{low,real}} - E_{\text{low,model}}$$
$$S_{\text{high}} = E_{\text{high,real}} - E_{\text{high,model}} \qquad (7)$$

Next, to identify and quantify the sources of error, the ONIOM2 error can be rewritten as

$$\text{Err} = S_{\text{low}} - S_{\text{high}} \qquad (8)$$

This means that, if S_{low} is equal to S_{high}, the ONIOM2 approximation has no error or it is exact!! It is clear from this result that the role of the low-level method in ONIOM2 is to reproduce the difference between the real and model systems, S_{low}, as close as possible to that difference in the high-level method, S_{high}. The S-value, one may call "the effect of the environment", represents the effects of substituents (thus called the S-value),[14−16] ligands, or any change in the real system, as compared to the model system.

Because the error of the ONIOM2 method is clearly defined, one can estimate the error for the particular choice of high and low levels and real and model systems used in ONIOM2

calculations, performing a few expensive target calculations. At a variety of candidates for low levels as well as the desired high level, one performs the expensive target calculations for a few sample cases (such as some simpler substituents and/or ligands) both for the real system and for the model system and evaluates S_{level}. If the S-value for a chosen low level is close to that for the target high level, the error (Err) is small, and this low level is a good method to use in combination with the present high level. This S-value test is strongly recommended for confirming the reliability of the chosen high- and low-levels combination for a chosen model system in the ONIOM

Table 1. Computed ΔS Value for Hydrogen Atom Dissociation from Iso-butane and Toluene by Using Methane as the Model System and B3LYP-Optimized Geometries[a]

method	iso-butane	toluene
G2MS(R)	−7.75 (0.00)	−16.21 (0.00)
UHF	−7.29 (+0.46)	−26.12 (−9.91)
RHF	−6.73 (+1.02)	−10.28 (+5.93)
UMP2	−7.72 (+0.03)	+6.93 (+23.14)
RMP2	−8.10 (−0.35)	−15.04 (+1.17)

[a]G2MS(R) method is the target high-level method. Reprinted with permission from ref 15. Copyright 2000 John Wiley & Sons, Inc.

calculation, if the size of the real system (e.g., nonproteins) is not too large to be treated by the high-level QM method. Vreven et al. used hydrogen atom dissociation from iso-butane and toluene for the S-value test (Table 1).[15] When using methane as the model system and G2MS(R) method as the target method, the S-value test showed that UMP2 and RMP2 methods give similar ΔS values for the dissociation from iso-butane and toluene, respectively. These S-value test results demonstrate that ONIOM(G2MS(R):UMP2) and ONIOM-(G2MS(R):RMP2) methods should give the least error of the dissociation energy of iso-butane and toluene, respectively. Alternatively, the RMP2 method could also be applied as the sole lower-level QM method to evaluate the dissociation energy of both iso-butane and toluene.

2.1.3. Multilayer Multilevel ONIOM Method. The ONIOM extrapolative scheme is not restricted to two layers. Svensson et al. combined the extrapolative two-layer IMOMM and IMOMO schemes to develop a three-layer ONIOM3-(QM1:QM2:MM) method (so-called Our own N-layered Integrated molecular Orbital and molecular Mechanics, ONIOM).[17] As shown in Figure 1b, the entire "real" system can be divided into three systems, "model", "intermediate", and "real", and three levels of theory, "low", "medium", and "high", can be used. With this three-layer scheme, ONIOM3, the energy of the real system at the high level is approximated as[17]

$$E_{ONIOM3(high:medium:low)} = E_{high,model} + E_{medium,intermediate}$$
$$- E_{medium,model} + E_{low,real} - E_{low,intermediate} \quad (9)$$

Any combination of three levels in the decreasing order of accuracy can be adopted in ONIOM3. The typically adoptable levels are high = QM1, medium = QM2, and low = QM3 or MM, where high-level QM1 often is an ab initio or DFT method, medium-level QM2 is a low-level ab initio, DFT, or semiempirical (SE) QM method, and low level is an SE QM method or an MM method. As an early example, Vreven et al. combined three different QM methods, ONIOM3-

(QM1:QM2:QM3), to study bond dissociation energy of hexaphenylethane.[14] Of course, ONIOM3 is reduced to ONIOM2, if two levels (among high, medium, and low levels) are the same or two systems (among model, intermediate, and real systems) are the same.

The error in ONIOM3 (Err$_{ONIOM3}$) with respect to the target $E_{high,real}$ calculation can be evaluated using S-values, as in ONIOM2, and can be written as

$$Err_{ONIOM3} = E_{ONIOM3(high:medium:low)} - E_{high,real}$$
$$= (E_{low,real} - E_{low,intermediate}) + (E_{medium,intermediate}$$
$$- E_{medium,model}) - (E_{high,real} - E_{high,model}) \quad (10)$$

The ONIOM3 S-values[16] are defined as

$$S_{low,(real-intermediate)} = E_{low,real} - E_{low,intermediate}$$
$$S_{medium,(intermediate-model)} = E_{medium,intermediate} - E_{medium,model}$$
$$S_{high,(real-model)} = E_{high,real} - E_{high,model} \quad (11)$$

Thus, ONIOM3 error can be rewritten as

$$Err_{ONIOM3} = S_{low,(real-intermediate)} + S_{medium,(intermediate-model)}$$
$$- S_{high,(real-model)} \quad (12)$$

This means that ONIOM3 is exact or has no error, if the sum of the low-level S-value ($S_{low,(real-intermediate)}$ from the intermediate system to the real system) and the medium-level S-value ($S_{medium,(intermediate-model)}$ from the model system to the intermediate system) is equal to the high-level S-value ($S_{high,(real-model)}$ all of the way from the model system to the real system). The role of the low level is to reproduce the environment/substituent effect going from the intermediate system to the real system, and that of the medium level is to reproduce the environment/substituent effect going from the model system to the intermediate system.

The ONIOM method can be easily expanded and generalized to an n-layer n-level method (e.g., QM, SE, MM, coarse-grained (CG),[18] and continuum model (CM) methods), ONIOMn, depicted in Figure 1c:

$$E_{ONIOMn} = \sum_{i=1}^{n} E[\text{level}(i), \text{model}(n + 1 - i)]$$
$$- \sum_{i=2}^{n} E[\text{level}(i), \text{model}(n + 2 - i)] \quad (13)$$

Implementation has not been made in Gaussian[19] for n = 4 or larger. However, it should be noted that no special code is required to perform ONIOMn single-point calculations (with $(2n − 1)$ independent subcalculations (eq 13)).[9b,17] In practice, the significance of using more than three layers may need to be examined carefully for any particular situation. There are many hierarchical electronic structure methods, such as Gn theory (see section 2.1.9),[20] in which higher correlation methods combined hierarchically with decreasing basis sets are adopted to approximate the highest correction method with a large basis set, for a given molecule. The ONIOM extrapolative method can be considered as a hierarchical method combining both the size of the molecule (or system) and the accuracy of the theory (or level) that approximates an accurate calculation for a large molecule.
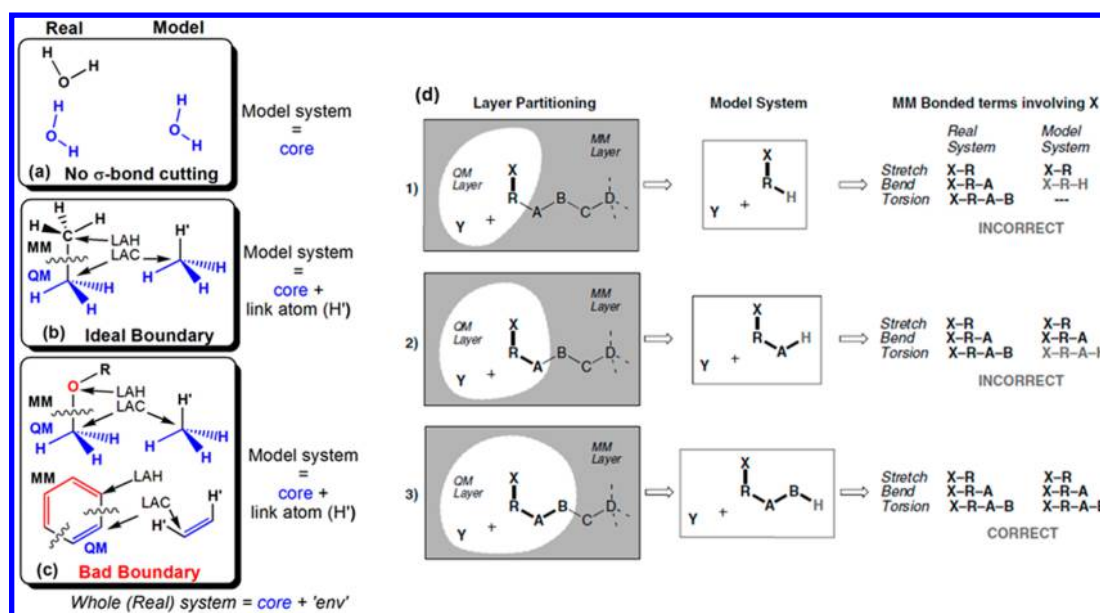
Figure 2. Three schematic QM/MM boundary cases: (a) without and (b,c) with a covalent bond cutting through the QM/MM boundary. (c) Examples of the bad QM/MM boundary. ONIOM definition of model, environment ("env") and real systems as well as link atom (LA, H′), link atom host (LAH), and link atom connection (LAC). (d) Effect of the position of LA on MM energy terms for a substitution of X by Y in three different QM/MM boundaries. Reprinted with permission from ref 25. Copyright 2010 Wiley-VCH Verlag GmbH & Co. KGaA.

It is not straightforward to combine two different QM methods with the MM method in an additive QM/MM fashion. Within the framework of the additive QM/MM scheme to evaluate E_{QM-MM}, Chung et al. proposed to combine the ONIOM2(QM1:QM2) method with MM to derive a version of the mixed QM1/QM2/MM method:[9b,d]

$$E_{QM1/QM2/MM} = (E_{QM1,model} + E_{QM2,intermediate}$$
$$- E_{QM2,model}) + E_{MM} + E_{QM-MM} \qquad (14)$$

Likewise, n-layer QM/MM schemes are feasible by using the extrapolative ONIOM approach for the $(n − 1)$ QM methods.

2.1.4. Mechanical and Electronic Embedding Schemes in ONIOM(QM:MM). A mechanical embedding[21,22] (ME) scheme was first implemented in the original ONIOM method (ONIOM-ME).[8f,10,23] This scheme is the simplest and least computational demanding method to treat the QM/MM electrostatic interactions in a classical manner ($\sum_i \sum_j (q_i(core) q_j(env))/(R_{ij})$), by using fixed atomic point charges (q) in the core and environment systems (Figure 2). However, the polarization of the QM wave function by the MM environment system is not included. The QM2/MM electrostatic interactions are treated in the same way in the ONIOM-(QM1:QM2:MM)-ME scheme. Therefore, the accuracy of QM/MM electrostatic interactions, which can be critical for the total energy of the real system, depends strongly on the atomic charges of the core system (or the intermediate system), which must be defined by the user. We note that these charges could be less important for geometries[24] (in the absence of highly polar immediate MM environment based on our experience). On the other hand, the energy difference between different electronic states as well as different geometries (such as reactant and transition state) is more sensitive to the polarization of the QM wave function, and performing an ONIOM electronic embedding (EE) scheme single-point calculation is recommended.

Using default atomic charges parameterized for one specific force field in the ME scheme is the easiest approach. However, using a set of the fixed atomic charges for the model system (or the intermediate system) will not give accurate QM/MM electrostatic interactions, particularly when describing changing structures during chemical reactions or changing electronic states such as photoinduced processes. This simple approach must be used with caution and verified, particularly when there is significant change in the charge distribution within the model system (or the intermediate system), as is the case for reactions and excited states involving significant charge transfer.

The MM atomic charges of the "core" system (excluding link atoms, LAs) can be computed and updated (denoted as ONIOM-MEUC[9b]) after each or several ONIOM geometry optimization steps to reflect a geometry-consistent electronic state and charge distribution, until the ONIOM energy converges to a threshold (e.g., 0.1 kcal/mol).[26] To give more reliable QM/MM electrostatic interactions in the ONIOM-ME scheme, a six-step charge-fitting/updating step was proposed (using ESP[27] or RESP charge).[26] Some conventional charges, for example, Mulliken[28] and Löwdin charges, can be adopted.

The net charges of the real, core, and environment systems should ideally be integer.[6] Also, no net charge of the real, core, and environment systems should be artificially created or destroyed. For the ONIOM-MEUC method, the total net charge of the real system can change in every optimization step, if the atomic charges for the core system are used without any modification and the atomic charges of LA are nonzero. There are several possible solutions: (1) assigning the updated atomic charge of LA to LAH (link atom host), while leaving the updated charges of the core system unchanged;[29] (2) fitting ESP or RESP charges for the core system by constraining the charge of LA to be zero;[26,30] and (3) applying an "effective charge operator" to the electrons in the core system with a scaling factor, and setting the zero charge of LA to redistribute the charge of LA to all atoms in the core system.[31]

2.1.4.1. ONIOM(QM:MM)-EE Scheme. To improve the QM/MM electrostatic interactions and include polarization of the QM wave function by the MM environment, an one-electron term describing the atomic charges in the MM environment system can be added to the QM Hamiltonian that is applied to the QM model system. In this case, the energy of the whole system is written as eq 15:[8f]

$$E_{\mathrm{ONIOM(QM:MM)-EE}} = E_{\mathrm{QM,model}}^{\mathrm{v}} + E_{\mathrm{MM,real}} - E_{\mathrm{MM,model}}^{\mathrm{v}} \tag{15}$$

where the Hamiltonian is expressed as follows:

$$H_{\mathrm{QM,model}}^{\mathrm{v}} = H_{\mathrm{QM,model}} - \sum_{I}\sum_{N}\frac{s_N q_N}{R_{IN}} + \sum_{J}\sum_{N}\frac{Z_J s_N q_N}{R_{JN}} \tag{16}$$

is used for the QM calculation of the model system. N, J, and I denote the MM atom, QM atoms, and QM electrons, respectively, and q_N and s_N are the embedded charge and a scale factor for the MM atom N; Z_J is the nuclear charge of the QM atom J. Here, the QM/MM electrostatic interactions (based on fixed MM point charges) and the QM density are self-consistently computed for the QM region. This is the so-called EE scheme.[8f,21,22] It should be noted that polarization of the MM environment system by the QM region is not accounted for in the EE scheme. Unfortunately, there are two inevitable QM−MM boundary problems for the EE scheme: (1) overpolarization of the QM wave function by nearby MM charges (especially for the link atom (LA) by its adjacent link atom host (LAH); see Figure 2 and section 2.1.5), and (2) under- or overcounting QM/MM electrostatic interactions. The latter problem is due to the fact that electrostatic interactions among nearby atoms (such as 1−4 bonded atomic pairs) are implicitly included in the parameterized stretching, bending, and dihedral terms of general biomolecular force fields. Several charge-scaling,[8f] charge-shift/redistribution,[32,33] or Gaussian smeared-charge[34,35] approaches can be applied to reduce this overpolarization problem and correct the under- or overcounting problems.[36] However, the charge-scaling/deletion approaches may undercount electrostatic interactions with QM atoms that are far from the QM/MM boundary.[8f]

Vreven et al. developed and also implemented ONIOM-(QM:MM)-EE in the Gaussian program.[8f,28] The ONIOM-(QM:MM)-EE method implementation (eq 15) is different from the additive QM/MM-EE schemes.[8f] The MM point charges are embedded into the two model calculations ($E_{\mathrm{QM,\,model}}^{\mathrm{V}}$ and $E_{\mathrm{MM,\,model}}^{\mathrm{V}}$, eq 15) in the ONIOM-EE scheme, while the MM point charges are only incorporated into the QM model calculation and the classical QM/MM electrostatic term is removed in the generic QM/MM-EE scheme.[6,8f] To avoid overpolarization of the QM model system, atomic charges of the MM environment system within three bonds of the QM/MM boundary are deleted in the two model calculations in the default ONIOM-EE implementation. This was found to give the least error of deprotonation energy of histidine (Figure 3).[8f] Notably, even though the MM charges around the boundary are deleted in the two model ONIOM calculations, the missing electrostatic interactions with these MM charges are still considered by a classical Coulomb equation in the calculation of the real system ($E_{\mathrm{MM,real}}$) in ONIOM-EE.[8f,28] This is unique to ONIOM-EE and can remedy both overpolarization and the under-/overcounting problems. Another major difference between the QM/MM-EE and ONIOM-EE methods is that
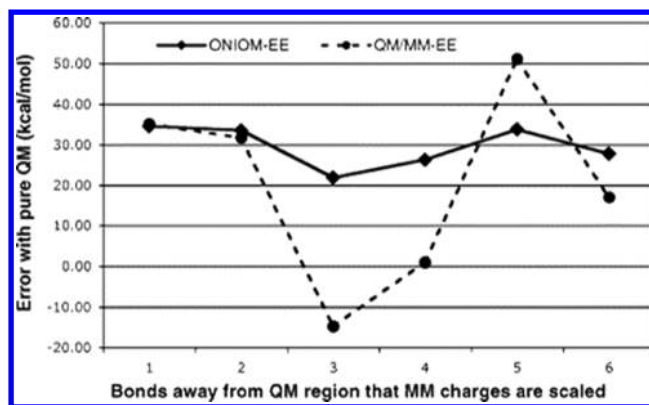
Figure 3. Error of the ONIOM-EE and QM/MM-EE methods combined with the charges-deletion approach for different bonds away from the QM part. Reprinted with permission from ref 8f. Copyright 2006 American Chemical Society.

atomic charges for the model system should be added using ONIOM.[8f]

2.1.4.2. ONIOM(QM1:QM2:MM)-EE Scheme. Vreven et al. developed and implemented two extensions of the original EE scheme to the three-layer ONIOM method: ONIOM-(QM1:QM2:MM)-EE and ONIOM(QM1:QM2:MM)-EEx (eqs 17 and 18):[8f]

$$E_{\mathrm{ONIOM(QM1:QM2:MM)-EE}} = E_{\mathrm{QM1,model}}^{\mathrm{v}} + E_{\mathrm{QM2,intermediate}}^{\mathrm{v}}$$
$$- E_{\mathrm{QM2,model}}^{\mathrm{v}} + E_{\mathrm{MM,real}} - E_{\mathrm{MM,intermediate}}^{\mathrm{v}} \tag{17}$$

$$E_{\mathrm{ONIOM(QM1:QM2:MM)-EEx}} = E_{\mathrm{QM1,model}} + E_{\mathrm{QM2,intermediate}}^{\mathrm{v}}$$
$$- E_{\mathrm{QM2,model}} + E_{\mathrm{MM,real}} - E_{\mathrm{MM,intermediate}}^{\mathrm{v}} \tag{18}$$

The MM charges here are embedded in the model calculations in ONIOM(QM1:QM2:MM)-EE, whereas the MM charges are completely excluded in ONIOM(QM1:QM2:MM)-EEx, which mimics the screening effect of the intermediate system on the model system.

2.1.5. The Boundary between QM and MM Layers. In ONIOM, the whole system is divided into small models or regions. For example, in ONIOM2, it is trivial to separate the "model" and "environment" systems if there is no covalent bond between them. Taking a water dimer as an example (Figure 2a),[37] one H_2O can be treated as the model system by QM methods, and the whole dimer can be treated as the real system by MM methods, with no complications. ONIOM2-(QM:MM) should give results identical to those of the additive QM/MM scheme, due to cancellation of MM terms.[8f] Using the same approach for CH_3-CH_3, for example (i.e., one CH_3 group is the core system and the whole CH_3-CH_3 is the real system, Figure 2b), one would have to cut the C−C σ bond; this will lead to dangling bonds or radicals and may introduce complications due to the unphysical boundary. Such QM/MM boundary cutting is inevitable in many cases. Many different approaches have been proposed to deal with this "boundary" problem in multilayer approaches. In general, there are three boundary approximations: link atom (LA), boundary atom (or pseudobond), and frozen localized orbital.[6,8c] Some of these approximations will be discussed in section 2.2.

In ONIOM, the link atom approach has been employed in the Gaussian program.[8f,10,23] ONIOM uses hydrogen link atoms by default: all dangling σ bonds in the model system are

capped with hydrogen atoms. This is the simplest and most common boundary approximation, which was used earlier by the Kollman and Karplus groups.[38] However, other monovalent atoms (e.g., fluoride link atom[23]) can alternatively be used as link atoms to complete the dangling single bond. Likewise, divalent atoms (e.g., oxygen, sulfur) could be used to saturate the dangling double bond (although it is strongly recommended this is avoided, if alternative choices exist).[23]

The positions of LAs can be independent of those of the link atom host (LAH, the atom replaced by the link atom) and the link atom connection (LAC, the atom bound to LAH in the "real" system and to LA in the "model" system), as the simplest LA treatment shown in Figure 2. However, this artificially increases the degrees of freedom in the system, and leads to unnecessary complications, as in earlier implementations of generic QM/MM methods. An alternative approach, used in early IMOMM, and IMOMO and ONIOM implementations, is to fix the LAC−LAH and LAC−LA bond distances at reasonable values (the bond angles and dihedrals involving LA are also fixed), meaning that the position of LA is independent of the position of LAH.[10,13,17] This early implementation results in fewer degrees of freedom, and thus vibrational analysis cannot be performed. The IMOMO method was modified by adding a harmonic term to improve this problem, so-called Integrated Molecular Orbital with Harmonic Cap (IMOHC).[39]

The best and now-standard treatment of LAs in ONIOM was proposed and implemented by Dapprich et al. (eq 19).[23] In this method, the position vectors of LA, R_{LA}, LAH, R_{LAH}, and LAC, R_{LAC}, are set, which enables the position of the LA to be determined as follows:

$$R_{LA} = R_{LAC} + g(R_{LAH} - R_{LAC}) \qquad (19)$$

This means that the position of the LA is directly on the bond between the LAC and the LAH (i.e., along the C−C bond in the previous CH_3−CH_3 example). The length of the LAC−LA bond (the C−H′ bond) is scaled by a constant g from the LAC−LAH C−C bond (a variable g value was also proposed[40]). One of the greatest strengths of defining LA position in this way is that the position of the fictitious LA is determined by the position of the atoms in the "real" system. Thus, the degree of freedom of the ONIOM system remains to be $3N - 6$, where N is the total number of atoms in the "real" system. The ONIOM energy is therefore well-defined as a function of the coordinates of the atoms in the "real" system (as the full QM energy), as are the gradient of the energy and the Hessian. This enables optimization, vibrational analysis, and molecular dynamics (MD) simulations to be performed. In practice, more than one covalent bond can be cut from the real system, and each dangling bond should be capped with a link atom. Ideally, cutting more than one bond on the same (LAC or LAH) atom at the QM/MM boundary should be avoided.

The error introduced by LAs can be minimized in the ONIOM method, and artifacts derived from the LAs can be implicitly correct if the force fields for the LAs can reproduce the QM energies for LAs.[8f] Notably, because of eq 19, stretching the LAC−LAH bond (described with the MM method) transfers to stretching the LAC−LA bond (which is evaluated quantum mechanically).[8f] The ONIOM boundary treatment can also be considered as the classical correction of the link atoms to the LAH atoms.[8f] One hopes that the error of the link atom for different structures may fortuitously cancel to get a reliable relative energy (e.g., reaction barrier or energy).

A default value of g is usually used in eq 19. Recently, Vreven et al. implemented an alternative ONIOM link atom treatment in Gaussian,[8f] in which two different g values are used in the QM and MM model systems. For the MM model system, g can be set to 1, the Jacobian matrix (see section 2.1.6) is set to the unit matrix, and the MM atom type of LA is set to that for LAH in this alternative settings. All MM terms for LA from the model and real systems cancel each other, and the QM/MM boundary is solely dependent on the QM calculations involving LA.

To minimize errors from hydrogen LAs in QM/MM and ONIOM methods, the bond cutting through the QM/MM boundary should be examined thoroughly.[6,8f] To be consistent with an electronegativity of the hydrogen LA, ideally an inert C_{sp3}−C_{sp3} bond should be cut (Figure 2b). Cutting polar bonds with strong inductive effects (e.g., C−O, Si−O) and conjugated bonds with strong conjugation effects should be avoided in QM/MM and ONIOM calculations (Figure 2c). Furthermore, the QM/MM boundary should be at least three bonds away from the site at which bonds are being formed/broken in the model system, to avoid discontinuous PESs (Figure 2d).[8f,25] Taking a substitution of X by Y (i.e., the R−X bond broken and the R−Y bond formation, Figure 2d) as an example, all MM bonded energy terms involving the link atom are canceled out only when the QM/MM boundary is put at least three bonds away from the reaction site.

To cut a polar bond, Dapprich et al. examined the use of a F link atom to mimic the CF_3 group.[23] However, a very long C−C boundary bond of 1.841 Å was found and concluded that F was not a good LA for mimicking the C−CF_3 bond. In this connection, a shift operator developed by Koga et al.[41] was suggested for incorporating electronic effects between LAH and LA in the ONIOM(QM:MM) method, by changing the one-electron energy and tuning the electronic properties of LA.[12,23]

The QM/MM boundary problem in the QM/MM and ONIOM methods is inevitable for many systems, and there is no perfect and efficient solution. However, one can use ONIOM3(QM1:QM2:MM) with an immediate environment system as a "link layer" to alleviate the QM/MM boundary problem. The link layer effectively moves the QM/MM boundary, and the MM environment is further away from the QM model system,[16,42] decreasing LA errors.

2.1.6. Energy, Gradient, Hessian, and Molecular Properties. The positions of LAs in ONIOM are defined by eq 19. The ONIOM2 energy, given by eq 4, can be rewritten as

$$E_{ONIOM2(high:low)}(\mathbf{R}) = E_{high,model}(\mathbf{R}_{model}) + E_{low,real}(\mathbf{R})$$
$$- E_{low,model}(\mathbf{R}_{model}) \qquad (20)$$

Here, all coordinate-dependent energy terms are specifically indicated. $E_{ONIOM2(high:low)}$ and $E_{low,real}$ are functions of the coordinates of the real system ($\mathbf{R}$), whereas $E_{high,model}$ and $E_{low,model}$ are generally functions of $\mathbf{R}_{model}$, the coordinates of the model system (including LAs, see Figure 2). The energy gradient of $E_{ONIOM2(high:low)}(\mathbf{R})$ with respect to the nuclear coordinate of the real system $\mathbf{R}$ can therefore be written as

$$\frac{\partial E_{ONIOM2(high:low)}(\mathbf{R})}{\partial \mathbf{R}} = \frac{\partial E_{high,model}(\mathbf{R}_{model})}{\partial \mathbf{R}}$$
$$+ \frac{\partial E_{low,real}(\mathbf{R})}{\partial \mathbf{R}} - \frac{\partial E_{low,model}(\mathbf{R}_{model})}{\partial \mathbf{R}} \qquad (21)$$

The ONIOM2 gradient is a vector of $3N$ dimension. Using the chain rule between the coordinate of the real system $\mathbf{R}$ and that of the model system $\mathbf{R}_{model}$, one gets

$$\frac{\partial}{\partial \mathbf{R}} = \frac{\partial}{\partial \mathbf{R}_{model}} \frac{\partial \mathbf{R}_{model}}{\partial \mathbf{R}} = \frac{\partial}{\partial \mathbf{R}_{model}} \cdot \mathbf{J}(\mathbf{R}_{model}; \mathbf{R}) \tag{22}$$

where $\mathbf{J}(\mathbf{R}_{model}; \mathbf{R})$ is the Jacobian between $\mathbf{R}_{model}$ and $\mathbf{R}$.[23] As the position of the link atom is defined by eq 19 (depending on the positions of $\mathbf{R}_{model}$ and $\mathbf{R}$),[23] the Jacobian can be easily evaluated regardless of the methods (QM or MM). Combining eqs 21 and 22:

$$\frac{\partial E_{ONIOM2(high:low)}(\mathbf{R})}{\partial \mathbf{R}} = \frac{\partial E_{high,model}(\mathbf{R}_{model})}{\partial \mathbf{R}_{model}} \cdot \mathbf{J}(\mathbf{R}_{model}; \mathbf{R})$$
$$+ \frac{\partial E_{low,real}(\mathbf{R})}{\partial \mathbf{R}} - \frac{\partial E_{low,model}(\mathbf{R}_{model})}{\partial \mathbf{R}_{model}} \cdot \mathbf{J}(\mathbf{R}_{model}; \mathbf{R}) \tag{23}$$

Thus, the ONIOM2 gradient can be obtained from the three gradients $(\partial E_{high,model}(\mathbf{R}_{model}))/\partial \mathbf{R}_{model}$, $\partial E_{low,real}(\mathbf{R})/\partial \mathbf{R}$, and $\partial E_{low,\,model}(\mathbf{R}_{model})/\partial \mathbf{R}_{model}$,[23] which are calculated with standard QM and MM programs. Note that when LAs are not introduced (Figure 2a), $\mathbf{J}$ is the unit matrix and the ONIOM2 gradient has its simplest form.

Further derivation of eq 23 with respect to $\mathbf{R}$ gives the expression of the second derivative matrix,[23] or Hessian, as follows:

$$\frac{\partial^2 E_{ONIOM2(high:low)}(\mathbf{R})}{\partial \mathbf{R}^2} = \mathbf{J}^T \cdot \frac{\partial^2 E_{high,model}(\mathbf{R}_{model})}{\partial \mathbf{R}_{model}^2} \cdot \mathbf{J}$$
$$+ \frac{\partial^2 E_{low,real}(\mathbf{R})}{\partial \mathbf{R}^2} - \mathbf{J}^T \cdot \frac{\partial^2 E_{low,model}(\mathbf{R}_{model})}{\partial \mathbf{R}_{model}^2} \cdot \mathbf{J} \tag{24}$$

Because vibrational frequencies evaluated by QM methods are usually overestimated relative to the experimentally observed frequencies, an empirical scaling factor is often used for each theoretical method to increase accuracy of the computed frequencies. Likewise, scaling factors, $c1$, $c2$, $c3$, for different methods can be applied in the ONIOM calculations and easily incorporated as follows:[23]

$$\frac{\partial^2 E_{ONIOM2(high:low)}(\mathbf{R})}{\partial \mathbf{R}^2} = (c1)^2 \cdot \mathbf{J}^T \cdot \frac{\partial^2 E_{high,model}(\mathbf{R}_{model})}{\partial \mathbf{R}_{model}^2} \cdot \mathbf{J}$$
$$+ (c2)^2 \cdot \frac{\partial^2 E_{low,real}(\mathbf{R})}{\partial \mathbf{R}^2} - (c3)^2 \cdot \mathbf{J}^T \cdot \frac{\partial^2 E_{low,model}(\mathbf{R}_{model})}{\partial \mathbf{R}_{model}^2} \cdot$$
$$\mathbf{J} \tag{25}$$

The Hessian is a $3N \times 3N$ matrix. Because of the relationship shown in eq 19 for the positions of the LAs, the ONIOM Hessian and gradient have correct dimensionality and can be used directly for geometry optimization, vibrational normal modes, and frequency calculations and MD simulations.[23]

The above gradient and Hessian expressions for ONIOM2 can be easily generalized for the gradient and Hessian for ONIOM3 and ONIOMn methods. For brevity, no explicit expressions will be given in this Review. The energy, gradient, and Hessian for ONIOM2 and ONIOM3 have been implemented in Gaussian by the original authors, enabling geometry optimizations, vibrational frequency calculations, and molecular dynamics simulations. One may also note that any

electronic structure codes, which provide energy and gradient (and Hessian if needed), can also be used as an "external" part of ONIOM calculations in the Gaussian program.

ONIOM Hessian can be used to compute vibrational normal modes and accurate infrared (IR) spectra of large molecular systems.[43] ONIOM infrared (I_{IR}) and Raman (I_{Raman}) intensity of the whole system can be expressed as

$$\mathbf{I}_{IR,ONIOM} = \frac{\partial^2 E_{ONIOM2(high:low)}(\mathbf{R})}{\partial \mathbf{R} \partial \mathbf{F}} = \mathbf{J}^T$$
$$\cdot \frac{\partial^2 E_{high,model}(\mathbf{R}_{model})}{\partial \mathbf{R} \partial \mathbf{F}} \cdot \mathbf{J} + \frac{\partial^2 E_{low,real}(\mathbf{R})}{\partial \mathbf{R} \partial \mathbf{F}}$$
$$- \mathbf{J}^T \cdot \frac{\partial^2 E_{low,model}(\mathbf{R}_{model})}{\partial \mathbf{R} \partial \mathbf{F}} \cdot \mathbf{J} \tag{26}$$

$$\mathbf{I}_{Raman,ONIOM} = \frac{\partial^3 E_{ONIOM2(high:low)}(\mathbf{R})}{\partial \mathbf{R} \partial \mathbf{F}_a \partial \mathbf{F}_b} = \mathbf{J}^T$$
$$\cdot \frac{\partial^3 E_{high,model}(\mathbf{R}_{model})}{\partial \mathbf{R} \partial \mathbf{F}_a \partial \mathbf{F}_b} \cdot \mathbf{J} + \frac{\partial^3 E_{low,real}(\mathbf{R})}{\partial \mathbf{R} \partial \mathbf{F}_a \partial \mathbf{F}_b}$$
$$- \mathbf{J}^T \cdot \frac{\partial^3 E_{low,model}(\mathbf{R}_{model})}{\partial \mathbf{R} \partial \mathbf{F}_a \partial \mathbf{F}_b} \cdot \mathbf{J} \tag{27}$$

where $\mathbf{F}$ is an electric field.

ONIOM is capable of computing various molecular properties of large systems. For instance, the ONIOM2 density can be defined as

$$\rho_{ONIOM2(high:low)} = \rho_{high,model} + \rho_{low,real} - \rho_{low,model} \tag{28}$$

Using this definition, a variety of one-electron molecular properties can be calculated with the ONIOM approximation. The equations of the other molecular properties (e.g., polarizability and hyperpolarizability tensors), which were expressed in a previous seminal work,[23] are not expressed in this Review for brevity.

2.1.6.1. Nuclear Magnetic Resonance. Computational prediction of nuclear magnetic resonance (NMR) chemical shifts is popular for the structural and geometrical assignment of compounds. The computationally demanding Gauge Invariant Atomic Orbital (GIAO) method has been proposed as a particularly accurate method for NMR parameter calculations, and ONIOM has received much attention for calculating NMR chemical shifts in large molecular systems. For a two-layer ONIOM(MP2-GIAO:HF-GIAO) scheme, Karadakov et al. used the following expression to calculate ONIOM isotropic NMR chemical shieldings:[44]

$$\sigma_{isoONIOM2(MP2-GIAO:HF-GIAO)}^N = \sigma_{isoMP2-GIAO,model}^N$$
$$+ \sigma_{isoHF-GIAO,real}^N - \sigma_{isoHF-GIAO,model}^N \tag{29}$$

This method was applied to calculate absolute isotopic (^{13}C, ^{17}O, and ^{19}F) proton NMR chemical shieldings in the water dimer, ethanol, acetone, acrolein, fluorobenzene, and naphthalene. ONIOM(MP2-GIAO:HF-GIAO) was consistent with the full MP2-GIAO results. The ONIOM method has also been applied to compute accurate NMR chemical shifts of a number of systems.[45]

2.1.7. ONIOM Energy Decomposition Analysis. MM methods in ONIOM(QM:MM) are often used to investigate the steric effects of substituents.[10] Even when the whole system

is too large for the pure QM method, using a low-level QM method, one can perform ONIOM(QM:QM) calculation that includes the electronic effects as well as steric effects of these
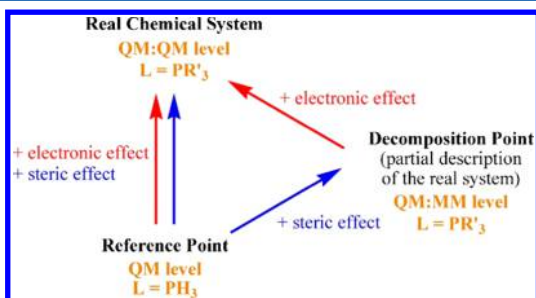

Figure 4. Energy decomposition analysis of the steric and electronic effects of the substituent. Reprinted with permission from ref 46. Copyright 2010 Elsevier.

substituents. Ananikov et al. proposed three-stage calculations ((1) the high-level QM model system, (2) ONIOM(QM:MM) for the real system, and (3) ONIOM(QM:QM) for the real system) to decompose the substituent effects into steric and electronic effects (Figure 4).[46] Hirao also combined the Kitaura−Morokuma energy decomposition analysis[47] (EDA) and ONIOM(QM:MM) to study the effects of protein in Cytochrome P450.[48]

2.1.8. Geometry Optimization and Microiteration Methods. Geometry optimization[49] of equilibrium structures, transition states (TSs), and minimum points on the seam of crossing (MSXs) is critical for understanding mechanisms of chemical reaction and photoinduced processes. Prior to the development of IMOMM, the influence of substituent effects during geometry optimizations was approximated with an iterative, "by-hand" technique: geometry optimization of the model system was performed using a QM method; substituents were then added and optimized using an MM method with the QM-optimized model system frozen ("QM-then-MM" optimization).[50] The optimization with the ONIOM method more rigorously incorporates the substituent effect on the geometry of the real system, without the need for tedious parameterization (e.g., empirical valence bond method (EVB)[51] or transition state force field[52]). In general, geometrical parameters of the model and environment systems by ONIOM geometry optimization are similar to those individually optimized by the high- and low-level methods, respectively.

2.1.8.1. Microiteration Method. Because there are significant degrees of freedom in the environment system as compared to the model system and the computational cost of the MM calculation for the real system is much lower that of the QM calculation for the model system, ONIOM uses an efficient hybrid optimization method. First, a complete geometry optimization of the environment system is performed with MM, with the fixed model system (microiterations). One expensive QM optimization step of the small model system with the entire environment system fixed is then performed (macroiterations). This process is repeated until atomic forces of the whole system converge to some specific threshold.[10,17,23,53] Such separate geometry optimization method can not only reduce the number of the expensive QM calculations, but it can also make use of two different and efficient optimization methods, such as a memory-demanding second-order algorithm (e.g., the Newton−Raphson (NR) or

rational function optimization (RFO) in redundant internal coordinates) for the small model system and a first-order algorithm (e.g., steepest descent or conjugate gradient optimization in Cartesian coordinates) for the large environment system. This efficient microiteration method has been implemented in many QM/MM programs.[54]

2.1.8.2. Quadratically Coupled Optimization Method. The hybrid macro-/microiteration geometry optimization method is an efficient method for the ONIOM(QM:MM) optimization of large systems, but it suffers from a few drawbacks.[55] First, the Hessian update used in the macroiteration step (which can be regarded as a formal ONIOM(QM:MM) optimization step) by the RFO method is not well-defined, as the QM and MM regions use different coordinate spaces. It can lead to bad force constants and incorrect curvature. Second, this macro-/microiteration optimization method excludes Hessian coupling between the QM coordinates and MM coordinates, which can result in oscillations in the optimization steps. Vreven et al. developed and implemented a quadratically coupled ONIOM-(QM:MM) geometry optimization scheme in Gaussian to solve this problem, which allows explicit Hessian coupling between the QM and MM parts in the QM optimization steps.[55] The MM contributions to the QM/MM Hessian coupling are computed analytically. In addition, an iterative Davidson diagonalization method was applied to solve the RFO equations without storing the Hessian:

$$
\begin{bmatrix} H^{\mathrm{ONIOM}} & g^{\mathrm{ONIOM}} \\ (g^{\mathrm{ONIOM}})^t & 0 \end{bmatrix} \begin{bmatrix} \Delta q^{\mathrm{ONIOM}} \\ 1 \end{bmatrix}
$$

$$
= \begin{bmatrix} H^{\mathrm{QM}} & H^{\mathrm{coupling}} & g^{\mathrm{QM}} \\ H^{\mathrm{coupling}} & H^{\mathrm{MM}} & g^{\mathrm{MM}} \\ (g^{\mathrm{QM}})^t & (g^{\mathrm{MM}})^t & 0 \end{bmatrix} \begin{bmatrix} \Delta q^{\mathrm{QM}} \\ \Delta q^{\mathrm{MM}} \\ 1 \end{bmatrix} = \lambda \begin{bmatrix} \Delta q^{\mathrm{QM}} \\ \Delta q^{\mathrm{MM}} \\ 1 \end{bmatrix}
$$

(30)

where H, g, and Δq represent Hessian, gradient, and magnitude of the step, respectively. The ONIOM geometry optimization with quadratic coupling was found to reduce the expensive macroiteration steps, improve optimization stability without erratic steps in the initial optimization, as well as converge to nearby local minimum.[55]

2.1.9. ONIOM Method Combined with High-Accuracy Methods. Quantitative prediction of chemical properties can be achieved by using the high-level ab initio methods, such as CCSD(T) with the very large basis sets. However, these methods can be applied for relatively small molecules due to poor scaling of computational costs with the size of the system. Several extrapolative schemes, Gaussian (Gn) models,[20,56] Weizmann (Wn) methods,[57] and complete-basis-set (CBS),[58] were proposed in the literature for predicting energies at a relatively low computational cost. These methods are referred as the "compound model chemistries", where a series of calculations with different levels of theories and basis sets are combined and applied to the entire molecular system.[59] These methods are very different from the present hybrid methods, such as IMOMO or ONIOM, where more accurate levels of theory are only applied to the smaller size of the subsystems (e.g., model system).

Froese et al. proposed IMOMO(G2MS) for accurate energy and property calculations of large molecular systems at a low-computational cost (Figure 5).[60] The G2-type approach can be
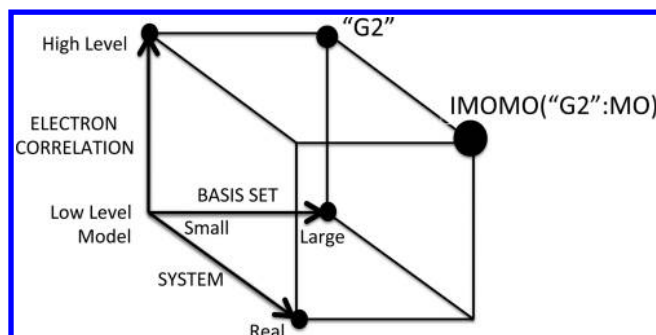
Figure 5. Three-dimensional extrapolation scheme connecting the G2-type and IMOMO methods. Reprinted with permission from ref 60. Copyright 1997 American Chemical Society.

used as a two-dimensional extrapolation to estimate the high-level electron correlation with a large basis set, where the effect of a large basis set can be evaluated at a lower level (e.g., MP2), while the effect of high-level electron correlation (e.g., CCSD(T)) can be calculated with a small basis set. Another dimension then can be included to represent the size of the system by using the IMOMO method. This approach extrapolates the results of a high-level calculation of the small model system and a low-level calculation of the real system to estimate the high-level result for the real system.

2.1.10. ONIOM Solvent Methods. The solvation effect is significantly important for many chemical and physical properties. To include the effect of solvent into the ONIOM calculation, two approaches have been used. One is the explicit solvent model, which describes the solvent molecules explicitly as low-level atoms. The other is the implicit solvent model, which describes the solvent as continuum medium. Especially, two methods, ONIOM-XS and ONIOM-PCM, were developed to include the solvation effect in the ONIOM calculation effectively. Here, their calculation schemes are explained. Their applications will be discussed mainly in section 8.

2.1.10.1. ONIOM-XS for Explicit Solvent Model. One can explicitly introduce many solvent molecules, which can be described by QM and/or MM methods, to solvate a molecular system. The total energy of the whole system then depends on configurations within the solvent shell. Sampling methods (such as MD or Monte Carlo (MC)) can be used to obtain different solvent configurations. However, conventional sampling methods combined with the multilayer methods have
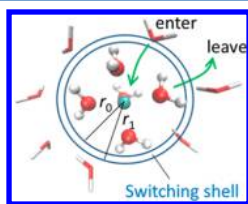
Figure 6. Schematic diagram of the ONIOM-XS method.

problems, because the solvent molecules in the high level often enter and leave the active region during the simulation, which results in the discontinuous potential energy and forces. Kerdcharoen et al. developed an adaptive ONIOM MD method to solve this problem, so-called "ONIOM-XS" (Figure 6).[61] In this method, a thin switching shell located between high- and low-levels is introduced to smooth the transition due to the solvent exchange.

The energy of the system depends on how the switching shell is defined. When a solvent molecule on the switching shell is included in the high-level region, the total energy can be written as

$$E_{\text{ONIOM}}(n_1 + l; N)$$
$$= E_{\text{high}}(n_1 + l) - E_{\text{low}}(n_1 + l) + E_{\text{low}}(N) \quad (31)$$

where $E_{\text{high}}(x)$ and $E_{\text{low}}(x)$ represent the energies at high- and low-levels for the systems including atoms x, and n_1, l, and n_2 define the number of particles (both solutes and solvents) in the high-level region, the switching shell, and the low-level region, respectively. The total number of particles is $N = n_1 + l + n_2$. Alternatively, when the switching shell is not included in the high-level region, the total energy can be written as

$$E_{\text{ONIOM}}(n_1; N) = E_{\text{high}}(n_1) - E_{\text{low}}(n_1) + E_{\text{low}}(N) \quad (32)$$

When a solvent molecule enters or leaves the switching shell, the total energy evaluated with only one energy expression should be discontinuous. To make the potential energy smooth, the total energy is taken as a hybrid between two energy expressions and expressed as follows:

$$E_{\text{ONIOM-XS}}(\{r_l\}) = (1 - \overline{s}(\{r_l\}))E_{\text{ONIOM}}(n_1 + l; N)$$
$$+ \overline{s}(\{r_l\})E_{\text{ONIOM}}(n_1; N) \quad (33)$$

where $\overline{s}(\{r_l\})$ is an average over a set of switching functions $s_i(x_i)$ for individual exchanging solvent molecules in the switching shell:

$$\overline{s}(\{r_l\}) = l^{-1} \sum_{i=1}^{l} s_i(x_i) \quad (34)$$

If there is no particle in the switching shell ($l = 0$), the switching function is zero, and only eq 32 is computed. When a particle moves into the switching shell from either side, both ONIOM energy terms (eqs 31 and 32) must be evaluated, and the contribution from each term is weighted by the switching function. Kerdcharoen et al. employed the following polynomial expression as the switching function (eq 35).

$$s_i(x_i) = 6\left(x_i - \frac{1}{2}\right)^5 - 5\left(x_i - \frac{1}{2}\right)^3 + \frac{15}{18}\left(x_i - \frac{1}{2}\right) + \frac{1}{2}$$

where

$$x_i = (r_i - r_0)/(r_1 - r_0) \quad (35)$$

Here, r_0 and r_1 are the radii of the inner and outer surfaces of the switching shell, respectively, and r_i is the distance between the center of mass of the exchanging solvent molecule and the center of the high-level region. The polynomial form and parameter sets are derived to have an S-curve that converges to 0 and 1 at r_0 and r_1, respectively. The polynomial form is preferred over the ST2 switching function,[62] which are employed in the conventional QM/MM simulations,[63] because the first and second derivatives of the polynomial are continuous. Both energy and forces can be smoothed by employing the ONIOM-XS method, even if a solvent molecule moves from the high-level to low-level region or vice versa. The solvation structure around solutes is also better than that produced using classical MD simulations. The one disadvantage of ONIOM-XS is that two QM calculations are required for geometries with solvents in the switching shell, which results in
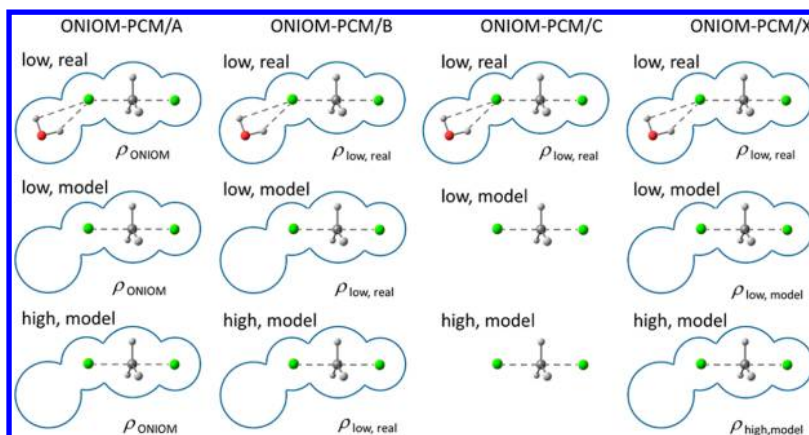
Figure 7. Schematic diagram of four ONIOM-PCM methods. The first, second, and third rows are the definitions of the cavity and the solute charge distribution ρ for (low, real), (low, model), and (high, model) levels, respectively. Reprinted with adaptation by permission from ref 66a. Copyright 2004 Springer.

higher computational cost. ONIOM-XS has been used only for studying the dynamical solvent structures around solutes (see section 8.1.3). However, the concept of ONIOM-XS (adaptive MD) can also be applied for many other systems, which have nonlocalized active regions.

2.1.10.2. ONIOM-PCM for Implicit Solvent Model. Solvation effects can also be described implicitly using a polarizable continuum model (PCM).[64] Here, the solvent is represented by a homogeneous polarizable continuum with a given permittivity, and the solute is represented in terms of a charge density contained by a cavity built in the continuum medium. The charge distribution of the solute inside the cavity polarizes the dielectric continuum, which in turn polarizes the solute charge distribution. This interaction leads to a self-consistent scheme, which can be solved iteratively. In the integral equation formalism (IEF)-PCM model,[65] the Poisson equation can be expressed as follows:

$$-\mathrm{div}[\varepsilon(x)\nabla V(x)] = 4\pi\rho(x) \tag{36}$$

Here, $\varepsilon(x)$ is the dielectric function, whose value is constant outside the cavity and 1 within the cavity. The solute charge-distribution $\rho(x)$ is assumed to lie only inside the cavity; its value outside the cavity is 0.

To embed an ONIOM calculation in PCM,[66] the cavity is defined based on the real system, and the integrated solute charge-distribution $\rho(x)$ is calculated by using the extrapolative ONIOM fashion (see eq 28):

$$\rho_{\mathrm{ONIOM}} = \rho_{\mathrm{high,model}} + \rho_{\mathrm{low,real}} - \rho_{\mathrm{low,model}} \tag{37}$$

Apparent surface charge (ASC) should be calculated by using the potential obtained with the integrated charge distribution in eq 37. However, unlike in standard IEF-PCM,[65] the wave function and ASC cannot be optimized simultaneously. The integrated charge distribution can only be obtained and used in the IEF-PCM scheme after the three subcalculations are completed. This results in a double-iteration scheme, called ONIOM-PCM/A.

$$E_{\mathrm{ONIOM\text{-}PCM/A}} = E_{\mathrm{high,model}}(\rho_{\mathrm{ONIOM}}) + E_{\mathrm{low,real}}(\rho_{\mathrm{ONIOM}})$$
$$- E_{\mathrm{low,model}}(\rho_{\mathrm{ONIOM}}) \tag{38}$$

Because such an optimization is computationally very demanding, three approximations were proposed to avoid the use of a double-iteration optimization of the wave function and

ASC. The first of these is ONIOM-PCM/B. The reaction field determined at the low level for the real system is used, instead of integrated reaction field used in ONIOM-PCM/A. The ASC is determined by $\rho_{\mathrm{low,real}}$ via a regular efficient IEF-PCM calculation, and is subsequently used in the two-model system calculations as follows:

$$E_{\mathrm{ONIOM\text{-}PCM/B}} = E_{\mathrm{high,model}}(\rho_{\mathrm{low,real}}) + E_{\mathrm{low,real}}(\rho_{\mathrm{low,real}})$$
$$- E_{\mathrm{low,model}}(\rho_{\mathrm{low,real}}) \tag{39}$$

The second approximation is ONIOM-PCM/C, in which solvation effects are only included in the low-level calculation on the real system, and the model system calculations are performed in a vacuum (eq 40).

$$E_{\mathrm{ONIOM\text{-}PCM/C}} = E_{\mathrm{high,model}} + E_{\mathrm{low,real}}(\rho_{\mathrm{low,real}}) - E_{\mathrm{low,model}} \tag{40}$$

The extrapolation to the high level is assumed not to be affected by the reaction field.

The third approximation, ONIOM-PCM/X, is an approximation to the correct ONIOM-PCM/A and does not fit in the hierarchy of ONIOM-PCM/A, ONIOM-PCM/B, and ONIOM-PCM/C. The same cavity, based on the real system, is used for three subcalculations, but each of the subcalculations has its own ASC as follows:

$$E_{\mathrm{ONIOM\text{-}PCM/X}} = E_{\mathrm{high,model}}(\rho_{\mathrm{high,model}}) + E_{\mathrm{low,real}}(\rho_{\mathrm{low,real}})$$
$$- E_{\mathrm{low,model}}(\rho_{\mathrm{low,model}}) \tag{41}$$

ONIOM-PCM/X can be regarded as an alternative to ONIOM-PCM/A, and is not a simplification. The schematic representation of the four ONIOM-PCM schemes is shown in Figure 7. The three approximations, ONIOM-PCM/B, ONIOM-PCM/C, and ONIOM-PCM/X, reproduce the exact ONIOM-PCM/A quite well in the examples shown in section 8.2.1. The ONIOM-PCM/X approximation is used as the default scheme for ONIOM-PCM in the Gaussian 09 program. Many studies have been published in which the ONIOM-PCM method was applied for organic, inorganic, and biomolecular systems, and they will be discussed in sections 8.2 and 8.3.

2.1.11. ONIOM Methods for Excited States. The correct treatment of electronically excited states is generally more challenging and computationally demanding, as compared to

that of the electronically ground state. This is especially the case for large systems, in which many of these excited-state methods are computationally prohibitive for accurate QM methods. However, with proper choices of high- and low-level methods, as well as the size of the model system, ONIOM can provide a promising approximation to study photochemistry, photophysics, and photobiology, when electron excitation and an electronically excited state are involved mainly in the model system.[15]

For a two-layer ONIOM method, the excited-state energy can be expressed as

$$E^*_{\text{ONIOM}} = E^*_{\text{high,model}} + E^*_{\text{low,real}} - E^*_{\text{low,model}} \qquad (42)$$

The excited-state gradient and Hessian have the same forms as those for the ground state (eqs 23 and 24). If electron excitation in the real system is sufficiently localized in the model system, energetic contributions from the environment system ($E^*_{\text{low,real}} - E^*_{\text{low,model}}$) may be approximated by using a ground-state energy, at either the QM or the MM level.[15,67] In such approximation, an extrapolated ONIOM result depends largely on the high-level excited-state calculation in the model system for the ONIOM(QM:QM) or ONIOM(QM:MM) method. However, electrostatic interactions between the environment and excited-stated core systems may not be well described by the ground-state method, if the ground- and excited-state wave functions of the model system are very different.

When the excitation is not confined to the model system, the combination of the methods and size of the model system becomes critical. One can treat interactions between the environment and excited-stated core systems by using a low-level QM excited-state method, along with a high-level QM excited-state method for the model system in ONIOM-(QM:QM) calculations. For instance, Vreven et al. reported such ONIOM(QM:QM) treatments to study protonated Schiff base of retinal and accurately reproduce the first singlet excited-state (S_1) energy profile for photoisomerization by using UHF triplet state (T_1) as the low-level method.[68] TD-HF or CIS as the low-level method can reproduce the energy difference between S_0 and S_1 states very well. This excited-state ONIOM(QM:QM) approach can further be extended to the ONIOM(QM:QM:MM) scheme for large systems (such as photobiology, see section 9.3), which has been applied to study an absorption energy for bacteriorhodopsin and bovine rhodopsin.[8f,69] The proper low-level QM method can be employed to treat the less important delocalization effect from the substituents, while the accurate high-level QM method describes the key excitations in the model system. Irrespective of the high- and low-level methods here, it must be assured that the same electronic state is modeled in both QM calculations, because the order of electronic states varies in different QM methods. Currently, there is no method that automatically matches the same electronic state in different QM methods, and thus the users have to manually check and define the states. This state-order problem is particularly severe for optimization and molecular dynamics around crossing regions, which has probably been one of the reasons hindering the wider use of the method.

2.2. Recent ONIOM Method Improvements and Alternative Hybrid Methods

We now turn to a discussion of more recent developments to the ONIOM method as well as alternative hybrid methods.

2.2.1. ONIOM-Like and Alternative Hybrid Schemes.
The ONIOM method was originally implemented in the Gaussian program by Morokuma and co-workers.[8f,23] Extrapolative (subtractive) and flexible ONIOM-type or ONIOM-like QM/MM methods have since been implemented and developed in a number of other computational chemistry programs (e.g., ADF,[70] CHARMM,[71] COBRAMM,[72] ComQum,[73] GROMACS,[74] NWChem,[75] PARAGUASS,[76] Q-Chem,[77] and QMMM[78]). Eichler et al. developed a subtractive QM/MM scheme with ME scheme for geometry optimization in periodic environments and finite-size molecular systems, using shell model potentials to treat the environment system.[40,79] Shluger et al. also implemented a combination of the subtractive QM/MM scheme with a shell model:

$$E_{\text{tot}} = E_{\text{QM}}(\text{cluster}) + E_{\text{GULP}} - E_{\text{GULP}}(\text{cluster})$$
$$- E_{\text{coul}}(\text{cluster-env}) \qquad (43)$$

where $E_{\text{QM}}(\text{cluster})$, E_{GULP}, and $E_{\text{Coul}}(\text{cluster-env})$ are the QM energy of the cluster (model) system, the total energy of the crystal by the shell model method, and the Coulomb interaction of the classical cores replaced by QM ions with the remaining crystal.[80] The last three terms in eq 43 contain short-range interactions between the QM cluster ions and the surrounding classical crystal lattice described by classical interatomic potentials (CIP), as well as polarization energy of the classical crystal lattice.

A similar extrapolative approach has recently been developed to combine two different QM methods and applied to photochemical reactions in the molecular crystal, in which the photoexcited model system and the whole lattic bulk are treated by an excited-state method (e.g., TD-DFT) and a ground-state method (e.g., DFT).[81] Notably, all interactions between the photoexcited model system and the surrounding bulk lattice are approximately described by the ground-state method. Such approximation works well, when the electron density difference between the ground- and excited-state model systems is very small (see section 2.1.11).

2.2.1.1. SIMOMM Scheme. Shoemaker et al. modified the IMOMM method to allow LA and LAH to be freely optimized in the QM and MM calculations, respectively, so-called SIMOMM (Surface Integrated Molecular Orbital/Molecular Mechanics) scheme, which was implemented in GAMESS.[82] This scheme was aimed for modeling surfaces to avoid constraints in a lattice. SIMOMM was first used to study cluster models on a Si(100) surface, whereas the LAC−LA and LAC−LAH bond distances were fixed in the original IMOMM and ONIOM methods. As compared to the IMOMM and SIMOMM methods, a better treatment for the positions of LA and LAH atoms as well as the correct degrees of freedom were later proposed for the ONIOM method (eq 19).

2.2.1.2. QtMMOD Scheme. The "Quantum to molecular mechanical overlapping domain" (QtMMOD) method was recently proposed,[83] in which only the outer part of the model
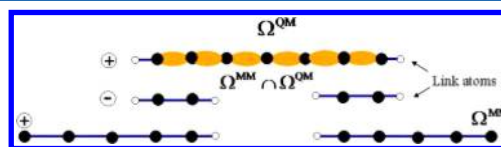

Figure 8. Schematic partition of QtMMOD method. Reprinted with permission from ref 83. Copyright 2008 Elsevier.

system is described by both QM and MM methods ("minimal-overlap", Figure 8), rather than the complete model system used in the ONIOM methods ("full-overlap"). Therefore, the MM calculations on the inner model system, which cannot be described by existing classical functions, are skipped in the QtMMOD method. It should be noted that the long-range interactions between the environment and inner model systems are missing in this method. The QtMMOD method was further combined with a finite-element continuum mechanical method by the bridging domain method (QM/MM/CM method). They applied these methods to investigate properties of graphene sheets with defects.

2.2.1.3. Dual-Level Scheme. A dual-level QM1:QM2/MM scheme was proposed by two groups[54e,84] as an alternative to the extrapolative ONIOM(QM1:QM2:MM) method, in which the energy of the whole system is written as

$$E_{tot} = E_{QM1(gas),model} + E_{QM2\text{-}MM(int+pol)} + E_{MM}$$

$$= E_{QM1(gas),model} + (E_{QM2,pol} + E_{QM2,int}) + E_{MM} \quad (44)$$

The interactions and polarization of the model system with the environment system, $E_{QM-MM(int+pol)}$, are approximated by the lower-level semiempirical (SE) method in the dual-level scheme. The first three terms of eq 44 can be used for geometry optimization of the model system, while the last three terms are used for the geometry optimization of the environment system.[54e] Also, one can use the low-cost QM2 method for demanding statistical sampling.[84a] This scheme is conceptually similar to the ONIOM(QM1:QM2:MM) method with a few differences. There are only two layers, and the QM2 method was used to treat the model system in the dual-level scheme, whereas there are three layers and the QM2 method was used to treat the larger intermediate system in the ONIOM-(QM1:QM2:MM) method.

2.2.1.4. QM/Me Scheme. It is challenging to model chemical reactions in delocalized metallic systems using high-level QM
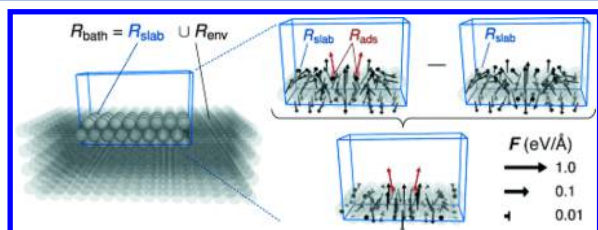
Figure 9. A schematic picture in the QM/Me method for metallic systems. The arrows represent computed force (F). Reprinted with permission from ref 85. Copyright 2014 Wiley-VCH Verlag GmbH & Co. KGaA.

methods. Because a finite-size cluster model is not realistic, PBC supercell approaches have been widely used. However, the cost of the QM method increases significantly with increasing size of the QM supercells. Very recently, Meyer et al. proposed a QM/Me method (Figure 9):[85]

$$E_{QM/Me} = (E_{QM,(slab \cup ads)} - E_{QM,slab}) + E_{Me,bath} \quad (45)$$

While generic QM/MM and ONIOM(QM:MM) methods involve only one QM calculation, two QM calculations of the same PBC supercell with two slightly different model systems are performed in the QM/Me method: one QM calculation includes the adsorbate atoms ($E_{QM,(slab \cup ads)}$), and the other

QM calculation excludes them ($E_{QM,slab}$). The energy difference between these two QM model calculations contains the short-range adsorbate–substrate and adsorbate–adsorbate interactions, whereas the remaining long-ranged substrate–substrate interactions ($E_{Me,bath}$) are described by many-body CIPs method. The subtractive step is performed in the two QM calculations in the QM/Me method, while this step can be regarded in the two MM calculations in the ONIOM2-(QM:MM) method (eq 2). The QM/Me method was used to study a highly exothermic O_2 dissociation on Pd(100).

2.1.1.5. Alternative Hybrid Schemes. Additive schemes cannot easily yield a coupling Hamiltonian for all types of interactions between two different QM methods. However, a number of approximate methods for combining two different QM methods have been proposed and developed, such as frozen-density embedding (FDE) (or frozen DFT (FDFT)) method,[86] and its constrained DFT (CDFT) variant,[87] as well as ab initio-in-DFT method.[88] Cui et al. also proposed iterative QM/SE methods (e.g., QM/SE-I).[89] Gogonea et al. adopted the divide-and-conquer approach[90] to combine DFT and SE through a chemical potential scheme.[91] Wanko et al. developed additive QM1/QM2/MM method,[92] which only describes classical Coulomb interaction between the two QM regions, but does not include charge transfer, exchange, and electron correlation (which are included in the ONIOM3 method treated by the lower-level QM approximation). CDFT was also combined with the MM method.[93]
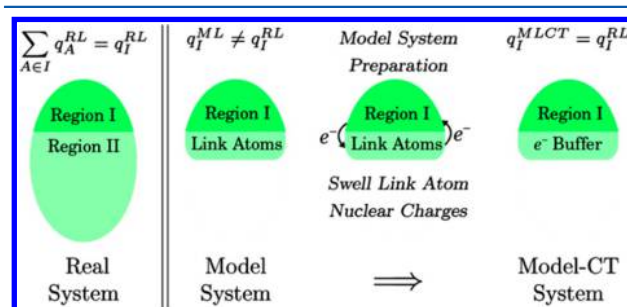
Figure 10. Schematic diagram for the ONIOM(QM:QM)-CT method. Reprinted with permission from ref 94. Copyright 2010 American Chemical Society.

2.2.2. Boundary Treatments. *2.2.2.1. ONIOM2-(QM1:QM2)-CT Method.* The model system is generally considered to be a closed system. No charge transfer (CT) between the QM/MM or QM/QM boundary is generally allowed in generic QM/MM and ONIOM calculations. Recently, Mayhall et al. developed a method to include CT between the two QM layers, ONIOM(QM1:QM2)-CT (Figure 10).[94] To incorporate consistent CT effects or charge redistribution between different layers, nuclear charges of the link atoms are tuned to modify a one-electron potential in the model system preparation step, until the total QM2 charge distribution of the core system (region I) in the model system calculation becomes identical to that in the real system calculation (i.e., $q_{QM2,model}(core) = q_{QM2,real}(core)$).[94] The hydrogen link atoms are regarded as an electron buffer region. The ONIOM-CT method was found to improve a test set of 20 chemical reaction energies by more than 35%. Very recently, the Raghavachari group further extended and improved ONIOM-CT method by matching the electrostatic potential

(ESP) between the model and real systems (ESP-ONIOM-CT).[95] This new method was also applied to one- and two-link atom reactions and was found to improve the accuary of reaction energies by 40–60%, as compared to the conventional ONIOM method.

A charge-transfer method for the additive QM/SE method was developed by means of chemical potentials and a divide-and-conquer method.[91] A charge-transfer method for QM/MM methods was also proposed and developed on the basis of the principle of electronic chemical potentials equalization.[96]

2.2.2.2. Double Link Atom Method. A double link atom method, in which two link atoms (MM LA and QM LA) saturate the two cutting QM/MM atoms to form a closed model system and a closed environment system, has been proposed.[34] This preserves the net charge and dipole moment to form the closed systems. All classical bonded and electrostatic terms involving the MM LA and MM atoms are included, but interaction between the QM and MM LA is excluded.

2.2.2.3. Boundary Atom (or Pseudobond) Approaches. Zhang et al. developed an alternative boundary treatment, a so-called pseudobond approach, in which a monovalent (F) atom with a modified effective core potential (ECP) is used as the boundary atom, instead of the link atom.[97] Parameters of the F pseudopotential were tuned to reproduce some properties (e.g., bond length and strength, atomic charges) of the LAC–LAH bond computed by the QM method. There are several advantages of this pseudobond method: (1) no additional link atom is introduced (no error of the link atom); (2) no new/additional implementation is necessary; (3) the parameters can be transferable to different chemical environments; and (4) the parameters depend on the basis set and the hybridization of the MM boundary atom (LAH), but not the force field.

Recently, this pseudobond approach was extended to different boundary atoms. Pseudopotentials for substituted cyclopentadiene C atoms were modified to incorporate electronic effects of the substituents in ONIOM calculations.[98] Considerable improvements in computing CO stretching frequencies for a series of $(Cp^R)Zr(CO)_2$ complexes were observed by using the optimized pseudopotential and ONIOM-(QM1:QM2). The development of the divalent pseudoatom is essential to describe bonding and reactions in surface or materials chemistry. The divalent pseudoatoms with the modified ECP parameters are developed to combine with sulfur atoms as the divalent silicon pseudoatoms.[99] This has been demonstrated in the case of Si surfaces, including Si(100) cluster and slab models (which were used to study water dissociation and hydrogenation). Moreover, a tuned and balanced redistributed charge scheme (TBRC) was proposed by tuning the pseudopotential of F link atoms and balancing and redistributing charges close to the boundary.[100] Related approaches,[101,102] including the adjusted connection atom method,[103] the effective group potential (EGP) method,[104] the quantum capped potential (QCP) method,[105] the multicentered valence electron effective potential (MC-VEEP) method (for electronically ground and excited states),[106] frontier orbital consistent quantum capping potential (FOC-QCP),[107] and the link molecule method (LMM with a silicon=pseudoselenium molecule),[108] have also been developed. Boundary atom approaches have been actively developed, and could be successful in their treatment of electronic effects due to LAH in ONIOM calculations.

2.2.2.4. Frozen Localized Orbital Schemes. The third set of QM/MM boundary approaches is based on frozen localized (hybrid) orbitals, for example, the hybrid orbital method,[4] the local self-consistent field method (LSCF),[109] the generalized hybrid orbital method (GHO),[110] and frozen orbitals.[111] Although frozen localized orbitals can give an accurate description of the boundary, the parameters of one boundary are not in general transferable to the other boundaries. In addition, extensive parameterization and implementation are required. Very recently, Sun et al. proposed exact link orbitals and optimal link orbitals for the QM/MM boundary, in which the exact link orbitals can be an exact treatment for the QM/
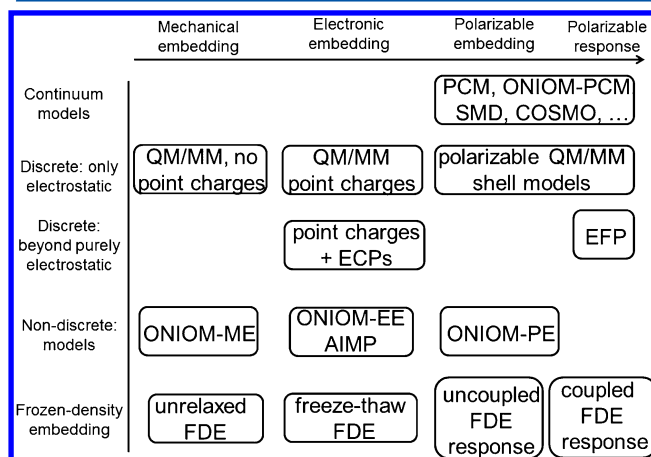
Figure 11. Schematic overview of different embedding schemes. COSMO, conductor-like screening model; EFP, effective fragment potential; AIMP, ab initio model potential. Adapted with permission from ref 113. Copyright 2012 The Royal Society of Chemistry.

MM boundary.[112] Two optimal link orbitals were also applied for a challenging QM/MM sp^2 boundary cutting through a double bond.

2.2.3. ONIOM Electronic and Polarizable Embedding Schemes. Bakowies et al. categorized all schemes to compute $E_{QM–MM}$ into three groups:[21,22] mechanical embedding (ME), electronic embedding (EE), and polarizable embedding (PE) (Figure 11). The ME scheme is the simplest scheme. Singh et al. reported the additive QM/MM calculations with mechanical embedding (QM/MM-ME) scheme in the 1980s,[22,38a] whereas Warshel and Levitt adopted the additive QM/MM method with polarizable embedding (QM/MM-PE).[4]

2.2.3.1. ONIOM(QM1:QM2)-EE Scheme. The Raghavachari group extended the EE scheme to the ONIOM(QM1:QM2) method.[114] The high-level QM wave function (or charge density) of the model system can be polarized by the low-level QM charge distribution of the environment system in this ONIOM(QM1:QM2)-EE scheme. Atomic charges (Mulliken, asymmetric Mulliken, Löwdin, or scaled Löwdin charge) or electronic densities of the real system evaluated at the lower QM level were used to construct the embedding potential. As opposed to the ONIOM(QM:MM)-EE method with fixed MM charges, derivation and implementation of analytic gradients for the ONIOM(QM1:QM2)-EE method becomes more difficult, as the ONIOM(QM1:QM2)-EE method depends on the variable charges in the real system. To obtain the analytic expression for the ONIOM(QM1:QM2)-EE gradient, they proposed equations related to the coupled-perturbed Hartree–Fock (CPHF) equations, and applied the *z*-vector method

developed by Handy and Schaefer to reduce it to a single set of SCF response equations.[114d] HF or DFT method can only be used as the QM2 method in the ONIOM(QM1:QM2)-EE method. The ONIOM(QM1:QM2)-EE method has so far been applied to a few systems: a spherosiloxane cube, water-solvated glycine, and dye-sensitized solar cell.[114b,d] The same research group also commented that if the polarization of the model system by the environment system is not large, or similar polarization effects are obtained with both low-level and high-level QM methods in the model system, then the ONIOM-(QM1:QM2)-ME method should be a reasonable approximation. As compared to full QM calculations, the ONIOM-(QM1:QM2)-EE method generally gives smaller errors than the ONIOM(QM1:QM2)-ME method.

2.2.3.2. ONIOM(QM:MM)-PE Scheme. Very recently, Caprasecca et al. derived and implemented the first analytical derivatives for a QM/MM PE scheme based on an induced dipole approach in the Gaussian program.[115] This scheme uses fixed MM charges and induced dipoles represented by atomic isotropic polarizabilities (denoted QM/PMM-ID). In this QM/PMM-ID scheme, the QM wave function of the model system can be polarized by the MM charges and induced dipoles, whereas the MM dipoles can also respond to the QM electron density (electric field) leading to induced dipole moments. The QM wave functions and the MM induced dipoles therefore mutually polarize each other through self-consistent calculations. QM/PMM-ID, which can combine with many available polarizable force fields, was implemented within the extrapolative ONIOM approach, ONIOM(QM:MM)-PE (eq 46). As compared to the ONIOM(QM:MM)-EE implementation,[8f] it adopts a different and more flexible implementation of the ONIOM(QM:MM)-PE scheme,[115a] in which all MM non-electrostatic terms are separated from the MM electrostatic terms (i.e., electrostatic (es) and polarization (pol) interactions between the QM and MM parts):

$$E_{\text{ONIOM(QM:MM)-PE}} = (E_{\text{QM,model}} + E_{\text{real,es}} + E_{\text{real,pol}})$$
$$+ E_{\text{MM,real,noele}} - E_{\text{MM,model,noele}} \quad (46)$$

By switching off the electrostatic interactions (noele) in all MM calculations, the MM electrostatic and polarization terms are separately added in the QM contribution. In addition, the LAs were assigned to have no charge or polarizability.

The ONIOM(QM:MM)-PE method was first applied to the guanine−cytosine pair and the merocyanine dimer, which have strong hydrogen bonds and dipole−dipole interactions, respectively. The polarization effect on the geometry was found to be small. ONIOM(QM:MM)-PE was then applied to study a rhodopsin protein structure. The MM protein environment system was divided into two regions. Atoms within 15 Å from the chromophore atoms were assigned as the polarizable MM region (and so were atomic charge and polarizability), whereas the remaining MM atoms were described with nonpolarizable force fields. A minor increase in the bond-length alternation in the chromophore was observed, when including polarization effects. In a similar vein, additive QM/MM-PE schemes (e.g., based on point-dipole, induced-charge, fluctuating charge, or drude oscillator model) have also been developed by different groups.[4,21,103,116,117]

2.2.4. Geometry Optimization Methods. *2.2.4.1. Micro-iteration Method.* In addition to the ONIOM microiteration method, the Kollman and Yang groups proposed an alternative QM/MM microiteration method, in which complete QM geometry optimization of the model system (with a fixed environment system) is followed by complete MM geometry optimization of the environment system (with a fixed model system) until convergence.[38a,118] Recently, least-squares minimization and mixed-coordinate (redundant internal and Cartesian coordinates for the QM and MM parts, respectively) methods have also been proposed and combined with ONIOM geometry optimization. Tests demonstrate that this optimization method is stable and efficient.[119]

2.2.4.2. Intrinsic Reaction Coordinate (IRC) Method. Hratchian et al. developed an efficient (first-order) Euler predictor-corrector reaction path integration method combined with ONIOM to obtain steepest-descent reaction paths[120] for large systems.[121] Critically, this algorithm avoids the computationally demanding Hessian diagonalization, which scales as $O(N^3)$. A microiterative-based procedure for additive QM/MM IRC method on large systems, in which the core system walks along the IRC path and the remaining system is minimized after each IRC step, was also recently proposed.[122] QM/MM reaction paths computed using other methods (e.g., nudged elastic band (NEB) and replica path methods) have also been proposed.[8c,123]
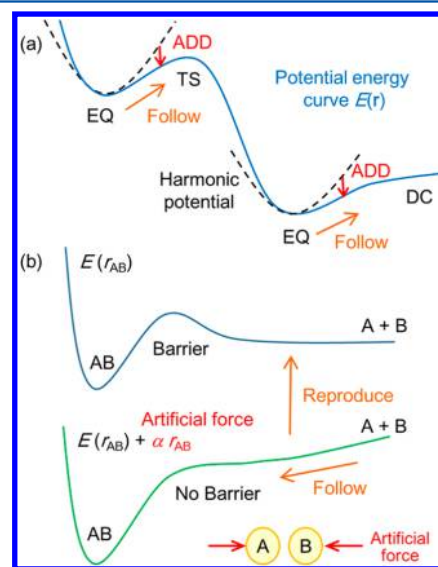
Figure 12. Concepts of the ADDF and AFIR methods.

2.2.4.3. Global Reaction Root Mapping Strategy. The global reaction root mapping (GRRM) strategy[124] is one of the most powerful tools to explore critical points on PESs exhaustively, such as local minimums, transition states, dissociation channels, minimum energy conical intersections (MECI), and minimum seams of crossing (MSX).[125] This strategy consists of two methods: the anharmonic downward distortion following (ADDF) method[126] and the artificial force induced reaction (AFIR) method[127] (Figure 12). The ADDF method is able to locate all local minima and transition states, given one or several local minima. On the other hand, AFIR explores approximate reaction pathways starting from dissociation limits or local minima, by placing an artificial force between reaction centers. These two methods only require electronic energy, energy gradient, and Hessian (mandatory for ADDF and updated for AFIR), and therefore in principle they

can be combined with any electronic structure method. In the case of ONIOM, these three quantities can be calculated as described in eqs 4, 23, and 24, thus making it possible to combine ONIOM with GRRM to search for complex systems.[128]

The microiteration approach, essentially the same approach used in ONIOM (see section 2.1.8), can also be used in both ADDF[129] and AFIR[130] geometry optimization to reduce computational cost. The only complication is the treatment of the Hessian matrix for the high-level region (see section 2.1.8). In practice, an effective Hessian is used to account for couplings between the high and low layers:[55]

$$
\frac{\partial E(\mathbf{Q})}{\partial q_i \partial q_j} = h_{ij}^{\text{high}} - \sum_{m=1}^{3N_{\text{low}}} \sum_{n=1}^{3N_{\text{low}}} h_{im}^{c} W_{nm}^{\text{low}} h_{nj}^{c}
$$
(47)

where h^{high} and h^{c} are the matrix elements of the Hessian for the high-level and high-low levels coupling blocks, respectively. q_i are coordinates of atoms in the high level, N_{low} is the number of atoms in the low level, and W^{low} is the inverse Hessian matrix of the low-level block.

Exhaustive explorations of reaction pathways of large and flexible molecules using ADDF and AFIR currently have a high computational cost. If the size of the low-level block is large, the calculation of the Hessian's inverse is demanding. To reduce computational cost here, the outer shell atoms that are far enough from the reactive center are omitted.[129,130] Computational cost can be reduced further using some ONIOM method in an early stage of study; for example, in a recent application of the AFIR method for a multicomponent reaction,[131] all reaction pathways were identified quickly by using inexpensive ONIOM calculations before important geometries were reoptimized at a higher level of theory.

2.2.5. ONIOM Method Combined with High-Accuracy Methods. The Guo group developed an ONIOM-G3B3 method, and benchmarked 63 experimental bond dissociation energies (BDEs) of diverse molecules.[132] These ONIOM-G3B3 results are in excellent agreement with experimental values. The ONIOM-G3B3 approach has been successfully used to calculate BDEs of antioxidants,[133] carbohydrates,[134] oximes,[135] natural antioxidants,[136] allylic disulfides,[137] and carbanions.[138] The ONIOM-G4 method was also recently developed and used to benchmark hydride dissociation energies against 48 bulky organic molecules.[139] Three-layer ONIOM-G2R3 (OG2R3) method has also been applied to calculate dissociation energies for 34 donor–acceptor complexes,[140] and to study donor–acceptor complexes containing fluoroalkyl and aryl substituents on the acceptors.[141]

The Wilson group combined the correlation consistent composite approach (ccCA) into the ONIOM multilayer methodology,[142] so-called ONIOM-ccCA. This approach was used to predict the C–H bond dissociation energies of 18 anthracene and fluorene analogues (up to 43 atoms, with an average error of only 1.2 kcal/mol with respect to experimental results), and to calculate proton affinities (PAs) of small biomolecules.[143] In addition, a relativistic pseudopotential correlation-consistent composite approach within the ONIOM framework (ONIOM-rp-ccCA) was developed to study oxidative addition of the ethane carbon–carbon bond to Ni, Cu, Pd, and Pt atoms.[144] In this instance, ONIOM-rp-ccCA effectively reproduced CCSD(T)/aug-cc-pCV∞Z results.

2.2.6. ONIOM Methods for Molecular Properties. *2.2.6.1. Hessian and Frequency.* As discussed in detail in

section 2.1.6, the energy and its derivatives are well-defined in the ONIOM method, and therefore stationary points on the PESs (minima or transition states) can be calculated.[53a,55] It is important to note that the resulting stationay point(s) is not a stationay point for any of the individual subcalculations. After the stationary points are determined, Hessian and normal-mode analysis can be performed by using the harmonic approximation. For a complex molecular system, DFT can be used for energy or gradients calculations, but analytic frequency calculation may be very expensive due to memory requirements.[145] However, ONIOM(QM:QM) analytic frequency calculations, for instance, ONIOM(QM:SE), can be achieved by using much less memory.

According to Vreven et al.,[145] the diagonalized ONIOM Hessian of the whole systems can be partitioned into the contributions of individual subcalculations:

$$
X^{t,\text{ONIOM}} H_{\text{model}}^{\text{high}} X^{\text{ONIOM}} + X^{t,\text{ONIOM}} H_{\text{real}}^{\text{low}} X^{\text{ONIOM}}
$$
$$
- X^{t,\text{ONIOM}} H_{\text{model}}^{\text{low}} X^{\text{ONIOM}} = \alpha^{\text{ONIOM}}
$$
(48)

where H, X^{ONIOM}, and α^{ONIOM} represent Hessian, eigenvectors, and eigenvalues, respectively. The following matrixes were defined:

$$
\beta_{\text{size}}^{\text{level}} = X^{t,\text{ONIOM}} H_{\text{size}}^{\text{level}} X^{\text{ONIOM}}
$$
(49)

Each matrix β then can be split into a diagonal matrix γ and an off-diagonal matrix.[145] As the sum of the off-diagonal matrixes must be zero:

$$
\alpha^{\text{ONIOM}} = \beta_{\text{model}}^{\text{high}} + \beta_{\text{real}}^{\text{low}} - \beta_{\text{model}}^{\text{low}} = \gamma_{\text{model}}^{\text{high}} + \gamma_{\text{real}}^{\text{low}} - \gamma_{\text{model}}^{\text{low}}
$$
(50)

According to the above equation, the ONIOM curvature along a vector can be obtained by using the three individual curvatures. Pseudofrequency f_i' then is related to the ONIOM eigenvalue α_i and can be obtained as follows:

$$
f_{\text{size},i}'^{\text{level}} = \sqrt{\gamma_{\text{size},i}^{\text{level}}}
$$
(51)

ONIOM frequency can now be expressed as a combination of three components:

$$
(f_i^{\text{ONIOM}})^2 = (f_{\text{model},i}'^{\text{high}})^2 + (f_{\text{real},i}'^{\text{low}})^2 - (f_{\text{model},i}'^{\text{low}})^2
$$
(52)

Using this approach, the effect of the substituents on the ONIOM frequency can be determined.

This approach can be applied for the study of transition structures and higher-order saddle points. Vreven et al. successfully applied this approach to cycloaddition of quinodimethane to a carbon nanotube and that of cyclohexadiene to maleic anhydride.[145]

Thompson et al. proposed a relatively straightforward implementation of the second derivatives of the energy for complex systems.[43c] The second derivatives of one- and two-electron integrals are summed into the force constants, where the density derivatives are obtained from the CPHF method. According to Frisch et al.,[146] the second derivatives can be expressed as

$$
\langle P^x F^{(y)} \rangle - \langle W^x S^y \rangle
$$
$$
P^x = \bar{U} - S_{\text{OO}}^x = U^x + U^{x\dagger} - S_{\text{OO}}^x
$$
(53)

In the above equations, x and y are nuclear coordinates, and U^x can be computed by solving the CPHF equations, which

required a significant amount of storage and I/O of intermediate quantities. For larger molecular systems, computational cost of these steps can be immense. The second derivative term can be rearranged as follows:

$$\langle P^x F^{(y)} \rangle - \langle W^x S^y \rangle = \langle P^x B^y \rangle = \langle \bar{U}^x B^y \rangle - \langle S^x_{OO} B^y \rangle \quad (54)$$

In this equation, the first and the second terms are relatively straightforward to compute. In the case of EE, the QM wave function depends on the coordinates of the whole system. As the basis functions of the QM calculation are independent from the positions of the MM atoms, a simple one-electron operator can be used for the displacement of MM atom a in the x direction (F^{x_a}):

$$F^{x_a}_{\mu\nu} = h^{x_a}_{\mu\nu} = \frac{\partial}{\partial x_a} \int \chi_\mu(\vec{r}) \frac{1}{|r - R_a|} \chi_\nu(\vec{r}) \, dr \quad (55)$$

Thompson et al. used this approach to calculate vibrational frequencies (both with and without the EE) of a GFP protein by using three different QM model sizes (the QM model and MM environment systems: ~100 and ~5000 atoms, respectively).[43c] Calculated frequencies and dipole derivatives were used to interpret the experimental results.

2.2.6.2. Optical Rotation. The relationship between optical rotation (OR) and molecular structure is complex, making QM calculation of OR particularly challenging. ONIOM method has been used to simulate OR of carbohydrates, which is very useful in validating the structures. The electric dipole-magnetic dipole polarizability (β) of the real system[147] can be defined as

$$\beta_{ONIOM} = \beta_{high,model} + \beta_{low,real} - \beta_{low,model} \quad (56)$$

These $\beta_{level,system}$ terms can be obtained from electric and magnetic field derivatives of the ground-state electronic wave function:

$$\beta_{ab} = \frac{hc}{3\pi} Im \left\langle \frac{\partial \Psi}{\partial E_a} \bigg| \frac{\partial \Psi}{\partial B_b} \right\rangle \quad (57)$$

where $\partial\Psi/\partial E$ and $\partial\Psi/\partial B$ are derivatives of the ground-state electronic wave function with respect to the electric field E and magnetic field B, which can be calculated via analytical derivative methods and field-dependent atomic orbitals (AOs).[148]

The optical rotation can be calculated in terms of the specific rotation $[\alpha]_\nu$:

$$[\alpha]_\nu = 13.43 \times 10^{-5} \frac{\beta \bar{\nu}^2}{M} \quad (58)$$

where $\bar{\nu}$ and M represent the wavenumber used for OR and the molar mass. ONIOM was used to study OR of small systems representing glucose prototypes with one and two chiral centers.[147] Different ONIOM partitions were tested and compared for the mono- and bichiral prototypes.

2.2.7. ONIOM Methods for Excited States. *2.2.7.1. Approximated Methods for MECI Optimization.* MECIs and MSXs are known to facilitate nonadiabatic transitions and are therefore critical in photochemistry and photobiology. Bearpark et al. developed an MECI search method (originally for CASSCF and MMVB) for ONIOM.[67a] In this ONIOM MECI optimization method, the ONIOM energy difference between the two states was approximately described by $\Delta E_{high,model}$ only, while the low-level calculation was treated by a ground-state method (denoted as "constrained low-level state" (CLS)). The

modified gradient for the MECI search algorithm can then be approximated as

$$g_{ONIOM-CLS} = 2(E^*_{high,model} - E_{high,model}) \frac{\mathbf{x}^{high}_{model}}{|\mathbf{x}^{high}_{model}|}$$
$$+ P' \frac{\partial E^*_{ONIOM-CLS}}{\partial q} \quad (59)$$

where $\mathbf{x}$ is the gradient difference vector between the two states, and the P' operator projects out the two degrees of freedom that lift the degeneracy.

By using this algorithm, the S_0/S_1 intersection of the previtamin D structures was located with a 100-fold speed-up and little loss of accuracy, as compared to a full QM target calculation. Recently, Meada et al. extended the capability of the AFIR method (see section 2.2.4.3) to search MSXs by using a seam model function using ONIOM.[130] It demonstrated the ability to systematically find MSXs in a complex protein and solution environments without the need for an initial guess.

2.2.7.2. Effect of Link Atom. The bond length of the LA in ground-state ONIOM calculations generally has little effect on the energy. This was recently tested to be also the case for excited-state ONIOM calculations, provided that the combination of the low-level method and the size of the model system is appropriately chosen.[149] However, when the link atom is within an electron excitation region, the ONIOM result can be considerably affected. These findings again emphasize the importance in the choice of the partition and the low-level method in ONIOM.

2.2.7.3. Oscillator Strength. Oscillator strength is important in simulation of optical spectra, because it is related to the intensity of the electronic transition. The ONIOM oscillator strength f_{ONIOM} is defined as follows:

$$f_{ONIOM} = \frac{2}{3} \Delta E_{ONIOM} D_{ONIOM} \quad (60)$$

where the ONIOM dipole strength (D_{ONIOM}) can be obtained using:

$$D_{ONIOM} = \sum_i (\mu_i^{ONIOM})_{0k} \times (\mu_i^{ONIOM})_{k0}, \, i = x, y, z \quad (61)$$

where $(\mu_i^{ONIOM})_{0k}$ represents the components of the integrated ONIOM transition dipole between states of interest: 0 and k. A simpler alternative for obtaining an approximate oscillator strength ($\tilde{f}_{ONIOM}$) has also been proposed:[150]

$$\tilde{f}_{ONIOM} = f_{high,model} + f_{low,real} - f_{low,model} \quad (62)$$

and this does not require the integration of the transition dipoles. Accurate oscillator strengths can be obtained with ONIOM if the combination of the low-level method and the size of the model system is appropriate.[150]

2.3. Advanced ONIOM Simulation Methods and Guidelines

2.3.1. ONIOM Method Combined with Molecular Dynamics Methods. QM/MM and ONIOM method combined with MD simulations[151] are sometimes adopted to study dynamics of chemical processes and ultrafast photodynamics involving electronic excited states. MD also enables statistical sampling of the systems.

2.3.1.1. Born–Oppenheimer Molecular Dynamics (BOMD). For large systems, direct dynamics using energy and forces

computed on-the-fly is more practical than constructing accurate global PESs spanning all degrees of freedom. This approach typically assumes the Born–Oppenheimer (BO) approximation, in which classical Newtonian equations of motions are used to describe nuclear motion in both the model and the environment systems, with energy and forces computed using QM in the model system, and with MM in the environment system. As the computational cost of the QM/MM or ONIOM MD simulations is extremely high, semiempirical methods (e.g., DFTB,[152,153] AM1[154]) are often employed as the QM method.[155] Matsubara et al. implemented BOMD with ONIOM, by linking the Hondo and Tinker programs, to study biochemical systems (e.g., the hydrolytic deamination in cytidine deaminase).[156] Thermal motion of the nearby residues was found to play a key role in the geometry and energy of the substrate in the active site, as well as the elementary step.

2.3.1.2. Nonadiabatic MD Methods. To treat nonadiabatic (NA) processes and to determine a transition between electronic states, approximated surface-hopping (e.g., Laudau–Zener, Zhu–Nakamura,[157] and diabatic-hop[158]) methods have been used in NA QM/MM MD simulations. Other more computationally demanding and sophisticated surface-hopping schemes have also been employed.[155a,159] Recently, Li et al. developed a NA ONIOM(QM:MM) MD method to study ultrafast photodynamics in fluorescent proteins and bacteriorhodopsin, by using the Laudau–Zener or Zhu–Nakamura surface-hopping method.[160] A NA ONIOM(QM1:QM2) MD method by using a ground-state method (HF) as the low-level QM method (constrained low-level state)[15,67a] was also developed to study photodynamics of DNA.[161] Moreover, nonadiabatic ONIOM(QM:MM)-like MD was also implemented to study photoisomerization of rhodopsin.[157a,162]

2.3.1.3. Adaptive ONIOM MD Method. When the definition of high- and low-level regions has to be switched during an MD simulation, discontinuity of potential energy and forces can be large and result in numerical instabilities. To avoid the discontinuities, an adaptive MD algorithm[63a,163] combined with the ONIOM method (so-called ONIOM-XS) was developed.[61] Its detailed theory and application are discussed in sections 2.1.10 and 8.1.3, respectively. Although the ONIOM-XS method has been applied only for solvation chemistry, it can be applied to systems with nonlocalized active regions, such as processes on catalytic surfaces, nanoparticles, and membranes.

2.3.1.4. Quantum Wavepacket Ab Initio MD Method. The Iyengar group developed a combination of the ONIOM(QM:MM) or ONIOM(QM1:QM2) method with quantum wavepacket ab initio MD (QWAIMD) method to include quantum nuclear effects,[164] which are neglected in classical MD methods. This ONIOM-QWAIMD method is based on BOMD. The testing results demonstrated that the ONIOM-QWAIMD method can be applied to study accurate dynamics in large systems.

2.3.1.5. Atom-Centered Density Matrix Propagation Method. Rega et al. combined the ONIOM method with an atom-centered density matrix propagation (ADMP) approach,[165] which expands the one-electron density matrix in an atom-centered Gaussian basis set and is regarded as an extended Lagrangian MD method (conceptually close to Car–Parrinello (CP) MD method).[166] In this scheme:

$$\mathcal{L}_{\text{ADMP}} = 0.5*Tr(\mathbf{V^T MV}) + 0.5*Tr([\mu^{1/4}\mathbf{W}\mu^{1/4}]^2)$$
$$- E_{\text{ONIOM}} - Tr[\Lambda(\mathbf{PP} - \mathbf{P})] \tag{63}$$

where $\mathbf{V}$, $\mathbf{M}$, $\mathbf{P}$, $\mathbf{W}$, and μ are velocities, masses, the density matrix, the density matrix velocity, and the density matrix fictitious mass tensor, respectively. The ONIOM-EE ADMP method was well behaved (e.g., energy was conserved, partly due to the proper treatment of the LA by using eq 19). They also applied ONIOM ADMP to study a proton-transfer/hopping process in the Gramicidin A ion channel. A rare event sampling method was recently combined with an ONIOM(QM:MM) ADMP method to investigate dynamics of hydrogen atom transfer in the soybean lipoxygenase-1 (SLO-1).[167]

2.3.1.6. Free Energy Simulations. Most QM/MM and ONIOM applications are based on "static" geometry optimization to evaluate energy profiles. However, free energy simulations (such as free energy profiles that include system/
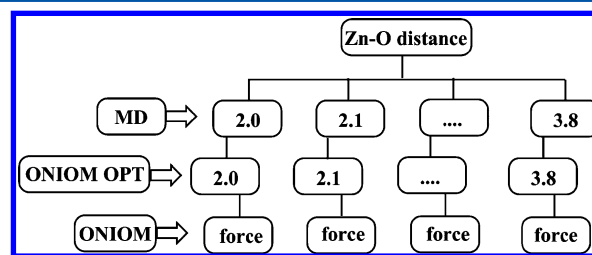
Figure 13. A schematic flowchart for the combinatoin of MD and ONIOM methods. Reprinted with permission from ref 172. Copyright 2006 American Chemical Society.

thermal fluctuations) are a more realistic approximation of experimental conditions. Unfortunately, there are very few applications of free energy simulations of complex systems[8c,168] using QM/MM or ONIOM methods (mostly in conjunction with semiempirical QM methods, highly parameterized potentials, for example, EVB,[51,93,169,170] and specific reaction parameters[171]), due to the extreme computational expense required for sufficient statistical sampling.

Yao et al. proposed an approximated free energy method by combining classical MD simulations with an ONIOM(B3LYP:PM3) method (Figure 13) to study deamination of cytosine in yeast cytosine deaminase.[172] Classical MD simulations were initially performed to generate different configurations of the protein and solvent systems with a restrained reaction coordinate (Zn–O bond). The inner part of the reaction site was then optimized at several MD snapshots, and forces of the reaction coordinate were evaluated using ONIOM (by fixing the outer part and the constraint). Integration of the computed force between the Zn–O bond (in which the force is averaged over the snapshots) gave an approximate potential of mean force (PMF) along the reaction coordinate.

Several other free energy approximation approaches, which avoid the high-level QM sampling, have been proposed for QM/MM methods. Chandrasekhar et al. proposed a QM free energy (QM-FE) method to study S_N2 reaction of methyl chloride in water.[173] Here, the gas-phase reaction path for the solutes was initially obtained with the QM method. The frozen QM-optimized structures were then placed to an environment of solvent molecules, and statistical samplings of the solvent

configuration were performed using MM MC. This QM-FE approach was applied to study the mechanism of methyl transfer reaction in catechol *O*-methyltransferase.[30] Using a similar approach, Zhang et al. studied enzymatic reactions by taking the reaction path optimized with QM/MM, and performing MM sampling simulations (via MD and free energy perturbation (FEP) methods) of the environment system (denoted as QM/MM-FE).[118] A few QM/MM-FE applications on enzymes were also reported.[174] A related free energy correction was recently extended to the ONIOM(QM:MM) method (ONIOM-FE or QM:[MM-FEP], eq 64) by Kawatsu et al. to study enzymatic reactions in isopenicillin N synthase.[29] Here:

$$\Delta F_{ONIOM} = \Delta E_{ONIOM} + \Delta f_{QM,model} + \Delta F_{FEP,int/NB}$$

$$- \Delta E_{MM,int/NB} \tag{64}$$

where $\Delta f_{QM,model}$, $\Delta F_{FEP,int/NB}$, and $\Delta E_{MM,int/NB}$ represent the free energy correction of the model system derived from the frequency calculations of the gas-phase model system, the free energy correction of the nonbonded interactions between the model and environment systems based on FEP approach, as well as the ONIOM energy component for the nonbonded interactions between the model and environment systems. Hu et al. further developed a more elaborate QM/MM free energy method (QM/MM minimum free-energy path (MFEP)), in which the model system is optimized on an approximated QM/MM PMF (or free energy gradient[175]) to get the free-energy reaction path.[8c,176] Related QM/MM MFEP methods were also recently developed.[177] The initial structure becomes less sensitive to energetic profiles, and effect of the protein conformational changes or fluctuation is allowed in the QM/MM MFEP methods.

2.3.2. ONIOM Method Combined with Fragmentation Methods. QM/MM and ONIOM usually divide a system into two distinct regions (Figure 1a). Alternatively, various fragmentation methods, mostly based on a many-body expansion (MBE) approximation (eqs 65 and 66),[178] can be used to study large systems.[90,179] In fragmentation methods, the whole system is divided into *M* fragments (f_i denotes the *i*th fragment), each of which is treated individually using the high-level QM method. The total energy of the whole system is then approximated by the sum of many-body (MB) interaction energies:

$$E = V_{1B} + V_{2B} + V_{3B}\cdots+V_{MB} \tag{65}$$

$$V_{1B} = \sum_{i=1}^{M} E(f_i)$$

$$V_{2B} = \sum_{i<j=1}^{M} E(f_i + f_j) - V_{1B}$$

$$V_{3B} = \sum_{i<j<k=1}^{M} E(f_i + f_j + f_k) - V_{1B} - V_{2B} \tag{66}$$

Truncation of the many-body interaction energies to a two-body (V_{2B}) or three-body (V_{3B}) interaction energy is usually adopted to estimate the total energy of the real system, due to a higher computational cost of the higher-order interactions. It should be stressed that ONIOM is a very general and flexible method for large systems, and ONIOM and fragmentation
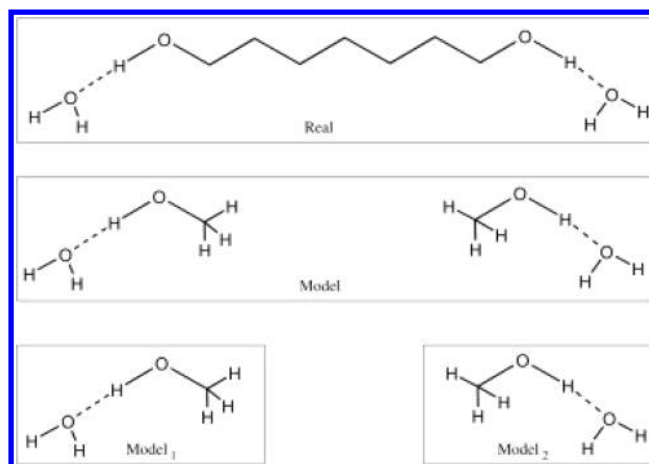
Figure 14. Schematic diagram for the multicentered ONIOM-(QM:QM) approach based on the nonoverlapping approach. Reprinted with permission from ref 180a. Copyright 2003 Wiley Periodicals, Inc.

methods are not mutually exclusive. Therefore, it is not difficult for ONIOM to be further generalized by approximating the
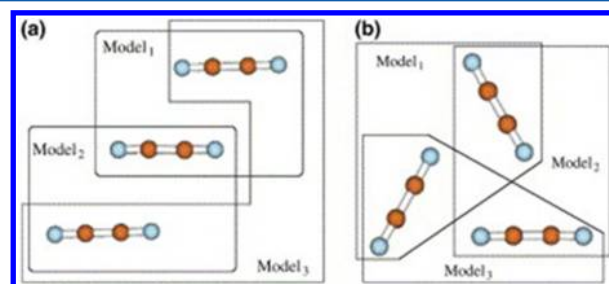
Figure 15. Schematic diagrams for the multicentered ONIOM-(QM:QM) approach based on (a) the overlapping and (b) two-body expansion approaches. Reprinted with permission from ref 180b. Copyright 2005 Elsevier B.V.

total QM energies of the various subsystems (e.g., model, intermediate, and/or real systems) via many-body expansion. Several research groups have independently proposed the combination of the QM/MM or ONIOM methods with the fragmentation methods.[9b,180]

The Tschumper group first proposed this combination (multicentered (mc) integrated QM/QM method) by dividing distant nonoverlapping fragments[180a] of the model system (Figure 14 and eq 67). Later, the multicentered ONIOM-(QM:QM) method was extended for overlapping fragments (model(*i*)∩model(*j*)) (Figure 15a and eq 68)[180b,c] and for two-body (where model(*i+j*) is a dimer of monomers *i* and *j*, Figure 15b and eq 69) and three-body interactions of the model system.[180d,f]

$$E_{ONIOM(QM:QM),mc(non\text{-}overlap)} = E_{low,real}$$

$$+ \sum_{i=1}^{M} [E_{high,model(i)} - E_{low,model(i)}] \tag{67}$$

$$E_{\text{ONIOM(QM:QM),mc(overlap)}} = E_{\text{low,real}}$$
$$+ \sum_{i=1}^{M} \left[E_{\text{high,model}(i)} - E_{\text{low,model}(i)} \right]$$
$$- \sum_{i=1}^{M-1} \sum_{j>1}^{M} \left[E_{\text{high,(model}(i)\cap\text{model}(j))} - E_{\text{low,(model}(i)\cap\text{model}(j))} \right] \tag{68}$$

$$E_{\text{ONIOM(QM:QM),mc(2B)}} = E_{\text{low,real}}$$
$$+ \sum_{i=1}^{M-1} \sum_{j>1}^{M} \left[E_{\text{high,model}(i+j)} - E_{\text{low,model}(i+j)} \right]$$
$$- (M-2) \sum_{i=1}^{M} \left[E_{\text{high,model}(i)} - E_{\text{low,model}(i)} \right] \tag{69}$$

The multicentered ONIOM(QM:QM) method for geometry optimization and frequency was also recently developed.[180e,g,h]

A similar fragmentation-type ONIOM method based on the overlapping (inclusion-exclusion) principle (so-called eXtended ONIOM (XO)) was also proposed to reduce boundary error by expanding the model system; this approach was employed to study zeolites, polypeptides, and cyclodextrins.[180j,181] Moreover, the Raghavachari group developed similar fragmentation-type ONIOM methods (MIM method),[180l] based on overlapping and many-body expansions. Chung et al. also proposed to combine the merits of the extrapolative ONIOM method with those of MBE (generalized ONIOM (GONIOM) method).[9b] Fragmentation of various systems (e.g., model, intermediate, and/or real systems) can be used to estimate energies of the model, intermediate system, and/or real systems through many-body expansion (eqs 65 and 66), whenever their corresponding full QM calculations are too expensive to be performed. On the basis of the hierarchical nature of ONIOM, various approximations can further be used: for example, short-ranged correlation interactions via two- or three-body interactions evaluated with a high-level QM method (such as CCSD(T) and MP4), and the remaining medium- or long-ranged interactions estimated by the extrapolation process via a lower-level QM calculation (e.g., MP2, DFT, HF, and SE) (eqs 70−73). For instance:

$$E_{\text{ONIOM(QM:MM)}} \sim E_{\text{GONIOM(QM:MM)}} = E_{\text{QM,model,MB}}$$
$$+ E_{\text{MM,real}} - E_{\text{MM,model}} \tag{70}$$

$$E_{\text{ONIOM(QM1:QM2)}} \sim E_{\text{GONIOM(QM1:QM2)}}$$
$$= E_{\text{QM1,model,MB}} + E_{\text{QM2,real}} - E_{\text{QM2,model}}$$
$$= E_{\text{QM1,model,MB}} + E_{\text{QM2,real}} - E_{\text{QM2,model,MB}}$$
$$= E_{\text{QM1,model,MB}} + E_{\text{QM2,real,MB}} - E_{\text{QM2,model,MB}}$$
$$= E_{\text{QM1,model,MB}} + E_{\text{QM2,real,MB}} - E_{\text{QM2,model}}$$
$$= E_{\text{QM1,model}} + E_{\text{QM2,real,MB}} - E_{\text{QM2,model}} \tag{71}$$

where $E_{\text{QM,model,MB}}$ represents the QM energy of the model system estimated by many-body expansion (MBE) or truncated MBE.

$$E_{\text{ONIOM(QM1:QM2:MM)}} \sim E_{\text{GONIOM(QM1:QM2)}} + E_{\text{MM,real}}$$
$$- E_{\text{MM,intermediate}} \tag{72}$$

$$E_{\text{ONIOM(QM1:QM2:QM3)}} \sim E_{\text{GONIOM(QM1:QM2:QM3)}}$$
$$= E_{\text{QM1,model,MB}} + E_{\text{QM2,intermediate}} - E_{\text{QM2,model}}$$
$$+ E_{\text{QM3,real}} - E_{\text{QM3,intermediate}} \tag{73}$$

Any fragmentation combination between various systems in ONIOM2 and ONIOM3 can be easily generalized, and is not expressed here (eqs 72 and 73) for brevity. Also, linear-scaling
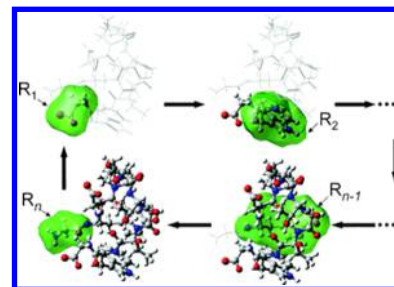
Figure 16. Schematic diagram for the MoD-QM/MM method. Reprinted with permission from ref 180n. Copyright 2014 American Chemical Society.

methods,[182] local correlated methods,[183] and local explicitly correlated methods[184] can be used as the QM methods in GONIOM. Geometry optimization by an GONIOM method was preliminarily tested to give good-quality geometries at a lower computational cost.[9b]

Gascon et al. combined ONIOM with fragmentation via a space-domain decomposition approach, to get accurate ESP in protein in a self-consistent manner (the so-called Moving Domain-QM/MM (MoD-QM/MM) method).[180n,185] In this scheme, the whole system is divided into many small molecular domains (e.g., each amino acid residue, see green part in Figure 16), whose ESP charges of each domain are computed by an ONIOM(QM:MM)-EE method. The newly determined ESP charges of one domain in each ONIOM-EE calculation are updated as the new MM charges and used to determine ESP charges of the rest of the domains by ONIOM-EE calculations. Because of the self-consistent approach with the updated MM charges (until the ESP atomic charges converge to a certain threshold), electrostatic potentials of each domain are mutually polarized and respond to the other domains.

2.3.3. QM/MM and ONIOM Setup/Pitfalls. The reliability of the ONIOM method strongly depends on the choice of the low method and the size of the "model" system. As a first rule of thumb, ONIOM users should identify the major player(s) of the whole system based on chemical intuition of the structure and reactions involved. Ideally, all correlation interactions should be localized fully or mostly within the model system. The *S*-value test provides valuable information on the accuracy of the ONIOM approximation (see sections 2.1.2 and 2.1.3). Recently, Clemente et al. outlined 12 guidelines for ONIOM calculations (e.g., (1) careful identification of the (localized) model system; (2) ONIOM only applied for relative energies (with the same partitioning); (3) a LAH having a single LA; (4) the constant total charge for the MM part in ONIOM-EE calculations along the reaction path; (5) large computational

costs for different methods and large size difference between the model and whole systems).[25] Gaussian Inc. also offered a technical note for usage of the ONIOM methods (http://www.gaussian.com/g_whitepap/oniom_technote.htm).

Although applying QM/MM and ONIOM to complex systems is becoming increasingly popular, a careful and proper system preparation of large systems and the ONIOM setup must be carried out for reliable results. Errors from improper preparation and setup are very difficult to identify and correct. The user will not always receive warning messages for improper system and ONIOM setups. Also, the user should be familiar with principles and shortcoming of both QM and MM methods and calculations, which are essential for ONIOM calculations. In addition, as compared to calculations on small systems, it is very hard for readers to reproduce the reported results for complex systems (see below), often because of a lack of

Figure 17. Schematic flow-chart for the QM/MM or ONIOM setup for biological systems.

detailed description of the calculation setup. Therefore, reliability of QM/MM and ONIOM results of complex systems depends heavily on the users. Recently, Tao et al. implemented and released a Toolkit to Assist ONIOM calculation (TAO), which can help the ONIOM users to set up, prepare, monitor, and analyze ONIOM calculations.[186] GaussView is also useful software to set up and analyze ONIOM calculations.

Stable geometry optimization of large complex systems with huge degrees of freedom and conformations is very challenging. Different research groups have discussed QM/MM and ONIOM setups for complex biological systems (Figure 17).[6b,8f,23,36,169,187] For instance, the PES of a single enzymatic reaction was demonstrated to be largely determined by the initial protein configurations in the QM/MM calculations; variations of 6 kcal/mol were reported.[169,187e] Therefore, proper preparations of initial structures are essential, and multiple starting structures are recommended when using QM/MM and ONIOM calculations. Even then, for a single starting structure, geometry optimization of a flexible region and/or molecules (e.g., mobile water) is potentially problematic. Conformational changes and fluctuations (e.g., change of hydrogen-bond networks) can sometimes take place during geometry optimizations; this can dramatically change the MM energy contribution and lead to a discontinuous PES (based on some of our experience). The common way to avoid such

possible discontinuous PESs is to allow only the inner MM region surrounding the model system to be optimized and freeze the outer flexible MM region. However, while this can stabilize the optimization process, it can artificially suppress the system relaxation in response to the reaction process. One can also perform iterative geometry optimizations (in the forward and backward directions) of all stationary points until the relative energies of the stationary points converge.[188,189] On the other hand, it is highly recommended for the users to decompose the total QM/MM or ONIOM energy of the whole system[48,190] into the QM and MM contributions, analyze and document details of the environment effects, as well as compare the optimized structures of the whole systems. If the large change of the MM or QM/MM contribution and/or the large structural change are observed, one should further validate and confirm that the result is not related to discontinuous PES.

3. APPLICATIONS TO ORGANIC SYSTEMS

With its low computational cost, ONIOM has been applied to small- and modest-sized organic systems to obtain accurate ab initio energies and to large systems to understand mechanisms involving, for instance, chiral catalysts. From early applications of IMOMO to the most recent ones of ONIOM, in this section we chose to highlight studies that demonstrate how ONIOM can be applied effectively for various purposes, reactions, and organic systems. The section is divided into three subsections. The first one deals with the properties and reactivity of "classical" organic systems. The next two subsections are focused on organocatalysis (nonchiral and chiral catalysts) and polymerization, respectively. Systems involving metals (section 4), macro/nano systems (section 6), and solvation (section 8) are not considered here.

3.1. Properties and Reactivity of Organic Systems

3.1.1. Molecular Structure. The use of ONIOM in organic chemistry can be separated into three different types of
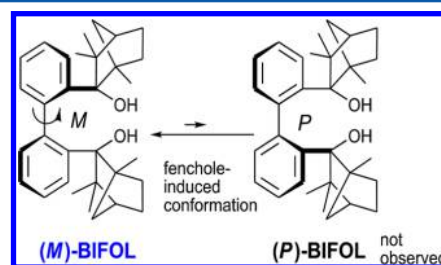
Figure 18. Atropisomerism of C_2-biaryl.[192] Reprinted with adaptation by permission from ref 192. Copyright 2008 Beilstein Institute for the Advancement of Chemical Sciences.

studies. The first type is focused on the geometry of the system. The ONIOM approach permits rapid determination of different conformers or stereoisomers and assessment of their relative energies to predict or confirm the most stable one. Goldfuss et al. used this approach to confirm X-ray structures. In their first study, they investigated the origin of the atropisomerism of biphenyl scaffolds,[191] and more recently they focused on four C_2-symmetric biaryls.[192] In the latter study, four biaryls were optimized with ONIOM(B3LYP/6-31++G(d,p):AM1). Only the two OH groups were modeled at the high level, while the rest of the molecule was modeled with AM1 (Figure 18). Theoretical results confirmed the structures of experimentally observed diastereoisomers. These stereo-

Table 2. Experimental and Calculated Bond Dissociation Energies (in kcal/mol) at 298 K with Various IMOMO Methods[a,194]

			UMP2	G2MSu	UMP4	CCSD	CCSD(T)	G2MSu	G2MSr	G2MSu	G2MSr	G2MSu	G2MSr
	high level →												
	low level →	exp. value	UHF	UHF	UMP2	UMP2	UMP2	UMP2	UMP2	ROMP2	ROMP2	B3LYP	B3LYP
a	H−CH$_3$	105.1 ± 0.2	95.8	101.9	96.8	96.0	96.5	101.9	101.6	101.9	101.6	101.9	101.6
b	H−CH$_2$Me	98.2 ± 1	93.3	99.4	94.1	93.3	93.8	99.1	98.8	99.0	98.6	97.0	96.7
c	H−CHMe$_2$	95.1 ± 1	91.0	97.2	91.8	90.9	91.5	96.8	96.4	96.5	96.1	92.9	92.6
d	H−CMe$_3$	93.2 ± 2	89.3	95.6	90.2	89.3	89.9	95.2	94.9	94.8	94.5	89.8	89.5
e	H−CH$_2$Ph	88.0 ± 1	73.3	79.4	107.7	106.8	107.4	112.4	112.1	90.4	90.1	84.5	84.1
f	H−CHMePh	85.4 ± 1.5	72.3	78.3	106.0	105.2	105.7	110.7	110.4	88.2	87.8	81.3	80.9
g	H−CMe$_2$Ph	84.4 ± 1.5	72.7	78.8	106.0	105.2	105.7	110.7	110.4	87.6	87.2	79.6	79.2
h	H−CHPh$_2$	84 ± 2	60.9	66.9	126.4	125.6	126.2	131.0	130.6	82.9	82.6	75.4	75.0
i	H−CMePh$_2$	81 ± 2	63.1	69.2	126.9	126.1	126.7	131.7	131.3	82.9	82.6	75.2	74.8
j	H$_3$C−CH$_3$	90.4 ± 0.3	91.2	88.2	89.2	86.4	88.1	88.2	87.4	88.2	87.4	88.2	87.4
k	H$_3$C−CH$_2$Me	85.8 ± 1	89.8	86.9	89.0	86.2	88.0	87.9	87.2	87.8	87.0	85.0	84.2
l	H$_3$C−CHMe$_2$	85.7 ± 1	88.2	85.4	88.7	85.9	87.7	87.6	86.9	87.3	86.6	81.8	81.1
m	H$_3$C−CMe$_3$	84.1 ± 1	86.2	83.4	88.2	85.4	87.2	87.1	86.4	86.7	86.0	78.5	77.8
n	H$_3$C−CH$_2$Ph	75.8 ± 1	69.6	66.5	103.0	100.2	102.1	101.7	101.0	79.7	79.0	72.1	71.4
o	H$_3$C−CHMePh	74.6 ± 1.5	68.2	65.2	102.8	99.9	101.8	101.4	100.7	78.9	78.1	69.1	68.3
p	H$_3$C−CMe$_2$Ph	73.7 ± 1.5	66.6	63.6	102.5	99.7	101.6	101.1	100.3	77.9	77.2	65.9	65.2
q	H$_3$C−CHPh$_2$	72 ± 2	55.4	52.3	123.0	120.2	122.1	121.5	120.8	73.5	72.7	62.1	61.3
r	H$_3$C−CMePh$_2$	69 ± 2	55.6	52.7	123.7	120.9	122.8	122.3	121.6	73.6	72.9	60.5	59.8
	root mean square error		10.9	9.3	27.2	25.9	26.7	28.1	27.7	2.8	2.4	5.4	5.9

[a]For the nine first examples (a to i), only the H−C bond was computed at the high level. For the last nine examples (j to r), only the CH$_3$−C was computed at the high level. Reprinted with permission from ref 194. Copyright 1999 AIP Publishing LLC.

isomers are favored due to an intramolecular hydrogen bond between the two OH groups, and reduced intramolecular repulsion between the terpenol scaffolds (Figure 18). Lomas et al. also employed the ONIOM approach to study alkanol derivatives,[45h] and Wieczorek et al. focused on helical structures of peptides.[193]

In addition to the interest in structural analysis, many investigations employed the ONIOM method to investigate other properties. Thus, the second type of ONIOM calculation is based on the study of physical and chemical properties, and the third is based on reactivity/mechanistic aspects. These two types of approaches are discussed in the next two subsections.

3.1.2. Physical and Chemical Properties. *3.1.2.1. Bond Dissociation Energies.* Soon after its development, the IMOMO approach was used to obtain accurate bond dissociation energies (BDE). These calculated BDEs were compared to experimental data or used to predict unknown BDEs. The Morokuma group has actively studied this subject. Hydrocarbon BDEs were calculated, and the results were quite close to the experimental values (Table 2).[194] This study focused on the R$_1$−R$_2$ → R$_1$ + R$_2$ dissociation (R$_1$ = H, Me, and up to R$_2$ = CPh$_2$Me) process for various hydrocarbons. Among all tested high-level models, the G2MS calculations (r and u) showed the best results, especially when a phenyl group was involved (see reaction e in Table 2). The best low level was obtained with ROMP2 calculations; restricted open-shell calculations were carried out to avoid spin contamination. Thus, the IMOMO(G2MSr:ROMP2/6-31G(d)) level was found to be the best approach with the lowest root-mean-square (RMS) error (2.4 kcal/mol). Results were in very good agreement with the experimental ones with a huge reduction in computational cost. BDEs have also been predicted for similar systems such as H−CPh$_3$, H$_3$C−CPh$_3$,[194] and Ph$_3$C−CPh$_3$.[14]

ONIOM-based BDE calculations are not restricted to C−C or C−H breaking. Indeed, larger heterosubstituted molecules involving silicon, sulfur, halogens, or oxygen atoms have been investigated successfully.[195] Recently, a series of natural phenol

moieties were investigated by Nam et al. using ONIOM-(ROB3LYP/6-311++G(2df,2p):PM6). The BDE for the O−H group of phenol was calculated to be 87.2 kcal/mol, which is in very good agreement with the 87.5 ± 1.6 kcal/mol measured BDE.[196]

3.1.2.2. Acidity. Remko et al. have used ONIOM to investigate the relative acidities of different biologically active molecules. For these studies, the most stable conformations were considered before calculating the difference between the ONIOM energies of A$^−$ and AH to obtain the deprotonation energies and gas-phase Gibbs energies. An ONIOM(B3LYP/6-
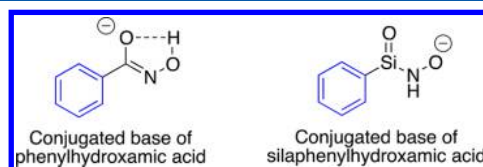
Figure 19. Conjugated base of phenylhydroxamic and silaphenylhydroxamic acids. The low and high levels of the ONIOM models are represented in blue and black, respectively.

311+G(d,p):MNDO) method has been used for sulphonamide,[197] clonidine, and rilmenidine,[198] and also zileuton and its N-dehydroxylated metabolite.[199] In the first two studies, ONIOM energies were found to be close to those obtained by full-DFT calculations. Replacing MNDO by AM1 for the low level also gave very good results for moxonidine[200] and hydroxamic acid derivatives.[201] In the latter case, phenylhydroxamic acid was found to be more acidic than silaphenylhydroxamic acid (Figure 19). The reverse acidity order as compared to carboxylic acids was attributed to a strong intramolecular hydrogen bond in the hydroxamic acid derivatives.

3.1.2.3. Other Properties. ONIOM approaches have been used in several studies to determine NMR parameters.[44,45k,202] Conformers of β-D-glucopyranose have been investigated with

ONIOM(MP2-GIAO:HF-GIAO) to determine the isotropic NMR chemical shielding.[203] Careful choice of the low level (especially for ^{17}O) led to results that were in good agreement with experience. An ONIOM approach has also been used to obtain vibrational frequencies and oxidation/reduction potentials.[204] Notably, redox potentials were calculated for a series of cyclic nitroxide radicals.[205] Using ONIOM(G3(MP2)-RAD:RMP2/6-311++G(3df,2p)), redox potentials were found to be close to the experimental values when available (within 40 mV).

3.1.3. Reactivity of Organic Systems. *3.1.3.1. Nucleophilic Substitutions.* For mechanisms of simple organic reactions, such as the nucleophilic substitution of alkyl chlorides by a chloride ion, several investigations have proven the reliability of the ONIOM approach.[13,206] In the case of the nucleophilic substitution of OH$^-$ on chloroalkanes $CH_{(4-n)}Cl_n$ (n = 2, 4), only the nucleophile and methyl chloride were
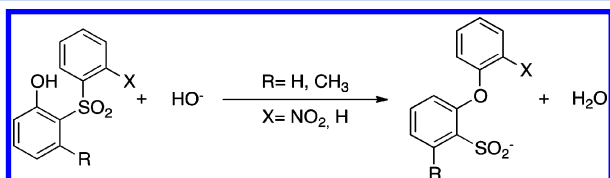
Figure 20. Smiles rearrangement.

modeled at the high level.[207] ONIOM(CCSD(T)/aug-cc-pVDZ:MP2/6-31+G(d))//ONIOM(MP2/aug-cc-pVDZ:B3LYP/6-31+G*) results were found to be as accurate as other published results[208] using CCSD(T)/aug-cc-pVDZ//MP2/aug-cc-pVDZ. Solvent effects have also been taken into account by adding implicit[209] and/or explicit solvation[210] (see section 8.1 for more details). In addition to allowing obtainment of highly accurate results, the ONIOM method can also be used to understand electronic and steric effects on the activation of a reaction. A notable case is an intramolecular aromatic nucleophilic substitution: the Smiles rearrangement (Figure 20).[211] Musaev et al. found through B3LYP and ONIOM(B3LYP:UFF) calculations that electronic and steric effects of the ortho group impact the efficiency of the process.[212] However, recently Chéron et al. pointed out that the lack of sufficient exact exchange in B3LYP is the reason for the inability to locate the Meisenheimer complex intermediate[213] and that others factors (e.g., hydrogen bonds with the ortho group) may also contribute to this reaction.[214]

3.1.3.2. Diels−Alder and Related Reactions. Diels−Alder cycloaddition has also been studied with the IMOMM, IMOMO, and ONIOM methods. For instance, the cycloaddition from acrylic acid and 2,4-pentadienoic acid was studied with the IMOMO(G2MS:MP2) method, using B3LYP/6-31G optimized geometries.[60] Four early transition states leading to four products have been considered (Figure 21). The reaction was found to be concerted but largely asynchroneous. The barrier increases in the following order: T1 < T2 < T3 < T4, and among the four products, the two most stable are *trans* (P2 < P4). From the IMOMO relative free energies at 383 K, a 76:23:1:1 ratio was predicted, in good agreement with the experimental ratio 61:22:9:8.

Other dienes (butadiene, cyclopentadiene, etc.) have been investigated using similar approaches with different dienophiles. The studied dienophiles have been as simple as ethylene, acrolein, acetylenic derivatives, or as complex as chiral
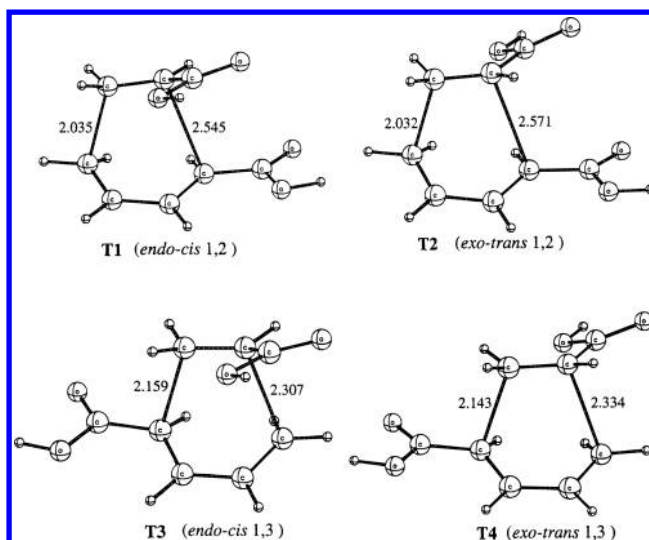
Figure 21. Transition states for the Diels−Alder cycloaddition between acrylic acid and 2,4-pentadienoic acid. Only the carboxylic groups were considered at the low level.[60] Reprinted with permission from ref 60. Copyright 1997 American Chemical Society.

hydroxyalkyl vinyl ketones.[60,206,215] Less expensive ONIOM-type calculations have also been applied successfully (e.g., MM3, AM1, PM3, HF, B3LYP, etc., for the low level).[216] For example, ONIOM(B3LYP:AM1) has been employed for the cycloaddition of bromo-pyranone, and the geometries were in good agreement with those obtained from full-DFT optimization.[217] Nevertheless, ONIOM energies with AM1 did not perfectly reproduce the experimental results, probably due to the effect of including the bromide in the low level. Indeed, for levels higher than AM1, good ONIOM energies were obtained. One must keep in mind that while the definition for the layers is important, the choice of the methods used to treat each layer must not be underestimated. In addition to its use for cycloadditions, the ONIOM method has also been extended to electrocyclizations. The oxy-Cope rearrangement has been studied by Paquette et al.,[218] and the Bergman rearrangement mechanism has also been explored for biologically active molecules.[219]
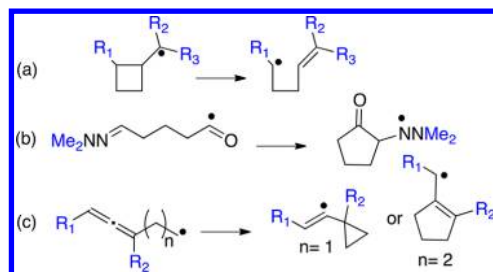
Figure 22. Radical reactions studied with ONIOM methodology. The low and high levels of the ONIOM models are represented in blue and black, respectively.

3.1.3.3. Radical Reactions. Izgorodina et al. evaluated the performance of various commonly used density functionals, such as B3LYP, for the prediction of BDEs or activation energies for various radical systems.[220] The results showed random errors up to 40 kJ/mol. Despite constantly growing computational resources, using very high-level ab initio
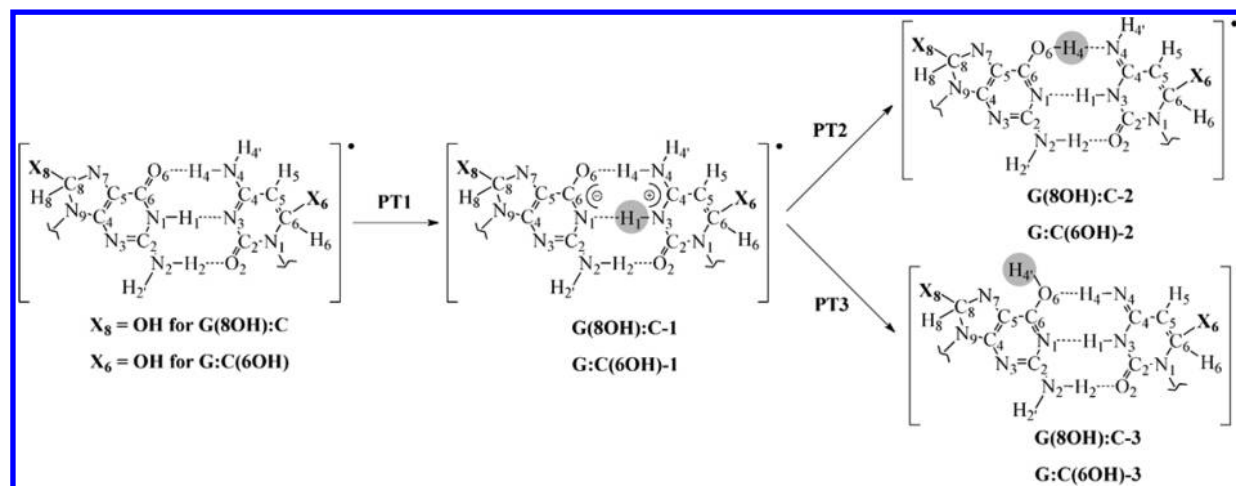
Figure 23. Proton transfers (PT) resulting from the hydroxyl radical addition to the guanine-cytosine base-pair.[226] Reprinted with adaptation by permission from ref 226. Copyright 2012 Royal Society of Chemistry.

calculations is often too demanding. Thus, they proposed an alternative approach, ONIOM(G3(MP2)-RAD:RMP2). BDEs or enthalpies of various addition, abstraction, and ring-opening reactions were explored to test this method. Several G3-based procedures were then used for radical systems,[221] and a variety of reactions were studied, including the ring opening of cyclobutyl moieties (Figure 22a).[222] The regioselectivity of the reaction was then rationalized, and the dependence between the stabilization of the radical product and the selectivity was underlined. For the hydrogen abstraction reaction, Espinosa-Garcia employed IMOMO(MP2/6-31G(d,p):HF/6-31G) to predict the geometries and high-level coupled cluster calculations were used for these reactions.[223] Other approaches, such as IMOMO(QCSID(T):DFT) and IMOMO(MP4:DFT), gave results in good agreement with the high-level calculations.[224] Ring closure has also been investigated. Whereas Izgorodina et al. used G3-type ONIOM for an azahexeneoyl radical cyclization study (Figure 22b),[221a] Shi et al. used ONIOM(QCISD(T)/6-311+G(2df,2p):UB3LYP/6-311+G(2df,2p)) to study cyclization of allenes (Figure 22c).[225]

Finally, radical reactions in some biological systems have also been investigated. Cerón-Carrasco et al. proposed two main paths for the addition of the hydroxyl radical on the guanine—-cytosine base leading to important structural modifications (interbase proton transfers) of the base pair (Figure 23).[226]

In addition to the above studies, other ONIOM-based work on organic systems can be found in the literature. Remko et al. used ONIOM to investigate amino—imino tautomerism for N-phenyl-substituted oxazolines, imidazoines, and thiazolines.[227] Several groups have also explored weak interactions,[228] such as those between dithiourea derivatives and amino acids[229] or anionic species (carboxylates, inorganic oxygen-based anions, and halide anions).[230] Different groups have also investigated host—guest systems including calix-arenas,[231] cyclodextrins,[232] and biological related systems.[233]

3.2. Organocatalysis

The present subsection focuses on the application of ONIOM to organocatalysis. Organocatalysts are organics catalysts in which no inorganic element is involved in the reactive region. The nature of the organocatalyst (alcool, phosphric acid, heterocycles...) and reactions (nucleophilic addition, electrophilic substitutions...) studied with ONIOM varies considerably from one study to the next. Thus, on an arbitrary basis, we chose to separate nonchiral and chiral catalysts and to present different type of reactions for a given catalyst to highlight how ONIOM is efficient with these systems.

3.2.1. Nonchiral Catalysts. Pliego et al. studied the S_N2 reactions involving halogenoalkanes, with NPTROL[234] or 1,4-benzenedimethanol[235] as the catalysts, using ONIOM(CCSD-(T):MP2) with large basis sets for single-point energy
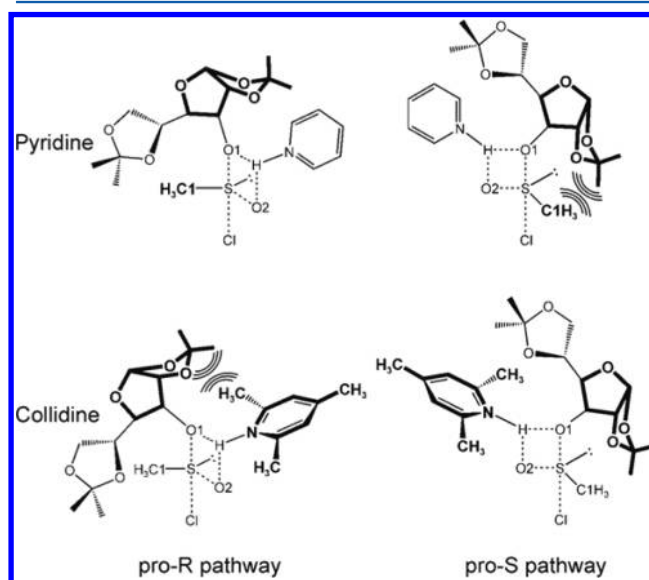
Figure 24. Effect of an achiral base on diastereoselectivity.[236] Reprinted with adaptation by permission from ref 236. Copyright 2007 Wiley-VCH.

calculations. These two polyol catalysts develop hydrogen bonds with the reactants, resulting in lowered reaction barriers and good selectivity. Balcells et al. used an ONIOM-(B3LYP:UFF) approach to investigate a dynamic resolution of sulfinyl chlorides in the presence of a protected D-glucose and an achiral base.[236] Depending on the nature of the base, a reversal of the diastereoselectivity was observed. In the case of the pyridine, a pro-R approach is favored with a 1.0 kcal/mol lower activation energy. Nevertheless, if the collidine is used as a base, the diastereoselectivity is reversed. Indeed, the pro-S approach is favored (with a 2.2 kcal/mol lower activation

energy) due to different repulsive interactions in the transition-state structures (Figure 24).

As compared to full QM calculations, ONIOM calculations are particularly efficient for large systems, such as catalysts that are designed to induce stereoselectivity. The next sections
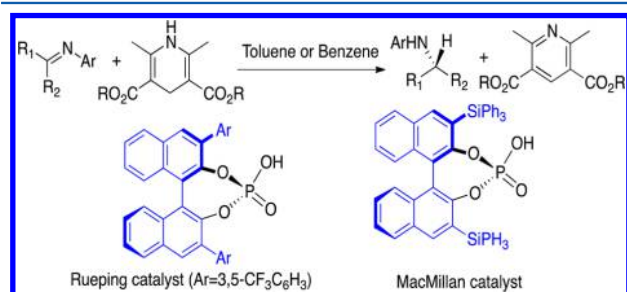

Figure 25. Study of the Hantzsch ester hydrogenation of imines. The low and high levels of the ONIOM models are represented in blue and black, respectively.

contain examples of catalysts based on phosphoric acids, phenols, alcohols, and nitrogen, and involve various kinds of interactions (e.g., steric interactions and hydrogen bonds) between the reactants and the catalyst. Most of the time, the aryl parts of catalysts are only treated at the low level, which can be an MM or QM method.

3.2.2. BINOL Phosphoric Acid Derivative-Catalyzed Reactions. *3.2.2.1. Hydrogenation of Imines.* Simòn et al. contributed actively to the understanding of organocatalytic reactions involving imines and BINOL-phosphoric acid derivatives with the ONIOM method.[237] In their study of the imine hydrogenation mechanism by Hantzsch ester (Figure 25), the ONIOM(B3LYP/6-31G*:UFF) method was used and found to reproduce geometries optimized by B3LYP/6-31G*.[237d,238] Energies were then obtained with single-point calculations at the MPWB1K/6-31G** level.

This work pointed out that one mechanism was favored, in which a "three-point interaction model" was considered to explain the stereoselectivity of the reaction. In this model, two stabilizing hydrogen bonds were considered between the catalyst and the reactants. The third interaction was a steric repulsion between the aromatic part of the imine and the bulky groups of the catalyst. This model was then used for two different catalysts, the Rueping and the MacMillan catalysts. For each of them, the transition states corresponding to the Z-imine are favored as compared to the ones related to the E-imine. In the case of the Rueping catalyst, transition states corresponding to the attack on the E-imines are 9.4 kcal/mol ((S)-product) and 6.5 kcal/mol ((R)-product) higher in energy. The lower transition state associated with the Z-imine leads to the expected (R)-enantiomer with a 1.1 kcal/mol lower energy than that leading to the (S)-enantiomer. The enantiomeric excess (ee %) was then found to be 70% for the reaction at 60 °C, which is consistent with the experimental value (72%). The same conclusion was obtained for the MacMillan catalyst. This study led them to propose the first model predicting the stereochemistry of this BINOL phosphoric acid-catalyzed Hantzsch ester imine reduction (Figure 26).

Recently, Shibata et al. proposed the same model as the one of Goodman to explain the hydrogenation of imine with benzothiazoline as a reducing agent, using M05-2X/6-31G*// ONIOM(B3LYP/6-31G*:HF/3-21G) calculations.[239]
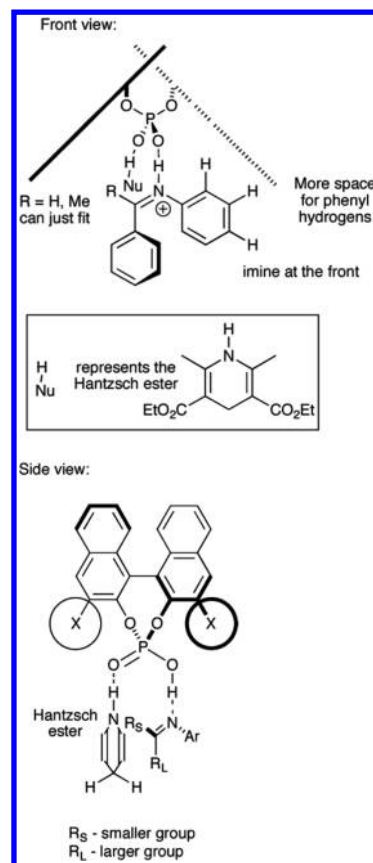
Figure 26. Model for the BINOL phosphoric derivative acid-catalyzed Hantzsch ester imine reduction.[237d] Reprinted with adaptation by permission from ref 237d. Copyright 2008 American Chemical Society.

3.2.2.2. Friedel−Crafts Reactions. Several groups have used ONIOM to study Friedel−Crafts reactions involving an indole and a phosphoric acid. In the first such work, Simòn et al. presented imines as a second partner in the reaction.[237a] Hirata et al. focused their study on nitroalkenes, using ONIOM-(B3LYP/6-31G*:HF/3-21G).[240] They proposed a mechanism that proceeds through a dicoordinated phosphoric acid involving hydrogen bonds to both nitroalkene and NH-indole. The energetic difference between the two competitive pathways increases with bulky groups. Specifically, while a difference of 1.4 kcal/mol between the (R) and (S) transition-state energies was found for the 9-anthryl group (0.4 kcal/mol with a single-point energy calculation at the B3LYP/6-31G* level), the use of the more bulky SiPh$_3$ group results in a 2.7 kcal/mol energetic difference (2.2 kcal/mol at the B3LYP/6-31G* level; Figure 27), which confirms the experimental observations. Finally, this study showed the importance of NH-indole for obtaining good enantioselectivities. Using a methylated indole avoids the hydrogen bond with the catalyst, reducing the energetic difference between the most stable transition structures, (R) and (S), to 0.1 kcal/mol (0.5 kcal/mol at the B3LYP/6-31G* level).

Fu et al. used a similar level of theory for the study of the Friedel−Crafts reaction between an indole and the trifluoromethyl ketone. The results pointed out the necessity of the electron-accepting CF$_3$ group for avoiding multiple electrophilic substitutions.[241]
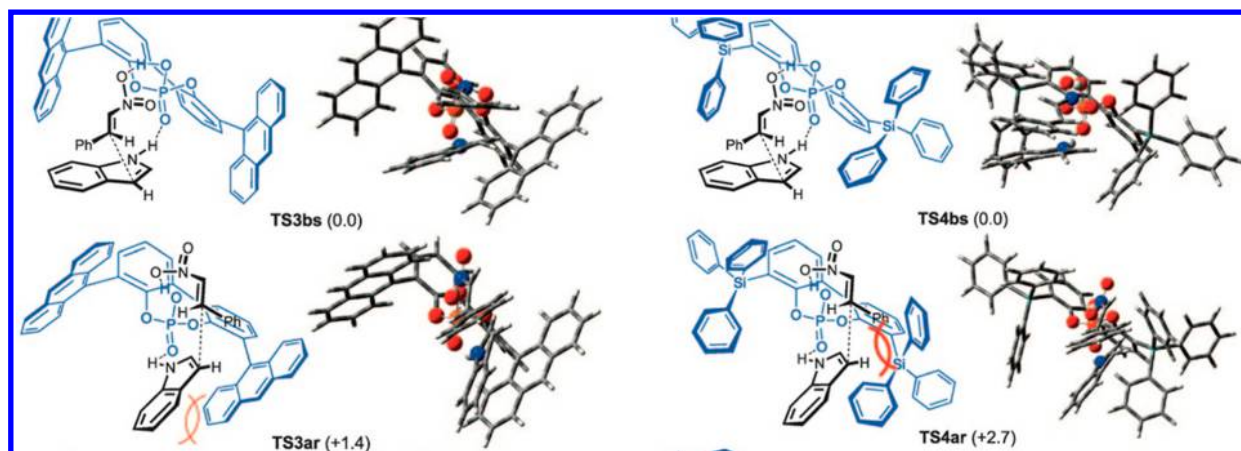
Figure 27. Friedel−Crafts reaction involving nitroalkene and indole derivatives studied with the ONIOM(B3LYP/6-31G*:HF/3-21G) method. Left and right sides show TS structures with 3,3′ substitution by 9-anthryl and SiPh$_3$ groups, respectively.[240] Reprinted with adaptation by permission from ref 240. Copyright 2011 Wiley-VCH.
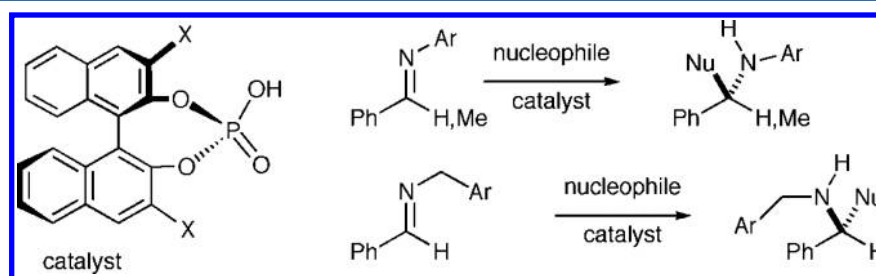

Figure 28. Stereoselective Strecker multicomponent reaction. Here, the nucleophile is a cyanide anion.[237b] Reprinted with adaptation by permission from ref 237b. Copyright 2009 American Chemical Society.
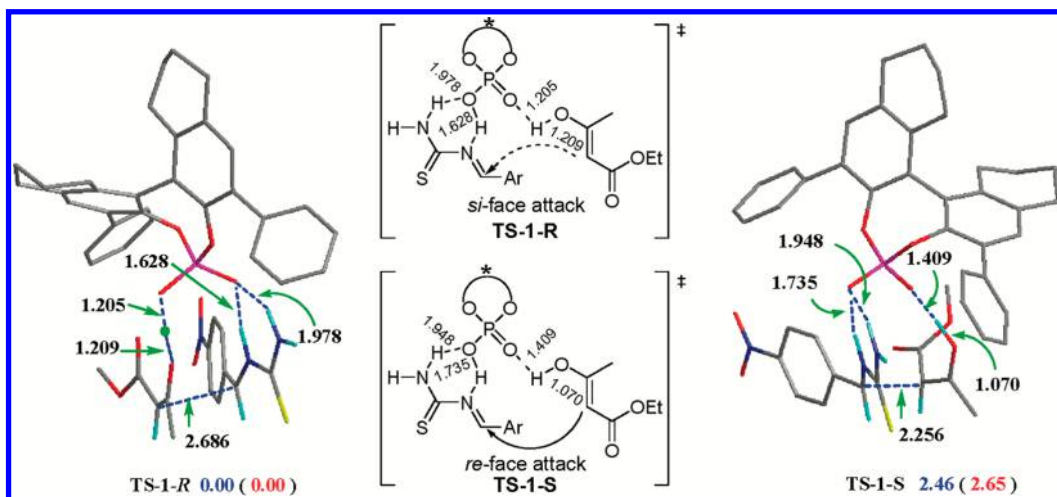
Figure 29. Enantioselective Biginelli reaction involving 3,3′-diphenyl-H$_8$-BINOL phosphoric acid. The lower transition-state structures are given in angstroms, and the relative energies are enthalpies (free energy in parentheses).[242] Reprinted with permission from ref 242. Copyright 2009 American Chemical Society.

3.2.2.3. Multicomponent Reactions. Simòn et al. explored the enantioselectivity of the Strecker reaction using M05-2X/6-31G**//ONIOM(B3LYP/6-31G*:UFF).[237b] In this case, they focused their study on the addition of the hydrogen cyanide on several imines (Figure 28). When the imine is obtained from the condensation of the benzaldehyde and aniline, the *Z* transition state is preferred with a 1.1 kcal/mol lower energy than that of the *E*-imine transition state. Replacing the aniline with the *N*-benzylamine results in higher selectivity, despite the rotation of the benzyl group. In this particular case, the

selectivity is increased due to a 2.9 kcal/mol lower energy for the *E*-imine TS structure. Relaxed scans of the dihedral angle, C=N−C−C, of the iminiums were used to aid their interpretation. This analysis showed that the most stable transition-state structures correspond to the most stable iminium rotamers. The same selectivity was observed with the imine obtained by using acetophenone and *N*-benzylamine as starting materials.

Li et al. carried out an enantioselective Biginelli reaction study, and successfully explained the experimental observations
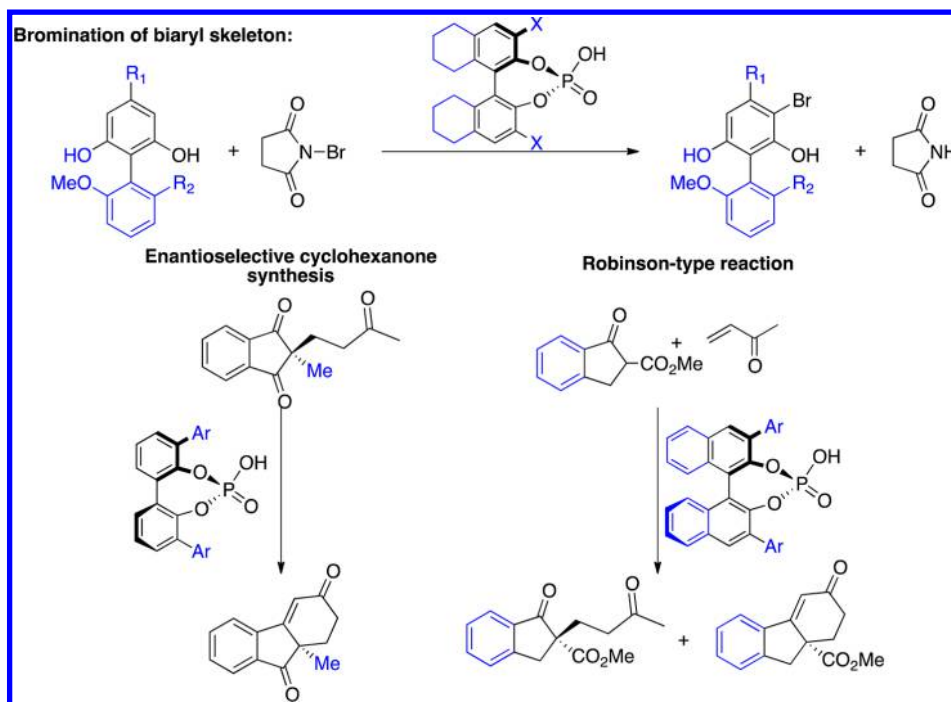
Figure 30. BINOL-phosphoric acid derivative-catalyzed reactions studied using ONIOM. The low and high levels of the ONIOM models are represented in blue and black, respectively.

by using ONIOM(B3LYP/6-31G*:UFF).[242] As in previous studies on similar systems, a transition-state structure with three hydrogen bonds was used to explain the stereoselectivity (Figure 29). Two of them involve the derived imine and the OH group of the phosphoric acid, while the third is between the OH group of the enol and the phosphoryl oxygen. In the case of a reaction between the enolacetate and the (E)-(4-nitrobenzylidene)thiourea activated by the 3,3′diphenyl-H_8-BINOL phosphoric acid, two transition structures were located. In addition to indicating a sterically favored attack on the *si* face, the corresponding transition-state analysis pointed out a stronger hydrogen bond between the enol and the phosphoric acid than in the *re*-face attack (1.2 Å PO−H bond for the *si* face versus 1.4 Å for the *re* face). This stronger interaction results in an earlier proton transfer to the acid, which increases the nucleophilicity of the carbon of the enol and leads to a 2.5 kcal/mol lower transition-state energy (Figure 29).

Other reactions involving imines and BINOL phosphoric acid, such as the hydrophosphonylation reaction,[243] have been studied. These extensive studies led Simòn and Goodman to propose a predictive model for this type of reaction based on analysis of the reactants.[237c]

The previous examples show how useful the ONIOM approach is for understanding the effect of reactant and catalyst substitution on mechanisms and enantioselectivities. BINOL phosphoric acid catalysis is not restricted to the activation of imines. Grayson et al. have studied allylboration of aldehydes.[244] The Yamanaka group has also reported studies of other BINOL phosphoric acid-catalyzed reactions. Using ONIOM for geometry optimization, experimental results were rationalized for the bromination of biaryl scarfolds,[245] synthesis of chiral cyclohexenones,[246] and the enantioselective Robinson-type reaction.[247] ONIOM(M05-2X/6-31G*:HF/3-21G) and ONIOM(B3LYP/6-31G*:HF/3-21G) methods were used for the first and the two last studies, respectively (Figure 30).
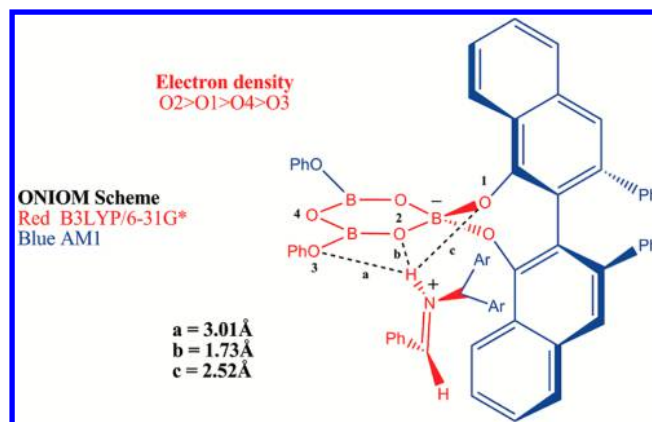
Figure 31. Activation of an imine by a VANOL catalyst.[248] Reprinted with permission from ref 248. Copyright 2010 American Chemical Society.

3.2.3. VANOL-Catalyzed Reaction. Desai et al. successfully employed the ONIOM method to study the aziridination reaction between an imine and ethyldiazoacetate or *N*-phenyldiazoacetamide in the presence of a VANOL catalyst (Figure 31).[248] Both *cis* and *trans* products were observed experimentally. For ethyldiazoacetate, the *cis* transition structure involving two hydrogen bonds is 3.1 kcal/mol lower in energy than the *trans* approach, but a different behavior occurs for acetamides. In the particular case of *N*-phenyl-diazoacetamide, the *trans* selectivity can be rationalized by a three hydrogen-bond transition structure. One hydrogen bond involves the CH of the diazo compound and O2/O1 of the catalyst, and another involves the NH of the iminium and O1/O3, as in the case of ethyldiazoacetate. With acetamides, there is a third interaction between the amidic proton and the O3/O1 atoms of the catalyst. These results were confirmed by using a tertiary acetamide. Avoiding the third hydrogen bond led to a
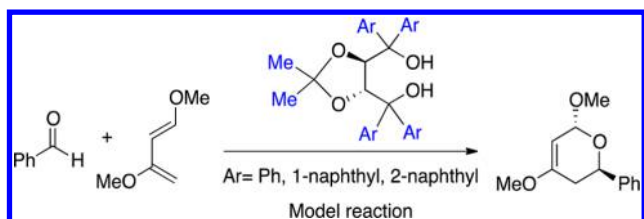
Figure 32. Model for the hetero-Diels–Alder. The low and high levels of the ONIOM models are represented in blue and black, respectively.

result similar to that obtained with ethyldiazoacetate: a *cis* approach.

3.2.4. TADDOL-Catalyzed Reactions. Zhang et al. have studied the enantioselective hetero Diels–Alder reaction.[249] Starting from benzaldehyde and Danishefsky's dienes in the
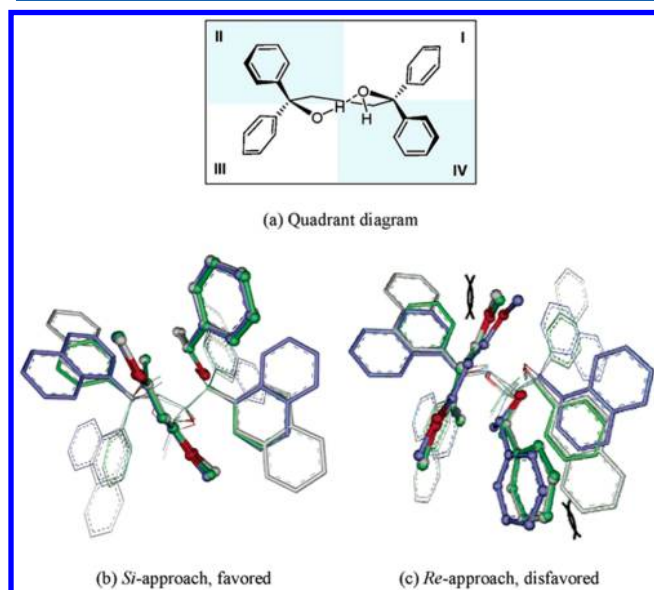
Figure 33. Hetero-Diels–Alder reaction catalyzed by TADDOL derivatives. (a) Quadrant diagram for the TADDOL catalyst. Superposition of the most favored (b) *si* and (c) *re* approaches. Substituents of the TADDOL catalyst are represented by different colors: 1-naphthyl (blue; the most selective one), 2-naphthyl (green), and phenyl (gray).[249] Reprinted with permission from ref 249. Copyright 2006 American Chemical Society.

presence of TADDOL derivatives, an enantioselective cyclo-addition is observed experimentally (Figure 32).

Zhang et al. employed a B3LYP/6-31G*//ONIOM(B3LYP/6-31G*:PM3) approach and considered one hydrogen bond between the catalyst and the benzaldehyde. Three TADDOL catalysts with different substituents were studied (Figure 32). The reaction proceeds through an asynchronous but concerted process, and no zwitterionic intermediates were found. The endo attack is favored, and irrespective of the catalyst, the *si* face of the hydrogen-activated benzaldehyde is favored. Whereas the relative reactivity of the three catalysts was confirmed theoretically, the prediction of the enantiomeric excess of the reaction was more difficult. Despite their simplified model, analysis of the π-stacking geometries offered a clear explanation of the relative reactivity (Figure 33). In the case of substitution with the 1-naphthyl group, a shorter hydrogen bond in the TS structure was found between the benzaldehyde and the catalyst. This stabilizing interaction lowers the activation energy, as the TADDOL catalyst becomes more acidic. To understand the preference of the *si* face attack of the benzaldehyde, a quadrant model was considered. In Figure 33a, the aryl groups of the catalyst point backward in quadrants I and III and forward in quadrants II and IV. Consequently, these last two quadrants are more hindered than I and III. When the TS geometries of the *si* and *re* approaches are compared (Figure 33b and c), an important steric interaction is observed in the latter. Indeed, the reactants are localized in the more hindered quadrants II and IV, explaining the preference for the *si* approach. In addition, stronger steric repulsions are observed in the 1-naphthyl-substituted catalyst (blue catalyst in Figure 33), which explains the better enantioselectivity observed experimentally with this catalyst.

Anderson et al. studied a similar system by employing M06-2X/6-31+G*//ONIOM(B3LYP/6-31G*:AM1).[250] In this study, they used AM1 for the low level of ONIOM for alkyl groups of the silyl ether of the diene and for the aromatic groups and acetal part (−OCMe₂CO−) of the TADDOL catalyst. They were able to confirm the stereoselectivity observed experimentally by considering a hydrogen bond between the aldehyde and the TADDOL. In contrast to the previous example of Zhang et al., the aldehyde was also stabilized by a CH−π interaction. ONIOM was also employed for the nitroso-aldol TADDOL-catalyzed reaction study by Akakura et al. to understand the origin of the regio- and enantioselectivity of this reaction.[251]

3.2.5. Nitrogen-Based Catalysts. *3.2.5.1. Amine-Based Catalysts.* Simón et al. explored the amidation of β-ketoester in the presence of chiral guanidine.[252] With a model similar to that for the hydrogenation of imine by Hantsch esters,[237d] they
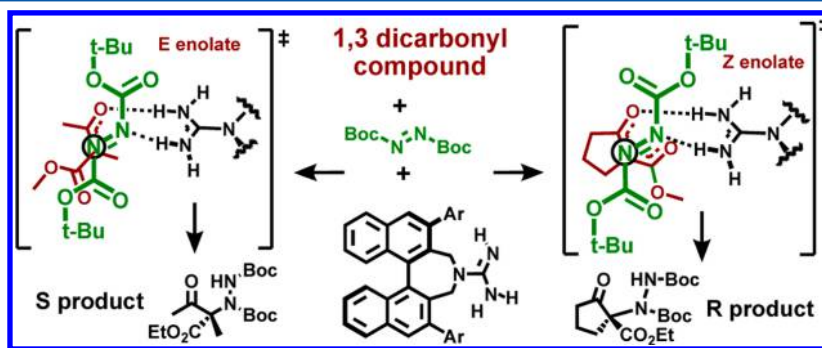
Figure 34. Amidation of β-ketoester in the presence of chiral guanidine.[252] Reprinted with permission from ref 252. Copyright 2012 American Chemical Society.
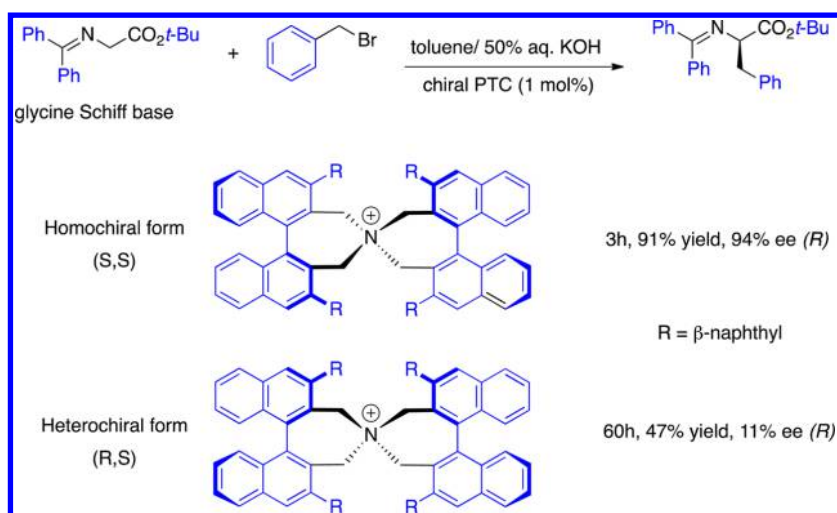
Figure 35. Benzylation of the glycine Schiff base in the presence of a chiral ammonium salt. The low and high levels of the ONIOM models are represented in blue and black, respectively.

investigated the reversal of enantioselectivity between cyclic and acyclic β-ketoesters (Figure 34). The analysis of the TS structures pointed out reactivity similar to that of BINOL-catalyzed reactions with a three-point contact model. While for cyclic β-keto esters the stereoselectivity can be easily predicted, the reactivity of acyclic β-ketoesters is trickier to rationalize, as the E-enolate has to be considered as a reactive species for the process.

Proline derivatives were also studied for their implication in the aldolization reaction[253] and in a triple cascade reaction (Michael−Michael-aldol).[254] The Corey−Bakshi−Shibata (CBS) catalyst,[255] also derived from proline, was studied by Korenaga et al.[256] A highly enantioselective reduction of the trifluomethylphenyl ketone in the presence of BH_3 was proposed by tuning the catalyst.

Quinine derivatives were investigated for their use in 1,4-Michael addition on aryl ketone[257] and the hydrophosphonylation of α-ketoesters.[258] In the case of α-bromination of acyl chlorides,[259] the tertiary amine of the quinine derivative catalyzes the formation of an intermediary ketene, which results in the α-bromination of the ketene. Using IMOMO energies, the estimation of the ee % of the bromination reaction was found to be 87%, which is in good agreement with experiments (88%).

3.2.5.2. Chiral Ammonium Salt Catalyst. Recently, chiral ammonium salt-catalyzed stereoselective benzylation of glycine derivatives has been examined (Figure 35) by Petrova et al.[260] Two catalysts were studied: the heterochiral (*R,S*) catalyst and the homochiral (*S,S*) catalyst, and geometries were obtained at the ONIOM(B3LYP/6-31G*:PM6) level. While the homochiral catalyst shows good yield and enantiomeric excess (91% yield and 94% ee (*R*)), the heterochiral catalyst presents a different behavior. Two factors have been proposed to explain this experimental result. First, when the tight ion-pair interaction between the amino-acid derivative and the catalyst is considered, the activation barrier for the formation of the (*R*)-product increases as compared to the one obtained with the homochiral catalyst. Second, the reaction can occur without considering this ion pair, resulting in an easier (*S*)-product formation. These two factors explain both the lower yield and the ee obtained with the heterocatalyst.

3.2.5.3. N-Heterocyclic-Based Catalysts. *N*-Heterocyclic catalysts have also been studied with the ONIOM method. Tang et al. studied β-lactam synthesis catalyzed by *N*-heterocyclic carbenes (NHCs).[261] Dudding et al. used the IMOMO method for the benzoin condensation by asymmetric triazolium and thiazolium catalysts.[262] The same group also studied the spiroligozyme-catalyzed transesterification of vinyl-trifluoroacetate by methanol, using the M06-2X/6-31G*// ONIOM(B3LYP/6-31G*:PM6) approach.[263] This study pointed out how the pyridine-alcohol and urea groups are able to activate the reaction. Apart from these studies, other thiourea-catalyzed reactions have also been studied, such as pyrrazole crotonization,[264] the enantioselective decarboxylative-protonation reaction,[265] and enatioselective amine 1,4-addition.[266]

3.3. Polymerization via Radical Systems

In the following subsection, ONIOM-based studies of polymerization via radical systems are reviewed. Polymerization
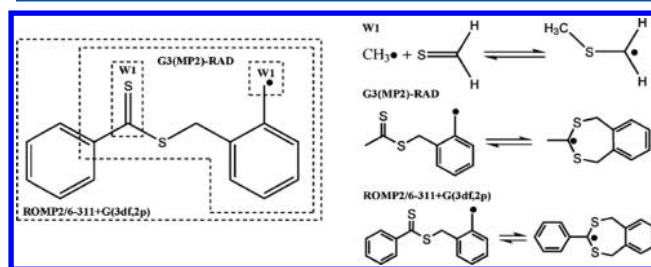
Figure 36. Example of an ONIOM scheme for the calculation of addition−fragmentation chain transfer agents.[267a] Reprinted with permission from ref 267a. Copyright 2006 American Chemical Society.

involving metals is not considered here (see section 4.3). Other types of organic radical reactions were detailed above in section 3.1.3.

3.3.1. Controlled Radical Polymerizations. *3.3.1.1. Reversible Addition−Fragmentation Chain Transfer.* The reversible addition−fragmentation chain transfer (RAFT) is one of the most practical controlled radical polymerization (CRP) methods. Several groups have employed the ONIOM approach to study the kinetics of this CRP process.[267] For
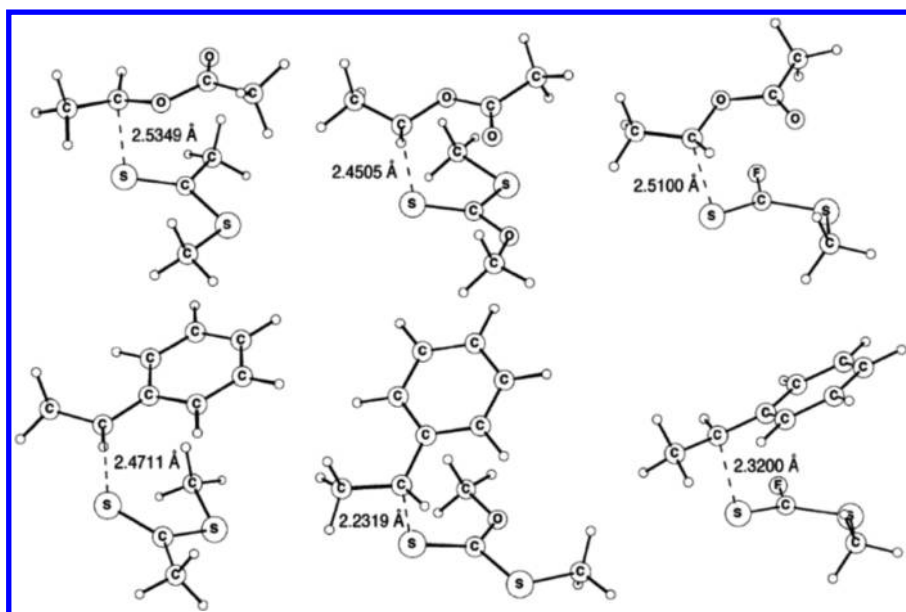
Figure 37. Transition-state structures of styrene and vinyl acetate polymerization. Reprinted with permission from ref 270. Copyright 2006 American Chemical Society.

example, a three-layer ONIOM (W1:G3(MP2)-RAD:MP2) approach was considered for the RAFT agents, where the inner core of each agent was calculated at the W1 level of theory, the α-substituents of radical centers were considered in the intermediate core and calculated with the G3(MP2)-RAD method, and the whole system was then calculated at the MP2/6-311+G(3df,2p) level of theory, as shown in Figure 36.[267a,268] These calculations indicated that highly stable intramolecular radicals might be formed from the proximal radicals and S═C bonds. To further identify an accurate and practical method for these large radical systems, Izgorodina et al. have tested several low-cost theoretical procedures.[269] They found that the commonly used density functionals are not able to quantitatively or qualitatively reproduce the values of the fragmentation enthalpy of these systems. On the other hand, the ROMP2 calculations were found to be better in most cases, but they fail when the radical leaving group is conjugated. A two-layer ONIOM-based approach was found to be practical and particularly accurate for these large systems. In this approach, the model system was calculated with G3(MP2)-RAD, and the whole system was calculated with ROMP2-(SCS-/SOS-MP2)/6-311+G(3df,2p).

Coote et al. further applied the ONIOM(W1:G3(MP2)-RAD)//B3LYP/6-31G(d) method to study the addition−fragmentation kinetics of fluorodithioformates in styrene, vinyl acetate, and ethylene polymerization (Figure 37).[270] On the basis of thermodynamic considerations, and as predicted earlier, these calculations suggested that fluorodithioformates should be able to function as genuine multipurpose RAFT agents. Regarding the leaving group abilities and reinitiation rates, S═C(F)SC(CH$_3$)$_2$CN and S═C(F)SC(CH$_3$)$_2$Ph reagents were found to be the best F-RAFT agents for styrene polymerization, while S═C(F)SCH$_2$CN and S═C(F)SC(CH$_3$)$_3$ were predicted to be optimal for vinyl acetate and ethylene polymerization. Furthermore, the chain length effects and penultimate unit effects were suggested to be significant in the RAFT process for the cumyl dithiobenzoate-mediated polymerization of styrene, based on the ab initio calculations with the ONIOM approach.[271] Simplified models to describe this system were

inadequate, particularly in modeling the initial stages of the process.

In addition, the ONIOM(W1:G3:ROMP2) approach was successfully applied to the design and synthesis of a novel class of RAFT agents.[272] These studies suggested that the electron-deficient benzyl methyl/phenylsulfonyldithioformate can efficiently mediate the polymerization of isobornyl acrylate and promote hetero Diels−Alder reactions with certain monomers, including styrene.

3.3.1.2. Nitroxide-Mediated Polymerization. In nitroxide-mediated polymerization (NMP), the ONIOM(G3(MP2)-RAD:B3LYP/6-31G(d)) approach was used to study side reactions with PCM solvation model.[273] The obtained thermodynamic energies were in good agreement with experimental data (within 4.5 kJ/mol). Megiel et al. used ONIOM(G3:ROMP2) to study the substituent effect on the strength of C−ON bonds in *N*-alkoxyamines models for dormant species in the copolymerization of styrene with acrylonitrile, and the results were in good agreement with experimental data.[274]

3.3.2. Noncontrolled Radical Polymerization. ONIOM approaches have also been used to study noncontrolled radical polymerizations. Izgorodina et al. carried out a systematic methodological test to calculate the propagation rate coefficients in free radical polymerization of acrylonitrile and vinyl chloride.[220,275] Some commonly used DFT methods (e.g., B3LYP) were found to fail to quantitatively or even qualitatively reproduce reaction barriers and enthalpies for chain-transfer/propagation reactions. However, the authors also mentioned that the most recently developed DFT functionals (e.g., the Minnesota functionals) have shown great promise in many problematic systems. In their study, they found G3(MP2)-RAD- and G3(MP2)-RAD-based ONIOM approaches yielded accurate results (<1 kJ/mol). The chain-length effects on the rate constants were found to largely converge to their long-chain limit at the dimer radical stage. Minor solvation effects were found when using an implicit solvent model (COSMO).

4. APPLICATIONS TO INORGANIC COMPOUNDS AND HOMOGENEOUS CATALYSIS

This section summarizes applications of the ONIOM method to inorganic compounds, and transition metal homogeneous catalysis, including polymerization reactions. Aiming for broad coverage of ONIOM applications to molecular inorganic compounds (section 4.1), the selected studies involve a diverse range of elements, from alkali metals to d-block, f-block, and main group metals. An additional emphasis is on covering studies that utilized ONIOM as a tool for purposes such as separating steric and electronic effects, rather than focusing only on applications to large systems that benefit from the efficiency of ONIOM. The use of ONIOM methods to study the mechanisms and selectivities of transition metal homogeneous catalysts is summarized in section 4.2. The selected studies range in scope from full catalytic cycles and selectivity, to those with a narrow focus on a single reaction step or transient intermediates. These examples show three roles of ONIOM calculations in the study of transition metal homogeneous catalysis: to rationalize a low-energy path to explain the mechanism, to compare competing reaction paths to explain the selectivity, and to identify a thermodynamically stable active intermediate to explain the reactivity or selectivity. The emergence of ONIOM methods has allowed these properties to be computed with chemical accuracy for realistic catalytic systems at low computational cost. The ONIOM method has also made significant contributions toward the study of polymerization reactions, including the prediction of regio- and stereoselectivity (section 4.3). The selected studies in section 4.3 show how IMOMM and ONIOM methods can be used to describe steric and electrionic effects of the ligands, substituents, cocatalysts, and even counterions for more realistic treatment of polymerization processes. From early applications of IMOMM to recent development of new methodology, the studies highlighted in this section all make particularly effective use of ONIOM and clearly demonstrate how it can be applied for various purposes to systems involving molecular inorganic compounds and homogeneous catalysis.

4.1. Inorganic Compounds

In this section, ONIOM studies of the structure, properties, and reactivity of molecular inorganic compounds are reviewed. The majority of the studies in this area involve d-block complexes, particularly organometallic species. Thus, the section on the structure of d-block complexes (section 4.1.1) is divided into several areas to showcase the versatility of ONIOM. The section on properties (section 4.1.2) encompasses studies of any inorganic compounds, whereas the discussion of reactivity (section 4.1.3) is limited to f-block and main group compounds. The reactivity of d-block complexes, including transition-metal homogeneous catalysis, is a very significant area of ONIOM-based research that is covered in section 4.2 in various subsections.

4.1.1. Structure. *4.1.1.1. ONIOM Treatment of Bulky Organometallic Systems.* Organometallic compounds often have bulky ligands that can be computationally demanding to treat at a high level of theory. ONIOM enables optimizations of large models with flexible ligands, but this comes with the complication of many new local minima; thus, conformational searches become necessary. Many such systems can now be treated in full with DFT, but it can be expedient to first perform the conformational search with ONIOM(B3LYP:UFF).[276] For some systems, it is appropriate to truncate the ligands for the
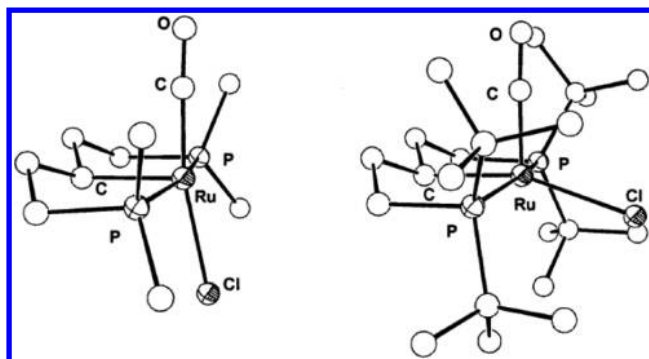
Figure 38. Optimized structures of $RuCl(CO)[CH(C_2H_4PMe_2)_2]$ (left) and $RuCl(CO)[CH(C_2H_4P^tBu_2)_2]$ (right) at B3LYP and ONIOM(B3LYP:HF) levels, respectively. Reprinted with permission from ref 278. Copyright 2002 American Chemical Society.

sake of simplicity, but there are many cases where steric effects attributed to the ligand override competing electronic factors, such as agostic interactions, leading to new global-minimum geometries and isomers.[277] To capture the largely steric influence of bulky ligands, it is often sufficient to treat them at the MM level. For example, Gusev et al. found that if the ^tBu groups in $RuCl(CO)[CH(C_2H_4P^tBu_2)_2]$ are truncated to Me groups, the most stable structure at the B3PW91 level has Cl *trans* to CO, which is inconsistent with the *cis* arrangement in the X-ray crystal structure (Figure 38).[278] However, when the ^tBu groups are included at the MM level using ONIOM-(B3PW91:UFF), the optimized structure becomes qualitatively correct, with Cl *cis* to CO due to steric repulsion. Taking advantage of the ONIOM method to combine multiple QM levels, they found that the use of ONIOM(B3PW91:HF) provides further improvements in the structure, for example, reducing the error in the average Ru–P distance from 0.06 to 0.01 Å. A variety of QM methods, including PM3,[279] DFTB,[280] HF,[98,281] and DFT,[282] have been used as low layers in ONIOM studies to capture both the steric and the electronic effects of the ligands.

4.1.1.2. Agostic Interactions. Agostic interactions between filled C–H (or, for instance, B–H, Si–H, C–C, B–B, Si–Si, B–C) σ orbitals and empty d orbitals of electron-deficient metal centers are commonly found in organometallic compounds. Such interactions often require significant structural distortion, and can be sensitive to the steric influence of bulky ligands.[283] For example, Jaffart et al. demonstrated through IMOMM(B3LYP:MM3) calculations that steric effects can explain why α- and β-agostic interactions are both observed in a niobium complex with ^iPr, whereas only an α-agostic interaction is observed in the Et complex.[284] In a subsequent study, Jaffart et al. showed that by truncating a ligand to reduce steric bulk the electronically favored β-agostic interaction became more dominant in the Et complex.[285] Other ligand–ligand interactions such as π-stacking can also compete and prevent the formation of agostic interactions, as shown in an ONIOM(B3PW91:UFF) study by Clot et al.[45m]

In contrast to the previously described systems, in some cases increased steric interactions are required for an agostic interaction to form.[277a,286] The X-ray crystal structure of $[Ir(H)_2(P^tBu_2Ph)_2]^+$, a 14-electron complex, shows two agostic interactions between CH_3 groups of the ^tBu substituents and the vacant coordination sites *trans* to the hydrides. B3LYP optimizations by Ujaque et al. of a model complex ($[Ir-

$(H)_2(PH_2Et)_2]^+$) with Ph and ^tBu truncated to H and Et, respectively, resulted in a structure lacking agostic interactions.[277a] However, when the full ligands were introduced using
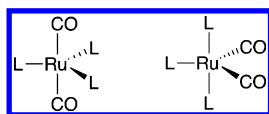
Figure 39. *trans*-CO (left) and *cis*-CO (right) isomers of $Ru(CO)_2L_3$, where L = PEt_3 or P^iPr_2Me.

IMOMM(B3LYP:MM3), while maintaining the same truncated model as the high layer, the optimized structure showed the two agostic interactions. It is clearly steric pressure that leads to formation of the agostic interactions in this compound, because the additional groups were included only at the MM level.

4.1.1.3. Relative Energies of Isomers. In addition to providing reliable structures of organometallic compounds, ONIOM calculations can be used to evaluate the relative energies of isomers. Thus, ONIOM studies have shown that steric interactions control the relative stabilities of trigonal bipyramidal and square pyramidal isomers of $Ru(NCH)(CO)$-$(NO)(P^tBu_2Me)_2^+$,[287] *cis,trans,cis* and all-*cis* isomers of some six-coordinate d^0 dioxo compounds,[277e] and *syn* and *anti* isomers of a Re-based olefin metathesis catalyst.[288] In a representative study of $Ru(CO)_2L_3$ complexes (L = PEt_3 or P^iPr_2Me), Ogasawara et al. examined how the relative energies of the *trans*-CO and *cis*-CO isomers (Figure 39) are affected by the ligand, L.[277d] On the basis of solution IR spectra, the isomers of the PEt_3 and P^iPr_2Me complex coexist. MP2 calculations on the model complex $Ru(CO)_2(PH_3)_3$ placed the *trans*-CO 3 kcal/mol higher in energy than the *cis*-CO isomer. The CO ligands prefer the equatorial positions that they occupy in the *cis* isomer, because they maximize back-donation. However, this electronic preference is partially negated by repulsive M−CO σ interactions. IMOMM(MP2:MM3) calculations with the PEt_3 ligands in the MM layer gave the same relative energies, but with the P^iPr_2Me ligands the *trans*-CO isomer was favored by 2.8 kcal/mol. The electronic energies of the QM part of the IMOMM calculations favored *cis*-CO by 3.1 and 1.7 kcal/mol for both PEt_3 and P^iPr_2Me, respectively, showing that it is the steric influence of the ligand that is responsible for the change in isomer preference. In this case, the most stable isomers predicted by IMOMM were those that were expected on the basis of the IR data. However, when dealing with these subtle energetic preferences, some systems present exceptions in which the extrapolated IMOMM-(B3LYP:MM3) energies are qualitatively incorrect.[289] In such cases, or indeed anytime more accurate energies are required, a useful strategy is to compute single-point full QM energies at the QM/MM geometries.[289,290]

4.1.1.4. Quantifying Steric and Electronic Effects. As in the previous example,[277d] IMOMM energies can be decomposed into electronic and steric contributions to gain detailed insight into ligand effects on organometallic compounds. Thus, even when resources are available for full QM calculations, the IMOMM or ONIOM method can be a useful analytical tool. One strategy introduced by Barea et al. involves energetic comparison of two IMOMM(MP2:MM3)-optimized structures: one with the real system optimized, and a second with the metal center and the atoms directly bonded to it fixed to positions determined by QM optimization of the model system.[291] If an MM method is used for the low level, the

difference in energy arises from geometric distortion due to steric effects. The fully optimized system has reduced steric repulsion, but this comes with an electronic penalty. For example, at the IMOMM(MP2:MM3) level, the fully optimized $ReH_5(PCyp_3)_2(SiH_2Ph)_2$ (Cyp = cyclopentyl) complex is stabilized by 7.3 kcal/mol relative to the restricted structure, which can be decomposed to 10.8 kcal/mol MM (steric) stabilization, and 3.5 kcal/mol QM (electronic) destabilization.[291] Further decomposition of the MM energies showed that van der Waals (vdW) interactions and bending terms were the major components of the steric stabilization, accounting for 7.9 and 2.9 kcal/mol, respectively. These terms were then analyzed in detail to see which ligands and groups of atoms impose the strongest steric influence. The restricted optimization strategy has been applied to other complexes,[277c,292]
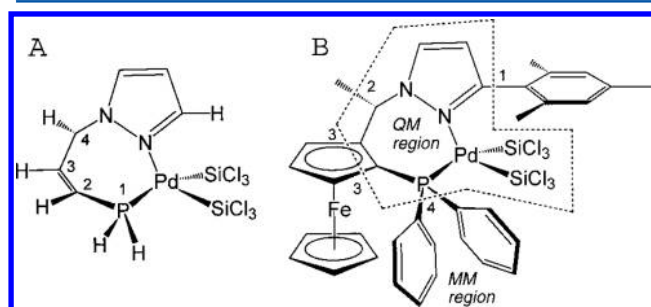
Figure 40. (A) QM model without substituents, and (B) IMOMM model with substituents in the MM region. Reprinted with permission from ref 294. Copyright 2000 American Chemical Society.

and the detailed analysis of MM terms is also useful for other tasks, such as comparing steric effects among isomers.[277e]

An alternative approach to separate steric and electronic effects is to compare geometric parameters obtained from QM/MM optimizations on a series of models with various layer definitions (see section 2.1.7). A basic form of this approach is the comparison of structures from QM-only model and QM/MM real-system optimizations. Such procedures can be carried out solely for the purpose of analyzing steric effects.[293] The use of a larger series is illustrated by Woo et al.,[294] who optimized six models with IMOMM(BP86:TRIPOS5.2[295]), as implemented in CPMD,[296] and with the ferrocene force field of Doman et al.[297] to determine why the Pd−P bond length in a chiral $Pd^{II}(SiCl_3)_2(L)$ complex is unusually long (2.50 Å). Three models, differing only in the treatment of the phenyl substituents of the phosphine, have been performed. DFT optimization of model A in Figure 40 consisting of only the QM region provided a baseline Pd−P bond length of 2.39 Å. The IMOMM-optimized structure of model B had a longer bond length of 2.46 Å, indicating that the steric influence of the ferrocene, phenyl substituents, and trimethylphenyl group is a major factor contributing to the long bond. The third calculation, in which the phenyl substituents in model B are treated with QM and thus their electronic effects are included, resulted in further elongation of the Pd−P bond to 2.50 Å, matching the experimental structure; thus, it is a combination of steric and electronic effects that contributes to the long bond length. The series of models was also used to identify the factors responsible for the distortion from ideal square-planar geometry.

4.1.1.5. Ion Pairs. In computational studies of charged inorganic complexes, counterions are often neglected. How-

ever, in solution, such species can exist as ion pairs in which the structure and reactivity are dependent on both ions.[298] ONIOM(QM:MM) and ONIOM(QM:QM) calculations have been used to examine ion-pair effects in Ir[299] and Ru[45g] complexes, with small counterions such as BF_4^- being included in the high layer. To treat ion pairs that have bulky groups on the metal complex as well as the counterion (e.g., BPh_4^-), Zuccaccia et al. divided both ions into high and low layers.[45g]

4.1.1.6. New ONIOM-Based Techniques. An interesting ONIOM method aimed at treating biradical systems that involves the use of the same DFT functional and basis set for both levels was presented recently by Kitagawa et al.[300] In their method, the low level is a spin-restricted calculation, while the high level follows their approximate spin projection (AP) scheme.[301] The AP method corrects the spin contamination error associated with the broken symmetry (BS) method that is commonly used to study systems with multireference character. The AP scheme is computationally demanding, as it requires
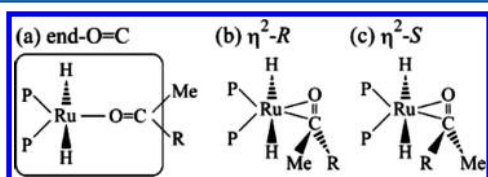
Figure 41. (a) Three coordination modes of $CH_3COCH_2COOCH_3$ on (R)-Ru^{II}H$_2$-BINAP: (a) CO end-on, (b) pro-R η^2, and (c) pro-S η^2. Only the P atoms of BINAP are shown. The box in (a) shows the boundary of the QM layer of the ONIOM model. Reprinted with permission from ref 128a. Copyright 2007 American Chemical Society.

high spin and broken symmetry (BS) energies, gradients, and $\langle \hat{S}^2 \rangle$ values, as well as a sampling of $\langle \hat{S}^2 \rangle$ values from $6N$ (N = optimized atoms) BS calculations. The ONIOM approach greatly reduces the computational cost and is successful because spin polarization is minimal in the peripheral regions of the ligands.

Another method that takes advantage of the efficiency of ONIOM to perform a large numbers of calculations is global reaction route mapping (GRRM, see section 2.2.4 for details). GRRM involves automated search of a potential energy surface starting from randomized initial structures. Maeda et al. used GRRM to study the binding of a substrate, $CH_3COCH_2COOCH_3$, to a model of a hydrogenation catalyst, (R)-Ru^{II}HL-BINAP (L = H, BINAP = 2,2′-bis-(diphenylphosphino)-1,1′-binaphthyl).[128a] The ONIOM-(B3LYP:UFF) model and three possible binding modes of the substrate are depicted in Figure 41. The search resulted in 135 unique, optimized structures, most of which featured the substrate bound through CO in an end-on mode, or in a pro-R or pro-S η^2 mode. The most stable structure was an η^2-R type, and it was 28.8 kJ/mol lower in energy than the most stable η^2-S structure, due to differences in steric repulsion. In support of this result, experiments show high enantiomeric excess of the (R) product.[302]

4.1.1.7. f-Block. The application of ONIOM to f-block complexes is analogous to that of d-block complexes: the metal center and a portion of the ligands are treated with a QM method, while large substituents are treated only with a more efficient method. Perrin et al. used a series of models to analyze the structure and agostic interactions of La(CH(SiMe$_3$)$_2$)$_3$.[303] One of the QM-only models, La(CH$_2$SiH$_2$Me)$_3$, had a local minimum with β-agostic Si−C interactions, but the global
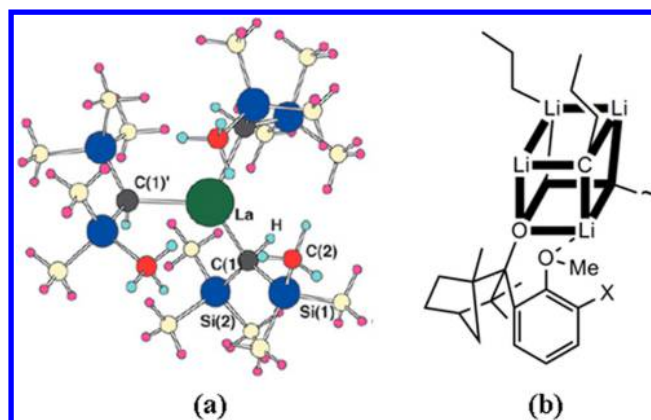
Figure 42. (a) ONIOM-optimized structure of La(CH(SiMe$_2$)$_2$)$_3$, with QM and MM layers represented by dark colors and pastel colors, respectively. Reprinted with permission from ref 303. Copyright 2003 Royal Society of Chemistry. (b) ^{n}BuLi aggregate with anisyl fenchol. A second anisyl fenchol is truncated in this representation, as marked by ∼. Thick lines in the aggregate indicate the QM layer in ONIOM optimizations.

minimum deviates significantly from the X-ray structure,[304] as the Me groups are oriented away from the La center. This conformation erroneously precludes agostic interactions, illustrating a potential pitfall of ligand truncations. When the full complex was optimized by ONIOM(B3PW91:UFF), with the low layer comprising the spectator methyl groups (Figure 42a), the structure reproduced the experimental results quite well. On the basis of examination of the β Si−C bond lengths and La−C−Si angles, Perrin et al. concluded that the complex has β-agostic Si−C interactions, rather than the γ-agostic C−H interactions suggested by the experimental nonbonded La···C$_\beta$ distance (3.12 Å). Interestingly, the elongation of the β Si−C bonds does not appear to stem from the agostic interaction itself, but to negative hyperconjugation with the lone pair of C$_\alpha$, enhanced by the relatively ionic nature of La−ligand bonds. In a related study, Perrin et al. showed that La(CH(SiMe$_3$)$_2$ has weaker agostic Si−C interactions because of reduced negative hyperconjugation with the nitrogen sp^2 lone pair.[305]

Eisenstein et al. used the same level of theory, ONIOM-(B3PW91:UFF), to analyze the electronic distribution in the trinuclear cluster (YbL)$_3$(THF), where L = [N(SiMe$_3$)C-(Ph)]$_2$CH.[307] To facilitate the analysis of individual Yb centers, the calculations were performed on related systems with Li in place of Yb. The study revealed an unusual electronic structure with both mixed-valence metal centers (2Yb^{II}/Yb^{III}) and mixed-valence ligands (L$^-$/2L^{3-}).

4.1.1.8. Main Group. As in the previous sections on inorganic structure, ONIOM-based studies of the structure of molecules containing main group elements are often centered on the relative stabilities of isomers, and the analysis of substituent effects. Such studies were conducted for Al-(NR$_2$)$_3$,[308] small models of polymeric dibutyltin(IV) complexes,[309] and [BCp$_2$]$^+$ and the decamethyl-substituted [BCp*$_2$]$^+$.[310] Similarly, relative energies of a phosphinofenchol and a phosphorane were computed to rationalize the unexpected synthetic production of the latter.[311] Some recent works were aimed at evaluating various ONIOM(B3PW91:HF) partition schemes for butyltin compounds, in terms of geometry, molecular properties, and NMR chemical shifts.[312]

Taking advantage of the absence of electronic effects in MM methods, Suresh employed a novel approach to quantify steric

effects of PR_3 ligand substituents, involving ONIOM-(B3LYP:UFF) optimizations of the isolated ligands, followed by molecular electrostatic potential (MESP) analysis of the QM layer.[313] Specifically, the effect of substituents was quantified in terms of the MESP minimum (V_{min}) at the lone-pair region of the phosphine, which is a measure of its electron donating ability.[314] The difference (S_{eff}) between the V_{min} of unsubstituted PH_3 ($V_{min}(PH_3)$) and that of the QM layer of the optimized PR_3 ligands ($V_{min}(ONIOM\_PR_3)$) correlated well with the Tolman cone angles, indicating that the purely electronic parameter V_{min} is a sensitive measure of steric effects. In a subsequent study, Mathew et al. also examined the electronic effect of the substituents (E_{eff}), by comparing $V_{min}(PR_3)$ and $V_{min}(ONIOM\_PR_3)$.[315] A broad range of phosphines were then categorized according to their S_{eff} and E_{eff} values, the sign and magnitude of which indicate the electron-withdrawing or -donating tendency of the ligand, as induced by steric or electronic effects.

4.1.1.9. Alkali Metals. Organolithium species are important reagents that can form aggregates in solution that act as reactive intermediates. In one example, chiral aggregates form mixtures of ^nBuLi and anisyl fenchols with various *ortho* substituents (X), H, $SiMe_3$, ^tBu, $SiMe_2{}^tBu$, and Me. X-ray crystal structures show that the aggregates form with ^nBuLi:fencholate ratios of 1:3 (X = H), 4:2 (X = Me), and 2:2 (X = others). Goldfuss et al. analyzed their formation energies using B3LYP//ONIOM-(B3LYP:UFF), with QM regions comprising the Li centers and bridging atoms, as in Figure 42b.[306] The coordination of alkoxido groups of fenchones is favored electrostatically, but opposing steric interactions of bulky substituents lead to the formation of mixed aggregates. In another ONIOM-based study, steric repulsion was shown to enforce the pyramidal structure of a dimeric three-coordinate Li species, in which electrostatics favor planar geometry.[316]

4.1.2. Properties. *4.1.2.1. Spectroscopic Properties.* ONIOM-derived vibrational frequencies,[277g,317] NMR parameters,[318] and Mössbauer quadrupole splittings[309] have aided structural determinations by serving as valuable links to experiments. For example, Yandulov et al. used IMOMM-(B3LYP:MM3) to calculate vibrational frequencies for various hydrogen-bonded adducts of $(CF_3)_2CHOH$ and the 16-
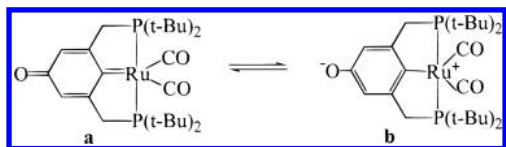

Figure 43. Two isomers of a metallaquinone: (a) quinoid-Ru(0) carbene and (b) Ru(II)-quinolate. Reprinted with permission from ref 317. Copyright 2000 American Chemical Society.

electron complex $OsHCl(CO)(P^tBu_2Me)_2$.[277g] The substituents of the phosphine ligand and CF_3 groups of the alcohol were allocated to the MM region. The vibrational frequency shifts upon adduct formation were consistent with experiment for the Cl···HO hydrogen-bonded adducts, whereas a CO···HO structure was ruled out. An Os ← O interaction energetically favored in small models was sterically prevented in the full model. Thus, adduct formation results in further unsaturation of the metal center through a hydrogen bond.

In 2000, Ashkenazi et al. synthesized the first metallaquinone, a ruthenium compound with a phenolic PCP ligand.[317] IR, UV−vis, and ^{13}C NMR spectra taken in methanol and benzene

showed significant solvent dependence, leading to the hypothesis that the compound has a quinoid-Ru(0) carbene form a in nonpolar solvents, and a Ru(II)-quinolate zwitterionic form b in polar solvents (Figure 43). ONIOM(B3LYP:HF) optimizations with the ^tBu groups in the low layer produced quinonic (a-type) geometries regardless of the initial structure; thus, in the gas phase, the compound is predicted to exist in the quinonic form. ONIOM IR spectra showed the $C_{para}=O$ stretching mode at 1689 cm^{-1}, $C_{meta}=C_{para}$ modes at 1624 and 1564, and a $C_{ipso}=Ru$ mode at 1036 cm^{-1}, all of which are consistent with the experimental frequencies of 1659, 1590, 1577, and 1030 cm^{-1}. These vibrational modes were not observed in methanol and are thus indicative of the quinonic form. The zwitterionic form was estimated by constrained optimization to be 13 kcal/mol higher in energy.

To identify the structure of a trinuclear ruthenium dihydride intermediate $(Ru_3(H)_2(CO)_9(PPH_3)_2)$ in the hydrogenation of phenylacetylene, Al-Ibadi et al. calculated ^1H NMR chemical shifts and coupling constants (J_{PH}) for 32 isomers using PBE1PBE//ONIOM(PBE1PBE:UFF).[318] The spectroscopic parameters complemented by the computed energetics favored a $Ru_3(\mu\text{-}H)(\mu\text{-}H)(\mu\text{-}CO)$ structure rather than a previously proposedterminal hydride $Ru_3(\mu\text{-}H)(H)$ species.[319]

4.1.2.2. Thermodynamic Properties. Transition metal hydrides are important intermediates in many processes, due to their diverse reactivity that includes proton, hydride, and H atom donation. Thus, their pK_a values and hydricities, defined as the standard Gibbs free energy ($\Delta G_{H^-}^\circ$) of the reaction in eq 74, are useful measures of their reactivity.

$$LMH \rightarrow LM^+ + H^- \qquad (74)$$

Qi et al. developed a protocol to calculate pK_a values of transition metal hydrides involving gas-phase ONIOM(CCSD-(T)/LANL2DZ+p:B3P86/LANL2MB) energy calculations at ONIOM(B3P86/LANL2DZ+p:HF/LANL2MB) geometries, followed by DFT-based solvation corrections, and calibration to experimental reference data.[320] The method was found to have an RMSD of 1.5 pK_a units for a set of 30 hydride complexes with various metals and diphosphine ligands. On the other hand, the same method performed poorly for hydricities, giving an RMSD of 6.6 kcal/mol for six metal hydrides.[45n] The failure was attributed to the basis set effects, as using B3P86 instead of CCSD(T) made little difference, but switching to 6-31+G* for all nonmetal atoms in full B3P86 energy calculations reduced the RMSD to 3.0 kcal/mol. Further improvement to 1.3 kcal/mol was achieved through full B3P86/LANL2DZ+p optimizations. Another study of DFT-derived hydricities used ONIOM(DFT:UFF) for the optimization of a Pd complex and obtained reasonable results, although the experimental hydricity was not available for comparison.[321]

The performance of ONIOM(DFT:UFF) for the binding energies of PMe_3 and PPh_3 ligands to tetranuclear gold clusters has been evaluated.[322] Despite good performance for geometry optimizations, the binding energies were only about one-half that of the full DFT-derived values. Similarly, ligand substitution enthalpies for processes such as the following:

$$(PH_3)_2Fe(CO)_3 + 2PR_3 \rightleftharpoons (PR_3)_2Fe(CO)_3 + 2PH_3 \qquad (75)$$
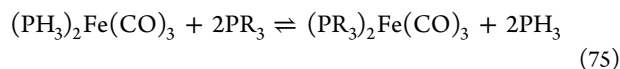
have been calculated using IMOMM(DFT:MM).[323] Again, quantitative agreement with experiment could not be obtained, due partly to the neglect of electronic effects of the R groups when PR_3 is modeled as PH_3 in the QM region.
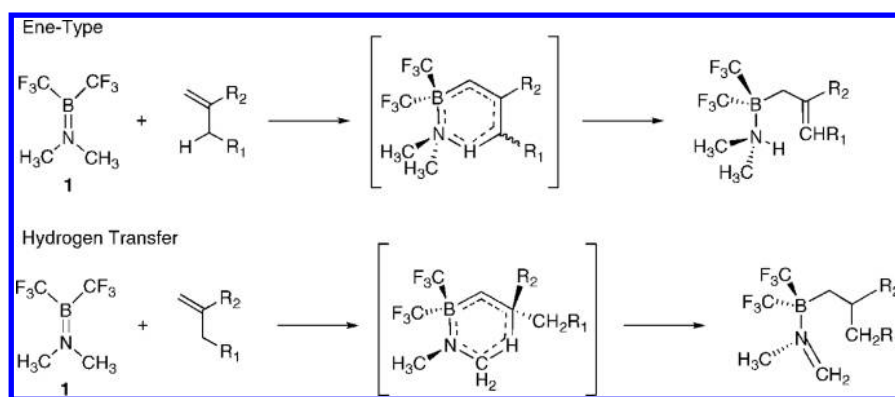
Figure 44. Ene-type and hydrogen transfer mechanisms for reactions of the aminoborane (**1**) with alkenes. Reprinted with permission from ref 334. Copyright 2011 American Chemical Society.

Accurate molecular energies can be obtained for small molecules using composite methods such as Gn[20a] that approximate high-level ab initio calculations through low-level optimization and vibrational correction, followed by a series of single-point energy calculations with various basis sets and various ab initio methods. To study larger molecules, Vreven et al. developed two-layer[194] and three-layer[14] ONIOM G_2-like methods (OG2R2 and OG2R3, respectively) that approximate the CCSD(T)/6-311+G(2df,2p) level (see section 2.2.5 for more details). The Gilbert group used OG2R3 to study bond dissociation energies in groups 13−15 donor−acceptor complexes.[141] Later, they tested the performance of this approach against experimental dissociation energies for a set of such complexes, and found nearly CCSD(T)/aug-cc-pVTZ-level accuracy with substantially reduced computational cost.[140] The Gilbert group also used OG2R3 to calculate binding energies of $B(C_6H_xF_{5-x})_3$ to NMe_3 and PMe_3.[324] The results indicated that the position of the fluorines strongly affects the Lewis acidity of the borane, and increasing the number of fluorines has an additive effect on binding energies.

4.1.3. Reactivity. *4.1.3.1. f-Block.* In a recent study, Wang et al.[325] examined a possible mechanism for the reaction of trinuclear Ln-phosphinidine (Ln = Y or Lu) clusters with CS_2, using a M06L//ONIOM(TPSSTPSS:HF) method out of necessity, as the clusters consist of nearly 250 atoms. In the studies highlighted below, ONIOM calculations provided additional insight by isolating the impact of steric effects on reaction mechanisms. The performanc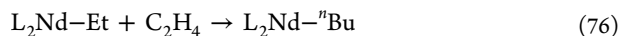e of ONIOM-(B3PW91:UFF) for reactivity studies involving lanthanocenes with bulky C_5Me_5 ligands has been evaluated by Perrin et al.[326] Two reactions were selected to serve as representative examples of lanthanocene reactivity: the insertion of ethylene into the Nd−C bond of L_2Nd−Et, as in eq 76:

$$L_2Nd\text{−}Et + C_2H_4 \rightarrow L_2Nd\text{−}{}^nBu \qquad (76)$$

and the H exchange between ethyl and ethylene ligands through β-H transfer, as in eq 77:

$$L_2Nd\text{−}C_2H_5 + C_2H_4 \rightarrow L_2Nd\text{−}C_2H_4H + C_2H_4 \qquad (77)$$
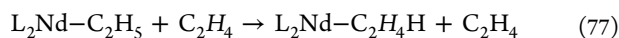
Free energy profiles of these reactions were calculated for the ligands L = C_5H_5 (Cp) and C_5Me_5, which was modeled at the full-DFT level (Cp*), or with the Me groups in the MM layer of an ONIOM model (Cp#). The use of Cl to model Cp was also tested and found to be inadequate. For example, the calculated free energy of coordination of ethylene to L_2Nd−Et was −3.2, 5.2, and 10.5 kcal/mol for Cl, Cp, and Cp*,

respectively. A value of 10.9 kcal/mol for Cp# revealed that the significant influence of the Me substituents is largely steric in nature. The ONIOM method performed very well for these reactions, but as the authors noted, the neglect of electronic effects from the substituents may have a larger impact in studies of other types of reactions, particularly those involving a change in oxidation state.

Maron et al. applied an analogous ONIOM model to study steric effects in a lanthanocene-hydride-catalyzed H/F exchange reaction, involving formation of C_6F_5H from C_6F_6.[327] Steric interactions disfavored a C_6F_6−Cp'_2LaH (Cp' = 1,3,4-${}^tBu_3C_5H_2$) π adduct that would be an intermediate species in a plausible hydride addition mechanism, but allowed a σ adduct that leads to H/F exchange via transient HF formation.

4.1.3.2. Main Group. An interesting new field in main group chemistry is the study of frustrated Lewis pairs (FLPs): mixtures of Lewis acids and bases that do not form adducts due to steric hindrance.[328] FLPs have unique reactivity including small molecule activation and catalytic hydrogenation of a wide range of substrates. The Gilbert group has used the OG2R3 three-layer ONIOM composite method discussed above (section 2.2.5) to investigate the mechanism of CO_2 reduction to CO by an Al−P FLP,[329] and the complexation of N_2O by a B−P FLP.[330] They have used DFT//ONIOM(DFT:DFT) methods to provide computational support in studies of the formation and reactivity of N-heterocyclic-carbene-Lewis-acid FLPs,[331] B−N FLPs,[332] and nonfrustrated phosphinoborane adducts.[333]

In another application of the OG2R3 method, Dutmer et al. compared two competing pericyclic reactions of the amino-borane $(F_3C)_2B\text{=}N(CH_3)_2$.[334] This aminoborane reacts with a variety of olefins through either ene-type or hydrogen transfer mechanisms (Figure 44), the latter of which does not occur in pure organic reactions. In comparison to reference data from modified G3(MP2) calculations,[334,335] the OG2R3 method was found to give much more reliable barrier heights and reaction energies than MP2 or DFT methods. The results indicated that the type of reaction that is favored depends on the location of alkene methyl groups and whether they are sterically hindered by other substituents.

Other topics in main group chemistry that have been examined with ONIOM methods include Al-catalyzed hydro-phosphonylation reactions,[336] and intramolecular free-radical cyclization reactions of selenium compounds.[337] The radical
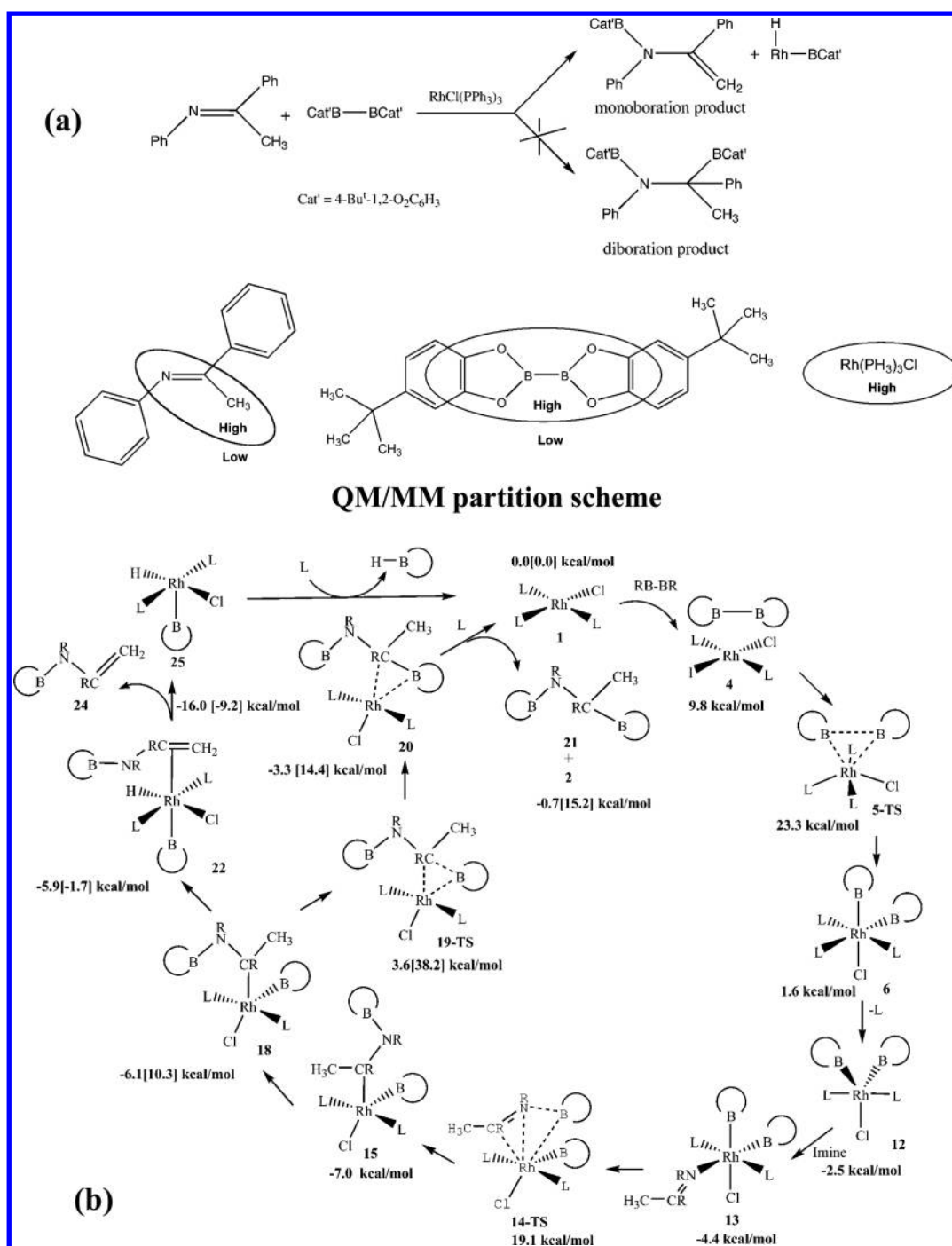
Figure 45. (a) Catalytic imine boration reaction. (b) Real and model (in circles) systems used in ONIOM(B3LYP:HF) calculations, and computed catalytic cycle for imine boration (ΔG valued for the model system is shown in full text and ΔG values of the real system are in brackets). Reprinted with permission from ref 341. Copyright 2005 American Chemical Society.

reactions were studied using another composite-based ONIOM approach.[338]

4.2. Transition Metal Homogeneous Catalysis

Transition metal homogeneous catalysis is one of the most efficient ways to perform catalytic reactions in a selective fashion, and it has become an indispensable tool with extensive applications in both industry and academia. Three Nobel prizes were awarded for the experimental studies of transition metal homogeneous catalysis: palladium-catalyzed cross-coupling (Heck, Negishi, and Suzuki in 2010), metathesis methods in organic synthesis (Chauvin, Grubbs, and Schrock in 2005), and

chirally catalyzed hydrogenation and oxidation reactions (Knowles, Noyori, and Sharpless in 2001). In terms of developing more efficient catalysis, precise mechanistic details are very important. However, reaction mechanisms are often complex, and difficult to characterize from experimental data alone. In this direction, computational chemistry has made very important contributions.[339] This section summarizes the applications of IMOMM, IMOMO, and ONIOM methods for mechanistic and selectivity studies of transition metal homogeneous catalysis. The selected examples consist of relatively large molecular systems, where the electronically
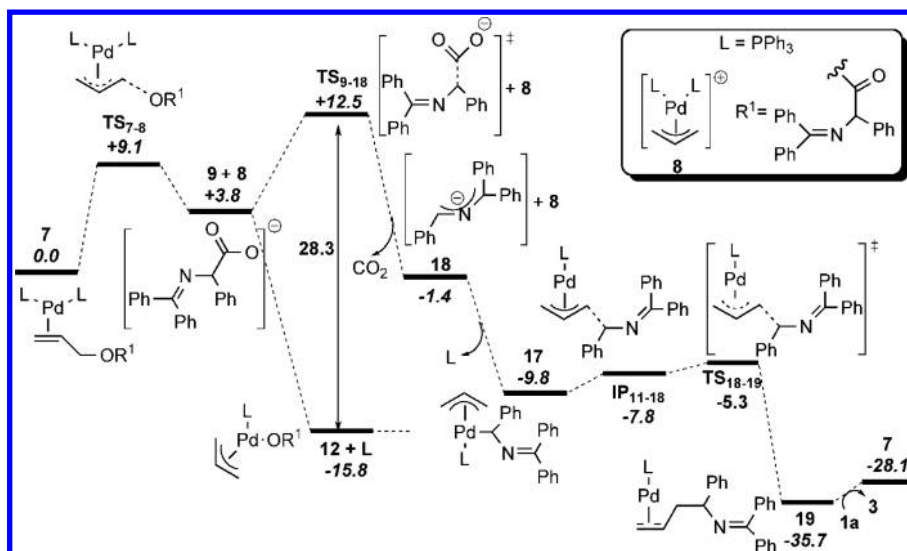
Figure 46. Computed mechanism for Pd-catalyzed decarboxylative allylation of α-imino esters (energies are in kcal/mol). Reprinted with permission from ref 342. Copyright 2012 John Wiley & Sons.
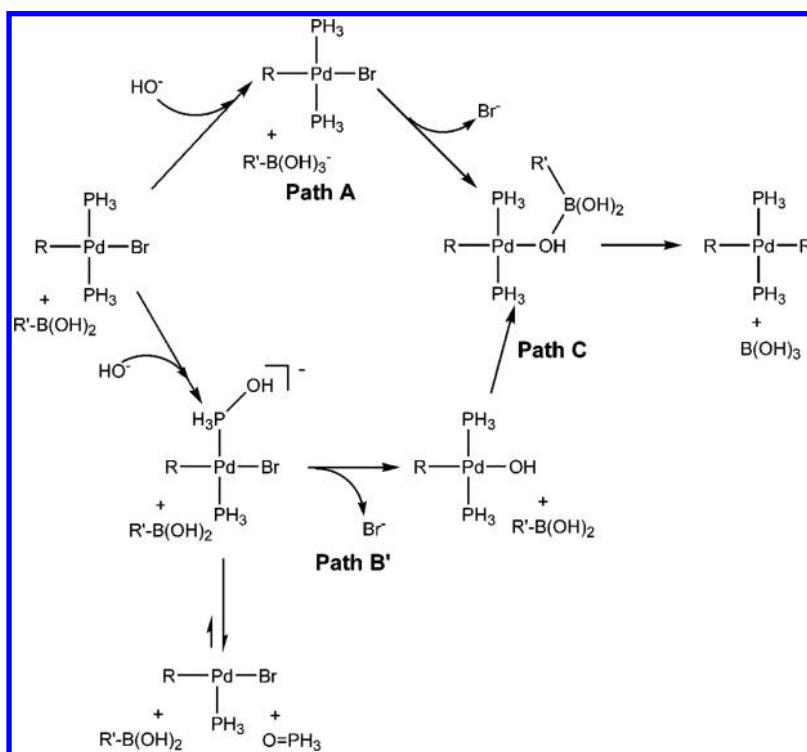
Figure 47. Proposed mechanisms for a Suzuki−Miyaura cross-coupling reaction. The model system consists of $Pd(CH{=}CH_2)(PH_3)_2Br$ as the starting catalyst complex, $CH_2{=}CHB(OH)_2$ as the organoboronic acid, and OH^- as the base. In ONIOM calculations, phenyl groups of the triphenylphosphine (PPh_3) were included in the MM partition. Reprinted with permission from ref 343. Copyright 2005 American Chemical Society.

important part of the molecule, the reaction center for instance, is described by a DFT or an ab initio method, while the remaining part (most commonly the bulky groups) is described by MM, semiempirical, or DFT methods. This strategy is useful for modeling large molecular systems.

4.2.1. Full Catalytic Cycles. One of the challenges in computational studies of transition metal homogeneous catalysis is to develop a full catalytic cycle for the reaction of interest, and it must be consistent with the experimental results. Then, rate-determining or selectivity-determining steps of the

mechanism then can be identified. In 1987, the first energy profile of a full catalytic cycle was published by Koga et al.[340] They applied the RHF method to determine the transition states and intermediates of the catalytic cycle for the Wilkinson olefin hydrogenation, and MP2 method to calculate energetics of the important steps. Nowadays, the most common tools for computational studies of full catalytic cycles are DFT and ONIOM methods. The latter method is particularly useful for large molecular systems.
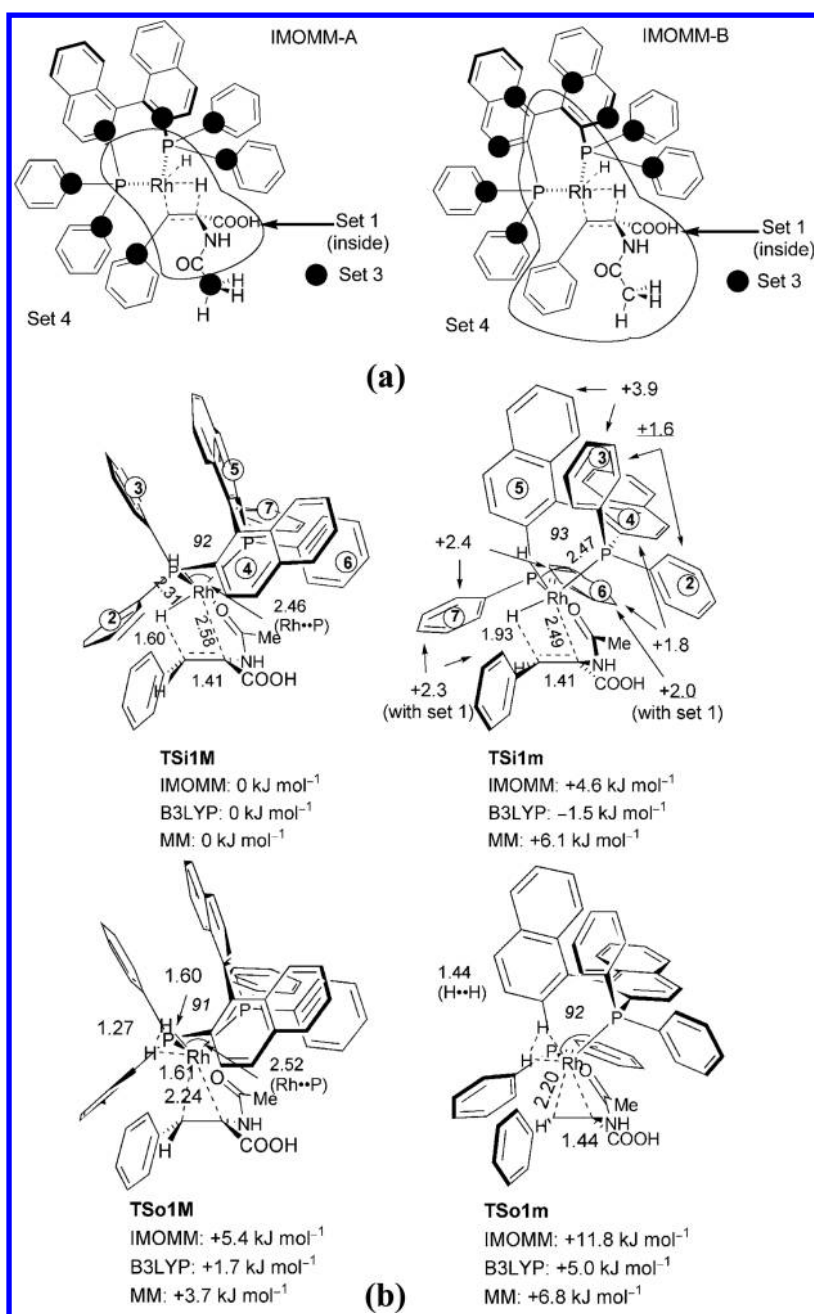
Figure 48. (a) QM/MM partitions: IMOMM-A was used for geometry optimization, and IOMMM-B was used for energy evaluation. (b) Important transition states for the oxidative addition of hydrogen molecule (**TSo**) and insertion of enamide into the Rh−H bond (**TSi**). Reprinted with permission from ref 358. Copyright 2006 John Wiley & Sons.

Ananikov et al. applied an ONIOM(B3LYP:HF) method to develop a catalytic cycle for Rh-catalyzed imine boration.[341] According to experimental results, only monoboration was observed (Figure 45a). ONIOM(QM:QM) results suggested that the catalytic cycle has four main steps: oxidative addition of B−B to the Rh complex, imine coordination, migratory insertion of the imine into the Rh−B bond, and β-hydrogen elimination (Figure 45b). In the case of alkene boration, two coordination orientations lead to different regio-products. However, only one coordination mode is possible for amine boration, leading to Rh−C and N−B bond formation. As a result, higher regioselectivity can be expected for imine boration.

Li et al. used an ONIOM(B3LYP:PM6) approach to rationalize the full catalytic cycle for Pd-catalyzed decarboxylative allylation of α-(diphenylmethylene)imino esters and allyl diphenylglycinate imines.[342] In their ONIOM calculations, all phenyl groups of the catalyst and substrate were included in the low level. On the basis of the ONIOM(QM:QM) results, the catalytic cycle consists of three steps: oxidative addition, decarboxylation, and reductive allylation (Figure 46). The initial oxidative addition is possible with a low-energy barrier, and the following decarboxylation proceeds via a solvent-exposed α-imino carboxylate anion, which is the rate-determining step of the overall mechanism.

A full catalytic cycle for a Suzuki−Miyaura cross-coupling reaction was developed by the Maseras group using B3LYP and

ONIOM(B3LYP:UFF) methods.[343] According to their calculations, the most feasible mechanism is path A in Figure 47. In path A, the base initially reacts with the boronic acid to form a boronate species, and then transmetalation occurs. It is important to note that the energy profiles are qualitatively similar to the B3LYP and ONIOM(B3LYP:UFF) methods. An ONIOM(B3LYP:UFF) study by the same group[344] showed the importance of selecting correct conformations for mechanistic studies of the Suzuki−Miyaura cross-coupling between CH_2=CHBr and CH_2=CHB(OH)$_2$ catalyzed by [(PPh$_2$)$_2$Pd] or [(P(^{i}Pr)$_3$)$_2$Pd]. Several other research groups[345] applied the ONIOM method to study the cross-coupling reactions.

ONIOM(B3PW91:HF) calculations by Li et al.[346] rationalized the mechanism of the full catalytic cycle of the intramolecular Heck-type coupling of oximes with aryl halides. In their ONIOM calculations, three phenyl rings of the triphenylphosphine ligand were placed in the low layer. The overall mechanism consists of four steps: oxidative addition, migratory insertion, β-H elimination, and catalyst regeneration. The free energy of the migratory insertion step is the highest among all of the transition states, and therefore it is the rate-limiting step of the mechanism.

Apart from the above studies, a number of applications of ONIOM to the characterization of full catalytic cycles can be found in the literature. The subjects of these studies have been cross-coupling,[347] hydrogenation,[348] metathesis,[349] hydroformylation,[350] hydroboration,[351] C−C and C−H bond activation,[352] atom transfer radical addition,[353] borylation,[354] hydrosilylation,[355] arylation,[356] and other reactions.[357]

4.2.2. Selectivity Studies. Another important objective in computational studies of transition metal homogeneous catalysis is comparison of competing reaction pathways to explain the selectivity. In common practice, many competing reaction paths can be found, and energy differences between them can be very small. For instance, a 3 kcal/mol energy separation leads to an enantiomeric excess of 99% at room temperature. Therefore, quantitative estimation of selectivity is challenging. The IMOMM(QM:MM) or ONIOM(QM:MM) methods are efficient for sampling competing reaction paths, as the computational cost for MM is low.

4.2.2.1. Enantioselectivity. In enantioselective reactions, diastereomeric transition states give rise to enantiomeric products starting from a single prochiral reactant. Enantioselectivity and enantiomeric ratios can be calculated by assuming the direct connection between the Boltzmann distribution of transition state energies and product amount.[339d] This section summarizes several IMOMM(DFT:MM) and ONIOM-(DFT:MM) studies focused on quantitative estimation of enantioselectivity.

Mori et al.[358] applied an IMOMM(B3LYP:MM3) approach to examine the origin of the enantioselectivity of binap-Rh(I)-catalyzed asymmetric hydrogenation. Two QM/MM partition schemes were used in this work: IMOMM-A was used for geometry optimization and IMOMM-B was used for energy evaluation (Figure 48). They systematically analyzed several possible paths leading to the major (**M**) and minor (**m**) enantiomers. Important transition states for the key steps in the mechanism, oxidative addition of hydrogen molecule (**TSo**) and insertion of enamide into the Rh−H bond (**TSi**), are shown in Figure 48, and both of these steps may contribute to the enantioselectivity-determining step. The oxidative addition step is the rate-determining step, and therefore provides the greatest contribution to enantioselectivity. For the oxidative-
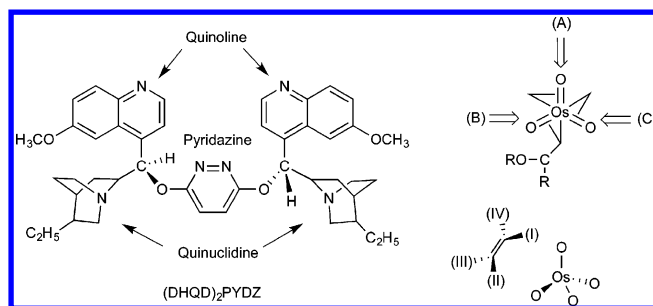
Figure 49. Ligand and the different approaches between substrate and catalyst in the enantioselective dihydroxylation of olefins.

addition transition states, both the QM and the MM energies contribute equally, whereas for the insertion transition states, steric repulsion between the naphthyl group on one of the phosphorus atoms and the phenyl group on the other phosphorus provides the largest contribution.

IMOMM(B3LYP:MM3) calculations by Ujaque et al.[359] explained the enantioselectivity of the dihydroxylation of styrene catalyzed by OsO$_4$(DHQD)$_2$PYDZ [(DHQD)$_2$PYDZ = bis(dihydroquinidine)-3,6-pyridazine]. The (DHQD)$_2$PYDZ ligand is bound to the metal via one of the quinuclidine ligands (Figure 49). They included OsO$_4$·NH$_3$ and the substrate in the QM partition, while the remaining part was in the MM partition. Twelve possible reaction pathways were classified according to the equatorial oxygen that reacts (**A**, **B**, and **C**) and the relative position of the phenyl group of the substrate (**I**, **II**, **III**, and **IV**) (Figure 49). According to the IMOMM-(B3LYP:MM3) results, substrate attack at the **B** region is favorable due to attractive interactions with the amine ligand. The orientation of the substrate is most favorable when the phenyl group is at position **I** or **III**. Position **I** is the lowest energy path that leads to the desired *R* enantiomer. The lowest energy path leading to the *S* enantiomer begins with the phenyl group at position **IV**, and the transition state is 2.6 kcal/mol higher in energy. This leads to a calculated enantiomeric excess of 99.4% for formation of the *R* product, which is in good agreement with the experimental value (96%).

The Maseras group explored the enantioselectivity of vanadium-catalyzed asymmetric oxidation of 1,2-bis(*tert*-butyl)-disulfide (Figure 50).[360] Several combinations of the R$_1$, R$_2$, and R$_3$ substituents were systematically analyzed: (A) R$_1$ = R$_2$ = R$_3$ = ^{t}Bu; (B) R$_1$ = R$_3$ = ^{t}Bu, R$_2$ = H; (C) R$_1$ = R$_2$ = ^{t}Bu, R$_3$ = ^{i}Pr; and (D) R$_1$ = R$_2$ = H, R$_3$ = ^{t}Bu. In their QM/MM model, ^{t}Bu groups of the substrate and R$_1$, R$_2$, and R$_3$ groups of the Schiff base were modeled with MM3, while the remaining part was treated with B3LYP. Their IMOMM(B3LYP:MM3) results are encouraging, as they reproduce the experimental enantiomeric excess (Figure 50). Their ONIOM-(B3LYP:MM3) results reproduce the experimental trends in enantiomeric excess and confirm the predictions of the IMOMM(B3LYP:MM3) study.

A three-layer ONIOM method was used by Feldgus et al.[361] to explore the potential energy surface for the Rh-catalyzed asymmetric hydrogenation of α-formamidoacrylonitrile. In their calculations, the bond-breaking and bond-forming region was modeled with B3LYP. The HF method and UFF were applied to describe the electronic and steric impact of the catalyst, respectively. The reaction occurs along two diastereomeric manifolds, corresponding to binding of the *re* or the *si* face of the olefin to the catalyst. Binding of the *re* enantioface of the
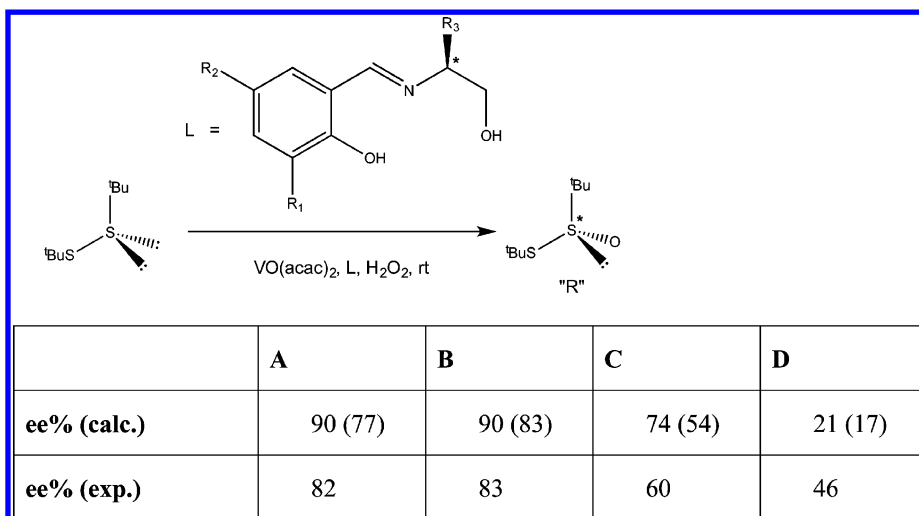
Figure 50. Vanadium-catalyzed asymmetric oxidation of 1,2-bis(*tert*-butyl)-disulfide, and calculated enantiomeric excess at 298.14 K. Values in parentheses are the calculated ee % from ONIOM(B3LYP:MM3) method.
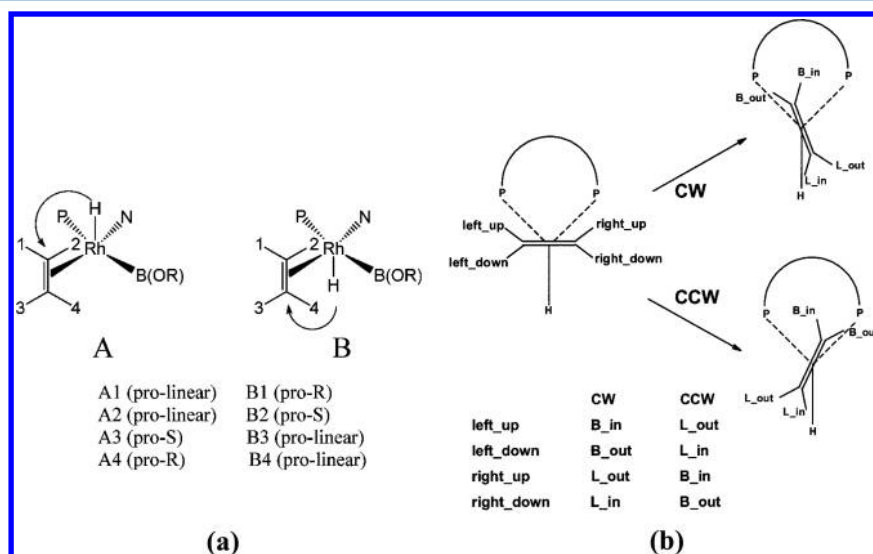
Figure 51. (a) The eight possible intermediates in styrene hydroboration. Reprinted in part with permission from ref 351a. Copyright 2004 American Chemical Society. (b) Definition of the eight possible reaction paths for alkene insertion from the key equatorial−equatorial pentacoordinate intermediate in Rh-catalyzed hydroformylation. Reprinted with permission from ref 351b. Copyright 2001 American Chemical Society.

enamide to the catalyst generates diastereomers, and the minor diastereomer is considerably more reactive. The calculated enantiomeric excess of 99.9% (R) reproduces the experimental enantioselectivity. García et al.[362] studied the origin of the enantioselectivity of pybox-ruthenium and box-copper-catalyzed cyclopropanation reactions with B3LYP and ONIOM-(B3LYP:UFF) methods. The ONIOM(B3LYP:UFF) geometries and relative energies of the key reaction intermediates and transition structures are in good agreement with the B3LYP results. The calculated enantioselectivities reproduce the experimental data.

Several other groups used ONIOM methods to study the enantioselectivity of the following homogeneous transition-metal catalyzed reactions: hydrogenation,[348c,361,363] the Pauson−Khand reaction,[364] cyclopropanation,[362,365] and other reactions.[366]

4.2.2.2. Regioselectivity and Stereoselectivity. Bo's group[351a] studied the origin of the regio- and stereoselectivity

of the rhodium-catalyzed vinylarenes hydroboration reaction, and also the role of steric and electronic features of the ligand and substrate. They included the metal, alkene, hydride, and boryl ligands, and the ligand backbone in the QM region, and the remaining parts of the system were in the MM region. The key intermediate in the catalytic cycle is a pentacoordinate species with eight possible isomers (Figure 51a). The internal orientation of this intermediate determines the regio- and enantioselectivity of the resulting product. Their QM/MM scheme was very useful for separating and evaluating the electronic and steric effects. The same group determined the origin of regioselectivity in rhodium diphosphine-catalyzed hydroformylation.[351b] The key intermediate in the mechanism is a pentacoordinated complex, $HRh(CO)(alkene)$-(diphosphine). They used eight possible conformations for their study, differing by the face of the alkene double bond that approached the $HRh(CO)$(diphosphine) intermediate and the clockwise (CW) or counterclockwise (CCW) rotation of the
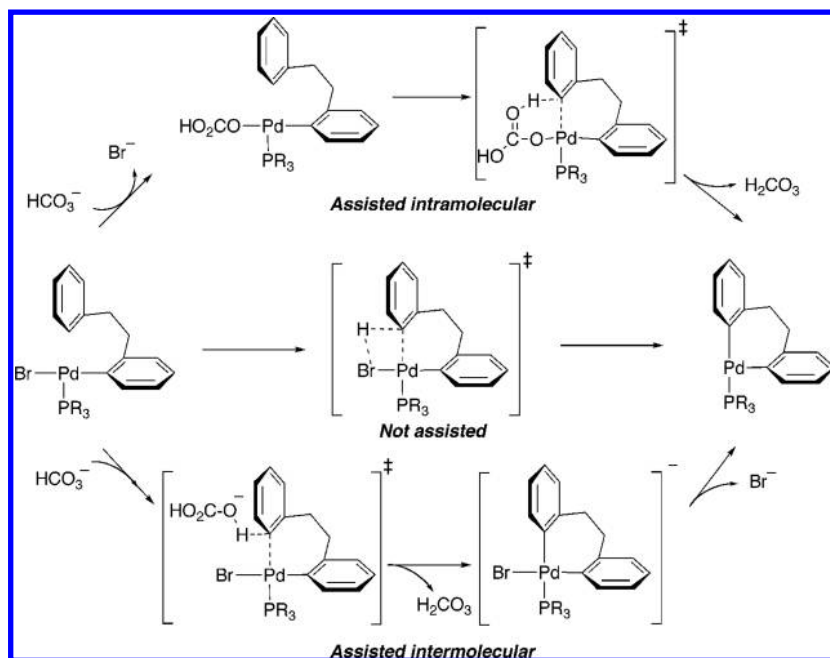
Figure 52. Proposed mechanisms for proton abstraction catalyzed by Pd complexes. Reprinted with permission from ref 366b. Copyright 2007 American Chemical Society.

olefin (Figure 51b). Subsequently, eight transition states were located and the regioselectivity was calculated by using the relative stabilities of all transition states. Their calculations show that formation of the linear product is more favorable than that of the branched product, and the calculated yields for the propene linear product are 83% and 73% for benzo and homoxantphos, respectively. This is in agreement with the experimental values (98.1% and 89.5%). Also, they argue that the nonbonding interactions between the diphenylphosphino substituents and the substrate play a very important role in the regioselectivity.

The regioselectivity of intramolecular palladium-catalyzed arylation was analyzed by Gracia-Cuadrado et al. using B3LYP and ONIOM(B3LYP:UFF) methods.[366b] Proposed reaction mechanisms are summarized in Figure 52, where the reaction starts from a species resulting from the oxidative addition of the C–Br bond. The proton transfer step may involve the bromide ligand (unassisted path), a base in the media (assisted path), the hydrogen carbonate, or an external base (intramolecular assisted path or intermolecular assisted path). Calculations support the mechanism involving a proton abstraction by the carbonate or a related basic ligand. The regioselectivity depends on the position of the substituent, and the *ortho* position closer to the C–H bond is the most favorable position. Electron-withdrawing substituents favor the reaction on the substituted ring, while electron-releasing substituents direct the reaction to the unsubstituted ring.

Le Paih et al. applied an ONIOM(B3PW91:UFF) method to explore the stereoselectivity of the reaction between two alkyne molecules and one carboxylic acid affording (1E,3E)-1,4-disubstituted-1,3-dienes (Figure 53a).[357a] In their QM/MM model, the metal, all atoms in the direct vicinity of the metal, and two carbons of each phenyl were included in the QM region, while the five methyl groups of C_5Me_5 and the remaining atoms of the two phenyl rings were included in the MM region. On the basis of the ONIOM results, they proposed a mechanism (Figure 53b). The metallacyclic biscarbene
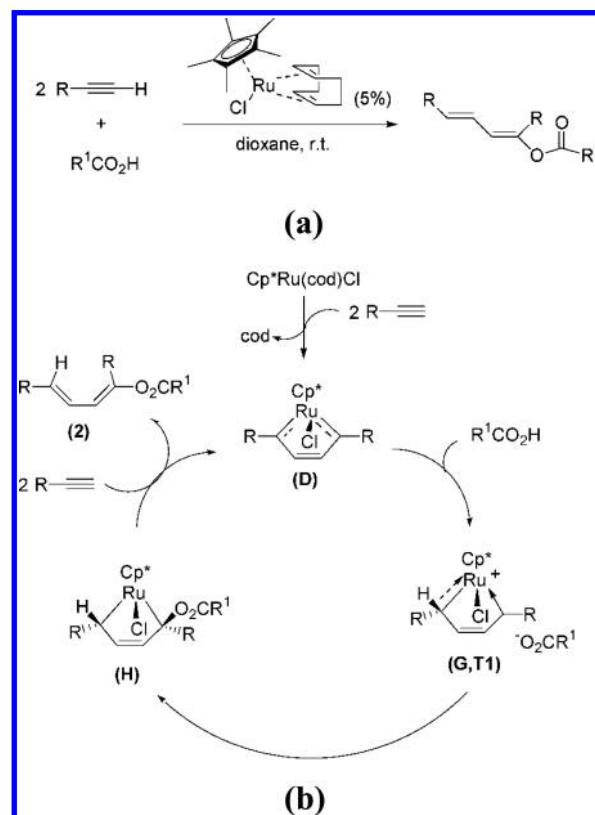
Figure 53. (a) Reaction of two molecules of alkynes and one of carboxylic acid to afford only one diene isomer, (1E,3E)-1,4-disubstituted-1,3-dienes, catalyzed by $RuCl(COD)C_5Me_5$. (b) Proposed catalytic cycle. Reprinted with permission from ref 357a. Copyright 2003 American Chemical Society.

intermediate is the active species on the mechanism. Their results indicate that the catalytic reaction combines alkynes and one of the carboxylic acids to afford only one diene isomer, and the head-to-head coupling of alkynes with concomitant
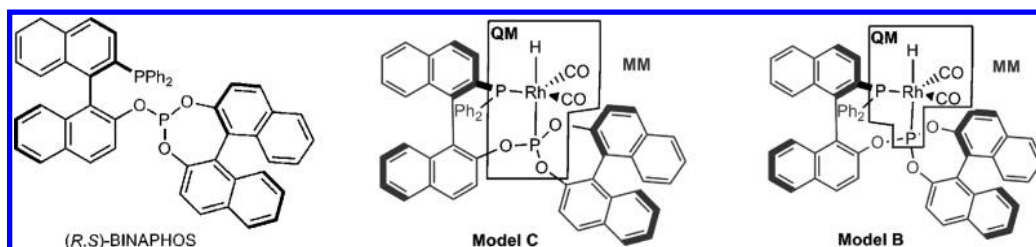
Figure 54. *R,S*-BINAPHOS ligand and the QM/MM partitions model systems.[350] Reprinted with permission from ref 350. Copyright 2012 John Wiley & Sons.
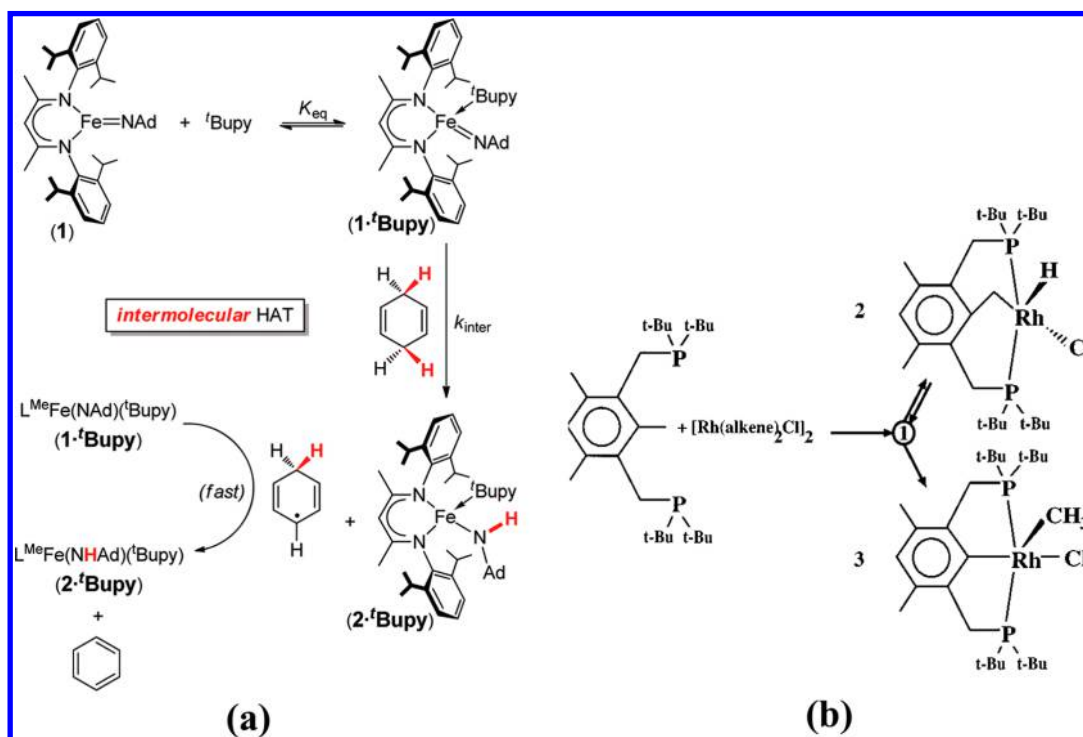
Figure 55. (a) Intermolecular HAT by L^MeFeNAd. Reprinted with permission from ref 377. Copyright 2011 American Chemical Society. (b) Carbon−hydrogen and carbon−carbon activation catalyzed by rhodium(I) complex with PCP-type ligands. Reprinted with permission from ref 378. Copyright 2000 American Chemical Society.

formation of the three C−C, C−H, and C−O bonds is the reason for the stereoselectivity. They evaluated the influence of the partition between the QM and MM, where structure optimization performed with the phenyl ring entirely in the QM part. The two partitions, phenyl QM and vinyl QM, give qualitatively similar relative energies and structures.

Aguado-Ullate et al.[350] studied the origin of stereoinduction in the hydroformylation of styrene catalyzed by [Rh((*R,S*)-BINAPHOS)(CO)$_2$H] complexes. In this study, two different QM/MM partitions were tested. In both cases, styrene was treated with the PB functional, while the remaining part was modeled with the SYBYL force field (Figure 54). According to their survey, the axial chirality of the phosphite and the axial chirality of the backbone are responsible for discriminating between the two competing equatorial-epical paths and the two enantiomers. Their energy decomposition analysis (EDA) indicates that the phosphite moiety at the equatorial site is favorable for BINAPHOS ligand coordination.

The ONIOM method has been used to study the regioselectivity and stereoselectivity of several other transition-metal homogeneous catalytic reactions. Studies of regioselectivity have been conducted for C−H activation,[367]

imine boration,[341] cross-coupling,[368] hydroformylation,[369] hydrogenation,[370] hydroarylation,[371] decarboxylation,[342] and H$_2$ addition.[372] Studies of stereoselectivity have been carried out for aryl zinc addition to aldehydes,[373] the Strecker reaction and hetero-Diels−Alder reactions,[374] cyclopropanation,[375] and cross-coupling.[376]

4.2.3. Studies of a Single Reaction Step and Transient Intermediates. Some computational studies of transition metal homogeneous catalysis were focused on a single reaction step of a mechanism or a single-step catalytic process. Matsubara et al.[12] used an IMOMM(RHF:MM3) approach to study the oxidative addition of H$_2$ catalyzed by Pt(PR$_3$)$_2$ (R = H, Me, ^tBu, and Ph) complexes. Final energies of the optimized structures were calculated at the IMOMM-(MP2:MM3) level of theory. The active part of the system was modeled by the RHF method, while the remaining part, specifically the −R groups, was treated by the MM3 force field. The IMOMM optimized geometries and relative energies are comparable with the MO(RHF) results. According to the calculated reaction barriers, the R = −H, −Me, and −Ph systems show early coplanar transition states, giving rise to the *cis*-product. In contrast, the R = ^tBu system showed a relatively
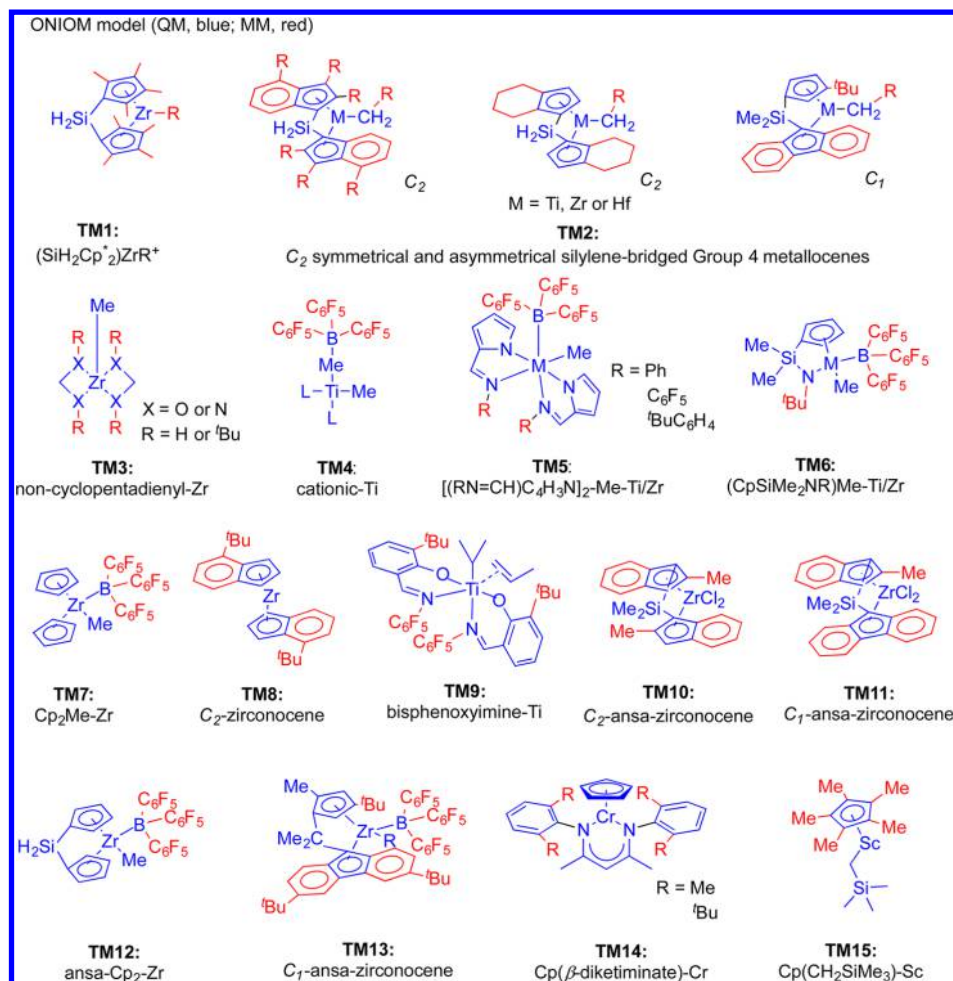
Figure 56. Studied ONIOM models of early d-block transition metal polymerization catalysts.

late nonplanar transition state with a relatively high barrier, indicating a difficult oxidative addition process.

Cowley et al.[377] explored hydrogen atom transfer (HAT) reactions catalyzed by an isolable iron(III) imido complex (Figure 55a), L^{Me}FeNAd (L^{Me} = bulky β-diketiminate ligand, 2,4-bis(2,6-diiso-propylphenylimido)pentyl; Ad = 1-adamantyl). In their ONIOM(B3LYP:UFF) approach, phenyl and methyl substituents of L^{Me} and the entire adamantyl group except the carbon directly attached to the imido nitrogen were in the low level. According to their proposed mechanism, HAT occurs in an intermolecular fashion (Figure 55b). Moreover, ONIOM(B3LYP:UFF) results suggest that the steric effects of the hydrocarbon substrate control the selectivity.

Sundermann et al.[378] compared the oxidative addition of carbon−hydrogen and carbon−carbon bonds catalyzed by a rhodium(I) complex with the PCP-type ligands (1,3-bis[(di-*tert*-butylphosphino)methyl]-2,4,6-methylbenzene) (Figure 55b). According to their ONIOM(B3LYP:HF) calculations, carbon−hydrogen bond activation is kinetically favorable, while the "CC product" is thermodynamically stable. The insertion into the C−H bond may be a reversible process, where the hydride complex ("CH product") **2** may be converted to a thermodynamically stable methyl complex ("CC product") **3**. This process occurs through a pentacoordinated transient intermediate. Relative to the barrier for the carbon−carbon bond activation, the carbon−hydrogen activation barrier is higher due to the electron-withdrawing substituents at the

phosphorus atoms of the PCP ligand. Rivilla et al.[379] examined Tp^XAg (Tp^X = hydrotris(pyrazolyl)borate ligand) as active catalysts from cross-coupling of diazo compounds. Their B3LYP results suggest that the active intermediate of the mechanism is a metallocarbene, L_nM=CH(R) where L_n = Tp^x, M = Ag, R = −H or −Ph. An ONIOM(B3LYP:MM3) method as implemented in the SICTWO program confirms that the electronic effects of the −Ph are very important for the stability of the metallocarbene transient intermediate, ultimately lowering the barrier for the cross-coupling path. In the absence of the electronic effect of the −Ph group, the homocoupling path is favorable.

Apart from the above examples, several researchers have applied ONIOM methods to the study of a single reaction step in catalytic reactions and transient intermediates.[277f,380]

4.3. Polymerization Catalyzed by Transition Metal Systems

Polymerization is one of the most important processes of the chemical industry, an example being the well-known Ziegler−Natta process. Computational chemistry is widely used to understand the catalytic activities, mechanisms, and selectivity problems of polymerization reactions, and it also provides guidelines for catalyst design. However, calculations perform with simplified models, which do not account for the complexity of the real polymerization systems. The ONIOM method can be used to take into account the steric and electronic effects on the polymerization systems from the auxiliary ligands/solvent/cocatalysts by combining different
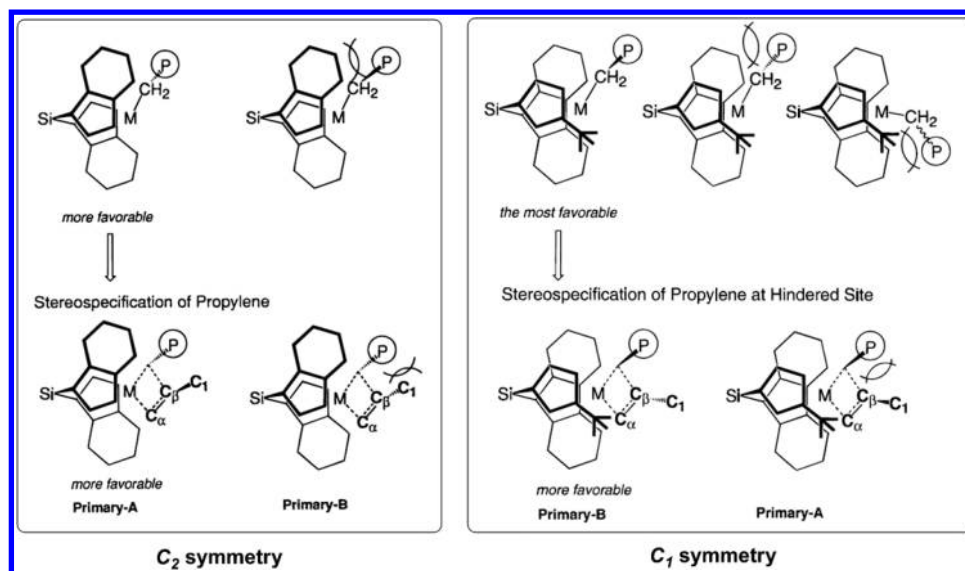
Figure 57. Indirect control of stereoregularity with one-blocked access: determination of the conformations of the polymer chain end. Reprinted with permission from ref 391. Copyright 1996 American Chemical Society.

levels of QM and MM methods. We mainly focus on important papers that show the advantages of large ONIOM models over small QM models in studying metal-catalyzed homopolymerization, copolymerization, and selectivity issues in polymerization. The discussion is organized into sections on early d-block, late d-block, and f-block metal catalysts.

4.3.1. Polymerization Catalyzed by Early d-Block Metal Systems. *4.3.1.1. Homopolymerization.* Early transition metal complexes are typical systems for polymerization, for example, the well-known Ziegler−Natta and metallocene catalysts. Figure 56 summarizes the early d-block metal systems studied using the IMOMM and ONIOM method.

In early 1992, Kawamura-Kuribayashi et al. studied the homogeneous olefin polymerization with a silylene-bridged zirconocene catalyst, $(SiH_2Cp^*_2)ZrR^+$ (**TM1**, Figure 56).[50c] On the basis of QM transition state structures, molecular mechanics (MM2) calculations were carried out to investigate the steric effects on the regio- and stereoselectivity, involving the alkyl substituents on olefins, the methyl or other substituents on the Cp rings, and the model polymer chain end. The primary insertion was found to be preferred to the secondary insertion, which well reproduced the experimental regioselectivity. Regarding the stereoselectivity, the computational results for the isotactic polymerization of propylene by $SiH_2(CpMe_n)_2ZrR^+$ suggested that the substituents on the Cp rings determine the conformation of the polymer chain end, and the fixed polymer chain end conformation in turn determines the stereochemistry of olefin insertion at the transition state. However, the direct steric effects of the Cp methyl groups on the olefin insertion stereochemistry are negligibly small. Although this early study used a QM-then-MM approach, this can be considered the seed for development of the combined QM/MM polymerization study,[381] as well as that of the IMOMM method.[10] In 2001, a systematic IMOMM-(B3LYP:MM3) study of polymerization of ethylene catalyzed by zirconium noncyclopentadienyl complexes (**TM3**, Figure 56) was reported by Vyboishchikov et al. to evaluate the effects of ligands and bulky substituents.[382] IMOMM(QM:MM) results showed that the bulky substituents destabilized the π-complex, resulting in a decrease of the insertion barrier by several kcal/mol.

Xu et al. investigated the cationic-Ti (**TM4**, Figure 56) catalyzed polymerization of ethylene, and the effects of their anionic counterions.[383] Their hybrid QM/MM results reproduced the behavior of the ion-pair system in the insertion process, and improved upon the QM-only results. Another system with anionic counterions, $[(C_6H_5N=CH)C_4H_3N]_2$-CH_3M-μ-$MeB(C_6F_5)_3$ (M = Ti and Zr) (**TM5**, Figure 56) catalyzed ethylene polymerization, was also studied by Vanka et al. with a hybrid QM/MM method, PWB91:SYBYL/TRIPOS5.2.[381] Wondimagegn et al. used the same method to investigate hydrogen transfer from the anionic counterion, $[MeB(C_6F_5)_3]^-$, to the methyl group of L_2MMe^+ (M = Ti and Zr) (**TM6**, Figure 56), and suggested that it could be a deactivation pathway in olefin polymerization.[384] The influence of the counterion $[MeB(C_6F_5)_3]^-$ and solvent effects on ethylene polymerization by various single-site Ti or Zr systems has also been studied.[385]

In 2005, Yang et al. studied the ethylene polymerization catalyzed by $[Cp_2ZrR(\mu$-$Me)B(C_6F_5)_3]$ (**TM7**, Figure 56) with a QM/MM CPMD method.[386] They provided a comprehensive potential energy and free energy profiles for ethylene insertion and chain termination, taking into account the counterion and solvent effects. They found that the free energy profile generally has a higher barrier than the potential energy profile due to entropic contributions. The rate-determining step for both profiles was ethylene insertion into the Zr-C_R bond, rather than coordination of monomer. QM/MM CPMD simulations without any constraint showed that the counteranion recoordinated to the metal center in less than 1 ps. Thus, it may recombine with the metal center before the coordination of a new monomer. In another QM/MM MD study of counteranion effects on zirconocene-catalyzed polymerization by Rowley et al., it was found that the β-agostic configuration was stabilized by 1 kcal/mol with the presence of the counteranion.[387]

Polymerization of propylene has also been widely studied with the hybrid methods. Talarico et al. reported a bis(phenoxyimine) group 4 metal complex (**TM9**, Figure 56)
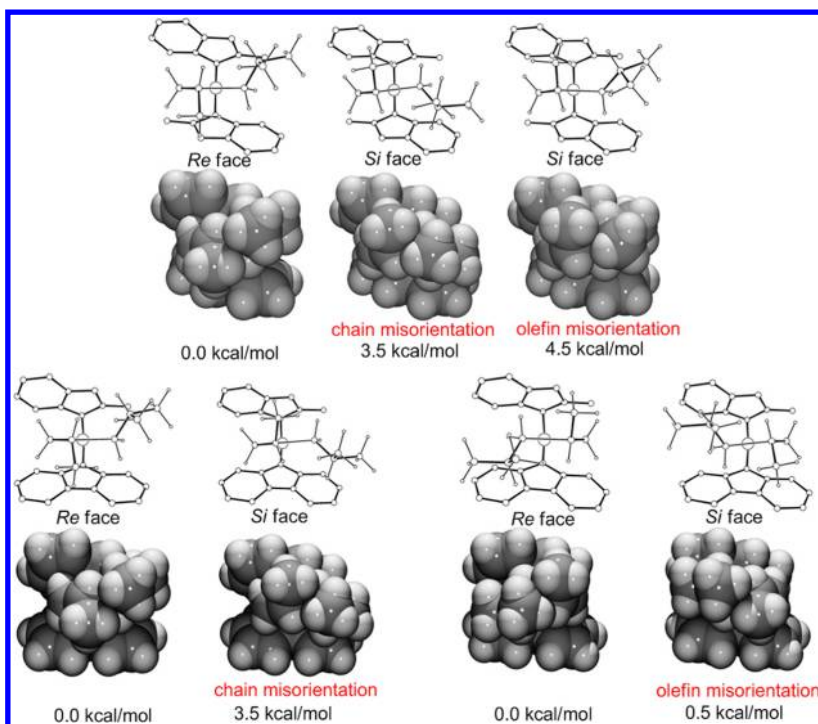
Figure 58. Transition states for the *C2*-ansa-zirconocene- and *C1*-ansa-zirconocene-catalyzed polymerization of polypropylene and poly(1-butene). Reprinted with permission from ref 392. Copyright 2007 American Chemical Society.

catalyzed "living" propylene polymerization with QM/MM calculations at a two-layer level, BP86:CHARMM.[388] Their results suggested the importance of a weak attractive interaction between the ortho-F and a close-in-space R−H of the growing chain for the "living" propylene polymerization. Pilme et al. reported an ONIOM(B3LYP:UFF) study of the 2,1 to 3,1 isomerization mechanism for ansa-Cp$_2$-Zr (**TM12**, Figure 56)-catalyzed polymerization of propylene.[389] Champouret et al. used an ONIOM(B3LYP:UFF) method to study the cyclopentadienyl β-diketiminate-Cr (**TM14**, Figure 56)-catalyzed radical polymerization of vinyl acetate,[390] and found an early transition state for the radical trapping process, with a very low energy barrier.

4.3.1.2. Selectivity. The stereoselectivity of substituted olefins is also an attractive topic for early transition metal-catalyzed polymerization. In 1996, Yoshida et al. applied the IMOMM method to extensively study the isotacticity control in propylene polymerization with C_2 symmetrical and asymmetrical silylene-bridged group 4 metallocenes (**TM2**, Figure 56).[391] They investigated the direct steric effects and the indirect steric effects at the transition states on the isotacticity of propylene polymerization. The direct steric effects are caused by the catalyst−olefin interactions, and the indirect steric effects are due to the catalyst−polymer and polymer−olefin interactions. The isotactic control can be explained by an indirect control mechanism with one-blocked access (Figure 57). They found that among group 4 bis(indenyl) and bis(tetrahydroindenyl) complexes, titanium complexes generally perform better in isotactic propylene polymerization than zirconium and hafnium analogs. Substituents at the 2- and 4-positions of the indenyl-based metallocene are very important for the control of stereoregularity. Asymmetric catalyst was suggested to show a high isotactic control, because it can completely allow one-blocked insertion.

An experimental and computational study of the influence of olefin size on the stereoselectivity of the polymerization of polypropylene and poly(1-butene) was reported by Mercandelli et al.[392] Their ONIOM(B3LYP:UFF) results suggested a site-control mechanism operating through the chiral orientation of the growing chain. For *C2*-ansa-zirconocene (**TM10**, Figure 56), as compared to the most stable transition state (propylene *re* face), other transition states were less favored due to chain misorientation (3.5 kcal/mol higher) or olefin misorientation (4.5 kcal/mol higher, Figure 58). C_1-ansa-zirconocene (**TM11**, Figure 56) has two types of insertion: inward and outward. The former was calculated to have high stereoselectivity, whereas that of the latter was low. A back-skip of the growing chain was suggested to play an important role. The stereoselectivity for poly(1-butene) was higher due to the size of the growing chain.

4.3.1.3. Copolymerization. In 2000, Longo et al. reported a QM/MM study on the copolymerization of *Z* and *E* isomers of 2-butene with ethylene catalyzed by C_{2v}-, C_s-, and C_2-symmetry group 4 ansa-metallocenes calculated at the two-layer level, BP86:CHARMM.[393] As shown in Figure 59, the C_{2v}-symmetric catalyst showed higher reactivity for the *E*-butene, due to its lower coordination ability. Regarding the stereoselectivity, the lower energy transition state for the C_s-symmetric catalyst is the butene insertion from the *re−re* enantioface. The lower energy transition state for the C_2-symmetric catalyst is the insertion from the *si−si* enantioface. Longo et al. applied hybrid approach (BP86:CHARMM) to study the copolymerization of 1,3-butadiene with ethane catalyzed with C_2-symmetric metallocenes (**TM8**, Figure 56).[394] Their computational results suggested the feasibility of a proposed cyclopropanation mechanism, and rationalized the *E* stereoselectivity for 1,1 and 1,3 constitutional units.

Wang et al. carried out QM/MM calculations (BP86:SYBYL/TRIPOS5.2) on C_1-ansa-zirconocene catalysts (**TM13**, Figure 56) to study why C_1-ansa-zirconocene-catalyzed
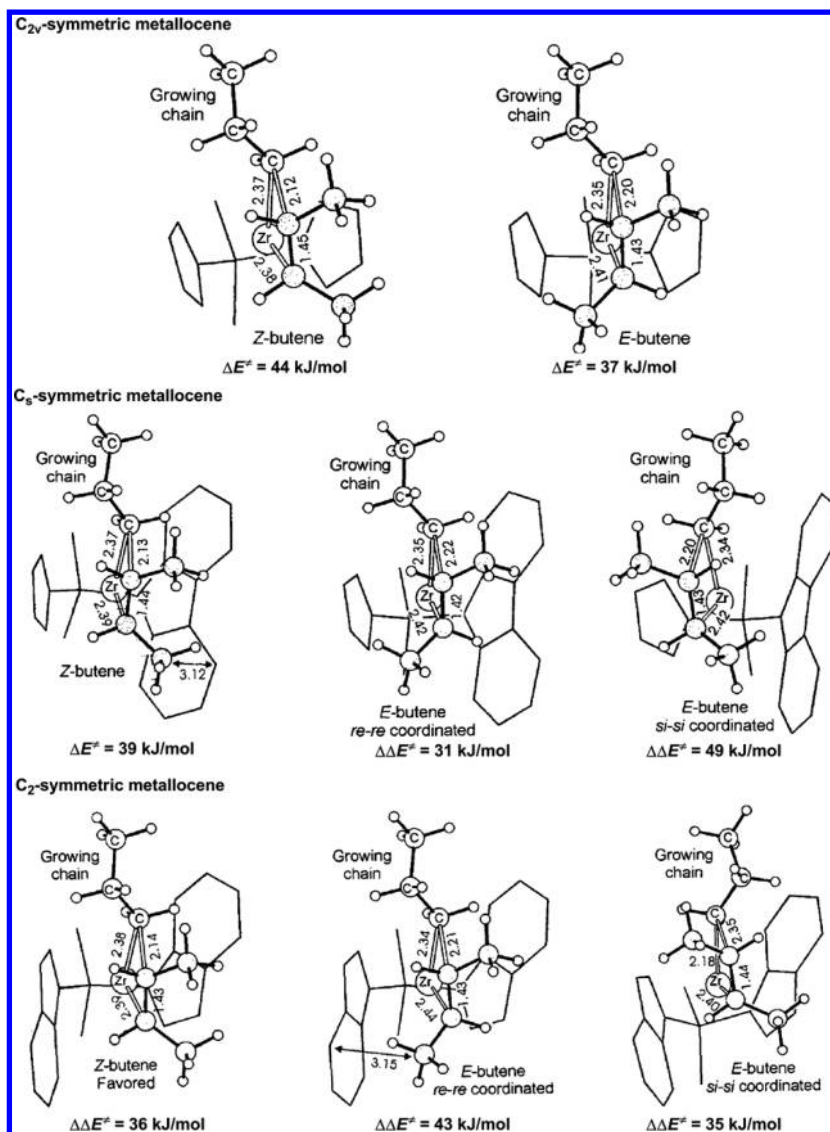
Figure 59. Transition states for the copolymerization of Z and E isomers of 2-butene with ethylene catalyzed by C_{2v}-, C_s-, and C_2-symmetry group 4 ansa-metallocenes. Reprinted with permission from ref 393. Copyright 2000 American Chemical Society.

copolymerization of ethylene/propylene produces lower molecular weight polymers than homopolymerization of ethylene or propylene homopolymerization.[395] Their study indicated that the chain propagation was preferred over chain transfer in ethylene homopolymerization, propylene homopolymerization, and propylene insertion into the polyethylene chain. However, the two processes were competitive in ethylene insertion into the polypropylene chain. These results explain the order of polymer molecules in ethylene or propylene homopolymerization and ethylene/propylene copolymerization. Luo et al. performed an ONIOM-(B3LYP:UFF) study on scandium-catalyzed (**TM15**, Figure 56) syndiospecific copolymerization of styrene and ethylene.[396] The styrene polymerization was found to proceed through 2,1-insertion, which was both kinetically and energetically preferred over 1,2-insertion. Styrene/ethylene copolymerization was also explained by the calculated results. The insertion of styrene into the chain with an ethylene end was energetically more favorable than continuous ethylene insertion into the chain with an ethylene end. The syndiospecific selectivity was determined by the substituent of the ancillary ligand Cp.

4.3.1.4. Miscellaneous. Agostic interactions are very important for polymerization. An IMOMM(B3LYP:MM3) study of Jaffart et al. shows that $Tp^{Me2}NbCl(CH_2Me)(HC\equiv CMe)$ is α-agostic only, whereas $Tp^{5-Me}NbCl(CH_2Me)(HC\equiv CMe)$ is β-agostic only due to the lack of methyl groups at the 3-positions of the pyrazole rings.[285] Zhong et al. have used ONIOM(B3PW91/BS1:B3PW91/STO-3G) calculations to predict model structures for active-site precursors in model Phillips polymerization catalysts. Calculated vibrational frequencies were also consistent with the experimental IR frequencies of the CO groups.[397]

4.3.2. Polymerization Catalyzed by Late d-Block Metal Systems. *4.3.2.1. Homopolymerization.* Late transition metal complexes are another typical type of systems for polymerization. Some of the late d-block metal systems, studied using the ONIOM method, are summarized in Figure 60. Froese et al. have performed a comprehensive study of diimine−M (M = Ni, Pd)-catalyzed ethylene polymerization with an IMOMM-(B3LYP:MM3) method.[398] As compared to the QM results on a simplified model, calculation on the full model with ONIOM led to a decrease in the migratory insertion activation barriers.
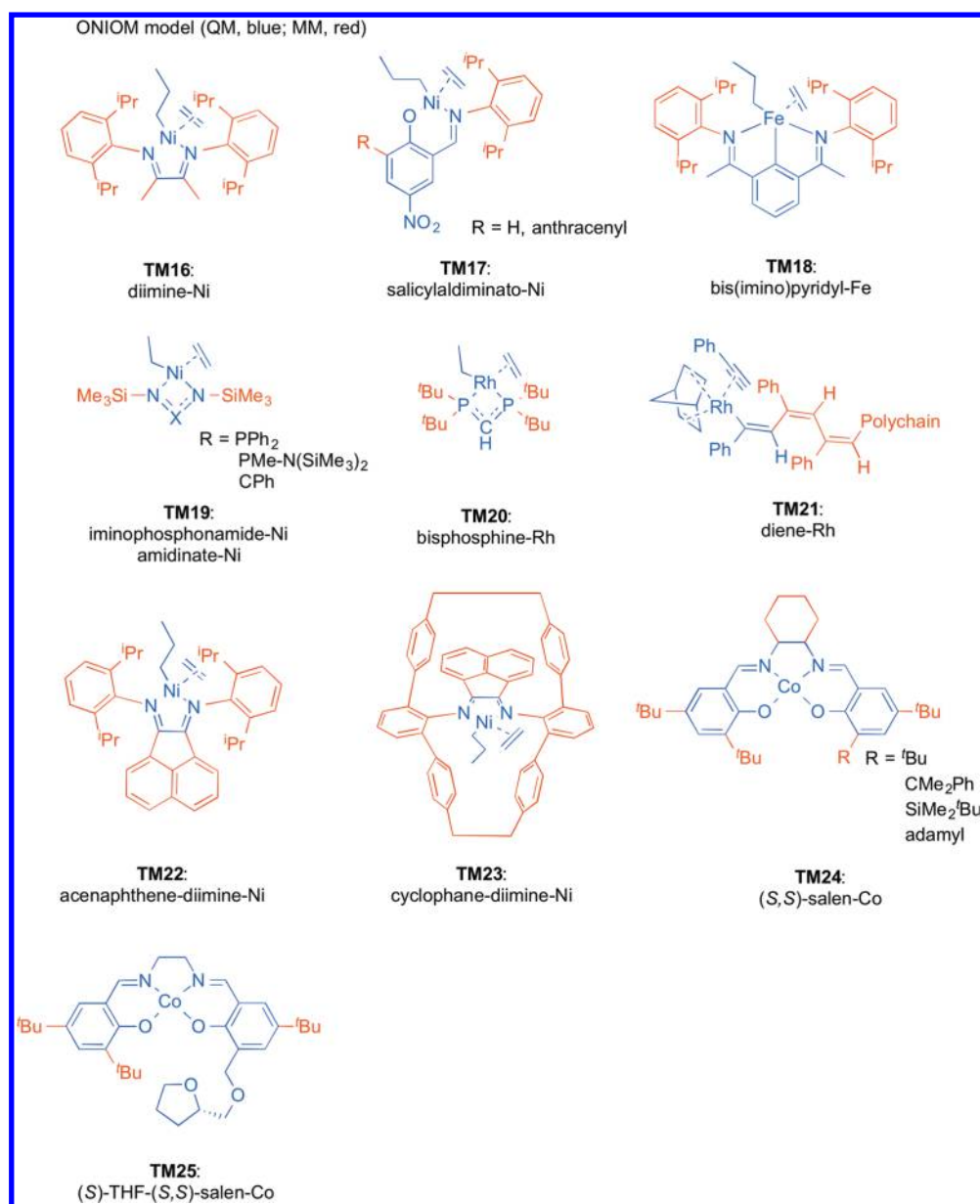
Figure 60. Studied ONIOM models of late d-block metal polymerization catalysts.

This study unambiguously indicated the importance of the steric interactions of the substituents in the MM part, which decrease the complexation energy. As shown in Figure 61, due to the substituent effects, the complexation energy of ethylene to metal center decreased by 7.5 and 1.9 kcal/mol for nickel and palladium, respectively. As a result, the reaction barrier for the ethylene insertion decreased from 9.9 kcal/mol (QM model) to 3.8 kcal/mol (IMOMM model) for the Ni complex, and from 6.2 kcal/mol (QM model) to 4.1 kcal/mol (IMOMM mode) for the Pd complex.

In 1999, Musaev et al. presented an DFT and IMOMM-(B3LYP:MM3) study on the mechanism of the ethylene polymerization reaction catalyzed by diimine−M(II) (M = Ni, Pd, and Pt) and Ti-/Zr-chelating alkoxides (Figure 60).[399] They studied several elementary reactions of the ethylene polymerization process, including chain termination/transfer reactions, as well as the role of steric effects on the elementary reactions. These results clearly demonstrated that the IMOMM method allows the study of realistic models for complicated

homogeneous catalytic processes. The combination of different levels of QM and MM can be used to take into account the steric and electronic interactions from the auxiliary ligands, solvent, cocatalysts, and counterions, etc., which are important for many transition metal-catalyzed inorganic, organometallic, and biochemical reactions. Woo et al. studied the Ni-diimine (**TM-16**, Figure 60)-catalyzed polymerization of ethylene, where the iso-propylphenyl groups and the methyl groups on diimine were treated at the MM level, and the remaining parts with the BP86 functional.[400] They also extended the study by combining the hybrid approach with ab initio molecular dynamics to estimate the free energy profiles for various processes of the Ni-diimine-catalyzed polymerization of ethylene.[400]

In 2000, Chen et al.[401] investigated the mechanism and the electronic/steric effects of various substituents of the catalyst of neutral salicylaldiminato Ni(II) complex (**TM17**, Figure 60)-catalyzed ethylene polymerization. The electron-withdrawing or -donating substituents at the 5-position of the salicylaldiminato
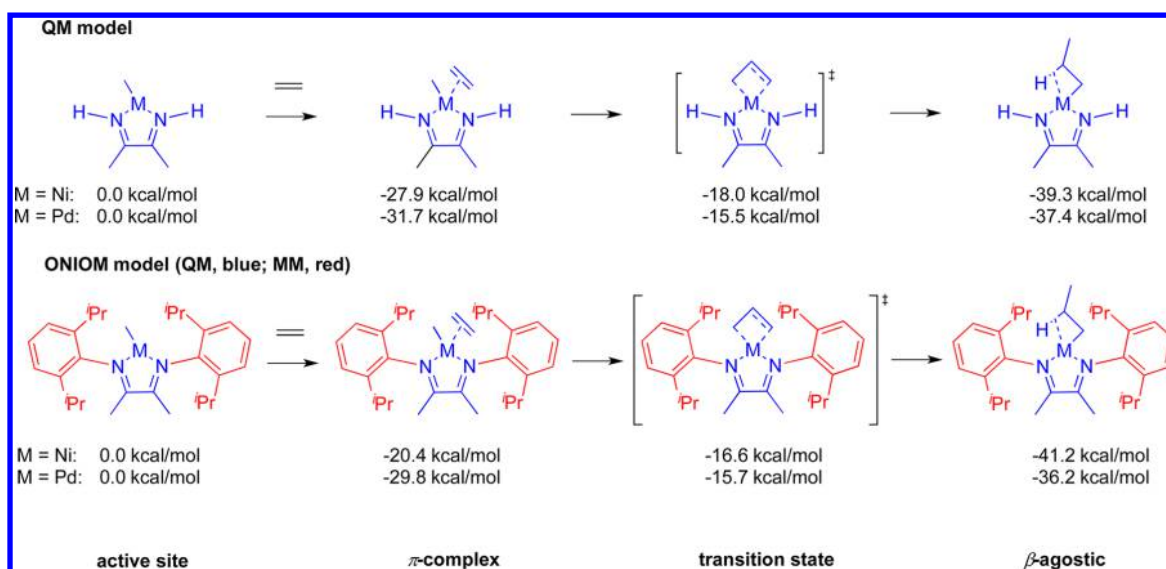
Figure 61. Substituent effects in the diimine-Ni/Pd(II)-catalyzed ethylene polymerization reaction as described by IMOMM(QM:MM) studies.

ring were found to have little effect on the polymerization mechanism. However, the electronic nature of the dative atoms affected the potential energy surface. Bulky substituents were found to play the most important role in increasing catalyst activity. Khoroshun et al. applied the IMOMM(B3LYP:MM3) method to bis(imino)pyridyl-Fe(II) systems (**TM18**, Figure 60) to study the dominance of different spin states in propagation and α-hydride transfer during polymerization.[402] For the first time in an IMOMM study of polymerization, a QM region with various multiplicities was successfully employed to analyze various electronic configurations. IMOMM results for a model in which the bulky *ortho* substituents on the Ar rings were included suggested the steric destabilization of the axial positions. The β-hydride transfer took place on the triplet or quintet state potential energy surface, as it could not compete with chain propagation on the singlet surface.

Iminophosphonamide-Ni and amidinate-Ni complex (**TM19**, Figure 60)-catalyzed ethylene polymerizations were studied by a hybrid QM/MM method as implemented in the ADF program[403] to provide insight into the polymerization behavior, and to investigate the role of steric effects on the insertion and chain-transfer processes. A similar bisphosphine-Rh system (**TM20**, Figure 60) was reported and studied with B3PW91 and ONIOM(B3PW91:UFF) methods,[404] and it was found that the computed insertion barrier was too high for the polymerization of ethylene at low temperatures. Recently, ONIOM(B3LYP:UFF) was employed to study another type of late transition metal system, the cyclophane-diimine-Ni complex (**TM19** and **TM23**, Figure 60).[405] All of the polymerization processes, including coordination, insertion, and chain isomerization, etc., were studied to evaluate the steric and electronic influence of the cyclophane ligand. They found that this cyclophane-diimine-Ni complex has stereo and electronic characteristics similar to that of Brookhart's bulky diimine-Ni catalyst.

4.3.2.2. Selectivity. In 2000, an IMOMM(QM:MM) study of the stereoselectivity of late transition metal-catalyzed 1-alkene polymerization was reported by Milano et al. for Brookhart-type Ni-diimine catalysts (**TM16**, Figure 60).[406] The primary insertion was suggested to be controlled by the chain

end. The chiral orientation of the chain was determined by repulsion between propylene enantiofaces. Very recently, the regio-/stereochemistry polymerization mechanism for polymerization of phenylacetylene catalyzed by a rhodium complex (**TM21**, Figure 60) was reported by Ke et al. using various computational methods, including DFT, ONIOM, and ONIOM MD simulations.[407] They found that there are equilibriums between Rh^I, Rh^{III}, and Rh-carbene types of species during polymerization. However, the Rh^I insertion mechanism is preferred over the Rh-carbene metathesis or the Rh^{III} insertion mechanisms (Figure 62). The origin of regioselectivity is due to a unique π-conjugative transition state, which is the driving force for the 2,1-insertion of phenylacetylene. ONIOM and ONIOM-MD revealed the conformational constraints of the parent propagation chain for the insertion transition state. The stereoregularity is controlled by kinetic factors, because the polymerization adopting a *cis–transoidal* conformation in the propagation chain is the most favorable for insertion. Other transition states with *cis–transoidal*-mix, *cis–cisoidal*, or *cis–cisoidal*-mix conformations in the propagation chain have more repulsion.

4.3.2.3. Copolymerization. In addition to homopolymerization,[408] the ONIOM method has been further applied to study late transition metal-catalyzed copolymerization reactions. The ONIOM method was employed in a study of the copolymerization of propylene and carbon monoxide catalyzed by unsymmetrical phosphine–phosphite Pd(II) complexes.[409] In 2001, Nozaki et al.[410] employed ONIOM calculations [ONIOM(B3LYP:MM3), ONIOM(B3LYP:HF), and ONIOM(B3LYP:B3LYP)] to study the regioselectivity-controlling factors for Pd-catalyzed alternating copolymerization of styrene and carbon monoxide. ONIOM results suggested that the regioselectivity was affected not only by electronic factors but also by steric factors. Also, the 2,1-insertion was favored electronically, whereas the 1,2-insertion was favored sterically. Later, an ethylene/1-hexene copolymerization system catalyzed by bisiminepyridine Fe(II) (**TM18**, Figure 60) was studied.[411] The active site with axial conformation was found to be more stable than that with equatorial conformation. Thus, the axial conformer was proposed to promote polymerization. The reaction barriers were further decomposed into QM and MM
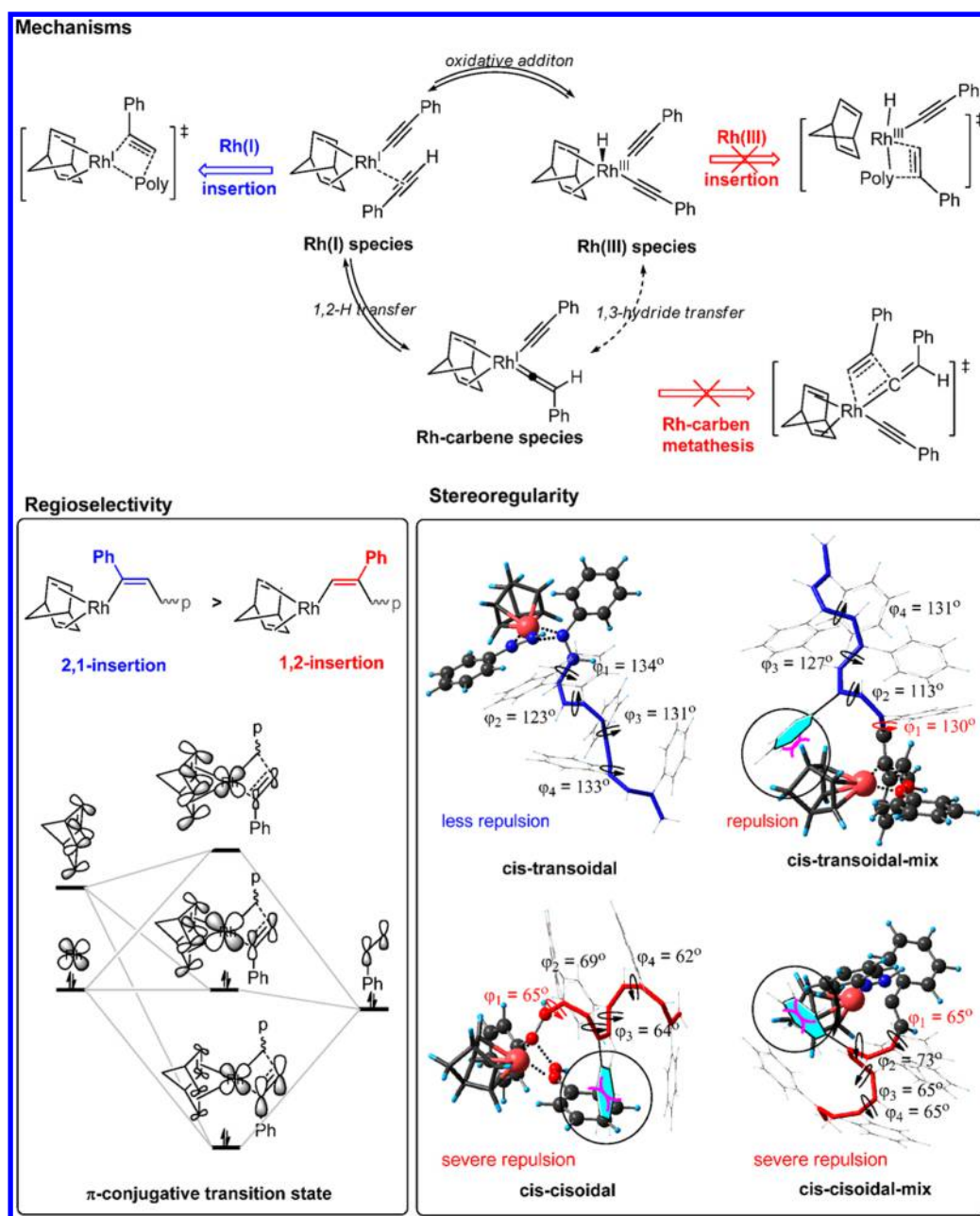
Figure 62. Mechanism and regio- and stereoselectivity for the Rh-catalyzed polymerization phenylacetylene found through ONIOM studies. Reprinted with permission from ref 407. Copyright 2011 American Chemical Society.
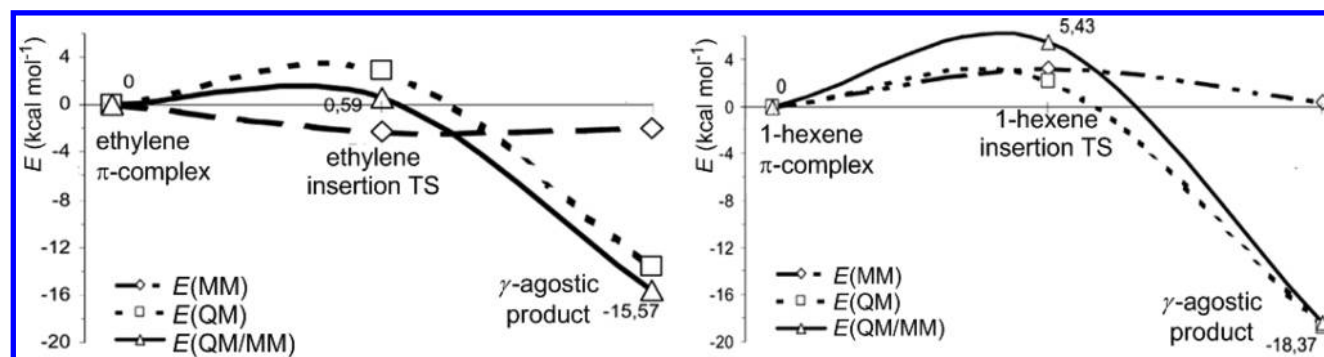
Figure 63. QM and MM contributions for the reaction barriers of bisiminepyridineFe(II)-catalyzed ethylene/1-hexene copolymerization. Reprinted with permission from ref 411. Copyright 2001 American Chemical Society.

contributions. As shown in Figure 63, the MM region contributed significantly for the bulky 1-hexene monomer. In accordance with experimental observations, the homo ethylene polymerization was preferred over ethylene/1-hexene copolymerization, which is consistent with experimental observations.

Copolymerization between ethylene and CH_2=CHX (X = −Me, −CN, −COOMe, −OC(O)Me, and −Cl) by cationic, neutral, and anionic diimine-Pd(II) active sites has also been systematically compared by Szabo et al. using DFT and QM/MM methods.[412] Recently, an ONIOM(B3LYP:UFF) study on the copolymerization of CO_2 and cyclohexene oxide was reported in combination with an experimental report.[413] The (S,S)-salen-Co(III) catalyst (**TM24** and **TM 25**, Figure 60) selectively cleaved the (S)-C−O bond of cyclohexene oxide, which was rationalized by the interaction between (S)-C−H of the coordinated cyclohexene oxide and the oxygen atom of an (S)-induction agent.

4.3.2.4. Miscellaneous. To assess the accuracy of ONIOM methods for treating bulky organonickel and organopalladium complexes, Li et al. performed geometry optimizations with a variety of methods.[281] The ONIOM(DFT:HF) calculations included several density functionals (B3LYP, PBEP86, B3P86, B3PW91, BPBE, PW91PW91,BP86) and the ECP basis sets (CEP-121G, CRENBL, LANL2DZ, LANL2DZCp, SDD, sbkjcvdz).[281] According to their survey, the best method for the geometry optimizations is ONIOM(B3P86/LANL2DZ +p:HF/LANL2MB).

4.3.3. Polymerization Catalyzed by f-Block Metal Systems. ONIOM studies of f-block metal-catalyzed polymerization are relatively rare. Perrin et al. have reported an ONIOM(B3PW91:UFF) study of f-block metal systems.[326] Their study found that the DFT and ONIOM(QM:MM) results for electronic properties, geometries, and energy barriers were very similar to each other, suggesting that steric effects outweigh the electronic effects of the Me groups of the cyclopentadienyl ligand.

5. APPLICATIONS TO HETEROGENEOUS CATALYSIS

Hetregeneous catalysis includes a vast number of systems, which, depending on their specific properties, could be modeled by means of differnt quantum-chemical or molecular mechanics/dynamics approaches. The ONIOM method has been successfully and widely applied in modeling covalent bound solid-state catalysts such as zeolites and metal−oxide surfaces. There are also a few rare examples of modeling the catalytic preformance of metal surfaces, which are preferably modeled using periodic boundary conditions, as ONIOM could hardly provide a proper description of the metal bond at the boundary region between the levels.

Zeolites are a class of aluminosilicate materials that have micro- or mesoporous structures characterized by regular networks of channels and cavities. They have broad applications as catalysts, ion exchange materials, and adsorbents. They have also shown good catalytic activity in the petrochemical industry, specifically in fluid catalytic cracking, aromatic alkylation, isomerization, hydrocracking, and oligomerization. The framework of zeolites and zeolite-like materials (such as silicoaluminophosphates and titanium silicates) is built by corner-sharing tetrahedral TO_4 structures (T = Si, Al, P, etc.). Substituting Si with a low-valence element, such as Al, at the tetrahedral sites results in the framework taking on excess negative charge, which is compensated by a proton or an extra framework cation. The proton is coordinated at one of the oxygen atoms

(which is connected to the Al center) and forms bridging hydroxyl groups, −Al−OH−Si−. The extra framework cation is usually located in close proximity to the Al center and forms coordination bonds with the framework oxygen atoms. Many experimental studies on the application of zeolites and metal oxide surfaces as heterogeneous catalysts have been reported. Experimental techniques such as XPS, IR, and XRD provide information about the reactive intermediates in these catalyzed reactions. However, many questions concerning the structure of the adsorbed complexes, or detailed reaction mechanisms, remain unclear or ambiguous using these techniques. If the catalytic properties of existing materials are to be improved, and new materials with novel qualities to be developed, knowledge at the molecular level is required. Toward this end, theoretical modeling has been extensively applied over the past several decades. This modeling has allowed us to gain better understanding regarding the structure and electronic properties of zeolites and metal oxide materials, and what role this plays during heterogeneous catalysis.

5.1. Theoretical Methods for Zeolites and Metal−Oxide Surfaces

Several computational approaches have been used for studying zeolites/zeolite-like materials and metal oxide surfaces: (i) isolated cluster models including only the active center (defect, hydroxyl group, extra framework cation, etc.) and its immediate surroundings at the same computational level; (ii) embedded cluster models, which model the active center with a high computational level and a larger part of the lattice with a low computational level; and (iii) models using periodic boundary conditions (PBC). In the following discussion, the standard notation of zeolite models is used, that is, nT/mT, where n/m corresponds to the number of TO_4 units included in the high/low-level part of the ONIOM calculation.

5.1.1. Isolated Cluster Models. In the isolated (constrained) cluster models, a small model containing the active center is cut out from the surface/bulk of the catalyst. It is assumed that interactions are localized in the vicinity of this active site; thus all long-range interactions are neglected. The model system is treated at a high QM level, and the atoms at the edge of the model are kept fixed to their crystallographic positions. This approach is acceptable so long as the zeolite framework effect on the active site and the subsequent properties/processes are negligible.

5.1.2. Embedded Cluster Models. The zeolite framework can play a significant role in altering reaction mechanisms, and because of this computational approaches must include it in some way. In the embedded cluster approach, the active site is embedded in a larger cluster of the material, which is usually treated with MM or a relatively cheap QM method. This approach provides a realistic description of the structure, properties, and catalytic performance of zeolites and zeolite-like materials by taking into account the effect of the material framework with low computational cost. Papayannis et al.[414] demonstrated that, as compared to the isolated 3T model, the use of a 3T/12T ONIOM(B3LYP:UFF) model substantially decreases the activation barriers and increases the energy difference in the conversion reactions of ethyl chloride on an acidic zeolite cluster. In a similar vein, Solans-Monfort et al.[415] compared adsorption of NH_3 in acidic chabazite using a 5T isolated cluster model, a 12T/48T embedded cluster with ONIOM(B3LYP:LL) (LL = MNDO, AM1, or HF), and a PBC model. The 5T cluster model failed to describe the adsorption
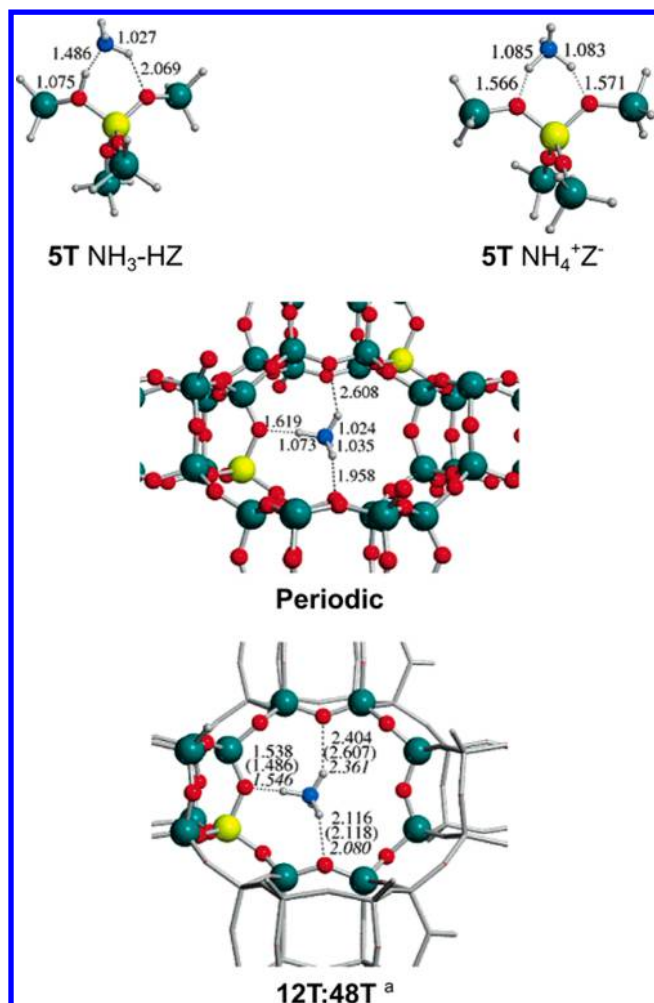
Figure 64. NH₃–HZ (Z = chabazite) optimized structures using three different approaches. 5T cluster model producing two structures (top two panels); PBC and 12T/48T embedded cluster approaches (middle and bottom panels) giving similar adsorption structures. Reprinted with permission from ref 415. Copyright 2010 American Chemical Society.

of NH₃ in chabazite (Figure 64). On the other hand, the 12T/48T embedded cluster and PBC models provided structures, in which the adsorption energy was close to experimental data. A comparative study of proton transfer in zeolite with isolated and embedded cluster models showed that geometry convergence in embedded cluster models requires fewer optimization cycles than in isolated models, and embedded cluster models speed up the optimization procedure by a factor of 3.[416]

The accuracy of any ONIOM embedded cluster model depends on both the proper combination of computational methods for the high- and low-level regions and the size of the embedded clusters (model system). Li et al.[417] performed a series of simulations of pure Si and Al-containing MCM-22 models using ONIOM with B3LYP/6-31G(d) as the high-level method, and AM1, PM3, MNDO, HF/3-21G(d) as the low-level method. The structural data were compared to full B3LYP/6-31G(d) optimized geometries. The performance of the ONIOM models improved in order of AM1 < PM3 < MNDO < HF/3-21G(d) < B3LYP/6-31G(d). Considering their relative computational costs, it was suggested that MNDO was the optimal low-level method in this system. NH₃

adsorption energies in acidic chabazite depended on the low-level method in ONIOM (12T/48T model), varying between −28.9 and −35.0 kcal/mol (the lowest value corresponding to AM1 and the highest to HF).[415] The ONIOM(B3LYP:HF) results are consistent with the value obtained using the PBC model, −36.9 kcal/mol.

The universal force field (UFF)[418] is often used as the low-level method (Table 3) in models of zeolite adsorption, and has been reported to provide an acceptable description of the van der Waals (vdW) interactions between adsorbates and the zeolite framework.[419] The influence of vdW interactions for adsorption is of critical importance, especially in the case of large adsorbates. Boekfa et al.[419a] found that the vdW contribution accounts for about 50% of the adsorption energy of L-alanine to ZSM-5. In the case of the smaller glycine molecule, this contribution is estimated to be 20−30%. On the other hand, dispersion contributions to the adsorption energy can be considered via a single-point energy calculation. Single-point energy estimation at ONIOM(B3LYP/6-311+G-(2d,p):B3LYP/6-31G(d)) and ONIOM(M05-2X/6-311+G-(2d,p):M05-2X/6-31G(d)) on the ONIOM(B3LYP/6-311G-(d,p):UFF) optimized geometries revealed that the M05-2X functional provided better results as compared to B3LYP.[420]

Several other "non-classical" ONIOM approaches have been used for modeling covalently bound zeolite-like materials. For example, by applying the SCREEP (the surface charge representation of the electrostatic embedding potential) surface to the ONIOM scheme,[419c,421,423] the Madelung potential field of the zeolite lattice is represented by a set of finite point charges. This allows the local electrostatic interactions around the site of interest to be understood. Maihom et al.[421] found that the SCREEP embedded ONIOM method (Figure 65) is better in describing the stabilization of transition structures and adsorption complexes, as compared to classical ONIOM models. Recently, the Xu group[180j,181,422] proposed a new eXtended ONIOM scheme (XO) by combining the fragmentation method[424] with ONIOM to deal with large active center model (Figure 66 and section 2.3.2). Benchmark studies on zeolites, polypeptides, and cyclodextrins (CDs) have been performed to validate this XO scheme.[181] Other hybrid QM/MM approaches for modeling zeolites and related covalent oxides have also been developed, such as the DFT/MM covEPE approach (covalent elastic polarizable environment) of Rösch et al.,[101,425] and the QM-pot scheme of Sauer and co-workers.[40,79] The former is based on the pseudo atom approach and force fields developed specifically for describing the oxide framework surrounding the QM model, while the latter is similar to the traditional ONIOM scheme, and uses hydrogen as link atoms between the high and low levels.

5.1.3. Periodic Boundary Condition Models. Zeolites, metal oxides, and metal-/covalent-organic framework (MOFs/COFs) materials have a well-defined crystal structure. Modeling the structure of these systems, and processes occurring on their surfaces, or within their channels/cages, are naturally amenable to first-principle simulations with periodic boundary conditions. A number of investigations using this approach have been reported.[426] Uzunova et al. compared 6T/100T ONIOM(B3LYP:UFF) and PBC (PBE functional) models for clinoptilolite.[426b] Some discrepancies in both the Al position and the exchanged cation positions were observed using these models. The ONIOM method was ultimately preferred over the PBC method for modeling the position of the exchanged cations, because too small value of the lattice c-parameter (~7.4

Table 3. ONIOM Examples of Reactions Catalyzed by Acidic Centers in Zeolites

zeolite	Al site	reaction	model/method	refs
ZSM-5	T12	H-exchange for ethene, benzene, ethylbenzene, and pyridine	5T/34T, ONIOM(MP2:M06-2X), ONIOM(MP2:B3LYP), ONIOM(MP2:HF), ONIOM(MP2:UFF)	423a
MOR	T4 in 12-MR, T3 in 8-MR	olefins protonation reactions	8T/112T for 12-MR, 8T/76T for 8-MR, B3LYP+D// ONIOM(B3LYP:MNDO)	450e
ZSM-5	T12	ethene methylation	34T/128T, ONIOM(B3LYP:UFF) and ONIOM(M06-2X:UFF)[a]	419c
H-β	T1	*tert*-butylation of phenol	14T/116T, ONIOM(B3LYP:UFF)	447b
ZSM-5	T12	methylation of 2-methylnaphthalene	12T/128T B3LYP‖ONIOM(B3LYP:UFF)	447c
ZSM-5	T12	toluene methylation	12T/128T, ONIOM(B3LYP:UFF)	447a
FER	T2	1-butene isomerization	5T/37T, ONIOM(MP2:M08-HX)	448c
ZSM-5	T11	1-hexene isomerization	3T/54T, ONIOM(B3LYP:UFF)	448a
MOR FAU	T2 T2	ring-shift isomerization of *sym*-octahydrophenanthrene to *sym*-octahydroanthracene	14T/120T, 14T/140T, ONIOM(B3LYP:UFF)	448b
ZSM-5	T12	thiophene cracking	5T/56T, ONIOM(B3LYP:UFF)	420
ZSM-5	T12	1-hexene cracking	10T/88T, ONIOM(B3LYP:UFF)	449
—[b]	—[b]	ethyl chloride conversion	3T/12T, ONIOM(B3LYP:UFF)	414
FAU		benzyl alcohol interaction with dimethyl carbonate	3T/36T, ONIOM(B3LYP:PM3); ONIOM(B3LYP:UFF)	450a
ZSM-5 SSZ-13 ZSM-22		ethylene dimerization	8T/72T, 8T/74T, 8T/66T, ONIOM(B3LYP:MNDO)	446
ZSM-5		ethanol conversion in hydrocarbons[c]	58T (only organic species treated at QM), ONIOM(B3LYP:PM6)	450b
ZSM-5	T12	furan to benzofuran	11T/132T, ONIOM(B3LYP:UFF)	450d
H-β	T5	methanol to propene conversion	16T/188T, ONIOM(M06-2X:UFF)[d]	450c
ZSM-5 MOR	T12 T2	propylene glycol dehydration	5T/52T, 5T/68T, ONIOM(B3LYP:AM1)	451

[a]The Madelung potential of the zeolite framework was also considered by applying the SCREEP method. [b]The model used in the study, 3T/12T (a rather modest one), could represent any type of zeolite framework with 12T rings. [c]The reaction mechanism is not modeled; only the structure and relative stability of different deposits on the zeolite support are considered. [d]Part of the QM region (8T) is treated with the same DFT method, but applying a lower basis set. Thus, the computational scheme is ONIOM(M06-2X/6-31G(d,p):M06-2X/3-21G:UFF).
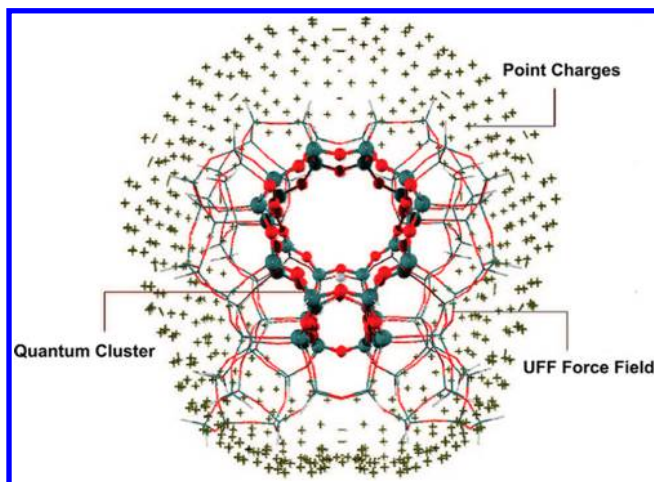
Figure 65. SCREEP embedded 12T/128T ONIOM model of H-ZSM-5 zeolite. Reprinted with permission from ref 421. Copyright 2010 American Chemical Society.

Figure 66. Comparative schematic representation of (a) ONIOM2 and (b) XO2.[180j,181,422] Reprinted with permission from ref 180j. Copyright 2010 Elsevier B.V.

Å) in the PBC calculations leads to artificially close cation–cation distances in one of the channels of the zeolite framework.

5.2. Characterization of Zeolites and Metal–Oxide Surfaces

5.2.1. Modeling the Structure. Experimental techniques can provide direct structural information for zeolites and metal–oxide surfaces. For example, X-ray-based approaches provide information on the crystal structure of the materials and, in some cases, detailed information about metal active centers and their immediate surroundings. FTIR of adsorbed

inorganic/organic molecules allows better characterization of the active centers and their adsorption properties. However, the interpretation of the experimental data may be rather sophisticated. Theoretical simulations can be successfully applied for explaining or even predicting the structure and properties of these heterogeneous catalysts.

Erbetta et al.[427] used ONIOM(B3LYP:MNDO) for modeling point defects in Si-containing materials such as SiO_2, Si_3N_4, and Si_2N_2O. As expected, the reliability of the ONIOM scheme depended on the size of the QM model and the methods in the computational scheme. In the case of nondefective materials,
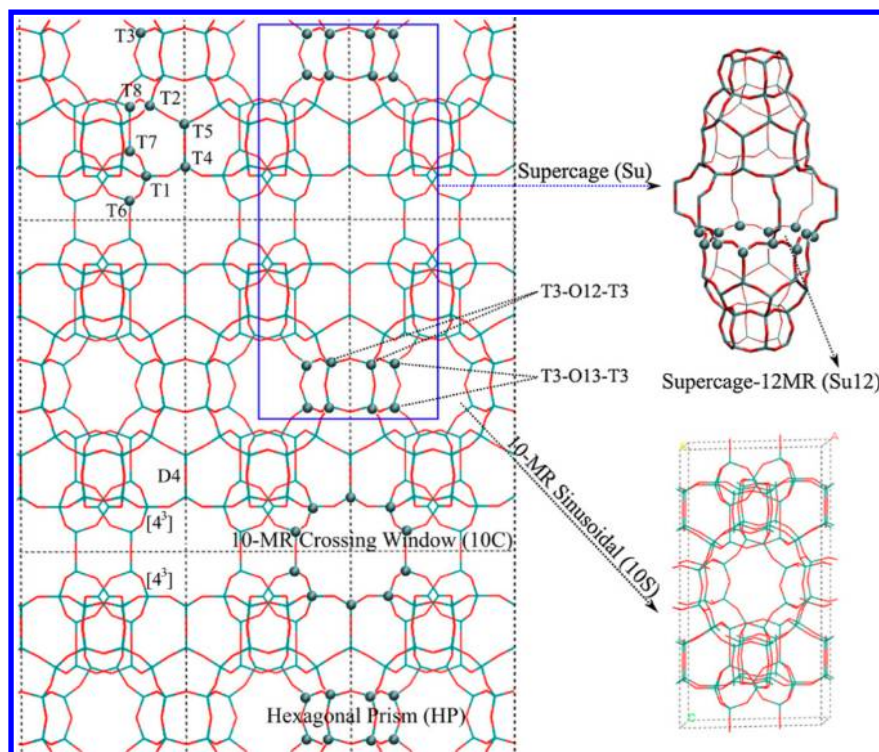
Figure 67. Schemes of MCM-22 zeolite structure with eight crystallographically inequivalent T sites and the possible location of extra framework Na$^+$−12-MR supercage, intralayer 10-MR sinusoidal channels (10S), 10-MR crossing windows (10C), or pore openings between layers and hexagonal prisms between supercages. Reprinted with permission from ref 417a. Copyright 2010 Elsevier B.V.

benchmark calculations using AM1 as the low-level method produced Si−O distances that were ca. 0.1 Å longer than experimental values.

Two- and three-layer ONIOM methods have been used to model the structure of MCM-22, to determine the positions of Al^{3+} in the framework of Na-MCM-22, and to determine the strength of Brønsted acid sites in the corresponding H-MCM-22 analogue.[417] Depending on the positions of Al^{3+} (8 inequivalent crystallographic positions are distinguished in MCM-22, Figure 67), several different 19−27T/72−116T cluster models of the system were optimized using ONIOM(B3LYP:MNDO). For the H-MCM-22 analogue, three-layer ONIOM(B3LYP:HF:MNDO) 8T/21−24T/80−94T models were considered with the aim of obtaining a better description of potential hydrogen bonding between the proton and framework oxygen centers. Several benchmark ONIOM calculations were also performed toward tuning the computational scheme with respect to the high/low-level combination and the core/lattice cluster size. For Al^{3+}, the T1 crystallographic position was preferable, resulting in an intensive absorption band at 3628 ± 6 cm^{-1} in the OH-region in the H-MCM-22 IR spectrum. Proton coordination at O13 and O12 (Al@T3) and O7 (Al@T4) was responsible for the bands at 3597 ± 4, 3574 ± 3, and 3592 ± 4 cm^{-1}, respectively, and matched closely to experimental bands at 3600 and 3575 cm^{-1}, respectively. H-bonded O−H groups exhibited stretching vibration frequencies in the range from 3401 ± 1 to 2575 ± 6 cm^{-1}, which accounted for the broad absorbance band at 3375 cm^{-1} in the experimental IR spectrum. Brønsted acidity of zeolite hydroxyls was estimated via adsorption energies of N$_2$ and CO at the isolated bridging OH species. The protons in the vicinity of Al@T3 and Al@T4 were predicted to have stronger Brønsted acidity with respect to protons close to Al@T1.

ONIOM(B3LYP/LanL2DZ:B3LYP/LanL2MB)// ONIOM(B3LYP/LanL2DZ:UFF) was used to estimate the relative stability of Ti sites in MFI zeolite.[428] Theoretically, T9 and T10 were the most stable sites for Ti substitution followed by T12 and T1. The energy difference between the most stable Ti@T9 structure and the Ti@T12 structure was about 80 kJ/ mol. The model used included all 12T crystallographic sites in a 12-membered ring of MFI structure. However, only the TiO$_4$ tetrahedron structure was included in the QM part; MM atoms were kept fixed to their crystallographic positions. Because a basic relaxation of the lattice was not performed, these results may not show a proper response of the zeolite framework following Ti substitution.

12T/56T model of ZSM-5 has been used to model the structure and properties of lanthanum (La) species in La-modified ZSM-5 zeolites at ONIOM(B3LYP:UFF).[429] Lanthanum cation forms a positively charged dihydroxide structure, La(OH)$_2^+$, and is located preferably close to T11 sites. In this position, weak hydrogen bonds are formed between La(OH)$_2^+$ and the oxygen atoms in the zeolite framework.

5.2.2. Adsorption of Probe Molecules. FTIR spectroscopy of adsorbed probe molecules is among the most powerful techniques for characterizing active species in zeolites/zeolite-like materials and metal−oxides surface.[430] Theoretical modeling of the stability and vibrational frequencies of adsorption complexes with such probe molecules enables the active species in zeolites to be defined through comparison with available experimental data.

The interactions between five probe molecules (pyridine, trimethylphosphine, water, ammonia, and acetone) and M^{4+}-doped 5T/17T MFI zeolite models (M = Ti, Zr, Ge, Sn, and Pb) have been investigated using ONIOM(B3LYP/6-311G-(d,p):B3LYP/3-21G) (with the LanL2TZ(f) ECPs for Ti, Zr
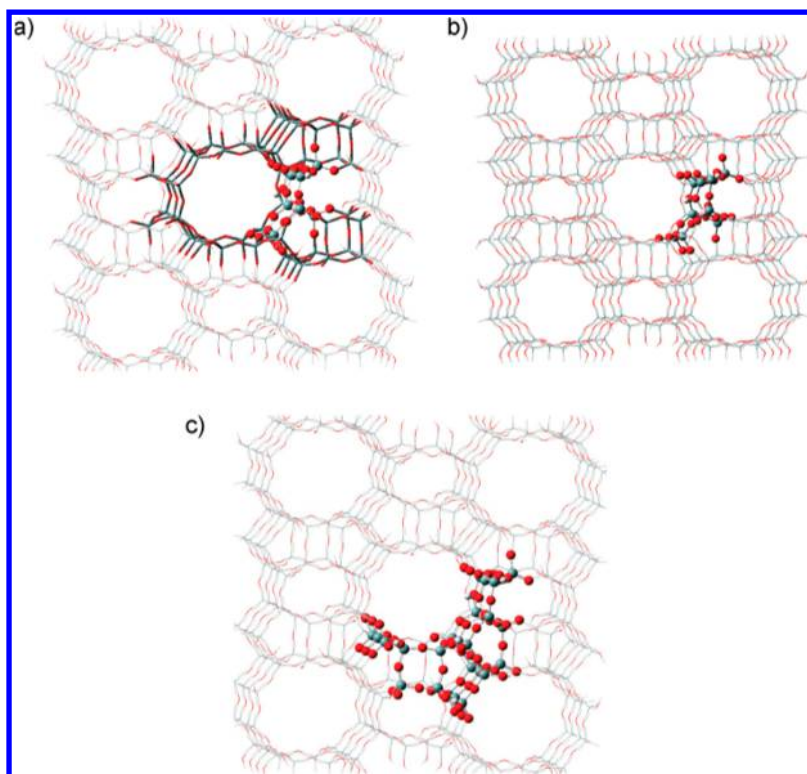
Figure 68. T1 site in MOR in several ONIOM models of the zeolite structure: (a) 10T/52T/202T at ONIOM(B3LYP:PM6:UFF), (b) 10T/254T at ONIOM(B3LYP:UFF), and (c) 25T/239T at ONIOM(B3LYP:UFF). Reprinted with permission from ref 436. Copyright 2010 American Chemical Society.

and LanL2DZ(d,p) ECPs for Ge, Sn, Pb) to estimate and to compare the Lewis and Brønsted acidities of the modified MFI structure.[431] Lewis acidity increased in order of Silicalite-1 < Ge < Ti < Pb < Sn < Zr, which was in agreement with available experimental data.

NO and CO interaction with the active site of H-ZSM-5 zeolite-supported Pd catalysts (7T/93T cluster model) has been modeled using ONIOM(B3LYP:UFF).[432] B3LYP calculations with a 7T isolated cluster model have also been performed, and the results of these two approaches have been compared. The adsorption of NO and CO on Pd-H-ZSM-5 was found to be energetically favorable, with calculated adsorption energies of −32.3 and −46.9 kcal/mol, respectively. The simulated vibrational frequencies for NO (1835.5 cm^{-1}) and CO (2138.3 cm^{-1}) in the zeolite complexes were in good agreement with available experimental data (1876 cm^{-1} for Pd^0-NO/H-ZSM-5 and 2110 cm^{-1} for Pd^0-CO/NaY, respectively).

ONIOM(B3LYP:UFF) has been used to investigate the structure and properties of one or two Au atoms[433] or a single Ga atom[434] supported on a 6T/126T (containing 506 atoms) model of SAPO-11 zeolite (silicoaluminophospate molecular sieve). ONIOM results showed that Au supported on SAPO-11[433b] interacted strongly with CO; the adsorption energies in the CO-Au/SAPO-11 and (CO)$_2$-Au$_2$/SAPO-11 complexes were −41.0 and −29.7 kcal/mol, respectively. Au can also catalyze thiophene hydrogenation to 2,5-dihydrothiophene or 2-butene.[433a] Ga-exchanged SAPO-11[434] has been modeled mainly as a potential DeSOx catalyst, because it exhibits a good adsorption affinity for SO.

NO adsorption on mono- and binuclear Cu(I) and Cu(II) centers in SAPO-34 (chabazite type structure) and faujasite (FAU) has been modeled at the ONIOM(B3LYP:PM6) level with a 6T/48T cluster model with the aim of analyzing the reactivity of the cationic centers in these zeolites.[426c] The structural parameters of the optimized models reproduced the experimental data. NO binding to the binuclear Cu−O−Cu was found stronger as compared to binding to the isolated Cu(I) species. The dissociation energy for the Cu−O−Cu(NO) complex was computed to be 144.5 kJ/mol.

The adsorption energies and vibrational frequencies of small inorganic molecules including NO$_x$,[435] SO$_2$,[435] and CO[436] on Au$_n$$^+$/MOR (n = 1, 3) have been modeled using ONIOM(B3LYP:UFF). A benchmark of several ONIOM schemes was performed by using different combinations of QM cluster size and computational levels (Figure 68).[436] Irrespective of the particular ONIOM scheme, the gold atom in the T4 site was slightly more stable than that of the T1 site by at least 5 kcal/mol, with the precise adsorption energy depending on the level of theory employed. While the choice of both the low-level method and the QM cluster size affected the energy difference between these two sites, the trend remained unchanged. Vibrational frequencies for CO adsorbed at the OH group in the protonated form of mordenite (MOR) with Al^{3+} at T1 and T4 positions were 2177 and 2185 cm^{-1}, respectively, and this was in good agreement with experimental data (2171 and 2180 cm^{-1}, respectively) for CO/MOR at low coverage. On the basis of these theoretical results, the frequencies below 2149 cm^{-1} arise from CO molecules adsorbed on Au$_3$$^+$ clusters, while those above 2150 cm^{-1} are attributed to the polycarbonyls at the Au$^+$ cation.

ONIOM(B3LYP:UFF) in conjunction with a 10T/96T cluster model of BaNaY zeolite has been used to determine the intermediates/products of nitromethane, aci-nitromethane, acetic acid, CH$_2$COOH, HNO$_3$, HNO$_2$, H$_2$O, and

O$_2$NCH$_2$COOH dissociative adsorption and reduction.[437] It was found that the stability of the intermediates is affected by both the Al^{3+} arrangements around the active sites and the acidity of the adsorbate molecules.

Adsorption of different organic molecules and possible intermediates has also been modeled and compared to available experimental data. Fang et al.[438] used ONIOM(M06-2X:AM1) to model the stability of carbenium ionic intermediates in different zeolite frameworks: H-ZSM-5, H-Y, and H-β, represented by 8T/72T, 8T/84T, and 8T/80T models, respectively. According to these simulations, the carbenium ions could form ion pairs, alkoxy species, and π-complexes in the zeolite framework. As a common trend, ion pair structures were found to be more stable than the corresponding π-complexes and alkoxy species; this is due to the electrostatic stabilization of the ion pair structure and/or steric constraint destabilization in the other two cases. As compared to the H-ZSM-5 zeolite, H-Y and H-β structures exhibited a much higher capacity for accommodating the bulkier adsorbates.

In a similar vein, the interaction of two amino acids, glycine and L-alanine, with the 12T/128T fragment of H-ZSM-5 zeolite was modeled using ONIOM(MP2:UFF)// ONIOM(B3LYP:UFF).[419a] The most stable adsorption complexes corresponded to ion pair structures formed via proton transfer from the zeolite framework to the organic adsorbates, with adsorption energies of −31.3 kcal/mol (glycine) and −34.8 kcal/mol (L-alanine). Adsorption complexes could also be formed via H-bonding through the carbonyl and hydroxyl groups of the amino acids. Such structures were 5 kcal/mol less stable than the ion pair adsorption complexes. The same ONIOM scheme has been successfully applied for modeling the adsorption of light alkanes on mordenite (14T/120T, Al@T1) and faujasite (14T/120T, Al@T2). Calculated adsorption energies of ethane, propane, and n-butane were in very good agreement with the available experimental data.[419b]

Adsorption of ethylene at several divalent d-element (Fe^{2+}, Co^{2+}, Ni^{2+}, Cu^{2+}, and Pd^{2+}) extra-framework cations, and at monovalent cations (Cu$^+$, Ni$^+$, and Pd$^+$) in the pores of clinoptilolite, has been modeled with ONIOM(B3LYP:UFF) and 10−16T/76−100T models of the zeolite lattice.[426a] The adsorption of ethylene was accompanied by the activation of both C═C and C−H bonds, as the C−C distance was significantly elongated at the monovalent active sites (Cu$^+$, Ni$^+$, and Pd$^+$) by up to 0.069 Å. Adsorption of a series of alcohols and nitriles on ZSM-5 has been modeled using several different DFT-based methods with different models of the system (cluster model representation and periodic boundary conditions).[426d] ONIOM(B3LYP:MNDO) with an 8T/46T extended cluster model gave results very similar to those obtained using PBC models. The efficacy of ONIOM for modeling the adsorption process was demonstrated further by comparing the calculated frequencies of the zeolite acid sites and the adsorbate functional groups with the experimental IR data.

Several studies of probe molecule adsorption on metal/ metal−oxide surfaces have also been reported in the literature. The first benchmark study of ONIOM in modeling metal surfaces was reported by Tang et al.,[439] who employed ONIOM3(B3LYP/6-31G*:B3LYP/6-31G:LL) and ONIOM2-(B3LYP/6-31G:LL) (LL = AM1, or HF/6-31G), to model two representative clusters Li$_{21}$(12,9)H and Li$_{45}$(24,21)H, respectively. These systems were designed to simulate the adsorption of H on the 4-fold hollow site of Li(110). These two- and
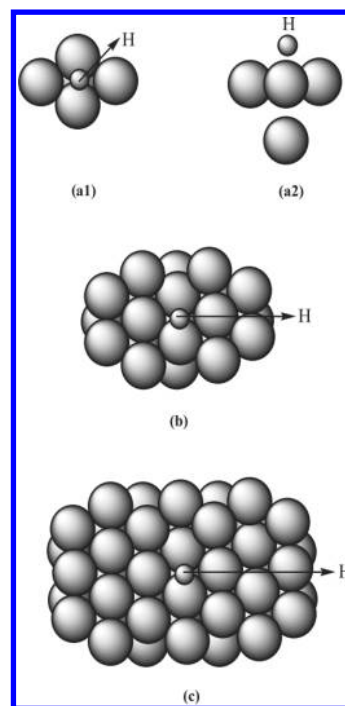
Figure 69. (a) Top and side views of small model system Li$_5$(4,1)H, (b) top view of intermediate system Li$_{21}$(12,9)H, and (c) top view of real system Li$_{45}$(24,21)H. (For Li$_{m+n}$(m,n), m and n represent the numbers of Li atoms in the top and subsurface layers, respectively.) Reprinted with permission from ref 439. Copyright 2000 Elsevier B.V.

three-layer ONIOM schemes are depicted in Figure 69a−c, respectively. As compared to full DFT calculations, the ONIOM method was both economical and reliable in modeling the metal surface. It was found that an appropriate high-level method, which includes electron correlation to describe the first nearest neighbor metal atoms around the adsorption site, was critical for accurate adsorption energies.

The adsorption of NH$_3$ at the isolated hydroxyl group of the silica surface was studied using an octahydrosilasesquioxane cluster model.[440] It was found that ONIOM(B3LYP:HF)
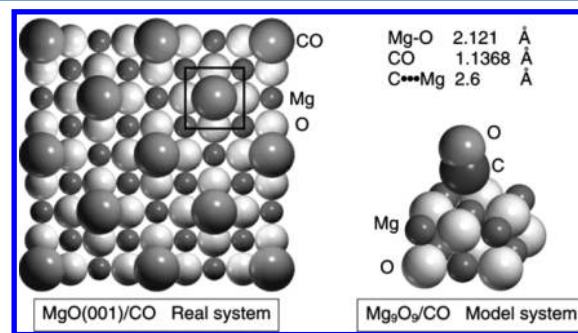
Figure 70. ONIOM2 scheme of real Mg(001)/CO and model Mg$_9$O$_9$/CO systems. Reprinted with permission from ref 444. Copyright 2002 Elsevier B.V.

reproduces well the structure and properties of the adsorbed NH$_3$ complexes on the silica surface. Similarly, the adsorption of water, acetate, and acetic acid on the tetrahedral and octahedral surfaces of clay minerals,[441] chemadsorption of small molecules (H$_2$, CO, CO$_2$, H$_2$O, and NH$_3$) on ZnO surface,[442] and the electronic properties and distribution of active sites on Au(100) surface[443] have been investigated using ONIOM with

large cluster models. In these studies, the ONIOM approaches were comparable with full-DFT or PBC results, and showed acceptable agreement with available experimental data. The size of the ONIOM layers and the theoretical level of each layer have also been discussed in detail, and these two aspects are very important for reproduction of the structure and properties of adsorbed molecules and the underlying surfaces.

Instead of using a large cluster model, Ugliengo et al. have investigated CO adsorption on MgO(111) using ONIOM-(MP2:B3LYP) approach (Figure 70).[444] The CO binding energy was estimated to be 12.7 kJ/mol, which was in good agreement with the experimental value, 13.5 kJ/mol. Similarly, CO adsorption and dissociative chemisorption of H_2O on (110) and (101) tetragonal zirconia surfaces was studied with ONIOM(B3LYP:UFF).[445] These studies demonstrate that the ONIOM method is a powerful and economical tool to investigate the structural and thermodynamics properties of surfaces.

5.3. Reaction Mechanisms in Zeolites and Similar Materials

Theoretical modeling has been successful in modeling reaction mechanisms involving small molecules in zeolites and other similar materials, and has enabled better understanding of their catalytic performances including detailed information regarding the reaction active sites. Usually two main types of active centers are used in zeolites or related oxide materials, the Brønsted acid centers (which enable isomerization, cracking, conversions, methylations, etc.) and exchanged cations.

Table 3 lists examples of ONIOM calculations using embedded cluster models to model reactions catalyzed by OH groups in the zeolite pores and channels. These reactions include protonation of organic species or hydrogen exchange with the zeolite framework,[423a,446] alkylation reactions,[419c,447] isomerization,[448] cracking,[420,449] conversion reactions,[414,446,450] and dehydration.[451] Acidity of the zeolite OH centers can be controlled by substituting Al with other elements like B and Ga, forming isomorphous structures.[447b,c,448b,452] Such structural modification has been theoretically investigated in the case of
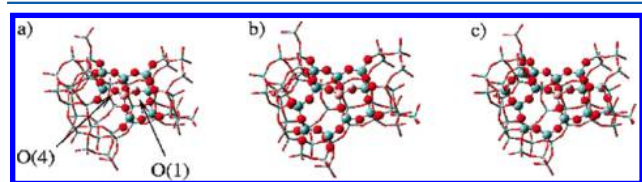
Figure 71. H-Y zeolite models applied in ONIOM calculations of proton transfer from O1 to O4 (labeled as O(1) and O(4)) using (a) 8T/53T, (b) 11T/53T, and (c) 16T/53T models. Reprinted with permission from ref 416. Copyright 2005 American Chemical Society.

H-ZSM-5, with the acidity being estimated by calculating proton affinity values, OH stretching mode, and NH_3 adsorption energy.[452] The theoretically predicted trend, B-ZSM-5 < Ga-ZSM-5 < Al-ZSM-5, is in good agreement with experimental observations. The importance of the Brønsted acid site strength was demonstrated on the example of ring-shift isomerization of *sym*-octahydrophenanthrene to *sym*-octahydroanthracene, which depends on both the acid strength and the framework pore structure.[448b] Therefore, the strength of the Brønsted acid site decreases in the order of Al−H-MOR > Ga−H-MOR > B−H-MOR. The weak acidity of B−H-MOR slows the reaction and decreases the catalytic activity of the zeolite.

Fermann et al.[416] have applied ONIOM(B3LYP:UFF) to model proton transfer in H-Y zeolite between the O1 and O4 oxygen atoms (Figure 71). To determine the dependence of the results on the size of the simulation model, these simulations varied the model size of both the embedded QM cluster and the full system. The QM cluster was enlarged from 3T to 22T, while the total size of the system was varied in the range of 23T (7 Å)–439T (19.9 Å). The size of the QM cluster was found to be critical for proper estimation of the reaction energy. The proton transfer energy of a small QM cluster consisting of only 3T/166T was only 1.8 kJ/mol. Increasing the QM region to 8T/166T gave rise to a higher reaction energy, 15.4 kJ/mol; that is, the proton transfer was sensitive to the atoms within about 5 Å of the reaction center. The activation energy of the process for 8T cluster embedded in 166T was 139.2 kJ/mol, and this is in agreement with the computational results of Sierka et al., who used the QM-pot approach to model the same reaction and reported a value of 100 kJ/mol.[40,453]

A theoretical study using B3LYP-D//ONIOM(B3LYP:MNDO) and an 8T/(112/76)T model of MOR has shown that the protonation of organic molecules depends on the pore confinement and the acid site strength.[446] Thus, for organic species smaller than the pore dimensions, for instance, ethylene in the 12-membered ring (12-MR) of MOR, the acid strength of the zeolite plays a key role in the protonation process. If the molecule fits well in the channel of the catalyst like propene in 8-MR channels, the effect of the pore confinement is predominant and compensates the weak acid strength in this channel. For bulkier organic molecules, however, steric repulsion in narrow channels destabilizes the system, and the protonation of such species selectively occurs only in 12-MR channels.

ONIOM(B3LYP:UFF) was successfully applied in modeling hydrogen reverse spillover on a tetrahedral Pd_4 cluster supported on a 6T/60T model of FAU zeolite.[454] The metal cluster was oriented with its base toward the 6T ring, and coordinated to the three O atoms oriented toward the center of the ring. A single hydrogen transfer from the zeolite to the metal cluster was observed to be an exothermic process, leading to the formation of stable Pd_4H species. The energy released in this process depends on the Al content in the zeolite framework. For instance, in the case of a high Si:Al ratio, the energy is above −60 kJ/mol, while high concentration of aluminum decreases the reaction energy to about −30 kJ/mol. In the case of zeolite structures with higher aluminum content, the stepwise transfer of the second or third proton is unfavorable.

The mechanism of dimethyl ether hydrolysis to methanol on amine-doped ZSM-5 (12T/128T model)[455] has been modeled at the ONIOM(M06:UFF) level. Two types of active centers were considered: zeolite hydroxyl groups and protonated/nonprotonated amine sites, formed via the doping procedure. Computational results provided the information required to predict the catalytic behavior of the modified zeolite materials. The hydroxyl active site showed the best catalytic performance for dimethyl ether hydrolysis, while the protonated amine site was considered to be inactive due to the very high activation barriers. Interestingly, the nonprotonated NH group favored the demethylation step in a stepwise mechanism. The formed methylammonium surface intermediate, however, was rather stable and blocked the active site.
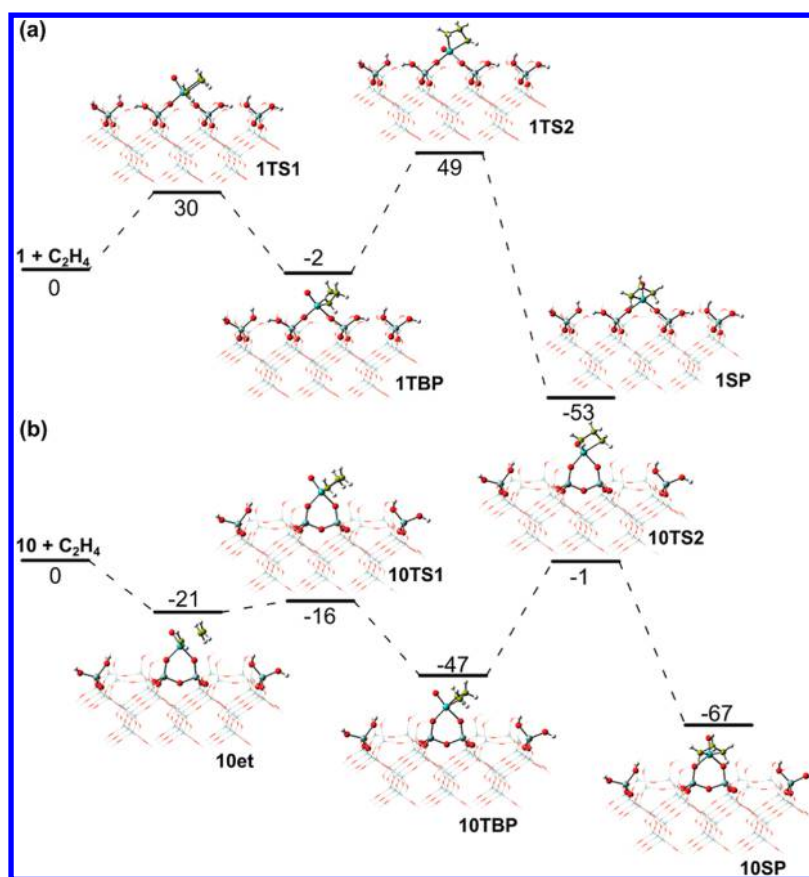
Figure 72. Potential energy surfaces of ethene metathesis at the four-coordinate Mo(VI) methylidene center on (a) fully hydroxylated and (b) partially dehydroxylated silica surfaces. Energies are in kJ/mol. Reprinted with permission from ref 459b. Copyright 2007 American Chemical Society.

Nie et al.[447] have applied ONIOM(B3LYP:UFF) to several alkylation reactions on H-β and ZSM-5 zeolites using 14T/116T and 12T/128T embedded cluster models. *tert*-Butylation of phenol in H-β[447b] undergoes as a concerted reaction, requiring coadsorption of the interacting species. For the methylation of 2-methylnaphthalene in ZSM-5,[447c] the stepwise path is kinetically favorable, where the methanol dehydration is the rate-limiting step, with a rather high activation energy of 41.6 kcal/mol.

ONIOM(M06-2X:PM6) with 12T/41T model of titanium silicalite-1 (TS-1) has been applied in modeling the hydroxyl-amine mechanism of cyclohexanone ammoximation.[456] The active species for the catalytic activity is Ti-OOH, and the reaction proceeds in a stepwise manner: catalytic oxidation of NH_3 molecule at Ti-OOH followed by noncatalyzed oximation of cyclohexanone outside the zeolite.

ONIOM(B3LYP:UFF) calculations suggest that Mg^{2+} exchanged Y zeolite catalyzes the carbonyl-ene reaction between formaldehyde and propylene.[457] The observed catalytic effect was rationalized by the stabilization of the formaldehyde/propylene coadsorption complex. The estimated reaction barrier in Mg-Y is 15.4 kcal/mol, and this is lower than that in Na-FAU,[458] 25.1 kcal/mol.

5.4. Other Heterogeneous Catalysts

Theoretical simulation is among the most powerful tools to explore reaction mechanisms catalyzed by metal/metal-oxide surfaces and related materials. As for zeolites, discussed above, the selection of the methods and model is critical if reaction mechanisms are to be understood reliably. Four- and five-coordinated Mo(VI) methylidene species, supported on fully hydroxylated and partially dehydroxylated silica surface, and their catalytic activity in ethylene metathesis were modeled at the ONIOM(B3LYP:HF) level.[459] The results show that four-coordinated Mo species supported on dehydroxylated surface
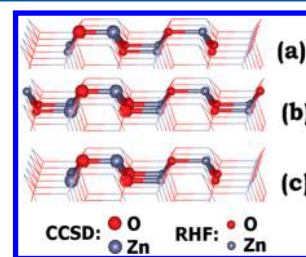
Figure 73. Schematic representation of ONIOM models used for modeling H_2 and H_2O dissociation on ZnO surface: (a) $(ZnO)_1/(ZnO)_3$, (b) $(ZnO)_3/(ZnO)_9$, and (c) $(ZnO)_3/(ZnO)_6$ layer configurations with n and m in $(ZnO)_n/(ZnO)_m$ corresponding to ZnO units in the high- and low-level layers, respectively. Reprinted with permission from ref 460. Copyright 2012 Wiley Periodicals, Inc.

are more active than the centers on fully hydroxylated surface. The barrier of the first step, ethylene cycloaddition to the active molybdenum center in the former case, is only 5 kJ/mol, which is 25 kJ/mol lower than that on the fully hydroxylated surface. On the other hand, five-coordinated Mo alkylidene sites are inactive in ethylene metathesis at low or moderate temperatures, because the barrier for ethylene cycloaddition exceeds 100 kJ/mol. On the basis of comparison between simulated and

experimental IR data, it was concluded that the four-coordinated Mo(VI) alkylidene species and the corresponding square pyramidal molybdacyclobutane forms are formed in experimental conditions (Figure 72).

ONIOM(CCSD:RHF:UFF) has been used to model H_2 and H_2O dissociation on ZnO.[460] Benchmark calculations with three models of the system (Figure 73), differing in the size of the inner and intermediate layers, suggest that the partitioning of the system and the size of the sublayers are the main influences over the energetics. The active centers were studied by employing a high-level method including the electronic correlation and polarization function (CCSD/6-31G*) to deal with the dissociation of H_2 and H_2O molecules.

Halls and Raghavachari[461] performed ONIOM(B3LYP/6-31G**:B3LYP/STO-3G) calculations to study the chemical reactions of H_2O and $Al(CH_3)_3$ on H/Si(111) surface. According to this study, a cluster model with sufficient size must be selected for investigating surface-catalyzed chemical reactions. Liu et al.[462] investigated the adsorption and dissociation channels of H_2O molecule on C-terminated SiC(001) surface with ONIOM(B3PW91:AM1:UFF). They established the adsorption preference and the dissociation pathways of H_2O molecule. ONIOM(B3LYP:HF) scheme was applied to study the activation barrier of the photon irradiation of benzene and chlorobenzene on Si(111) surface. The favorable reaction pathways obtained by the theoretical calculation explain experimental observations.[463]

ONIOM has been successfully applied in studying the adsorption of small molecules in metal or covalent organic framework materials (MOF and COF, respectfully).[464] CO_2 and CO adsorption on ZIF has been modeled by Hou et al.,[464a] who employed ONIOM(B3LYP:UFF). ZIFs represent a subfamily of MOFs built by MN_4 tetrahedral clusters, where M = Co, Cu, Zn, etc., and N corresponds to N atoms from an imidazolate linker. These materials have similar functionality to MOFs, but have higher chemical stability and greater structural diversity. They are usually utilized as gas capture materials. This theoretical investigation demonstrated that the functional groups of the imidazolate linkers have a significant effect on CO_2 uptake capacity of the material. CO_2 adsorption efficiency increases in the presence of electron-withdrawing groups, due to stronger interaction between the CO_2 adsorbate and the H atoms of the linker.

Another interesting feature of COF and MOF materials is hydrogen uptake capacity. The adsorption of multiple H_2 molecules in Li-COF has been modeled by using ONIOM(B3LYP:AM1).[465] According to these results, the adsorption of up to five H_2 molecules is exothermic, where the adsorption energy per H_2 molecule using MP2//ONIOM-(B3LYP:AM1) level decreases from −2.47 kcal/mol for a single adsorbed H_2 to −1.43 kcal/mol per molecule for five H_2 molecules.

Braga et al.[466] modeled the structure of IRMOF materials with a series of semiempirical and ab initio methods including ONIOM(HF:PM3). This ONIOM scheme reproduced the structure of the material, and was shown to be a powerful approach for describing adsorption and chemical processes occurring in the IRMOF cavities. This was demonstrated also by Cortese and Duca,[467] who studied the Knoevenagel condensation of benzaldehyde and ethyl-cyanoacetate catalyzed by IRMOF-3. ONIOM(B3LYP:UFF) calculations of the interaction between formaldehyde and propylene have been performed on two different catalysts, the Cu⁺ center in MOF-

11[468] and the Na⁺ center in FAU-type zeolite.[458] The respective activation energies for C−C bond formation were 24.1 and 25.1 kcal/mol, respectively. MOF-11 could therefore be potentially applied as a catalyst for the model carbonyl-ene reaction. The importance of the framework for the reaction mechanism has also been demonstrated with ONIOM(M06L:UFF) calculations, for example, the Mukaiyama aldol reaction catalyzed by Cu(II) in MOF-505 and ZSM-5.[469] This investigation demonstrated that both MOF-505 and Cu-ZSM-5 lower the reaction barrier, and are thus efficient catalysts in this case.

6. APPLICATIONS TO NANOMATERIALS

ONIOM has proved to be a powerful tool for probing the structure, properties, and reactivity of nanomaterials. Nevertheless, the application of ONIOM to organic and inorganic nanomaterials presents its own special challenges. For carbon nanomaterials, ONIOM partitioning requires cutting delocalized, conjugated π bonding systems. For inorganic nanomaterials, extended high-level regions and/or periodic boundary conditions are necessary to provide sufficient accuracy and realism. Here, we discuss examples of where ONIOM has advanced understanding regarding structure, chemical reactivity, and gas-phase absorption involving carbon nanomaterials, such as fullerenes and carbon nanotubes (CNTs), and inorganic nanomaterials, including transition metal/main group clusters and nanoparticles. We focus particularly on those investigations that specifically address the challenges, noted above, faced by ONIOM in modeling complex nanomaterials.

6.1. Carbon Nanomaterials

Carbon nanomaterials such as fullerenes, CNTs, and graphene form a cornerstone of modern nanotechnology and materials science. These nanomaterials are fundamentally related to each other; they are each composed entirely of sp²-hybridized carbon atoms, and it is only in the physical arrangement of these atoms that these allotropes differ. Thus, their properties and chemical behaviors are intimately related. Collectively, these materials possess outstanding physical properties, such as mechanical strength[470] and flexibility,[471] and excellent electronic[472] and optical properties.[473] Since their individual discoveries over the last three decades, they have continually provided new and exciting avenues of synthetic chemistry research.[474]

The uniqueness of C_{60} fullerene is reflected in its chemistry. For the purposes of understanding chemical reactivity, C_{60} is a nonoverlapping, octahedral arrangement of six individual pyracylene units, connected by a single reactive C=C double bond at the center of each unit. Many chemical reactions of fullerenes involve the scission of this double bond.[474a] The presence of pentagons in the C_{60} structure traps the position of these double bonds. Most chemical reactions of C_{60} are thus not selective, and this follows from the large number of equivalent reactive sites brought about by the molecule's high symmetry. This is the fundamental difference separating the chemical behavior of C_{60} from that of CNTs. However, although C_{60} and CNTs both consist purely of sp²-hybridized carbon atoms, the positive curvature inherent in their structures introduces a small amount of sp³ character.

The complexity inherent in carbon nanomaterial structure and chemistry makes it a fertile research area for computational chemistry. In the 1990s, the single largest hurdle in this respect was the physical size of the systems that needed studying;
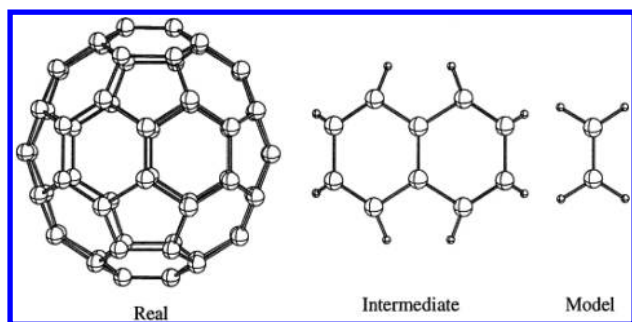
Figure 74. Extended conjugated systems such as C_{60} provide special challenges to the ONIOM method. However, partitioning the C_{60} cage with ONIOM3 as shown here enables near thermochemical accuracy. Reprinted with permission from ref 475. Copyright 1999 Elsevier B.V.

treating 60 atoms or more with correlated electron methods, or even DFT, was simply impractical. For this reason, many of the earliest successful computational studies of carbon nanomaterials were ONIOM-based. Because of this initial success, ONIOM remains a powerful technique in this context to the present day.

6.1.1. General Considerations. The application of the ONIOM technique to the study of reactivity and structure in extended π-conjugated carbon systems, such as C_{60} fullerene and carbon nanotubes (CNTs), is not trivial and presents special challenges. Partitioning the system into high/low regions invariably requires cutting delocalized carbon–carbon bonds. This need not be problematic; ONIOM3 with appropriate partitioning (Figure 74) has been shown capable of providing near thermochemical accuracy for bond energies in C_{60}.[475] ONIOM(G2MS:ROMP2/6-31G(d):ROHF/6-31G)
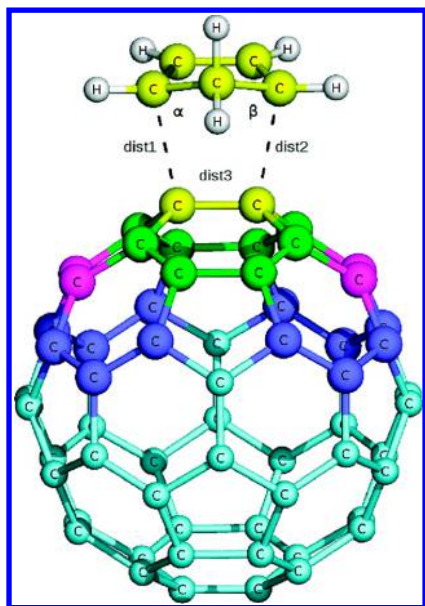
Figure 75. ONIOM2 partitioning schemes for studying reactivity in C_{60} complexes (in this case, Diels–Alder cycloaddition with cyclopentadiene) typically involve a high-level region consisting of an extended region of the fullerene cage. The inclusion of a pyracylene unit (yellow, green, pink, and blue carbon atoms) in the high level yields results within 1 kcal/mol as compared to full B3LYP calculations. Reprinted with permission from ref 477b. Copyright 2009 American Chemical Society.

predicts the $S_0 \rightarrow T_1$ energy to within 1 kcal/mol of the experimental value.[476]

More generally, the problem posed by these conjugated networks is somewhat alleviated by the fact that reactivity in these systems is typically highly localized, centering on the bound substituent and not the fullerene cage itself. The latter instead exerts influence via electron donation or acceptance. Such complexes typically consist of moieties complexing the C_{60}/CNT structure in a single location, or at most in a localized region. The nature of complexation can be either through covalent bonds or through dispersion interactions. Consequently, the high-level region must include a region of the C_{60}/CNT structure sufficiently large so that these effects and geometrical distortions in and around the reaction site are accounted for (Figure 75). Where possible, it is generally advised that the QM/MM boundary crosses C–C single bonds, and not the more problematic C=C double bonds. For C_{60}, a number of ONIOM2 examples featuring a high-level pyracylene unit have been reported, reflecting the generally accepted role of this unit in fullerene chemistry.[477] Applications of ONIOM2 to CNTs typically employ a pyrene unit[478] or larger sp^2-hybridized carbon fragments[224b,479] as the high-level region. In defective CNTs, a high-level region consisting of as few as nine atoms in the CNT has been reported.[480]
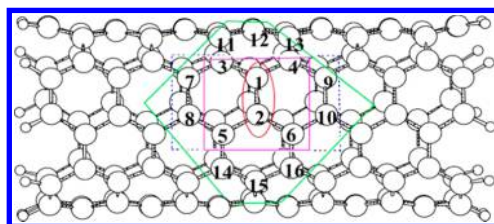
Figure 76. ONIOM2 partitioning schemes typically used for investigating atomic functionalization of carbon nanotubes: C_2 high level (red), C_{10} high level (blue), and C_{20} high level (green). Reprinted with permission from ref 486. Copyright 2004 Elsevier B.V.

6.1.2. Hydrogenation, Halogenation, and Oxidation of Carbon Nanotubes and C_{60}. Atomic functionalization reactions were among the first chemical reactions of CNTs to be studied with the ONIOM method. There is significant motivation for doing so; among the many potential applications of CNTs originally ascribed to them was their use in H_2 storage devices.[481] The mechanism and energetics of CNT hydrogenation were thus the focus of a number of early studies in this area. Similarly, the potential route toward controlling CNTs' electronic properties via oxidation[482] has driven research into understanding structure and reactivity in these complexes.

ONIOM approaches for studying atomic functionalization of single-walled CNTs (SWCNTs) are usually two-level. The high level typically consists of coronene,[483] pyrene,[484] or larger segments[484] of the nanotube sidewall; however, smaller segments have also been employed for investigations of atomic functionalization (Figure 76).[485] Bauschlicher et al.[483] have reported pathological problems regarding the optimization of low-level ONIOM regions for CNTs, which was seemingly independent of the specific MM force field employed (UFF is the standard choice in this context). Ultimately, the low-level MM region was used simply to constrain the geometry of the high-level QM region.
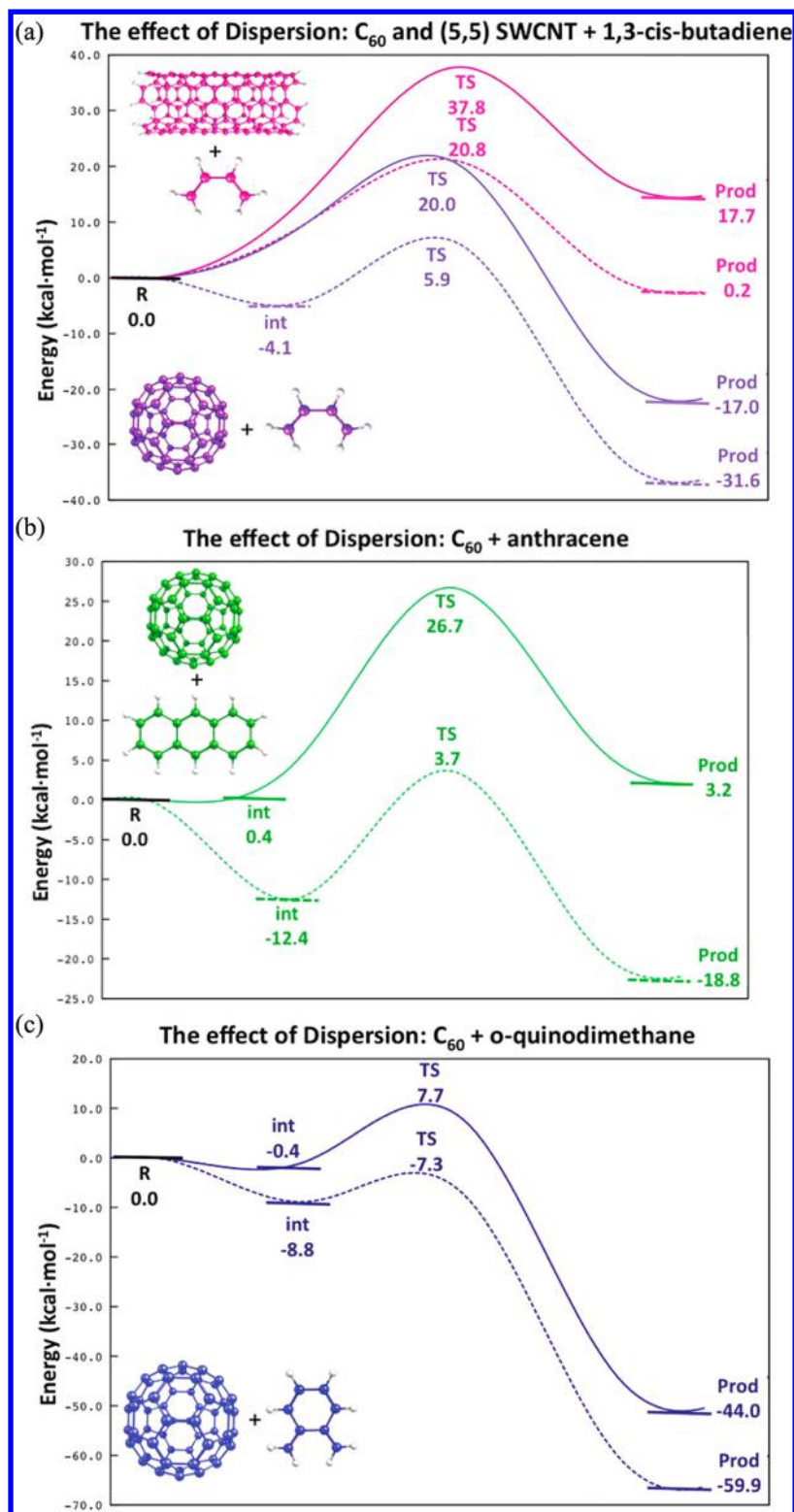
Figure 77. Inclusion of long-range dispersion in ONIOM calculations is critical for the study of Diels−Alder cycloaddition to C_{60} and SWCNTs. Reaction energy profiles (in kcal/mol) are shown for cycloaddition of (a) 1,3-*cis* butadiene to (5,5)SWCNT, (b) anthracene to C_{60}, and (c) *o*-quinodimethane to C_{60}, using ONIOM(B3LYP/6-31G(d):SVWN/STO-3G) (solid lines) and ONIOM(B3LYP/6-31G(d):SVWN/STO-3G) + dispersion (dotted lines). Reprinted with permission from ref 477c. Copyright 2011 American Chemical Society.

At low coverage, SWCNT hydrogenation is only slightly exothermic with respect to the SWCNT and H_2.[483a] 100% coverage is also unlikely on thermodynamic grounds. However, 50% hydrogen coverage was found to be the most energetically favorable density (ca. 4 wt %), and this is independent of the (*n*,*m*) chirality of the CNT.[483b,c] On the basis of ONIOM-(B3LYP/6-31G(d,p):UFF) calculations, Ng et al.[484] demonstrated that hydrogenation of SWCNTs itself consists of a three-step reaction mechanism, and that the barriers for this reaction are proportional to the reaction temperature. The

curved end-caps of SWCNTs are more reactive with respect to hydrogenation,[483c] as compared to the lower-curvature sidewall segments of the nanotube. Yang et al.[485] employed a variety of two-layer ONIOM approaches to investigate both exo- and endohedral hydrogenation of (5,0), (5,5), (7,0), and (9,0) zigzag SWCNTs. It was shown that hydrogen adsorption is dependent on tube diameter and chirality, and was also more favorable exo- to the SWCNT, as compared to endohedral adsorption. The latter is unsurprising, because the relative reactivity of the outside/inside of SWCNTs, stemming from the easier conversion of sp^2- to sp^3-hybridized carbon in the former case, is well established.

While hydrogenation of SWCNTs requires high coverage for favorable reaction enthalpies, fluorination of (5,5), (9,0), and (10,0) SWCNTs is energetically favorable even at low coverages.[483a] Using ONIOM(B3LYP/4-31G:UFF), the diffusion of exohedral F on SWCNTs is relatively labile, with barriers of 12.1 kcal/mol (as compared to 38.1 kcal/mol for H).[483a] Diffusion of F here occurs via a "hopping" mechanism, with F atoms moving between adjacent carbon atoms; no transition state corresponding to F atoms diffusing directly over hexagonal rings was observed.

The addition of ground-state O/N atoms to CNTs requires a surface crossing and involves a kinetic barrier (this is not the case however for $N(^2D)$ or $O(^1D)$). ONIOM calculations established the relative binding energies of O and N atoms on CNTs to be ca. 68 and 25 kcal/mol, respectively.[487] However, the first systematic investigation of ONIOM performance for oxidation of CNTs was reported by Kar et al.,[486] who compared different MO methods, the UFF and the AM1 method as the low-level ONIOM method. Because of the extensive rearrangement of electron density upon functionalization, these authors recommended that UFF and AM1 should be avoided, as they are incapable of describing polarization and charge transfer. By this rationale, these methods would presumably suffice for modeling physisorption to CNTs and fullerenes using ONIOM (we discuss such systems below, section 6.1.4). Nevertheless, a number of such investigations have been reported in the literature. For instance, Lu et al. investigated both the ozonization[478] and the epoxidation[488] of CNTs using ONIOM-(B3LYP/6-31G*:AM1). For armchair SWCNTs, ozonization was shown to have a directional preference, in regards to both kinetics and thermodynamics. The cycloaddition of O_3 to a (5,5) SWCNT was less kinetically favorable when the C–C bond perpendicular to the nanotube axis was attacked, as compared to the alternative C–C bond. However, ozonization of the latter bond was ultimately more thermodynamically favorable. Ozonization of monovacancy defect (5,5) SWCNTs has also been investigated using ONIOM calculations.[480] Irle et al.[489] employed ONIOM(B3LYP/6-31G(Od):B3LYP/STO-3G) in the first reported Raman spectrum of a pristine and oxidized SWCNTs, which consisted of a three-layer [12]-cyclacene model. The ozonolysis of C_{60} has also been characterized with ONIOM.[490] The structure and IR spectra of numerous C_{60}–O_3 adducts were characterized here using ONIOM(CCSD(T)/6-311G(d):B3LYP/6-31G(d)). In a similar manner, Yim et al. investigated the adsorption and desorption of O_3 onto/from (5,5) SWCNTs, and vibrational spectra of ozonized SWCNTs using ONIOM(B3LYP/6-31G*:AM1).[491]

6.1.3. Cycloaddition and Nucleophilic Addition Reactions.

The chemical functionalization of carbon nanotubes and fullerenes is a potential route to improving their notoriously poor aqueous solubility, enabling their physico-chemical properties to be exploited more easily. The complexation of C_{60} and SWCNTs with transition metals, or transition metal complexes, has also been studied with ONIOM on a number of occasions.[492] However, cycloaddition and nucleophilic addition are far more intensely studied branches of CNT/fullerene chemistry in this context.[474d] ONIOM is a widely used technique in this respect, and makes possible the accurate study of the complex reaction pathways involved in cycloaddition. Examples of ONIOM applications to CNT/fullerene cycloaddition reaction mechanisms abound. Specific examples include the [2 + 1] addition of carbenes and carbene analogues,[493] the [3 + 2] addition of transition metal oxide complexes[494] and azidotrimethylsilane,[495] and the [4 + 2] addition of azomethine ylide, ozone, nitrone, nitrile imine, nitrile ylide, nitrile oxide, diazomethane, methyl azide,[496] quinodimethane,[145] pyrrilodine,[497] and various dienes.[43b,477b] Similarly, the nucleophilic addition of sulfur-based compounds to C_{60}, including thiozone[479] and thiols,[477a] has been investigated using ONIOM, as has addition of diols to SWCNTs.[498] The reactivity of carboxylated SWCNTs has been the focus of several ONIOM studies.[114e,499] Amidation of SWCNT tips has also been studied using ONIOM.[500]

Osuna et al.[477b] performed extensive benchmarks of ONIOM2 calculations for the Diels–Alder cycloaddition of cyclopentadiene to C_{60}. Reaction energetics calculated using ONIOM(B3LYP/6-31G(d):SVWN/STO-3G) and ONIOM-(B3LYP/6-31G(d):AM1) using the high-level regions shown in Figure 77 were compared to full B3LYP/6-31G(d) results. The smallest high-level region, consisting of only two carbon atoms, was shown to be unsuitable irrespective of the levels of theory employed in high- and low-level regions. Somewhat unsurprisingly, ONIOM(B3LYP/6-31G(d):SVWN/STO-3G) results employing the high-level region including the pyracylene unit in the C_{60} cage and the reacting diene exhibited the smallest deviation (<0.5 kcal/mol) from the full DFT calculations. This was not the case when AM1 was employed in the low-level region, for which smaller high-level regions yielded lower errors. This was attributed to fortuitous error cancellations associated with the AM1 semiempirical method. In a subsequent investigation, these authors considered the inclusion of dispersion on the accuracy of the ONIOM-(B3LYP/6-31G(d):SVWN/STO-3G) approach to Diels–Alder cycloaddition of cyclopentadiene to C_{60}. It was concluded that the inclusion of long-range corrections is essential for reliable structures and energetics in Diels–Alder reactions on C_{60} and SWCNTs.[477c] In regards to the most suitable level of theory for the low-level region, it has been suggested that the UFF should be employed over the AM1 method, at least in the case of SWCNTs.[500a]

ONIOM has revealed the central role that SWCNT/fullerene geometrical curvature plays in determining the nature of cycloaddition chemistry. SWCNT curvature has been shown to be the critical parameter determining both cycloaddition reaction exothermicity and activation energies, with smaller diameter (higher curvature) SWCNTs exhibiting lower barriers and greater exothermicities than larger diameter (lower curvature) SWCNTs.[496b] ONIOM(B3LYP/6-31G(d):SVWN/STO-3G) calculations reveal equivalent diameter-dependence for the 1,3-dipolar cycloaddition of azomethine ylide onto Stone–Wales defective SWCNTs.[496c] However, the inverse trend was observed regarding the reaction barrier heights of retro-1,3-dipolar cycloaddition reactions.[496b] Osuna et al.[496a]

have shown that the barrier heights for cycloaddition of azomethane ylide and fulminic acid correlate exactly with the energy required to distort the carbon structure, whether it be C_{60}, curved graphene sheets, or SWCNTs. ONIOM has been used to elucidate this curvature-strain relationship for cycloaddition of azomethine ylide with carbon nanohorns[501] and graphene,[502] addition of diazomethane[503] to SWCNTs, and thiozonolysis of SWCNTs.[479] For acetone adsorption, the effects of curvature are dramatic; it will weakly physisorb on graphite (which has zero curvature), while strongly chemisorbing on SWCNTs.[504]

6.1.4. Gas-Phase Molecular Physisorption on Fullerenes and Carbon Nanotubes. The physical, chemical, and electronic properties of fullerenes and CNTs are determined by their structure. The use of fullerenes and CNTs as functional materials therefore often requires this structure to remain pristine, and this cannot be achieved through covalent functionalization as discussed above. The formation of covalent bonds invariably deforms the structure of the CNT or fullerene cage, and this can potentially result in the desired property of the material being altered, or lost completely. Physisorption of molecules to fullerenes and CNTs circumvents this issue, because it acts through noncovalent van der Waals and $\pi-\pi$ stacking interactions, which has minimal impact on either the geometrical or the electronic structure of the fullerene/CNT. This can be exploited in the production of functional CNT-based materials,[505] and also for separating CNTs on the basis of their chirality.[506]

These interactions are also important for understanding structure and properties of hybrid nanocarbon materials, such as functionalized C_{60} dimers,[507] C_{60}-OPV (organic photovoltaic) hybrid materials,[508] C_{60}-polyarene hybrid materials,[509] and pyrrolic amide-functionalized CNT materials that have potential for gas detection.[510] These materials also play a key role in biology and biochemistry, and ONIOM has been used on a number of occasions in this context. Parasuk et al.[511] used a combination of ONIOM, molecular docking, and molecular dynamics approaches to investigate the inhibition of HIV-1 protease using derivatives of C_{60}. Shukla and Leszczynski[512] have studied the interaction of C_{60} with nucleic acids such as guanine, comparing density functional and correlated wave function methods against ONIOM(MP2/6-31G(d):B3LYP/6-31G(d)). The C_{60}-guanine complex is the result of $\pi-\pi$ stacking interactions between a six-membered ring (C_{60}) and the guanine moiety. These authors noted that smaller basis sets such as 3-21G did not provide a bound complex, irrespective of the quantum chemical method used. This highlighted the need for efficient and accurate alternatives to correlated electron methods. Using MP2, the binding energy of this complex was calculated to be 8.1 kcal/mol, while ONIOM yielded 8.9 kcal/mol.

The weak interactions responsible for physisorption present special challenges for computational approaches. Typically DFT-based methods (either using the LDA or the GGA approximations) and semiempirical approaches are incapable of modeling them accurately; electron-correlation methods, such as MP2 and CCSD(T), are typically necessary for accurate structures and binding energies. The quintessential example of this problem is the benzene-dimer (see ref 513 and references therein).

In a series of studies,[486,499c,515] Kar et al. employed the "same level different basis set" to study functionalization and molecular physisorption to CNTs using MP2-based
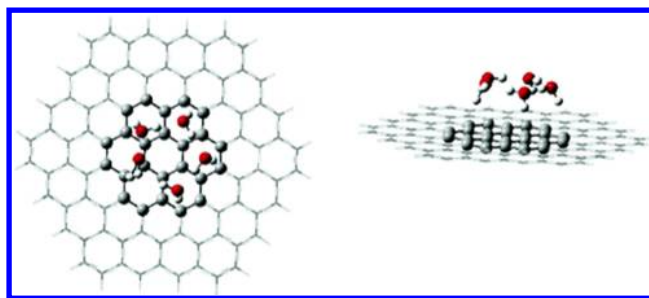
Figure 78. Structure of $(H_2O)_n$ adsorbed to a model graphite(0001) surface, optimized using ONIOM2(B3LYP:6-31+G(d)/DFTB-D). H-bonding between H_2O molecules dictates the structure of the entire adsorbed cluster. Spheres represent atoms included in the high-level calculation. Reprinted with permission from ref 514. Copyright 2005 American Chemical Society.

ONIOM2 calculations (typically with 6-31G or 6-31G(d) for the high level, and 3-21G for the low level). For benzene and naphthalene adsorption on (10,0) and (5,5) SWCNTs, $\pi-\pi$ stacking interaction was found to outweigh C–H$\cdots\pi$ H-bonding.[515] Both species preferentially absorbed parallel to the SWCNT structure. A number of different conformations with similar adsorption energies (<1 kcal/mol difference) were observed. This, combined with low diffusion barriers (1.3 kcal/mol for benzene), suggests that structure in such systems under standard conditions is dynamic.

Physisorption and dissociative adsorption of H_2O and H_2O clusters on graphite and fullerenes have been studied on a number of occasions.[516] ONIOM(B3LYP:6-31+G(d)/DFTB-D) predicts that H_2O binds extremely weakly to graphite (1.8 kcal/mol), and for the adsorption of $(H_2O)_n$ clusters, H-bonding between H_2O molecules largely determines the adsorbed cluster structure (Figure 78). These calculations also demonstrated that dissociative adsorption of H_2O on graphite, forming OH+H, can be either a single- or a multistep process when OH and H chemisorb onto carbon atoms in *para* positions relative to each other. Conversely, $H_2O \rightarrow OH + H$ is only a single-step reaction concerning *ortho* carbons. In either case, this process is highly endothermic, with prohibitive reaction rates. The fact that H_2O chemisorption on CNTs is observed experimentally at room temperature[517] indicates that the curvature of the sp²-hybridized carbon network leads to increased reactivity. ONIOM calculations of H⁺ and OH⁻ adsorption to SWCNTs indicate a highly exothermic process.[518] However, ONIOM and LMP2 calculations suggest that the H_2O-C_{60} interaction is quite weak,[516c] as are the interactions between a number of organic species and C_{60} (including dimethyl ether, dimethylamine, pyrrole, dimethyl sulfide, thiophene).[519] Similarly, a number of ONIOM studies of N_2[520] and O_2[521] adsorption on pristine and defective SWCNTs indicate very weak adsorption. Chemisorption of O_2 is energetically favorable; however, high barriers are involved in the absence of unterminated carbon dangling bonds.[521b] In the case of 1,3,5-triamino-2,4,6-trinitrobenzene (TATB), which interacts with SWCNTs primarily through $\pi-\pi$ stacking, ONIOM calculations[522] suggest that adsorption inside the SWCNT (i.e., *endo* adsorption, TATB@SWCNT) is more favorable than adsorption on the SWCNT itself (i.e., *exo* adsorption, TATB/SWCNT). For large diameter nanotubes, in which the confined TATB molecule is not geometrically strained, this difference can be large, approximately a factor of 2 for the (10,10) SWCNT.
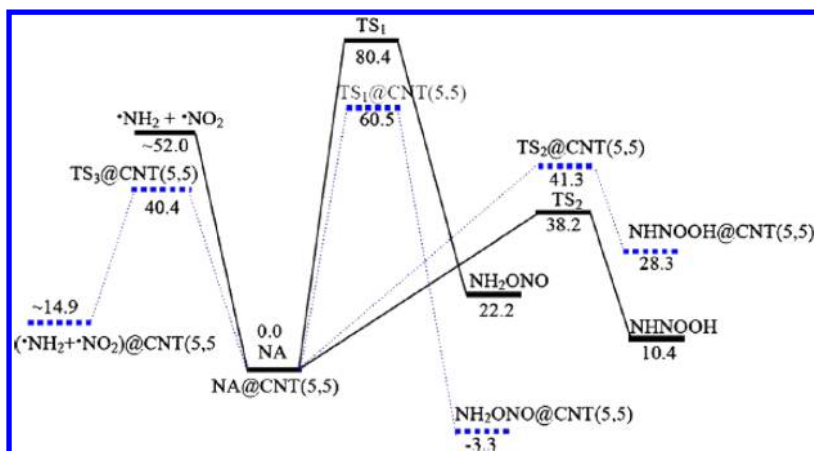
Figure 79. ONIOM(B3LYP/6-311++G(d,p):UFF) reactive potential energy surfaces for decomposition of methylnitramide in the gas phase (black, solid lines) and in a (5,5) SWCNT (blue, dotted lines). Transition state and intermediate structures are not shown here, but the effect of the SWCNT is evident by comparison of barrier heights and reaction energies with gas-phase values. "NA" stands for nitramide. Reprinted with permission from ref 536. Copyright 2011 Elsevier B.V.

For planar graphite, the kinetics of H_2O dissociative adsorption are significantly enhanced by the presence of structural defects in the graphite sheet, particularly mono-vacancy defects due to the presence of carbon dangling bonds at the reactive site (divacancy and Stone−Wales defects are less reactive in this respect).[516a] Xu et al. have reached similar conclusions regarding the physisorption and dissociative adsorption of CO_x and NO_x on graphite (0001), using ONIOM calculations.[523] Liu et al.[524] have also studied the interaction of NO_x at defect sites on SWCNTs, while Bauschlicher et al.[525] investigated CH_x adsorption on pristine SWCNTs.

6.1.5. Guest−Host Complexes: Effects of Confinement on Structure and Reactivity. The use of carbon nanomaterials, particularly CNTs, as nanoscale "reactors" shows significant promise for future applications. Molecules encapsulated within CNTs display peculiar and unexpected behavior, and establishing how and why this happens is a burgeoning field of research. For example, chemical reactivity and reaction mechanisms are altered,[526] physical properties can be changed (for example, liquid boiling points[527]), and UV/vis and IR spectroscopy of host molecules can be tuned,[528] or even masked completely.[529] The inner wall of the CNT never participates formally in bonding in these cases. Instead, it provides a highly constraining, electronic environment that polarizes the wave function of encapsulated species through electrostatic interactions; it is in some sense a "solid solvent".[530] ONIOM is therefore an ideal method for studying how confining molecules and materials inside CNTs changes their structure, reactivity, and properties, because it naturally takes these effects into account. It has been shown that the inclusion of electronic embedding in the ONIOM method is critical for studying UV/vis spectroscopy.[528]

This electronic environment has a distinct effect on encapsulated H-bonding and halogen-bonding;[531] both can be tuned toward stronger or weaker interactions, depending on the extent of intra- and intermolecular charge transfer, which in turn is determined by the field imposed by the surrounding SWCNT atoms.[532] ONIOM studies have also elucidated this phenomenon for inorganic and organic acids in macromolecular cage complexes.[533] Encapsulation of host molecules is not always a thermodynamically favorable process, and there

is an obvious influence of the SWCNT diameter in this respect. For example, ONIOM calculations show that encapsulation of 3,3′-diamino-4,4′-azofurazan inside a (6,6) SWCNT is endothermic ($\Delta E = 29.3$ kcal/mol), while for the (8,8) and (10,10) SWCNTs it is exothermic ($\Delta E = -38.0−33.6$ kcal/mol, respectively) and thus spontaneous.[534] Similar trends were observed for TATB, discussed above.[522]

While weaker bonds such as H-bonds are altered by encapsulation, this is not always the case with stronger covalent bonds. For example, ONIOM(B3LYP/6-31+G(d):UFF) calculations show that encapsulation of an azobenzene molecule inside a (8,8) SWCNT does not change its structure as compared to the gas phase.[535] Nevertheless, the relative energies of the *cis* and *trans* isomers of azobenzene are brought ca. 8 kcal/mol closer in energy relative to the gas-phase values. Indeed, the influence of encapsulation on chemical reactivity has been established using ONIOM calculations for a wide range of small molecules, including the isomerization and dissociation energetics of nitramine,[536] methylnitramine,[530,537] nitromethane,[538] mono- and dichloromethane,[539] and aliphatic amines.[540] The "solid solvent" effect (due to the encapsulating CNT structure) on long-range interactions is most pertinent to transition state structures, and so encapsulation can lead to altered chemical reaction pathways and reaction thermodynamics, as illustrated for the HONO-elimination pathway from nitramide in a (5,5) SWCNT (Figure 79).[536] This effect can be dramatic: for example, the production of $^{\bullet}NH_2$ and $^{\bullet}NO_3$ radicals from nitramide in the gas phase is barrierless and endothermic by 52 kcal/mol; this reaction inside a (5,5) SWCNT is endothermic by only 14.9 kcal/mol, but has a barrier of 40.4 kcal/mol.

6.2. Inorganic Nanomaterials

The ONIOM method is a powerful tool for the study of inorganic main group nanomaterials and metal clusters/nanoparticles, and has been shown to be a useful and accurate method for investigating site structures, equilibrium geometries, transition state structures, HOMO−LUMO energy gaps, and adsorption energies, etc., in these systems. However, intrinsic challenges remain when ONIOM is used to treat inorganic nanomaterials, because often the definition of high- and low-level regions is complicated and periodic boundary conditions are necessary. In this section, we discuss the application of
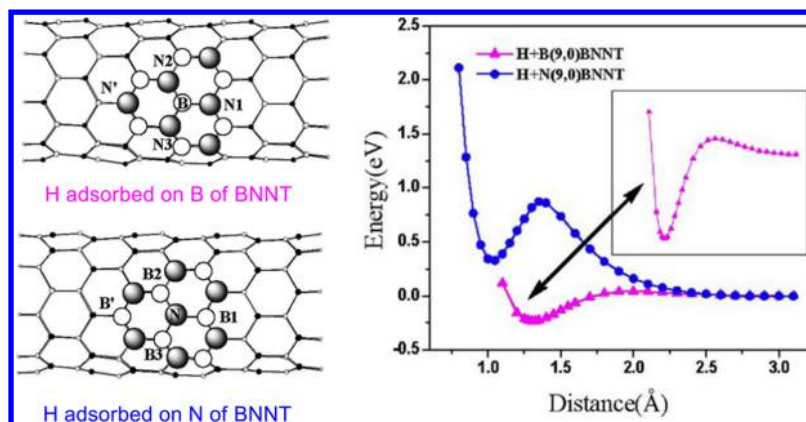
Figure 80. Adsorptions of hydrogen atoms on pristine boron nitride nanotubes (BNNTs). Reprinted with permission from ref 542. Copyright 2006 Elsevier B.V.

ONIOM to inorganic nanomaterials, highlighting these challenges and examples where ONIOM has been applied successfully.

6.2.1. Main Group Nitride Nanotubes. ONIOM methods are also widely applied in the study of main group nitrides nanomaterials. To evaluate the reliability of the ONIOM method in calculating adsorption energies, transition structures, change of HOMO–LUMO energy gaps, and equilibrium geometries, Ahmadi et al. carried out ONIOM studies on the interaction between NH_3 and N-enriched (A) or B-enriched (B) open ended boron nitride nanotubes.[541] ONIOM methods including B3LYP/6-31G(d) in the high-level, combined with various low-levels methods (AM1, PM3, MNDO, and UFF), were studied here. They suggested that the
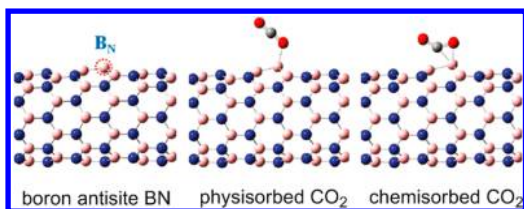
Figure 81. Physical and chemical adsorption states of CO_2 on boron antisite in boron-rich BNNT. Reprinted with permission from ref 543. Copyright 2011 American Chemical Society.

ONIOM is more reliable for the study of weak interactions while it should be applied cautiously for strong interaction cases. They also demonstrated that the reliability of ONIOM results was independent of tube length and diameter.

Li et al.[542] utilized ONIOM(B3LYP:AM1) to investigate the electronic structures of C-doped (9,0) boron nitride nanotubes (BNNTs) and hydrogen-decorated C-doped (9,0) BNNTs, and their adsorptions of hydrogen atoms (see Figure 80). The calculated adsorption energies for hydrogen atoms on different adsorption sites on BNNTs and C-doped BNNTs indicated that the C site of C-doped BNNT atom is the most favorable one for hydrogen atom adsorption. For pristine BNNTs, the boron sites are more likely to be adsorbed by hydrogen atoms.

Choi et al. studied the CO_2 adsorption on boron-rich boron nitride nanotube (BNNT) with ONIOM(ωB97X-D:6-31G(d)) calculations (see Figure 81).[543] They found that the boron antisite (B_N) in boron-rich BNNT can strongly adsorb CO_2, of which the adsorption energy is independent of tube diameter. Two adsorption states were proposed, that is, physical adsorption of linear CO_2 molecule on the B_N, and chemical adsorption of carboxylate-like distorted CO_2 on top of the B_N. Because the calculated chemisorption energy of CO_2 on BN was higher than the standard free energy of gaseous CO_2 at room temperature, they suggested that boron-rich BNNT could capture CO_2 effectively at ambient conditions.

Aluminum nitride nanotubes (AlNNTs) were studied by Ahmadi et al.[544] using ONIOM(B3LYP:AM1) to investigate the effect of surface curvature on the adsorption of NH_3, as shown in Figure 82. Their results suggested that the HOMO–LUMO energy gap of AlNNTs increases as the tube diameter increases, which is in contrast to semiconducting carbon nanotubes. The HOMO/LUMO interaction between NH_3 and AlNNTs increases as tube diameter decreases.
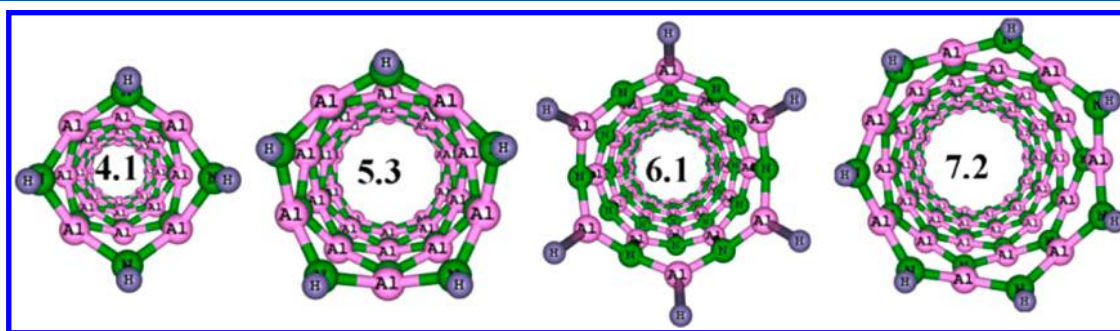
Figure 82. Models of (4,0), (5,0), (6,0), and (7,0) AlNNTs for the ONIOM studies of the adsorption of NH_3. Reprinted with permission from ref 544. Copyright 2011 Springer.

Cardelino et al.[545] presented an ONIOM(B3LYP:PM3) study on the adsorption and dissociation of trimethylindium on indium nitride substrates (InN). Later, they further investigated the dissociative chemisorption of trimethylgallium, trimethylindium, and ammonia on gallium (GaN) and indium nitride (InN) substrates with ONIOM(B3LYP:PM6).[546] With relative large substrate models, containing 44 units of GaN and 35 units of InN, they were able to confirm the validity of the model with experimental values by comparing the closest group III nitrogen bond distances and heat capacities. On the basis of these model substrates, they discussed adsorption and dissociation of typical adsorbates, such as the trimethylindium (TMI),[545,546] dimethylindium (DMI),[545] monomethylindium (MMI),[545] atomic indium (In),[545] trimethylgallium,[546] and ammonia.[546] These investigations also provided information on how the reaction progression was affected by coverage, pressure, and temperature.
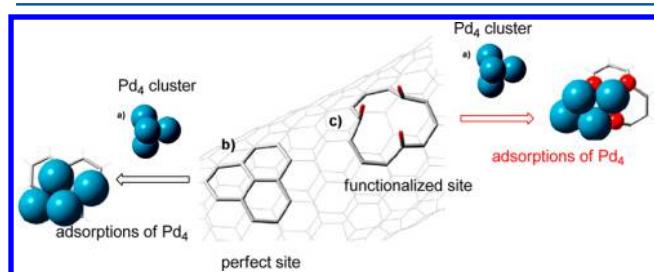
Figure 83. Adsorption of Pd nanocluster (4-atom) on normal site or functionalized site on SWCNT surface. Reprinted with permission from ref 548. Copyright 2010 Elsevier B.V.

6.2.2. Metal Nanoparticles. Ugliengo et al.[440] modeled the isolated hydroxyl group at the silica surface using the octahydrosilasesquioxane cluster with ONIOM. Although ONIOM(B3LYP:HF) was shown to give superior results, ONIOM(B3LYP:AM1) was cheaper and recommended for modeling very large silicate material structures.

Barraza-Jimenez et al.[547] used ONIOM(LSDA:UFF) to study the four-atom Au nanocluster supported by an (8,8) armchair carbon nanotube with and without defects. They found that the nanocluster anchored to the CNT in its pristine form had the longest bond length change. Binding energies were in agreement with the trend in structural changes. A higher binding energy corresponds to a smaller change in the cluster bond length. The incorporation of gold cluster decreased the LUMO of the CNT.

The binding of Pd nanoclusters on SWCNT surface was also studied by Prasomsri et al. with ONIOM(B3LYP:UFF) (see Figure 83).[548] These calculations demonstrated that oxygen-functionalized SWCNTs significantly enhanced the binding energy, due to electronic interaction of Pd atoms with oxygen at the defect sites.[548]

For larger metal cluster systems, ONIOM calculations performed well. A study of monolayer-protected gold clusters with ONIOM (BLYP:UFF) was reported by Banerjee et al.[549] Their structures calculated with ONIOM were readily compared to crystallographic data, indicating that the ONIOM approach was able to reach an accurate description of key structural and electronic signatures with low cost as compared to full quantum chemical treatment.

7. APPLICATIONS TO EXCITED STATES

In sections 3−6, 8, and 9, the capabilities of ONIOM for investigating a wide variety of ground-state phenomena have been demonstrated. However, the applicability of ONIOM is not restricted only to the ground electronic state. As briefly introduced in section 2.1.11, ONIOM can be applied in photochemistry, photophysics, and photobiology, where electron excitation and electronic excited state are involved, so long as the high-level and low-level methods are chosen appropriately and the change in excitation is localized in the model region.

In this section, we review ONIOM applications to photochemistry and photophysics (i.e., optical spectra, excited-state properties, and excited-state reactions, etc.) in a variety of systems, including organic molecules, solvated molecules, nanostructures, bulk phases, and crystal surfaces. ONIOM applications in photobiology will be discussed in section 9. Considering the large amount of literature reports, in this section, we mainly review the representative ONIOM studies either featuring new fields of application or contributing to excited-state computational schemes.

7.1. Applications in Absorption and Emission Spectra

Calculating excitation energies is one of the most common tasks required in excited-state applications. Because of geometrical strains and electrostatic interactions, the surrounding environment generally has a significant influence on excitation energy. Considering environmental effects explicitly in the large systems is beyond the capability of most excited-state QM

Table 4. Adiabatic $S_0 \rightarrow T_1(\pi, \pi^*)$ Excitation Energy (in kcal/mol) of Cyclopentene and Norbornene Calculated with Various Full MO and ONIOM Schemes[a]

full MO method		cyclopentene		norbornene
HF		47.6		43.4
B3LYP		72.1		68.7
MP2		74.8		73.4
MP3		70.5		67.9
MP4		70.3		67.6
CCSD(T)		72.0		69.5
G2MS		78.4		76.1

ONIOM method	C_2 model	C_4 model	C_2 model	C_4 model
MP2:HF	74.8	74.2	71.1	72.9
MP3:MP2	71.4	70.6	69.8	68.2
MP4:MP2	71.7	70.4	70.1	67.9
CCSD(T):HF	73.1	71.2	69.7	69.1
CCSD(T):MP2	73.6	71.9	72.0	69.7
G2MS:HF	80.1	77.6	77.1	76.0
G2MS:MP2	80.5	78.3	79.4	76.5
G2MS:MP3	79.5	78.2	77.5	76.2
experiment	>80		72.3	

[a]Adapted with permission from ref 550. Copyright 1996 Elsevier B.V.

methods. However, ONIOM can be used to calculate excitation energies between different electronic states in large molecular systems.

Depending on the leaving and targeting states, electron transition (i.e., $E^{*,\text{ONIOM}} - E^{\text{ONIOM}}$) may correspond to light absorption or light emission processes. The former can be calculated using the ground-state geometry, while the latter requires an excited-state geometry. Thus, geometry optimiza-

tion needs to be performed with the excited-state ONIOM method for the latter case.

7.1.1. Absorption Spectra of Organic Molecules in the Gas Phase.

The first ONIOM study on excited states was reported by Froese et al.[550] Adiabatic $S_0 \rightarrow T_1$ excitation energies for cyclopentene and norbornene, as well as $S_0 \rightarrow T_{1,2}$ energies for a series of enones, were investigated using several ONIOM(QM:QM) combinations. The calculated triplet electronic states in this case were the lowest states in different space symmetry, and, therefore, no excited-state methods were needed. As seen in Table 4, several accurate correlated methods (MP2, MP3, MP4, CCSD(T), and G2MS) were used as the high level, which was combined with HF, MP2, and MP3 in the low level. For both systems, the excitation of the π,π^* state in alkenes and the n,π^* and π,π^* states of the enones were essentially localized in the model systems, and the errors of ONIOM excitation energies were usually within several kcal/mol. For some cyclic alkene real systems (cyclopentene and norbornene), ONIOM calculations using a larger 2-butene (C4) model system gave better results than the smaller ethylene (C2) model system, because the C4 model better represents the delocalized electronic structure of the real system, especially for the triplet state. While using the same acrolein model system in different enones (real system), the substituent shifts are caused by changes of the geometry and/or the electronic structure. In general, ONIOM(G2MS:HF) and ONIOM(G2MS:MP2) agree well with full QM calculations and experiments. This pioneering calculation opened new opportunities for excited-state calculations.

In a similar vein, Caricato et al.[551] reported an ONIOM-(QM:QM) benchmark study on vertical excitation energy calculations of small organic molecules, with the aim of identifying less expensive methods that accurately approximate EOM-CCSD results. EOM-CCSD is one of the most accurate methods for describing single-electron excitations. However, applying this method to systems with more than 10−15 heavy atoms is currently impractical, due to its large computational cost. In ONIOM(EOM-CCSD:QM) calculations, the total CPU time is primarily governed by the EOM-CCSD calculation on the model system, with various approximate excited-state methods (including CIS, TD-HF, TD-DFT) used as low-level approaches. Among the various combinations that were considered, Caricato et al. suggested ONIOM(EOM-CCSD:TD-DFT) to be one of the best combinations balancing accuracy and computational cost, giving a RMS error in vertical excitation energies of 0.06 eV (with respect to the conventional EOM-CCSD). Caricato et al. also emphasized the importance of defining a proper model: the model system should contain the group mainly responsible for the excitation, but increasing the size of the model system substantially beyond that provides no notable improvement in accuracy. Thus, ONIOM is in general able to accurately approximate the excitation energy computed with a computationally expensive high level of theory (such as EOM-CCSD), provided that this condition is met.

It is necessary to emphasize here that for excited-state ONIOM(QM:QM) calculation in which electron excitation is not localized in the model region, both the high- and the low-level excited-state QM methods must model the same excited state. Unfortunately, it is easier to say than to evaluate because in most cases carrying out high-level excited-state calculation for full system is computationally prohibited. Probably some knowledge about the quantum chemistry models and their
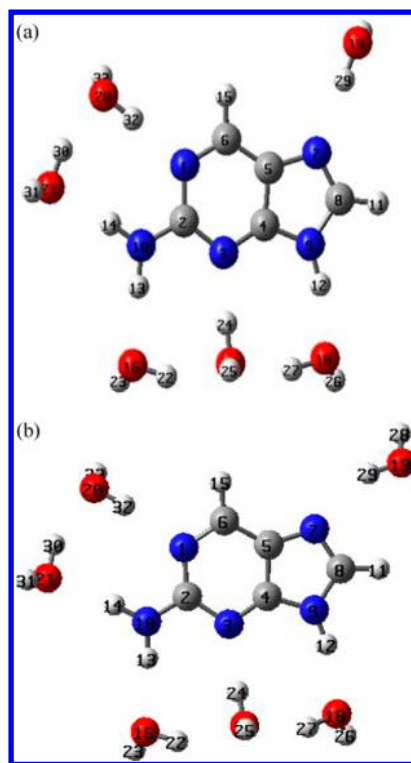
Figure 84. Orientations of 2Ap water cluster for (a) the ground state by B3LYP/6-31++G(d) level and (b) the lowest-energy excited states by CIS/6-31++G(d). In ONIOM(B3LYP/6-31++G(d):PM3) calculation, 2Ap was taken as the model system, and six water molecules were calculated at the low level (PM3). Reprinted with permission from ref 552. Copyright 2004 Elsevier B.V.

application areas, along with chemical intuition, are the perquisite for such applications.

7.1.2. Absorption and Emission Spectra in Solution.

As introduced in section 2.1.10 (and will be shown in section 8), polar solvents generally have a large influence on optical spectra. To accurately simulate absorption and emission spectra, implicit solvent models (such as COSMO solvent model, polarizable continuum model (PCM), etc.) or explicit solvent models have to be used.

Zhang et al.[552] investigated microsolvation effects on the vertical and adiabatic excitation of 2-aminopurine (2Ap) using ONIOM(TD-B3LYP/6-31++G(d):PM3). The optimized geometries of 2Ap, in both the ground and the first excited states, interact with six water molecules by H-bonding (Figure 84). Therefore, implicit solvent models are incapable of describing the interaction between solute and solvent molecules in this case. Two-layer ONIOM calculations of Zhang et al. showed that the first and second lowest-energy singlet excitations in 2Ap explicitly solvated with a water cluster correspond to $\pi \rightarrow \pi^*$ and $n \rightarrow \pi^*$ excitation, respectively. Their computed vertical excitation energies, 4.29 and 4.43 eV, are in good agreement with the reported experimental result (4.11 and 4.46 eV). In addition, ONIOM-predicted fluorescent emission energy (from the S_1 state), 3.87 eV, is also comparable with reported experimental and theoretical results. Zhang et al. suggested that ONIOM with TD-B3LYP/6-311++G(d) as a high-level method can provide good results for excited state and spectroscopic properties of 2Ap in the condensed phase.

Highly charged anions in solution are more difficult to describe computationally than monovalent anions or neutral
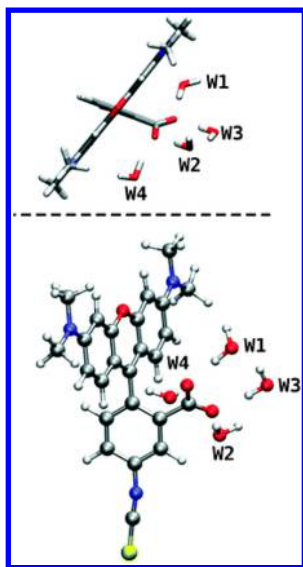
Figure 85. Ground-state optimized structure of TRITC interacting with 4 water molecules optimized at the QM level. Reprinted with permission from ref 554a. Copyright 2010 The Royal Society of Chemistry.

Figure 86. (a) Optimized structure of isolated *s-cis* β-carotene showing bond labeling and sketch of β-carotene structure inside (12,8) SWCNT optimized including (b) or not including (c) dispersion corrections. Reprinted with permission from ref 555. Copyright 2013 American Chemical Society.

molecules. Tossell reported the UV–visible absorption spectra of polysulfide anions in aqueous solution using ONIOM.[553] ONIOM(CIS/6-311+G(2d,p):CIS/6-31G*) calculations were performed on $S_4^{2-}\cdots 22(H_2O)$ cluster, in which S atoms were treated as the model system. The vertical excitation energy, 3.6 eV, was 0.2 eV higher than the experimental value. ONIOM results in this case were quite similar to CIS COSMO results for $S_4^{2-}\cdots 4(H_2O)$, leading the author to suggest that larger explicitly solvated clusters should be used to replace continuum solvent.

Implicit solvent and explicit solvent models, in some cases, can be combined to describe the contribution of both electrostatic effects and direct solute–solvent interactions. An ONIOM-PCM study of absorption and emission spectra of a fluorescent dye, tetramethyl-rhodamine iso-thiocyanate (TRITC, Figure 85), was reported by Pedone et al.[554] They found the B3LYP functional, coupled with mixed explicit/implicit solvent models, ONIOM(TD-B3LYP/N07D:MM)-PCM, reproduced the observed red shift between water and ethanol solvents, and the Stokes shift between absorption and emission spectra. The S_1-S_0 fluorescence spectra, obtained from several ONIOM calculations of sampled molecular configurations, showed a Stokes shift (32.4 nm), in good agreement with experimental data (25.0 nm).

7.1.3. Absorption and Emission Spectra in Encapsulated Nanostructures. The use of ONIOM in studying ground-state structure of molecules encapsulated in nanostructures, such as CNTs, was discussed in the previous section. Here, we build on this discussion to include applications regarding excitation energies and UV–Vis spectral calculations. Using ONIOM(TD-DFT/L:TD-DFT/S), where L stands for large basis sets and S stands for small basis sets, García et al.[555] studied the confinement effects on the electronic structure of a dye, β-carotene, encapsulated in a SWCNT (Figure 86), focusing on optical absorption spectra changes. ONIOM(TD-CAM-B3LYP/6-31+G(d,p):TD-PBE-D/6-31G(d)) predicted an intense excitation at 2.17 eV (571 nm), underestimating the energy of absorption maxima by ∼0.25 eV. Nonetheless, the computed bathochromic shift, 0.22 eV, is in near-perfect
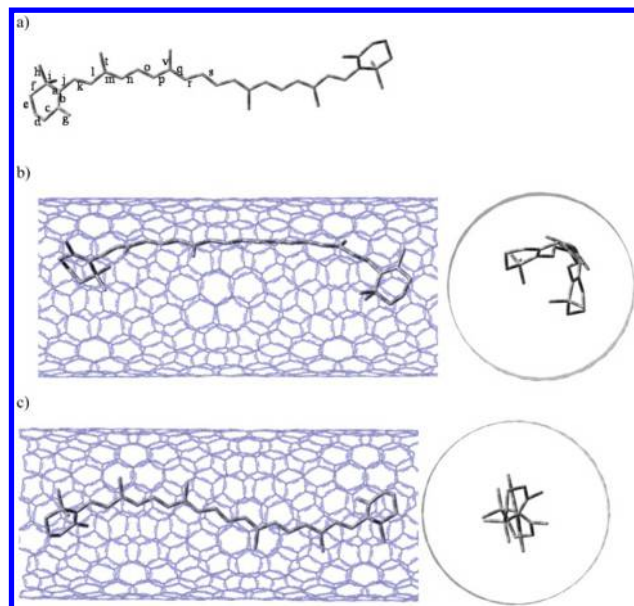
agreement with the experimental value (0.24 eV). The shifts in absorption energies were ascribed to both geometrical and polarization effects. These calculations demonstrate ONIOM's ability to reproduce the essential physics required to describe such complex host–guest interactions.

Wang et al., in a joint experimental and theoretical study,[556] investigated the structure and absorption wavelengths of inclusion complexes (Figure 87) of various spiropyrans (SPs) in the cyclodextrin cavities of the β-cyclodextrin polymer (CDP). Vertical excitation energies computed with ONIOM-(TD-BHandH/6-31+G(d,p):PM3) are consistent with the experimental spectra.

Similarly, Tzeli et al.[557] investigated confinement effects on absorption and emission spectra of encapsulated stilbene in two different capsules (labeled as 1·1 and $1\cdot2_4\cdot1$, Figure 88) using ONIOM(DFT:PM6) and ONIOM(TD-DFT:PM6). To obtain the emission spectrum of encapsulated stilbene, the optimization of the excited-state geometry of *trans*-stilbene within the cage is necessary, and therefore the ONIOM method must be used. As compared to the emission spectrum of free *trans*-stilbene, the emission spectrum of *trans*-stilbene with the presence of the $1\cdot2_4\cdot1$ cage is hardly changed. With the 1·1 cage, however, fluorescence is quenched, with the emission spectrum having no significant intensity above 300 nm. The local minima of *trans*-stilbene in the S_1 state with or without the $1\cdot2_4\cdot1$ capsule are both located ∼0.6 eV above the conical intersection. In the 1·1 cage, the relaxation of the twisted S_1 geometry goes directly to the S_1/S_0 conical intersection. Meanwhile, the absorption spectra of *trans*-stilbene with or without the $1\cdot2_4\cdot1$ cage are similar, because the S_0 geometry of *trans*-stilbene inside the $1\cdot2_4\cdot1$ cage remains unchanged. The absorption spectrum of *trans*-stilbene in the 1·1 cage shows only a small blue shift (8 nm) in the absorption maximum (λ_{max}) as compared to free *trans*-stilbene, with the S_0 geometry of *trans*-stilbene inside the 1·1 cage having the two phenyl groups twisted by about 45°.

Figure 89. (a) Scheme of the displacements in x and z directions for the case of five perylene pairs. (b) Scheme of the displacements in y and z directions for the case of five perylene pairs. The center of mass of the central dimer is shown in both schemes. In the ONIOM scheme, the central pair (in light gray and gray) is the high-level layer, and the black perylene pairs are the low-level layer in the same configuration as in the R-crystal. Reprinted with permission from ref 558. Copyright 2008 American Chemical Society.

Figure 87. Schematic structures for (a) SPs, (b) CDP, and (c) SP/CDP. Reprinted with permission from ref 556. Copyright 2012 Elsevier B.V.

7.1.4. Absorption Spectra in Crystals. Velardez et al.[558] reported the structures of the ground and excimer states of perylene pairs in vacuum, as well as in a crystal structure (Figure 89), and their spectroscopic properties for the most

stable configurations. The vertical excitation energies for absorption and emission were obtained using ONIOM(TD-B3LYP/6-31G*:TD-B3LYP/3-21G*). The absorption maxima were in line with the experimental value for the α-crystal at room temperature. These results suggested that the DFT, TD-DFT, and ONIOM procedures are adequate for estimating the vertical excitation energies and structures of the perylene excimer in both vacuum and crystal environments.

Recently, Yang et al.[559] applied ONIOM(TD-PBE0:UFF) to investigate the photoluminescence and carrier transport properties of two bow-shaped thiophene compounds. Opti-
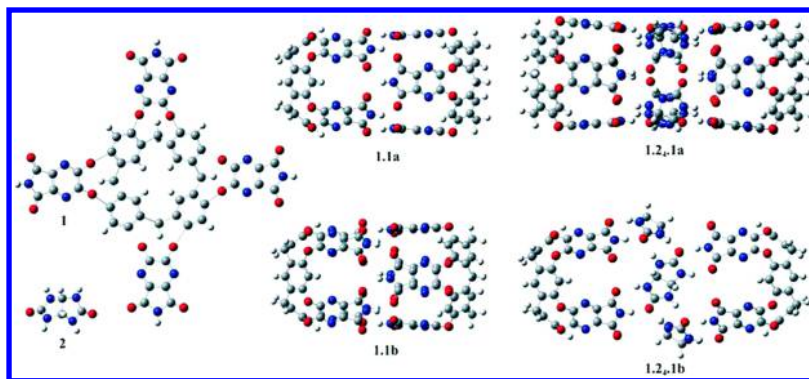
Figure 88. Structures of the cavitand (1) and glycoluril (2) components and structures of the cages 1·1 and 1·2$_4$·1. H atoms = white spheres, C = gray spheres, O = red spheres, and N = blue spheres. Reprinted with permission from ref 557. Copyright 2012 American Chemical Society.

mized geometries of the single-molecule and the solid-phase models were shown to have large deviations. The calculated vertical excitation energies, 56 and 20 nm, respectively, were red-shifted with respect to the experimental values. The obvious blue shifts of absorption and emission spectra in solid phase, as compared to the single molecule, were
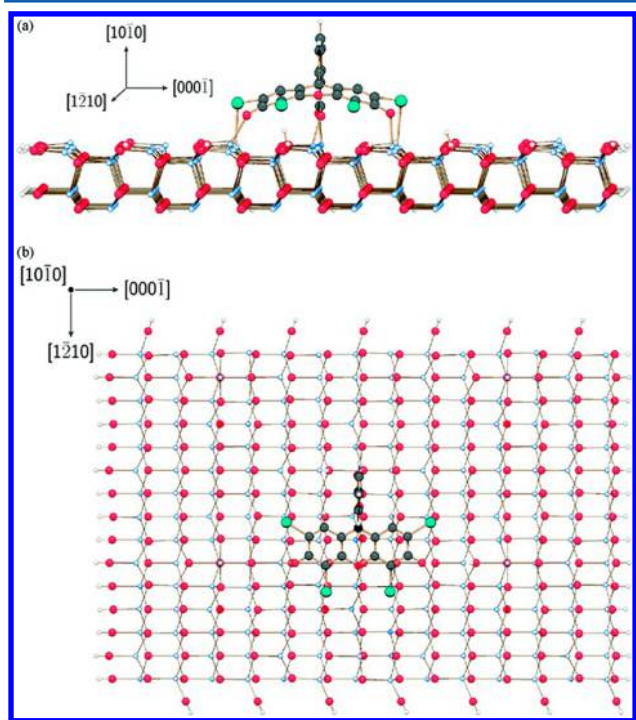
Figure 90. Side (a) and top (b) views of the 530-atom cluster used for UV−vis spectra simulations: carbon, bromine, zinc, oxygen, and hydrogen atoms are black, cyan, red, light blue, and white balls, respectively. Reprinted with permission from ref 114b. Copyright 2009 American Chemical Society.

postulated to arise from intermolecular interactions in the former.

Very recently, Mutai et al.[560] investigated the influence of intermolecular interactions on the solid-state luminescence of 6-cyano-2-(20-hydroxyphenyl)imidazo[1,2-*a*]-pyridine (6CN-HPIP) using ONIOM. In their calculations, they employed two finite cluster models for 2-O, 2-Y, and 2-R (labels adopted from ref 11, corresponding to three different crystal forms with bright colors, orange, yellow, and red), respectively; one is labeled as a monomer (one keto 6CN-HPIPs in S_1 (TD-DFT):16 enol 6CN-HPIPs in S_0 (PM3)), and another is labeled as a dimer (a pair of a keto and an enol (TD-DFT): 15 enols 6CN-HPIPs in S_0 (PM3)). The ONIOM results using these two models indicated that the dimer interactions between the keto form and the enol form, and not the perturbations from the surrounding molecules, play the dominant role in determining the emission color in the crystalline state.

7.1.5. Absorption Spectra on Surfaces. Labat et al. investigated eosin-Y (EY) loaded ZnO thin films (Figure 90), which are the basic components of a dye-sensitized solar cell (DSSC), using periodic DFT calculations.[114b] Vertical excitation energies for both the isolated EY (using TD-PBE0/6-31+G(d,p)) and the EY adsorbed on ZnO (using ONIOM-(TD-PBE0/6-31+G(d,p):SVWN/LANL2)) exhibited large discrepancies with respect to experimental data, implying the high-level calculation may not describe the electron excitation of the

model system properly. More recently, Labat et al.[561] investigated the ruthenium polypyridyl/TiO$_2$ system using periodic DFT, with the aim of understanding absorption phenomena taking place at the dye/semiconductor interface in DSSCs. It was found that ONIOM(PBE0/6-311G-(d,p):SVWN/LANL2) significantly underestimated the band at lower energy, with a computed maximum at ∼694 nm with respect to the experimental value (544 nm). The authors concluded that solvent effects are necessary to calculate accurate excitation energy for ruthenium-based molecular dyes adsorbed on surfaces.
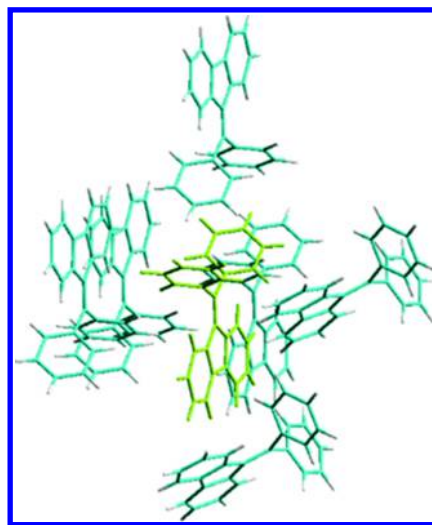
Figure 91. Solid-phase model. Single centered DPDBF molecule with the six nearest surrounding molecules is depicted. Reprinted with permission from ref 562. Copyright 2011 American Chemical Society.

7.2. Photophysical Deactivation and Photochemical Reactions

The ONIOM method can be used to describe the potential energy surfaces of photoreactions, which may involve both photophysical deactivation and photodecomposition via internal conversion or intersystem crossing. ONIOM calculations can also consider solvent effects and encapsulation effects on photoreactions of organic molecules. Here, we review the applications of ONIOM in photophysical and photochemical reactions.

7.2.1. Nonradiative Decay and Photochemical Reaction of Organic Materials in Solid Phase. Different fluorescence quantum yields between solution and solid phases for aggregation-induced emission (AIE) molecules indicate that nonradiative processes play an important role in luminescent characteristics.[114b,562] Li et al.[562] studied an experimentally AIE-active molecule, diphenyldibenzofulvene (DPDBF) (Figure 91), in the solid phase using ONIOM(DFT:UFF). These ONIOM calculations predicted that the nonradiative rate constant is 3.816×10^{10} s^{-1} in the solid phase. In the solution phase, their calculated results agreed with previous theoretical data.[563]

The AIE mechanism of the same molecule has been investigated by another group.[564] At the ONIOM-(CASSCF:UFF) level of theory, Li and Blancafort rationalized the solid emission of DPDBF by using a CI mechanism instead of a Fermi golden role approach. The energetically reachable S_1/S_0 CI in solvent is no more accessible in solid due to
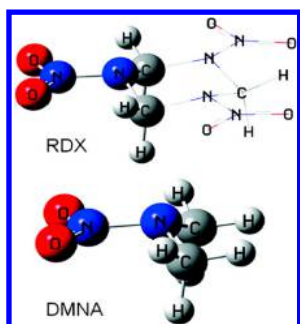
Figure 92. Schematic structures of RDX and DMNA. Balls: the QM region of RDX. Wire frame: the MM region. Reprinted with permission from ref 566. Copyright 2011 American Chemical Society.

restriction of bond rotation; therefore, radiationless decay to the ground state is blocked and DPDBF becomes emissive.

ONIOM(TD-DFT:DFT) applications on photochemical reactions in molecular crystal, including excited-state intramolecular proton transfer (ESIPT) process and photoisomerization reactions, were reported by Morrison et al.[81] A novel ONIOM implementation, in which TD-DFT and plane wave DFT were chosen as high- and low-level methods, respectively, was introduced in molecular dynamic simulation in molecular crystal phase.

7.2.2. Nonradiative Decay of Energetic Materials in the Gas Phase. Following the decomposition of energetic
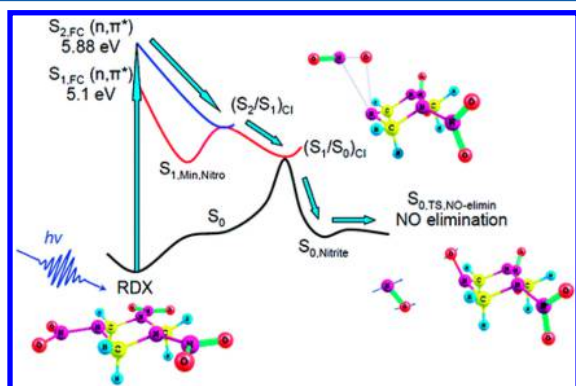
Figure 93. Schematic potential energy surfaces of RDX computed at the ONIOM(CASSCF:UFF) level of theory. Blue arrows indicate the unstable normal mode of vibration associated with the respective transition state. Adapted with permission from ref 566. Copyright 2011 American Chemical Society.

materials, such as cyclotrimethylenetrinitramine (RDX, Figure 92), the only product observed experimentally was nitric oxide (NO), which was rotationally cold (20 K) but vibrationally hot (~1800 K).[565] Bhattacharya et al.[566] used ONIOM to investigate the decomposition reaction mechanism of isolated RDX. On the basis of an assumption of local excitation (without further computational verification, which is probably the most questionable part of the report), the authors chose one of the three N−NO$_2$ subunits as the model of the excited-state ONIOM calculation, while leaving the other two moieties to be treated in low-level, ground-state method. Their ONIOM(CASSCF:UFF) results predicted that, upon irradiation, RDX is excited to, or near, the S$_2$ state in the Franck−Condon (FC) region, before decaying to the S$_0$ ground state through (S$_2$/S$_1$)$_{CI}$ and (S$_1$/S$_0$)$_{CI}$ conical intersections by following the barrierless steepest-decent pathway. This pathway
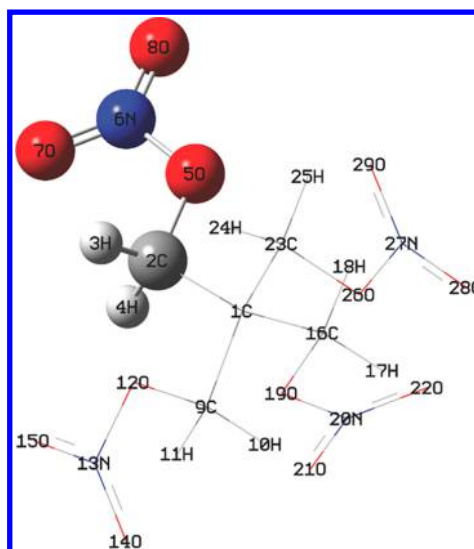
Figure 94. Structure of PETN. Ball: the QM region. Wire frame: the MM region. Reprinted with permission from ref 567. Copyright 2011 American Institute of Physics.

ultimately leads to a dissociation channel on the ground-state potential energy surface corresponding to rotationally cold/vibrationally hot NO (Figure 93), in agreement with the experimental observation.[565] The ONIOM method revealed the steric and inductive effects from the other N−NO$_2$ moieties at the six-membered ring of RDX, which play an important role in the system's dissociative behavior.

Similarly, ONIOM(CASSCF:UFF) calculations predicted that the decomposition of electronically excited PETN (Figure 94) occurs through a barrierless process, where the lowest energy pathway connects the FC point of S$_1$ state to the nitro-nitrite isomerization on S$_0$ through the (S$_1$/S$_0$) conical intersection, which then leads to NO elimination on S$_0$.[567]

Generally, the nitramine and related (NO/NO$_2$/NO$_3$) energetic materials generate a rotationally cold and vibrationally hot distribution of NO product via a NO elimination decomposition channel. The decomposition pathways are similar for each of these species, and conical intersections play a crucial role in the initial decomposition mechanics for electronically excited energetic materials.

7.2.3. Photochemical Reactions in Solution. Explicit solvent models combined with ONIOM calculations enable specific solute−solvent interactions during the photoreactions to be understood.[565] Recently, Prager et al.[568] employed ONIOM with TD-DFT to estimate the influence of polar environments on the mechanism of the photoinduced spiropyran-to-merocyanine isomerization (Figure 95). The ONIOM results showed that the solvent effect does not change the overall mechanism, nor the excited-state properties of spiropyran, such as the "bright state" (S$_1$) and the "dark state" (S$_2$). However, the relevant conical intersection in solution is shifted to a slightly larger C$_{spiro}$−O distance (3.6−3.8 Å), a smaller C-torsion angle (10°), and a larger O-torsion angle (74.8°), due to the electrostatic interaction of spiropyran with the water environment.

7.2.4. Photoreactions in the Cavity of One β-Cyclodextrin. Confinement effects on the photophysical and photochemical properties of aromatic molecules embedded in the cavity of one-cyclodextrin (CD) are usually attributed to the cavity size of the host molecule CD.[569] To explain the
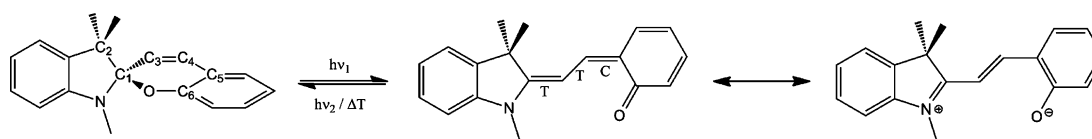
Figure 95. Photochemical isomerization of spiropyran to TTC-merocyanine. The mesomeric structures of TTC-merocyanine are shown as well. Reprinted with permission from ref 568. Copyright 2014 American Chemical Society.
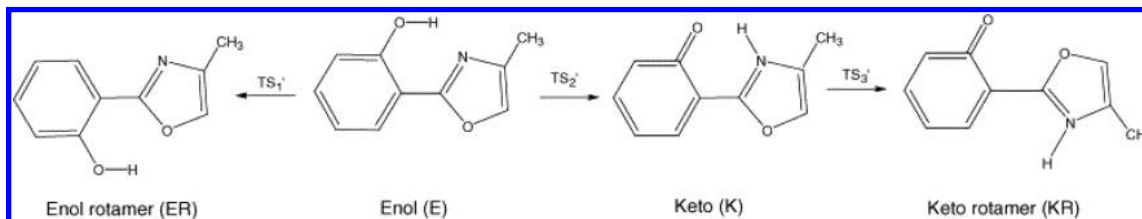
Figure 96. Scheme of the intramolecular proton transfer and the internal rotations of reactant and product. Reprinted with permission from ref 570b. Copyright 2005 Elsevier B.V.

reaction rate difference between the gas-phase reaction and the reaction in one β-cyclodextrin observed in time-resolved fluorescence experiments, Casadesús et al. applied ONIOM to determine the energies associated with intramolecular proton transfer[570] and the internal rotation of HPMO[570b] inside one β-cyclodextrin (Figure 96). These calculations predicted that on the S_1 surface the energy barrier is 0.35 kcal/mol for the $E(S_1) \rightarrow K(S_1)$ process, and 8.06 kcal/mol for the $K(S_1) \rightarrow KR(S_1)$ process, which are similar to the barriers in the gas phase. Using Rice−Ramsperger−Kassel−Marcus (RRKM) theory, Casadesús et al. attributed the difference in reaction rates to the slower internal rotation caused by the increment of rigidity of HPMO and intermolecular force occurring upon encapsulation.

8. APPLICATIONS TO SOLUTION CHEMISTRY

Most chemical reactions are carried out in the solution, and thus it is important to include solvent effects to make the calculations more reliable. Theoretical models to include solvent effects can be categorized into two groups: explicit and implicit solvent models. The explicit solvent model accounts for short-range electrostatic interactions and the effect of a hydrogen-bond network. Because solvent molecules are not involved in the reaction directly and their configuration is very flexible, the ONIOM method is one of the best ways to include explicit solvation effect at a low computational cost. The implicit solvent model includes the effects of long-range interactions. The merits of the implicit solvent model include reliable convergence and independence from problems associated with including too few explicit solvent molecules. Thus, the combined usage of an explicit solvent model for the first solvation shell and an implicit solvent model for the outer shell provides a good description of solvent effects and is becoming more common. Applications of ONIOM to solvation chemistry are summarized here, while details of the ONIOM solvent methods are reviewed in section 2.1.10.

8.1. Applications Using Explicit Solvent Models

8.1.1. Effect of Explicit Solvent Molecules on Chemical Reactions. In the early days of computational studies of chemical reactions, only the solutes were considered to reduce the computational cost. However, in the real reaction system, solutes are surrounded by solvent molecules, and they are often stabilized through electrostatic interactions and a hydrogen-

bond network. To describe these effects straightforwardly, some of the solvent molecules in the first solvation sphere can be added explicitly. Solvent molecules may not directly participate in the reaction and thus may not require as high a level of treatment as the solute molecules. Therefore, the ONIOM method is an appropriate way to include explicit solvent molecules in the calculation at lower computational cost. Re et al. examined the effect of microsolvation clusters for S_N2 reactions of methyl chlorides with one or two water molecules and showed that the ONIOM(QM:QM) methods reproduced the full QM results both for geometries and for reaction energies.[571]

The solvation energy depends on the structures of solutes, reflecting the different charge distributions of solutes, especially
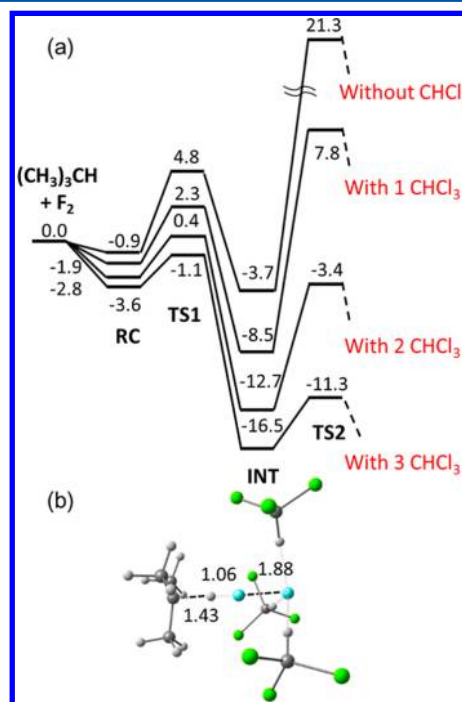
Figure 97. Potential energy profile (in kcal/mol with ZPE) for $(CH_3)_3CH + F_2 + n\ CHCl_3$ ($n = 0-3$) (a) and structure of TS2 with 3 $CHCl_3$ (b). Reprinted in part with permission from ref 572. Copyright 2003 American Chemical Society.

in polar solvent. Therefore, the energy profile along the chemical reaction in polar solution sometimes changes a lot as compared to that in the gas phase. One notable example is the fluorination of saturated hydrocarbons with F_2 in chloroform solvent.[572] The electrophilic pathway for the RH + F_2 reaction in general is a two-step process, starting from hydride abstraction leading to an intermediate of the type $R^{+\delta}\cdots HF\cdots F^{-\delta}$, followed by rearrangement to give the electrophilic substitution product RF + HF. The energy profile was compared with and without explicit solvent molecules using MP2 and ONIOM(MP2/6-31+G*:HF/6-31+G*), respectively. This reaction without solvent molecules had a high reaction barrier, whereas that with a few solvent molecules had a much lower barrier for the rearrangement of the intermediate (second step in Figure 97). This lower barrier can be explained by the different stabilization energies of each local minimum and TS by the explicit solvent molecules. The charge separations of the critical points increase in the following order: the reactant (RC) < the TS for the first step (TS1) < the intermediate $R^{+\delta}\cdots HF\cdots F^{-\delta}$ (INT) < the TS for the second step (TS2). Therefore, the highly ionic TS2 is stabilized more dramatically by specific interaction with the chloroform
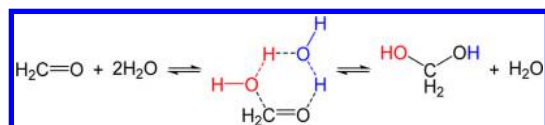
Figure 98. Hydration of formaldehyde.

molecules than the other TS and intermediates, which results in the lower reaction barrier. As shown in Figure 97, the energy of TS2 becomes more stabilized as the number of chloroform molecules increases and the barrier for the rate-determining step becomes about 30 kcal/mol lower than that without chloroform molecules. In this study, the ONIOM micro-solvation model is ideally suited for examining the effect of solvent molecules in the reaction. When the study was carried out, the combination of ONIOM with continuum models had not been developed, and thus they suggested that the best approach was to consider a few explicit solvent molecules surrounded by a continuum. Such combination studies will be discussed in section 8.3.

The effect of solvent polarizability was discussed in a study of the hydration of formaldehyde in aqueous solution.[573] In this reaction, two water molecules form a hydrogen-bond network with formaldehyde and provide a proton and a hydroxide ion as shown in Figure 98. The partial dissociation of the OH bond in the network makes the TS polar, which results in the stabilization of the TS by surrounding solvent water molecules. To examine the effect of the first and second solvation shells, several models were compared, with different numbers and coordination geometries of first-solvation-shell water molecules using ONIOM(HF/3-21G*:PM3). The model that best reproduced the activation free energy comprised five water molecules in the first solvation shell and 59 outer-sphere water molecules. Among the five first-shell water molecules, three bound to the active water molecules and two to the carbonyl oxygen and hydrogen, respectively. In this model, 60% of the solvation energy came from the first solvation shell and the remaining from the second solvation shell. As shown above, the microsolvation model allowed a detailed analysis of explicit hydrogen-bonding networks. The solvation energy was determined mainly by the first solvation shell. Outer-sphere solvent molecules are also necessary for quantitative calculations due to their long-range interactions.

The solvent polarizability also affects chemical properties, such as NMR chemical shifts. Vailikhit et al. reported the effect of the polar DMSO solvent on ^1H NMR chemical shift of nevirapine.[45r] To sample different configurations of the nevirapine-DMSO system, the conventional MM MD simulations were performed, and then a two-layer ONIOM-(B3LYP:PM3) method was used to optimize the structures of the solute and the first solvation shell. These structures were used to calculate the ^1H NMR chemical shifts using ONIOM(B3LYP-GIAO:HF-GIAO). The results showed that the chemical shift of the acidic amino proton is especially sensitive to the bound DMSO molecule and intermolecular hydrogen bonding. This approach reproduced experimental values successfully. The same group applied this scheme to a number of amines in DMSO solution and concluded that the explicit solvent model reproduced the experimental ^1H NMR chemical shifts with higher accuracy than the gas-phase and PCM calculations.[574] The importance of specific short-range and highly directional hydrogen bonds between solute and solvent was also pointed out by other groups.[45o,575]

Another type of explicit-solvent effect was shown in an isomerization process in a nonpolar solvent.[576] The solvent effect on isomerization of acetaldehyde N,N-dimethylhydrazone
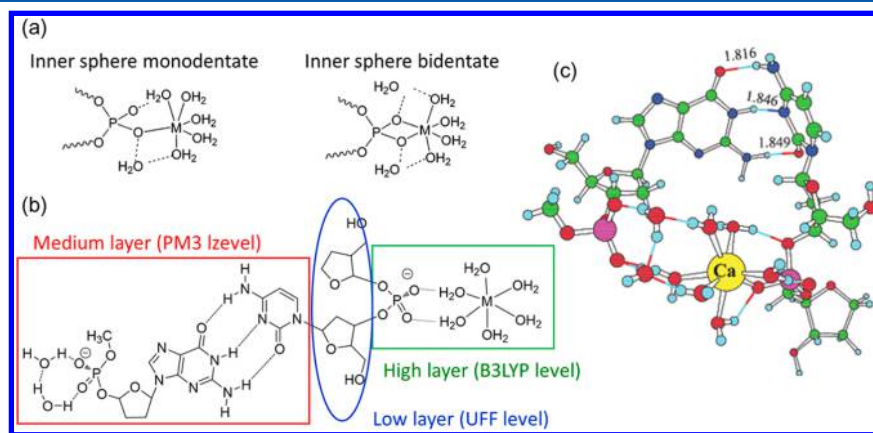
Figure 99. Two bonding patterns of dications to DNA (a), ONIOM scheme (b), and the ring structure of inner-sphere monodentate binding in the Ca^{2+} system (c). Reprinted in part with permission from ref 577. Copyright 2007 American Chemical Society.

in cyclohexane solvent was examined by comparing two calculation models. The first calculation model included six explicit cyclohexane molecules and was calculated using ONIOM(B3LYP/6-31G(2df,p):AM1). The second model did not include explicit solvent molecules, and the solvation energy was treated by the PCM model. Both calculation models gave very similar results for the geometries of the isomers and the TS structures, and the Gibbs free energy difference between the isomers. In contrast, the calculated free energy barrier of the second model was overestimated by 3−4 kcal/mol. The difference between the two calculation models came from the entropy contribution that was attributed to a reorganization of solvent molecules around the solute.

Consideration of explicit solvent is important not only for chemical reactions in solution but also for biomolecules.[577,578] In particular, water molecules around cations, such as Ca^{2+}, Mg^{2+},[579] Li^+, Na^+, and K^+,[580] affect their binding to DNA in terms of energies and structures. The binding energies depend on the hydrogen-bond network around the cations and phosphate groups as shown in Figure 99a. Suresh et al. examined several model systems, including one with a DNA fragment and hydrated Mg^{2+} and Ca^{2+}, calculated using the three-layer ONIOM(B3LYP/6-31G(d):PM3:UFF) method as shown in Figure 99b. They compared two models of the DNA fragment: anion and dianion models, where the left-end phosphate group was capped by a proton or two water molecules. For the anion model, monodentate binding structures (in Figure 99a) were the most stable both in Mg^{2+} and in Ca^{2+} systems. In contrast, for the dianion model, the interactions between dications ($Mg^{2+}$ and Ca^{2+}) and the DNA fragment gave rise to large structural deformations, leading to the formation of "ring" structures, where hydrated cations form a hydrogen-bond network with two water molecules coordi-
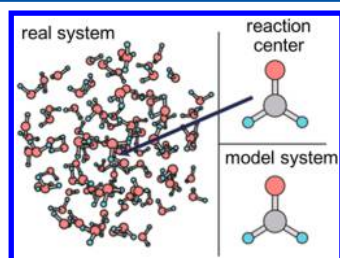
Figure 100. Definition of the real system, reaction center, and ONIOM model system for the $(H_2CO)(H_2O)_{100}$ system. Reprinted with permission from ref 129. Copyright 2009 American Chemical Society.

nated to the left-end phosphate group as shown in Figure 99c. They also clarified that the energetics of binding patterns depend on the dication and the charge of the DNA fragment. Their results provided insight into the biological roles of these metal ions in DNA binding.

As shown above, there are many advantages to using explicit microsolvation. However, it becomes more difficult to determine the solvation-shell structure as the number of solvent molecules increases. A new and promising solution to this problem is the Global Reaction Root Mapping (GRRM) strategy,[124] consisting of the ADDF and AFIR methods (see section 2.2.4.3). Maeda et al. examined both methods to explore all of the reaction pathways of solutes surrounded by water molecules, which were treated by low-level calculations. One study involved the decomposition and isomerization

Table 5. Performance of the ADDF Method with the Microiteration Method for the Real $(H_2CO)(H_2O)_{100}$ System As Compared to the ADDF Method for the Isolated H_2CO

number	$(H_2CO)(H_2O)_{100}$	H_2CO
reaction route	9	9
gradient	2665	2482
Hessian	117	101

pathways of formaldehyde surrounded by 100 MM water molecules using the ADDF with ONIOM(HF/6-31G:AMBER) shown in Figure 100.[129] For the isolated formaldehyde, nine reaction pathways were obtained by the ADDF method: two isomerization pathways to hydroxymethylene, two dissociation routes to H + HCO, one dissociation route to O + CH_2, and four dissociation routes to H_2 + CO. For the real system, the same nine reaction pathways for the QM part (reaction center in Figure 100) were fully explored by the ADDF method with an efficient microiteration technique. As shown in Table 5, the numbers of QM gradient and Hessian calculations for the real system were also very similar to those for the isolated formaldehyde. In other words, using the efficient microiteration technique, even if a large number of explicit solvent molecules are contained in the real system, the reaction pathways for the reaction center can be explored with a computational cost similar to that for the isolated system. Another study involved exploration of the aldol reaction between H_2CO and $H_2C=C(H)OH$ with a catalytic water molecule surrounded by 299 MM water molecules using the AFIR method with ONIOM(B3LYP/6-31G:AMBER).[130] In this case, the numbers of QM gradients and Hessians required in water solution were smaller than those without solvent, because solvation restricts the motion of reacting species due to the hydrogen-bond network. The GRRM strategy combined with the ONIOM microiteration scheme will be a useful tool to investigate the effect of microsolvation on reaction pathways and properties of solutes in future studies.

8.1.2. Quantum Mechanical Treatment of Solvent. In the previous section, the main role of the solvent was the stabilization of the solutes through various intermolecular interactions such as electrostatic interactions, hydrogen bonds, and entropic effects. However, protic solvent molecules often participate in a reaction as a source of protons or as part of the hydrogen-bond network for proton transfer. In such cases, some solvent molecules have to be treated by the high-level QM calculations. Tsuchida et al. studied the effect of the proton-transfer network in the Favorskii rearrangement, shown in Figure 101.[581] They considered nine methanol solvent molecules, and only the methyl groups of the solvent molecules were treated by the low-level PM3 calculations; thus, all of the OH groups in the solvent molecules were treated by the high-level QM calculation. Some of the methanol molecules interacted with lone pairs of heteroatoms in the substrate to stabilize the substrate, as shown in Figure 101a. Other solvent molecules participated in the methanol addition to form a proton relay network. As shown in Figure 101b, the reaction barrier for methanol addition became lower as the number of methanol molecules participating in the proton-transfer network increases. Similar situations can be observed in the addition of alcohols to disilenes.[582] In this case, an alcohol dimer inserts to ketone more easily than the monomer due to
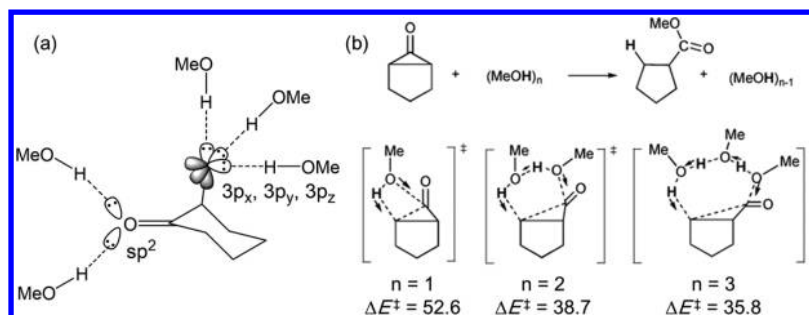
Figure 101. Schematic illustration of the hydrogen-bond network considered explicitly (a) and the concerted proton transfers in MeOH addition to the cyclopropanone intermediate (b). Activation barriers are in kcal/mol. Reprinted with permission from ref 581. Copyright 2008 Royal Society of Chemistry.
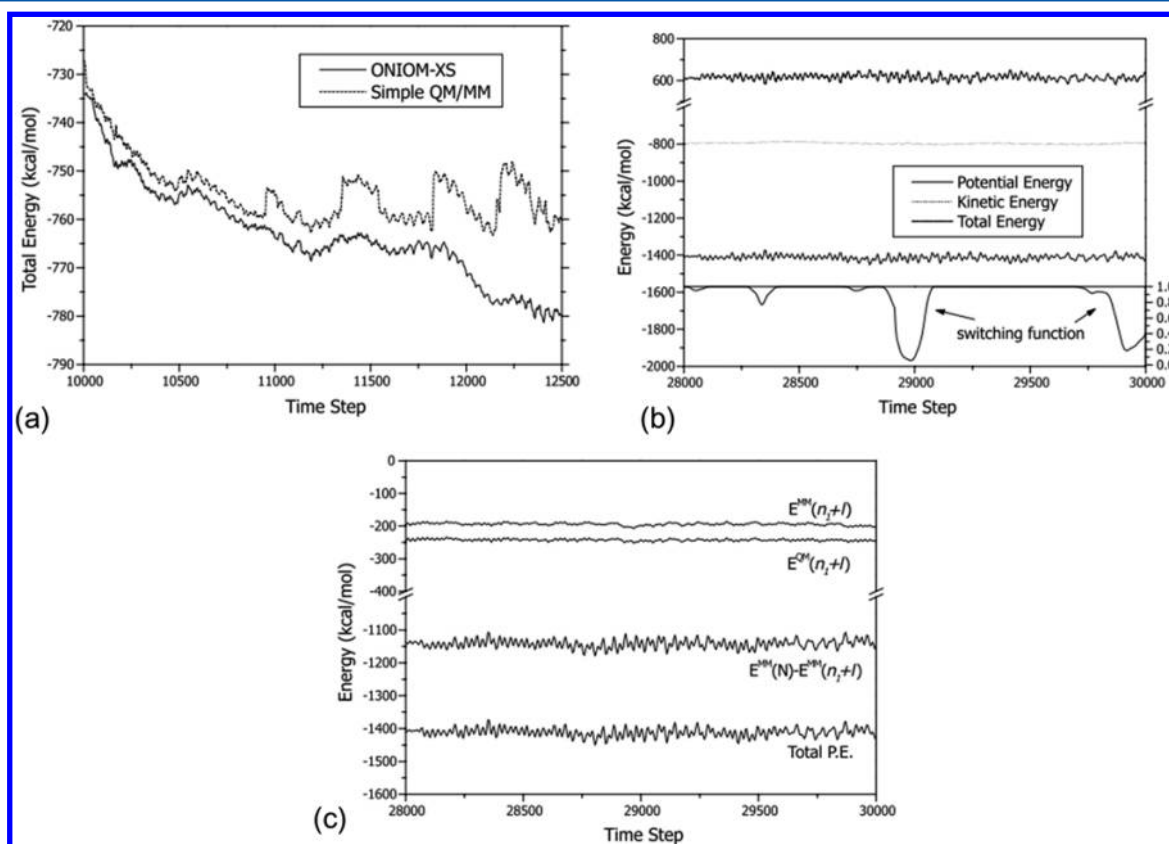
Figure 102. (a) Total energies from ONIOM-XS MD and classical QM/MM simulation without smoothing. (b) Kinetic, potential, total energies, and the values of switching function during a snapshot period of equilibrium from ONIOM-XS MD. (c) Component of the smoothed ONIOM potential energy. Reprinted with permission from ref 61. Copyright 2002 Elsevier.

the proton-transfer network involving two alcohols. The reaction barrier of the addition of alcohol depends on the substituent of the alcohol. For example, in the case of a bulky alcohol, such as *p*-(dimethylamino)phenol, the addition of the monomer is favored over that of the dimer because of the steric congestion caused by the substituent groups. Such effects cannot be described using continuum models.

Nowadays, ONIOM(QM:QM) calculations with highly accurate methods are also applicable to large systems, by for instance using the generalized energy-based fragmentation (GEBF) approach.[179p,583] Li succeeded in calculating the binding energy between methanol and water in their nanoscale clusters including 747 and 3351 atoms using two-layer GEBF-ONIOM(MP2-F12:MP2) and three-layer GEBF-ONIOM-(MP2-F12:MP2:cDFTB) calculations, respectively.[584] From

the calculations of these nanoscale clusters, it was found that the long-range interactions in methanol aqueous solutions are significant within 0.9 nm. The QM treatment of solvent molecules makes the models more reliable, and the QM:QM approach is a large advantage of the ONIOM method for solvation chemistry.

8.1.3. Dynamical Solvent Structures around Solutes. In the previous two sections, only static descriptions of solutions were considered or ONIOM was used for the single-point calculations at the structures obtained by conventional MM MD simulations. To investigate the solution dynamics with consideration of the solute–solution interaction at a high level, MD simulations with multilayer methods should be performed. However, conventional dynamical methods combined with the multilayer methods are problematic. The solvent

molecules in the high level often enter and leave the active region during the simulation, which results in the discontinuous energy and force. One of the techniques that solves this problem is the "ONIOM-XS" method.[61] The detailed algorithm of ONIOM-XS is described in section 2.1.10.1.

The first application of the ONIOM-XS method involved a periodic cube containing a Li^+ in 215 ammonia molecules.[61a] Long-range electrostatic interactions were represented by a classical implicit-reaction-field method. The radius of the high-level region was selected to be 4.0 Å, which was expected to be large enough to include the first and a part of the second solvation shell. For the switching shell, applying too thin of a layer results in too tight of a smoothing curve. On the other hand, if larger thickness is employed, there is less chance of having the switching shell free of exchanging particles, leading to increased computational demand (see section 2.1.10.1). In this study, a switching width of 0.2 Å was chosen between the QM region (a sphere of radius 3.8 Å) and the MM region (outside a sphere of radius 4.0 Å.

A comparison between a QM/MM simulation without smoothing and the ONIOM-XS simulation is shown in Figure 102a. Starting from a snapshot obtained by an MM simulation with a total energy of −730 kcal/mol, the energy gradually decreased to −780 kcal/mol, which is close to the average equilibrium energy by the ONIOM-XS. On the other hand, in the classical QM/MM simulation without smoothing, the total energy often surged suddenly because of the solvent exchange between the high- and low-level regions and the simulation could not reach equilibrium. The kinetic, potential, and total energies from a snapshot of the ONIOM-XS simulation are plotted in Figure 102b. The switching function is also plotted, and the zero value means that there is no solvent molecule in the switching shell. In almost all of the snapshots in Figure 102b, at least one solvent molecule is in the switching shell, because the values of switching function are nearly one. Three energies, potential, kinetic, and total energies, did not surge, and the effect caused by solvent exchange was negligible due to
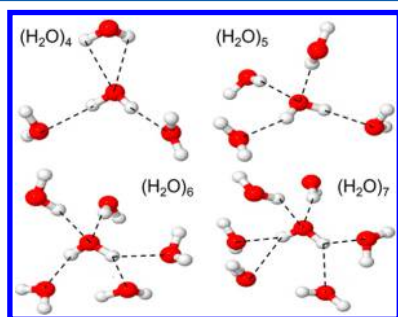
Figure 103. Selected hydrogen-bond network structures in aqueous solution obtained by ONIOM-XS simulation. Reprinted with permission from ref 587. Copyright 2012 Elsevier.

the switching function. It can be said that the ONIOM-XS scheme helps to link the QM/MM boundary seamlessly and creates no artificial effect on the statistical ensemble.

Using the ONIOM-XS scheme, coordination structures of Ca^{2+} in liquid ammonia,[61b] and those of K^+, Ca^{2+},[585] and Na^+[586] in aqueous solution, were investigated. The average number of solvent molecules around a solute cation obtained by the ONIOM-XS was usually different from that obtained by classical MM MD simulations, and the ONIOM-XS method reproduced the experimental data more reliably. The hydrogen-

bond network structure in aqueous solution was also studied by treating a central water molecule and its nearest-neighbor waters as the high-level region and the other surroundings as the low-level region.[587] The rearrangement of hydrogen bonds in aqueous media was found to occur readily; the nearest neighbors were either loosely or tightly bound to the central water molecule, as shown in Figure 103. Numerous water-exchange mechanisms were found with either short-lived or long-lived exchange periods. The number of hydrogen bonds changed during the simulation from two to six. In this simulation, the ONIOM(HF:MM) MD simulation was also compared and indicated that the number of hydrogen bonds around a central water molecule was overestimated as compared to that obtained by the ONIOM-XS method.

If all of the solvent molecules are included in the low-level region, the conventional MD schemes can be applied using the ONIOM energies and gradients directly. Matsubara et al. applied such direct ONIOM BOMD simulations for a number of enzymatic reaction studies including explicit solvent molecules (see sections 2.3.1.1 and 9.2.1).[156,588] Woo et al. combined the IMOMM methodology with the Car−Parrinello projector augmented wave (CP-PAW) code and applied it for the MD simulation of 3-methylhexane solvated by 14 isobutane molecules in a 20 Å cubic cell with periodic boundary condition.[70] Yao et al. used an approximate free energy method combining ONIOM with conventional MM MD simulations (see sections 2.3.1.6 and 9.2.1.7).[172]

In recent studies, other dynamical and statistical methods were also combined with the ONIOM method. For example, Shiga et al. performed the path integral molecular dynamics (PIMD) simulation that considers the quantum effect of the nucleus to analyze the hydration structure of *N*-methylacetoamide in aqueous solution, using ONIOM energies and gradients.[589] The Kovalenko group studied the electronic structure and binding energy of Streptavidin−Biotin supramolecular complex by using the ONIOM method, and applied the three-dimensional reference interaction site model (3D-RISM-KH)[590] calculations to investigate the water distribution in a protein, focusing on its binding pocket, as shown in Figure 104. Resolving both the solvation structure and the thermodynamics of a protein at the molecular level is a great challenge for both experiments and molecular simulations. This was made possible with the 3D-RISM methods. They obtained the hydration structures of a protein, streptavidin, with and without biotin and clarified the number of water molecules in the binding pocket. They found that an immobilized water molecule acted as a water bridge to stabilize the fold of the streptavidin/biotin complex.

8.2. Applications Using Implicit Solvent Models

8.2.1. Four ONIOM-PCM Treatments and Their Dependence on Chemical Properties.
Another useful theoretical treatment of solvent is the implicit solvent model, such as the polarizable continuum model (PCM), which is widely used as a conventional tool for theoretical chemistry. There are many advantages to the implicit solvent model, such as consideration of the long-range electrostatic effect of the bulk solvent, easier convergence, and independence from the number of included solvent molecules.

As mentioned in section 2.1.10.2, the ONIOM method can be combined with the PCM method, which is implemented in the Gaussian 09 program.[64a−d] To include the PCM in the ONIOM calculation, the apparent surface charge (ASC) needs
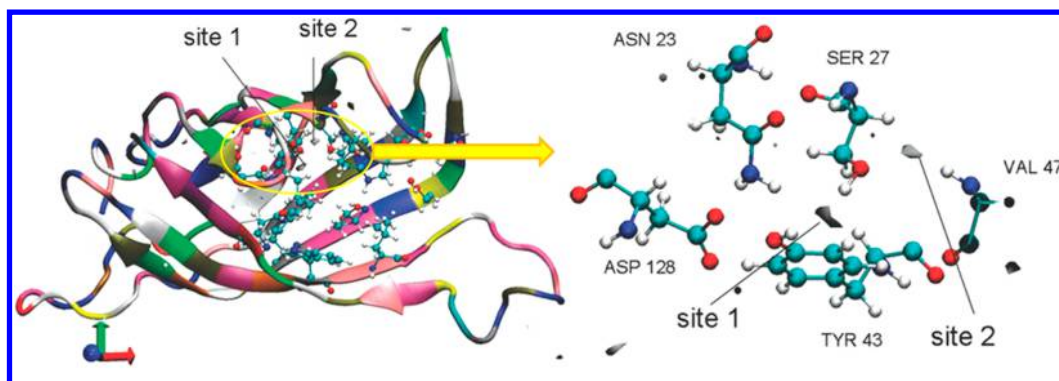
Figure 104. Isosurface representation of the solvation shell around the binding pocket of the streptavidin obtained by the 3D-RISM-KH method. The high-level region in the ONIOM calculation is represented in the CPK drawing. Reprinted with permission from ref 590. Copyright 2012 American Chemical Society.
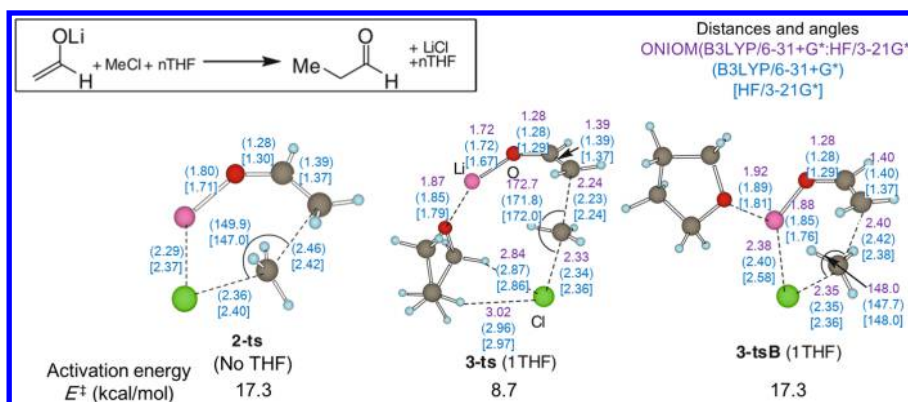
Figure 105. Transition states for S_N2 reaction with and without a microsolvent THF molecule. Reprinted with permission from ref 43a. Copyright 2011 Springer.

to be calculated on the basis of the integrated solute charge distribution. However, the wave function and ASC cannot be easily optimized simultaneously, as it results in very demanding calculations. The combined usage of ONIOM and PCM with the exact ASC is called ONIOM-PCM/A. To reduce the computational cost, three approximations, called ONIOM-PCM/B, /C, and /X, were proposed. Their schematic illustrations are shown in Figure 7. For ONIOM-PCM/B, the ASC is calculated on the basis of the charge distribution of the real system at low level and is used for all three sublevel-calculations. For ONIOM-PCM/C, which is more approximate than /B, the same ASC is used for the real system, whereas the model systems at low and high levels are calculated in the gas phase. ONIOM-PCM/X has a different concept; the ACS is evaluated separately at the level of each subcalculation. To examine the accuracy of the three approximate ONIOM-PCM schemes, they were compared with respect to the geometry and nuclear shielding of $H_2N(C_2H_3)_3CHO$,[66b] and the geometries and activation barrier of the S_N2 reaction of $Cl^-(H_2O)$ + CH_3Cl.[66a] All three approximate schemes performed well, and there were only small differences. The ONIOM-PCM/X scheme typically showed a slightly better behavior than ONIOM-PCM/B and ONIOM-PCM/C. As the model system became larger in comparison to the whole system, the result of ONIOM-PCM/X became close to that of ONIOM-PCM/A, which is the correct convergence behavior. For smaller model systems, the ONIOM-PCM/C scheme seemed to show slightly better performance. Practically, one usually employs small model systems in ONIOM studies, and therefore ONIOM-

PCM/C appears to be the most promising. According to the hierarchy of the ONIOM-PCM schemes, ONIOM-PCM/B is between the exact ONIOM-PCM/A and approximate ONIOM-PCM/C schemes, but it is not completely clear at this point why ONIOM-PCM/B does not show better results than ONIOM-PCM/C. One possible reason may be that in the ONIOM-PCM/B scheme the effect of the solvent on the model system is included twice, whereas in ONIOM-PCM/A it is included once, and in ONIOM-PCM/C it is not included at all. Alternatively, one could include the factor of 0.5 in the ONIOM-PCM/B scheme. The ONIOM-PCM/B, ONIOM-PCM/C, and ONIOM-PCM/X schemes are all comparable in computational requirements, because performing the model system calculations with or without reaction fields does not significantly contribute to the total computational time. On the other hand, the ONIOM-PCM/A scheme is the most expensive due to the double iteration scheme. Although the ONIOM-PCM/A scheme is always more expensive than the approximate schemes, it may eventually be the method of choice in many cases.

8.2.2. Effect of Implicit Solvent Molecules on Chemical Properties. The ONIOM-PCM method has been used in many studies. Wu et al. examined the geometries of DNA oligomers and showed that the geometries of oligomers obtained by ONIOM-PCM were similar to those obtained by ONIOM calculations that included solvent effects by using an 8.0 Å water box.[591] ONIOM-PCM is efficient for calculating energetics and geometries for chemical reactions in which solvent molecules do not participate in the reaction explicit-

ly.[204a,287,330,592] The properties of excited states, such as absorption and emission spectra, are sensitive to the change of charge distribution by surroundings. Thus, the consideration of polarizability of solvent is essential for such calculations (see section 7).[593] Other properties, such as pK_a,[594] reduction potential,[595] and NMR chemical shift,[29,36] were also examined by using the ONIOM-PCM method.

8.3. Applications of Combined Usage of Explicit and Implicit Solvent Models

In addition to the long-range effect of the bulk solvent, one can include some explicit solvent molecules in a lower level, so as to avoid a substantial increase in the computational cost. The combined usage of microsolvent and PCM can cover both short- and long-range interactions efficiently, and thus has become the mainstream for calculating solvation effects.

Ando et al. succeeded in obtaining a reasonable reaction barrier for the alkylation of the lithium enolate using ONIOM with both explicit THF molecules and the PCM model.[43a] In this study, the solute molecules, CH_3Cl, lithium enolate, and oxygen atoms of three THF molecules coordinating to the Li metal, were treated with the high level, and the other atoms in these three THF molecules and the remaining THF molecules were treated with the low level. Single-point PCM calculations in THF ($\varepsilon = 7.58$) were also performed with and without explicit THF molecules to examine the bulk solvent effect. As shown in Figure 105, alkylation without explicit THF molecules required high activation energy at a cyclic TS, **2-ts**, because of the strong interaction between the leaving chloride anion and the lithium cation. On the other hand, when a THF microsolvent is included in the reaction system, two types of TSs were found, **3-ts** and **3-tsB** in Figure 105. In the **3-ts** structure, the THF molecule participated in the formation of a large cyclic structure involving two substrates, in which the oxygen and hydrogen of THF interact with the lithium ion and leaving chloride, respectively. The strong interaction of Li···O(THF) and Cl···H(THF) stabilized the **3-ts**. The activation energy through **3-ts** in PCM was much lower than that in vacuum, which suggested that the bulk solvent considered by PCM still had a substantial effect even after one explicit THF molecule was included. Another TS including one THF molecule, **3-tsB**, had a much higher energy than **3-ts** and had a structure similar to **2-ts**. They also considered that more than two THF explicit molecules participated in the reaction. The second and third THF molecules coordinated to the lithium ion and further stabilized the TS. The fourth, fifth, and sixth THF molecules coordinated to the leaving chloride together with some extra weak hydrogen bonds with other THF molecules. The reaction barrier calculated in the gas phase and in PCM behaved differently. The activation energy in the gas phase decreased dramatically up to the TS with two THF molecules, after which it continued to decrease by 0.5−1.7 kcal/mol per THF molecule up to the TS with five THF molecules. In the case of activation energies calculated in the PCM, it decreased very slowly from the **3-ts** to the TS with three THF molecules and increased gradually to the TS with six THF molecules. This result suggested that both explicit and implicit solvent were needed to reproduce the solvent effect quantitatively for this reaction.

Both explicit and implicit solvent molecules often affect the geometry, chemical reaction, and chemical properties significantly in various cases, such as catalytic reactions,[596] enzymatic reactions,[597] and coordination structures of DNA and RNA

families.[226,591,598] For example, Marianski et al. discussed the role of explicit and implicit water solvent for the α-helix structure of polyalanine.[598a] They clarified that the explicit water molecules cooperatively hydrogen bonded to the C- and N-terminal of the helix, which resulted in an increase of the dipole moment of the helix/water complex to more than the summation of their own dipole moments. Therefore, the electrostatic interaction between the helix/water cluster and the bulk water became larger due to the explicit solvent molecules and had to be considered by the PCM model. As described above, many chemical properties including energetics, structures, NMR chemical shifts are affected both by short-range solute−solution interaction and by long-range electrostatic effects of the bulk solvent. Thus, the mixed explicit/implicit solvent ONIOM-PCM method is promising for future theoretical studies involving large molecular systems and chemical properties.

9. APPLICATIONS TO BIOLOGICAL MACROMOLECULES

Understanding the structures and functions, reaction mechanisms, and photoinduced processes in biological systems (such as proteins, DNA/RNA, and carbohydrates) is of great importance, because they are essential in many biological functions (e.g., O_2 formation, DNA repair, and signal transduction). Therefore, these areas have become the key subjects of ONIOM and QM/MM studies in the last two decades, because it is essentially impossible to treat whole and large biological systems by only QM methods.[6,8,9,15,599] Notably, mechanistic studies on enzymes and photobiology incited the development of QM/MM methods.[1,3,4] This section mainly summarizes some selected notable or influential ONIOM applications to diversified biological macromolecules. For instance, selected key structures and structure-related functions of various important biomolecules (including nonmetalloproteins, metalloproteins, DNA/RNA, and carbohydrates) are first discuseed (section 9.1). Mechanisms of key enzymatic reactions (e.g., hydrolysis, isomerization, redox reactions, and oxygen evolution) of various important biological systems (including nonmetalloproteins, metalloproteins, DNA/RNA, and carbohydrates) are summarized (section 9.2). Finally, critical photoinduced processes (e.g., signal transduction and photosynthesis in plants) in several photobiological systems (e.g., rhodopsins, fluorescent proteins, photoactive yellow protein, and DNA) are highlighted (section 9.3). Notably, ONIOM and QM/MM methods have been shown to be essential to include large environmental parts to realistically describe structures, reactions, and photoinduced processes of complex biological systems. The QM model system as well as the QM method should be carefully chosen in the ONIOM and QM/MM schemes, and the proper setup should be made (see section 2.3.3).

9.1. Applications to Structures and Functions of Biomolecules

In the last two decades, ONIOM has been widely and successfully applied to study the structure and structure-related properties of biological systems. Important ONIOM contributions to various biological systems (such as proteins and DNA/RNA) are summarized in this section.

9.1.1. Proteins. Selected ONIOM studies on structures and functions of nonmetalloproteins and metalloproteins are first outlined.

9.1.1.1. Nonmetalloproteins. Morokuma et al. evaluated the applicability of a three-layer ONIOM(B3LYP:AM1:AMBER) method for studying zwitterionic peptides using the example of $NH_3^+-CH^nBu-CO-NH-CH_2-CO-NH-CH^nBu-COO^-$.[16] The inclusion of a middle layer takes into account the electronic effects of the immediate environment on the active region and pushes outward the problematic QM/MM boundary. These ONIOM results indicated that the three-layer ONIOM(QM:QM:MM) approach, for which the computational cost is not high, was more reliable and accurate than ONIOM(QM:MM:MM) or the classical two-layer ONIOM(QM:MM) approaches. The estimated computational time with the three-layer ONIOM(B3LYP:AM1:AMBER) method is reduced by about 500, 10, or 5 times relative to that of full-QM, or the two-layer methods with AM1 or AMBER as the low level, respectively. Furthermore, by testing different computational methods including AMBER, AM1, and various two-layer ONIOM schemes, Prabhakar et al. demonstrated that an ONIOM(B3LYP:AMBER) method provided the best agreement with the X-ray structures of *Escherichia coli* NifS CsdB,[600] and mammalian glutathione peroxidase.[601]

On the basis of the results of an extensive theoretical study on the performance of different QM approaches for studying NMR shielding parameters for peptides, Moon et al. concluded that for an acetyl−glycine−glycine−methyl amide model system with an ideal β-sheet conformation, a mixed basis set method was more accurate than an ONIOM partitioning approach.[602]

The Dannenberg group has extensively used ONIOM(DFT:AM1) to study secondary structures of peptides,[193b,603−609] their dependence on amino-acid mutations,[193a,610] the solvation effect on secondary structure formation and its stability,[577,598a] and IR spectra.[611] Different secondary structures (such as β-strands, α-helices, and 3_{10}-helices) of capped polyalanines (acetyl(Ala)$_N$NH$_2$ with $N = 2−18$) were optimized using ONIOM(B3LYP:AM1) to compare their relative stabilities.[603] The 3_{10}-helix structure was found to be more stable than the α-helix structure for the short peptides, but the α-helix structure was preferred for the longer peptides due to more pronounced cooperative effects in the α-helix structures. The increased cooperativity in the α-helices was demonstrated by the increased stabilities of hydrogen bonds: shorter hydrogen-bond lengths of the peptides significantly increased the dipole moment with increasing N peptide unit. In addition, their ONIOM studies of amyloid-like peptide structures containing a VQIVYK fragment showed that the hydrogen bond formed between the side chains of glutamine (Q) increased the β-sheet formation energy, and decreased the distortion energy required for flattening the sheets during amyloid fibrils formation.[604,605a] The effect of the tenth alanine mutation (to Gly, Leu, Val, Phe, Ser, or Pro) on the stability of α-helix and β-strands of a capped peptide, acetyl(Ala)$_{17}$NH$_2$, was also studied theoretically.[193a] All mutations except Gly were found to destabilize β-strands. On the other hand, the α-helix structure was stabilized by the Leu or Ser mutation, but destabilized by the Val, Phe, or Pro mutation. The substitution of Gly with D-Ala or D-Ser in a collagen-like triple-helical protein with a repeating ProProGly unit was theoretically found to increase the hydrogen-bonding energy by 0.8 or 7.7 kcal/mol, respectively, whereas a Gly → L-Ala mutation decreased the hydrogen-bonding energy by 6.6 kcal/mol.[610] They concluded that the enantiomorphic Gly served as a D-amino

acid, and could be potentially substituted with any D-amino acid.

Alzate-Morales et al. combined docking and ONIOM methods in an attempt to predict the binding modes of different CDK2 inhibitors as well as their potency and selectivity.[612] Three-layer ONIOM(B3LYP:HF:PM3) single-point calculations were carried out to estimate the interaction energy between a set of inhibitors and the binding site of the T160pCDK2/cyclinA enzyme system, using structures generated from the docking method. A good correlation model, connecting the hydrogen-bond interaction energy derived from the ONIOM calculations and the experimentally observed biological activity of the inhibitors, was obtained for a set of 75 compounds.

BP86 and ONIOM(BP86:AMBER) methods were used to study the structure and interactions in different prion protein models to understand structural changes and deformations induced by coordination with different transition metal cations.[613] The relative binding energy of the cations was also estimated. The coordination ability of the transition metal cations to the prion protein increased in the order Zn(II) < Mn(II) < Cu(II) < Fe(II) < Co(II) < Ni(II), and was found to result in significant structural changes localized in the PrP(61−68) and PrP(69−76) octapeptide repeat regions. The binding energy for Mn(II) and Cu(II) (−317.4 and −304.9 kcal/mol, respectively) explained the experimentally observed blocking effect of Cu(II) on the pro-aggregatory activity of Mn(II).

ONIOM(B3LYP:AMBER) was adopted to study protein−ligand interactions to understand the contribution of C−X···H (X = Cl, Br, I) contacts to the binding affinity of the complexes.[614,615] According to the ONIOM results, C−X···H interactions were found to contribute significantly to the protein−ligand interactions, although less so than C−X···O halogen bonds.[614] Two-layer ONIOM(QM:MM) methods were applied to study the role of fluorine bonding in protein−ligand interactions, which are important for drug affinities and selectivities of biomolecules.[616] The interactions of flufenamic acid, 2,3,4,5,6-pentafluoro-SBB, or a LacNAc derivative, and their F → H mutated analogues with their corresponding protein receptors, transthyretin, carbonic anhydrase II, and human galectin-3, respectively, were computationally investigated. These ONIOM results showed that both structures and energetics of fluorine bonding are quite similar to sulfur-involved hydrogen bonding. Isolated fluorine-based interactions in simplified F-donor/F-acceptor model systems were found to be rather weak: −1.6 to −1.8 kcal/mol at the MP2/aug-cc-pVDZ level. However, fluorination of a ligand to target a specific biomolecule may result in increased binding affinity and specificity via fluorine-bonding interactions and indirect electronic effects.

The two- and three-layer ONIOM methods, ONIOM(MP2:AMBER) and ONIOM(MP2:B3LYP:AMBER), with ME and EE schemes, were employed to study thioredoxin and one-electron addition to the single disulfide bridge in this oxidoreductase enzyme.[617] The simulations showed that the size of the QM region was of crucial importance for the reliability of the ONIOM results. Increasing the size of the QM region caused up to 1 eV difference in the values of the adiabatic electron affinity. The Lys40 residue was shown to play an important role in the increased electron affinity. Furthermore, the protonated Asp30 side chain and the presence of a water molecule in the vicinity of the active site
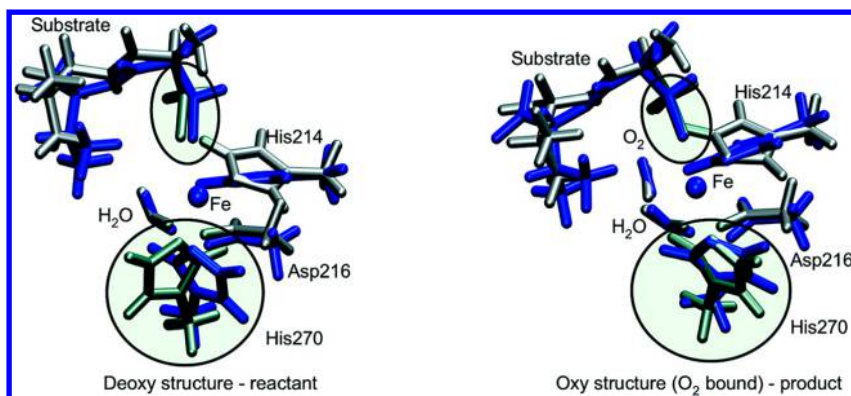
Figure 106. Computed structures for deoxy (left) and oxy (right) states in IPNS by the active-site model (silver) and ONIOM (blue) calculations. Reprinted with permission from ref 620. Copyright 2007 American Chemical Society.
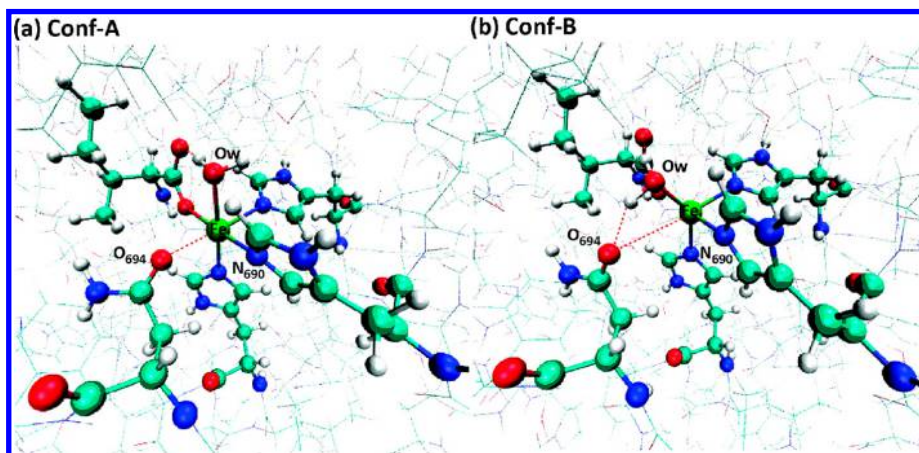
Figure 107. Two stable conformers in SLO-1. Reprinted with permission from ref 621. Copyright 2010 American Chemical Society.

were suggested to increase the electron affinity of the disulfide couple.

9.1.1.2. Metalloproteins. Applications of ONIOM to the structure of various metalloproteins have been reported by the Morokuma group and other groups. Such studies have focused on methane monooxygenase (MMO),[618,619] ribonucleotide reductase (RNR),[618] isopenicillin N synthase (IPNS),[620] soybean lipoxygenase-1 (SLO-1),[621] and ferritin.[622]

Torrent et al. applied ONIOM(B3LYP:AMBER) and ONIOM(B3LYP:HF:AMBER) methods to metalloproteins for the first time, focusing on MMO[618,619] and RNR.[618] With the X-ray structures of MMO and RNR as references, the computed structures of the di-iron active site with 62-residue protein models (RMSD: 0.34−0.48 and 0.23 Å for the ONIOM(B3LYP:AMBER) and ONIOM(B3LYP:HF:AMBER) methods, respectively) were found to be more accurate than those derived from active-site models (RMSD: 0.62−1.03 Å). An ONIOM(B3LYP:AMBER) method with the ME or EE scheme was also used to elucidate the significant protein effects on O_2 binding and activation in MMO through comparison with results from an active-site model. The protein environment was found to promote O_2 coordination to Fe (>1.0 Å) and electron transfer from Fe to O_2, and to elongate the O−O distance by 0.04−0.08 Å while shortening the Fe−Fe distance (>0.4 Å).[619] An ONIOM(B3LYP:AMBER) method with the ME or EE scheme was then extended to the study of O_2 binding in IPNS.[620] The protein was found to facilitate O_2 binding by 8−10 kcal/mol, whereas O_2 binding was an

endergonic process in the active-site model. The geometry of the Fe complex in the protein (Figure 106, about 3−6 kcal/mol contribution) and van der Waals interactions with the nearby residues (about 3−4 kcal/mol stabilization) were found to play important roles. The effect of polarization of the QM region by the IPNS protein was insignificant.

In the case of SLO-1, the coordination number of the ferrous resting state was observed to be six in the crystal structure, whereas a nearly equal mixture of two distinct ferrous forms, five-coordinate and six-coordinate, was observed by circular dichroism (CD) and magnetic circular dichroism (MCD).[623] Hirao et al. carried out ONIOM(B3LYP:AMBER) calculations on SLO-1 in the quintet ground state.[621] Two stable conformers, Conf-A and Conf-B (Figure 107), were found to have similar stabilities (1 kcal/mol at ONIOM(B3LYP-D:AMBER)-EE//ONIOM(B3LYP:AMBER)-ME, taking into account empirical dispersion (D) interaction correction[624]). The Fe−O_{694} distance in Conf-A was shorter (2.39 Å), whereas the distance was much longer in Conf-B (3.46 Å). Neither of these two conformers perfectly reproduced the crystal structure, but an averaged geometry of the two conformers was in excellent agreement with the crystal structure. Simulated CD spectra using TD-DFT and CASSCF/SORCI methods with the EE scheme were also consistent with the experimental spectra. These results suggest that the crystal and solution structures represent a mixture of the two conformers.

In a very recent study, Harris et al. used ONIOM(B3LYP:-AMBER) to optimize a series of single subunits of Fe(II)- and

Fe(III)-bound frog M ferritin by varying the hydration, protonation, and coordination states of the ferroxidase site.[622] The computationally preferred structure of the di-Fe(II)-bound state had five-coordinate iron sites without a bridging ligand, in agreement with CD/MCD data analysis, whereas the di-Fe(III)-bound state was found to have various possible water-derived bridging ligands. ONIOM-computed exchange coupling constants (J), Mössbauer parameters, and TD-DFT CD spectra calculated using the EE scheme were in good agreement with the experimental results.

The ONIOM approach has been successfully applied to study the structure of many metal-containing biological systems, such as copper-,[625−629] iron-,[630] and manganese-[631] containing enzymes. For example, ONIOM(DFT:AMBER) in combination with different experimental techniques was used to study the structure and reduction potential of blue copper proteins, such as rusticyanin (including M148Q and H143M mutants),[625] azurin, plastocyanin, and stellacyanin.[626] The reduction potential of the plastocyanin protein at pH = 7 was computed to be 376 ± 38 mV by ONIOM(B3LYP:AMBER)// ONIOM(B3LYP:UFF),[629] which was in very good agreement with the available experimental data (379 mV). The plastocyanin reduction in aqueous media required reorganization of the water shell surrounding the protein. Therefore, the interactions with the medium and the entropy change are, in some cases, important for correct evaluation of the reduction potential. A similar approach was applied to estimate the standard oxidation and reduction potentials of chlorophyll-*a* in acetonitrile.[632] The ONIOM-computed values for the oxidation and reduction potentials at 298.15 K were 0.75 ± 0.32 and −1.18 ± 0.31 V, respectively. The calculated values were in very good agreement with the available experimental data (0.76 and −1.04 V).

Recently, ONIOM(B3LYP:AMBER) was used to study the interaction of Fe(II)−heme with beta amyloid peptide.[633] The ferroheme showed slight preference for binding to His13, as complexes with His6 or His14 binding had higher relative energies by 31.0 and 28.2 kJ/mol, respectively. A two-stage protocol (a fast screening of 48 model inhibitors for the zinc metal-binding group with the M05-2X method, followed by a screening of some binders with ONIOM(M05-2X:AMBER)) was adopted to search a potential bidentate inhibitor for zinc-dependent histone deacetylases, which are important in epigenetic regulation.[634] The ONIOM results were consistent with the experimental results, and a few new zinc binding groups were also proposed.

9.1.2. Nucleic Acids.
ONIOM has been successfully applied to study nucleic acid interactions with different organic ligands[635−637] or with metal complexes.[578,638,639] Such interactions influence drug cytotoxicity and may affect damage and repair processes involving DNA.

In an attempt to define the best combinations of methods for proper large-scale modeling of systems involving $\pi−\pi$ stacking interactions, Rutledge et al. analyzed the performance of a variety of density functionals. Specifically, they calculated interaction energies of 129 nucleobase−amino acid dimers, using previous CCSD(T)/CBS calculations as references.[640] AMBER force field was found to be an appropriate choice for the low-level method to adequately describe $\pi−\pi$ interactions, while M06-2X and PBE-D functionals were found to be suitable methods for the high-level regions.

A proper theoretical modeling of cisplatin/DNA complexes was shown to require the use of the EE scheme and explicit treatment of the water solvent.[578] The DNA structural parameters for a complex with cisplatin calculated with ONIOM(BHandH:AMBER) were in good agreement with the available experimental data.

An extensive experimental and ONIOM(B3LYP:UFF) study of the interactions between DNA and the organochlorine herbicide chloridazon (5-amine-4-chloro-2-phenylpyridazin-3 (2H)-one) showed that the herbicide intercalated into DNA, with the chromophore CO group heavily involved in the herbicide−DNA interaction.[636] The theoretical results indicated that the herbicide−DNA interaction is dependent on the DNA base-pair sequence. The herbicide/CG complex was favored with an interaction energy of −29.6 kJ/mol, 4.2 kJ/mol more than the herbicide/AT analogue.

Three-layer ONIOM(MPWB1K/6-31G(d):MPWB1K/3-21G:AMBER) was applied to study intercalation of proflavine (3,6-diamine-acridine) into AT- and CG-rich DNA decamers.[637] The interaction energy in the case of CG-rich DNA was found to be about 40 kcal/mol higher than that for the AT-rich DNA decamer, which is in agreement with the experimental XRD evidence for CG preference. Proflavine intercalation in the AT-rich DNA decamer was found to induce significant structural changes in DNA.

ONIOM(M05-2X:PM6) was applied to study and better understand the radical cation deprotonation in DNA, which is a rather complex temperature- and pH-dependent process involving different competing reactions.[641] Radical cation species are usually formed via single-electron oxidation processes involving 2′-deoxyguanosine (2dG), which is considered to be the most easily oxidized element of the DNA structure. Two types of deprotonation were studied: proton transfer within the DNA base pairs and proton transfer to the surrounding water. At room temperature and pH ∼7.4, the latter process was found to be dominant.

Using nucleoside 3′,5′-bisphosphates as model compounds for both DNA and RNA, the C−H BDEs were estimated for all carbohydrate C−H bonds by means of ONIOM-G3B3.[132,134] Their results showed that the hydroxyl group provided better radical stabilization than the neutral phosphate group by 4.4 kcal/mol, but worse than the monoanionic phosphate group. In agreement with the experimental observations, RNA radiation damage was found to be mainly via hydrogen-abstraction at H−C2′, as the H−C2′ bond-dissociation free energy was about 5−6 kcal/mol lower than those of other C−H bonds in the model systems.

An ONIOM(B3LYP:UFF) method was used to simulate the Raman spectra of DNA and radiation-induced damaged DNA with a C5′−O bond cleavage.[642] Calculated spectra were in good agreement with experimental observations, including the appearance of O−H bending and CH_2 and CH_3 bending/ wagging bands in the spectrum of the damaged DNA structure and higher intensities of the DNA backbone bands.

9.1.3. Miscellaneous.
ONIOM(PM3:UFF) and ONIOM-(RHF:PM3) were applied to study gangliosides and their inhibitory effect on the enzyme activity of CD38 as an NAD glycohydrolase.[643] ONIOM(B3LYP:AM1) calculations combined with dynamic NMR spectroscopy, docking, and MD simulations were carried out to study the antihypertensive drug valsartan in solution and at the AT_1 receptor.[644] B3LYP combined with AMBER, AM1, PM3, or RM1 in an ONIOM approach was applied to study the interactions between an inhibitor (oxamate anion) and rabbit muscle L-lactic dehydrogenase.[645] The binding isotope effects of the carboxylic oxygen
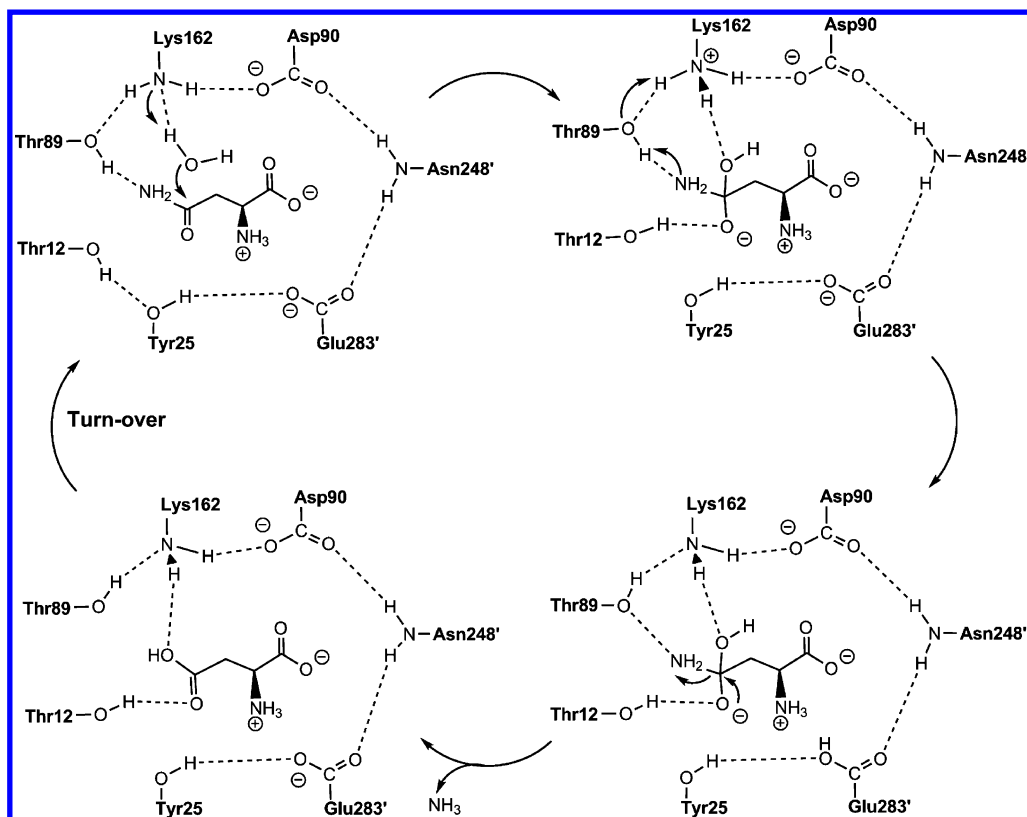
Figure 108. Proposed catalytic mechanism of L-asparaginase II. Adapted with permission from ref 663. Copyright 2013 American Chemical Society.

atoms were estimated on the basis of normal vibrational modes of the oxamate in aqueous media and in the enzyme active site, and compared to experimental data. According to ONIOM-(B3LYP:OPLS) results, the active site of the enzyme is best described as a dimer, consisting of one chain with the open-loop and another chain with the closed-loop conformation.

The Hannongbua group has performed extensive theoretical investigations of HIV-1 reverse transcriptase (HIV-1 RT), and published a series of papers discussing various related aspects of its structure and activity. In the initial study of the interaction of nevirapine with HIV-1 RT,[646] a relatively small model including only 16 amino acid residues around the binding site was considered using ONIOM(MP2:HF:PM3). Later, a larger model including 22 residues for the HIV-1 RT binding site with the nevirapine complex was adopted, and a three-layer ONIOM(MP2:B3LYP:PM3) method was used.[647] Counterpoise-corrected gradient optimization was found to be important for proper description of the interactions between the inhibitor and the residues at the HIV-1 RT binding site. The binding of tivirapine to HIV-1 RT and its Y181C mutated variant was also examined,[648] using a model system consisting of only 20 residues within a radius of 15 Å of the inhibitor molecule. The Y181C mutation reduced the binding energy of the inhibitor to the HIV-1 RT binding pocket. Analysis of different energy components suggested that the mutation may lead to destabilization of the binding pocket, with more energy required for deformation/rearrangement of the residue side chain in the pocket. The interactions between a water molecule and amino acids at the HIV-1 RT active site were also studied using a model consisting of 10 amino acid residues in a sphere of about 7 Å in diameter around the oxygen atom of the water molecule.[649] The water molecule was found to form a strong hydrogen-bond network with Asp186, Tyr183, and Tyr188 of

HIV-1 RT. Therefore, the water molecules induce the active-site conformation that enables the catalytic process and attract deoxyribonucleoside triphosphate to elongate the viral DNA during enzyme replication. The same group also studied interactions of saquinavir and HIV-1 protease with ONIOM-(B3LYP:PM3:UFF),[650] binding of efavirenz to HIV-1 RT and its mutated forms with ONIOM(B3LYP:PM3:UFF),[651,652] binding of flurbiprofen to cyclooxygenase enzyme with ONIOM(B3LYP:PM3),[653] IR spectra of volatile compounds from bread baking (acetaldehyde, acetylpyrazine, diacetyl, 2-ethyl-3-methylpyrazine, and acetylpyridine) and their interaction with a 703-atom model of bovine rhodopsin as a receptor with ONIOM(B3LYP:PM3),[43d] and interactions of oxaloacetic acid with phosphoenolpyruvic carboxykinase in the presence and absence of hydrazine with ONIOM-(B3LYP:PM6).[654]

An ONIOM(B3LYP:AMBER) method was used to study complexes of HIV-1 protease with various inhibitors to understand the role of a structural water molecule in the interaction.[655] According to the calculations, water molecules formed four hydrogen bonds, two with the C=O group of the inhibitor molecules and two with the amine/amide N atoms of the protease. Formation of this hydrogen-bond network leads to more rigid binding of the inhibitor molecule to the enzyme. The role of bridging water molecules in the interaction between inhibitors and glycogen synthase kinase 3β was studied with ONIOM(B3LYP:AMBER) calculations, MD simulations, and molecular docking methods.[656] The results showed that the presence of water molecule(s) in the vicinity of the binding site should be taken into account in drug design.

ONIOM(QM:MM), MM, ChemScore, and GoldScore scoring functions were used to discriminate the native pose from the nonnative poses in six HIV-1 protease complexes.[657]
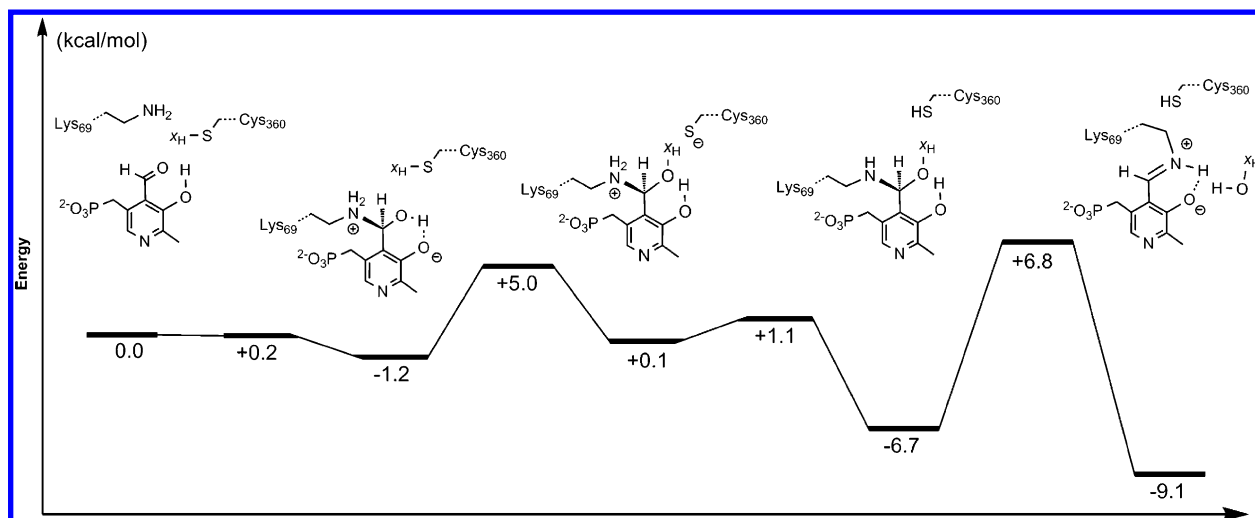
Figure 109. ONIOM-calculated relative energies for the most favorable pathway for the formation of the internal aldimine in pyridoxal 5′-phosphate (PLP)-dependent enzymes. Reprinted with permission from ref 676. Copyright 2011 American Chemical Society.

According to the calculated results, the best ONIOM-(QM:MM) scoring function was based on solvent-corrected ONIOM(HF:AMBER). The same group also studied interactions of nevirapine in the HIV-1 RT binding site aiming to estimate the accuracy of different QM and MM methods and to predict different effects of mutations on the binding energy.[658]

ONIOM methods have been successfully applied as a complementary methodology in drug discovery and drug design studies. For example, the ONIOM method has been used for reoptimization and rescoring GOLD derived cross-docking poses in fragment-like kinase inhibitors,[659] and for supplementing X-ray crystallography in structure-based drug design programs.[660]

9.2. Applications to Biological Reactions

To understand the mechanisms of enzymatic reactions, ONIOM has been widely used to describe bond formation and breaking processes, which cannot be well treated by MM methods and involve systems that are too large and computationally demanding for QM methods. Herein, the selected ONIOM studies on some biological reactions in proteins, DNA/RNA, carbohydrates, and artificial enzymes are discussed.

9.2.1. Proteins.
The ONIOM applications to nonmetalloproteins and metalloproteins will be addressed in this section. These computations provide more insight into the enzymatic reaction mechanisms.

9.2.1.1. Nonmetalloproteins. Butyrylcholinesterase (BChE) is an enzyme responsible for hydrolysis of cocaine. The understanding of this enzymatic reaction pathway can provide insight into the design of new BChE mutants. ONIOM-(MP2:AMBER)//ONIOM(HF:AMBER) calculations were carried out to study the catalytic mechanism in BChE.[661] The computed overall barrier for the BChE-catalyzed hydrolysis of cocaine was about 14 kcal/mol, which was about 4 kcal/mol higher than the hydrolysis of acetylcholine in acetylcholinesterase (AChE). The protein environment, especially the hydrogen-bond network among Gly116, Gly117, Ala199, and cocaine, was found to strongly influence the stabilization of the transition state of the first step and thus reduce the activation barrier.[661,662]

The reaction mechanism of the hydrolysis of L-asparagine to give L-aspartate in L-asparaginase II was investigated by using ONIOM(M06-2X/6-311++G(2d,2p):M06-2X/6-31G(d))//ONIOM(B3LYP:AM1).[663] The proposed three-step mechanism involves the nucleophilic attack of a water molecule on the substrate before the elimination of ammonia (Figure 108). The first step was suggested to be the rate-limiting step with a barrier of 20 kcal/mol, which is in agreement with the experimental barrier (16 kcal/mol). Two catalytic triads were proposed to play different roles in the reaction: Thr12-Lys162-Asp90 functions as a catalytic base for the nucleophilic attack of the water molecule on the substrate, and Thr12-Tyr25-Glu283 stabilizes the anionic tetrahedral intermediate after the nucleophilic attack.

β-Secretase (BACE1) is an enzyme that catalyzes hydrolytic cleavage of protein peptide bonds.[664] Very recently, ONIOM-(B3LYP:AMBER) was used to investigate the enzymatic mechanism, which involved formation of a gem-diol intermediate and cleavage of the peptide bond (rate-limiting step).[664a] The calculated reaction barrier for the wild-type substrate was higher than its Swedish mutant by 4−5 kcal/mol. This study provided important insight into the cleavage mechanism and substrate specificity.[664]

The reaction mechanism of serine acylation with penicillanic acid in class A TEM-1 β-lactamase, a clinically important enzyme, was computationally studied.[665] Two competitive pathways to facilitate the addition of Ser70 to the β-lactam carbonyl to form a tetrahedral intermediate were suggested by ONIOM(MP2:AMBER)//ONIOM(HF:AMBER) calculations. These ONIOM results are consistent with the experimental studies. In a subsequent step, protonation of the lactam nitrogen of the tetrahedral intermediate takes place followed by tetrahedral collapse to give the acyl-enzyme. Both Lys73 and Glu166 were suggested to play important roles in the reaction. In addition, the carboxylation of lysine in the OXA-10 β-lactamase was investigated by ONIOM-(B3LYP:AMBER).[666] One active-site water molecule was found to assist the carboxylation reaction with a computed barrier of 14 kcal/mol. The reaction was calculated to be exothermic in the protein environment, whereas it was endothermic in the gas phase. The deprotonated lysine carbamate in the enzyme was suggested to be the active

species.[666] Moreover, the same laboratory investigated the reaction mechanism of acylation and deacylation with a D-Ala-D-Ala peptide in penicillin-binding protein 5 (PBP5) by using ONIOM(MP2:AMBER)//ONIOM(HF:AMBER). The complex in the active site was suggested to reorganize to release the product and regenerate the catalyst.[667] The same group also explored the catalytic mechanism of the transpeptidation reaction in the penicillin-binding protein 1b (PBP 1b). Their ONIOM(MP2:AMBER)//ONIOM(HF:AMBER) calculations suggested that the *cis*-amide is required for the cross-linking, and that *cis−trans* isomerization of the amide is the driving force for releasing the product.[668] Recently, ONIOM-(B3LYP:AMBER) was employed to study the mechanism of acylation reactions with methicilin and nitrocefin in penicillin-binding protein 2a (PBP 2a). The calculated energy barrier for nitrocefin was lower than that for methicilin by about 10 kcal/mol, due to the larger resonance stabilization and releasing more ring strain during the ring opening. The effect of electrostatic interactions was proposed to be a key factor for the design of substituents.[669]

In addition, ONIOM(QM:MM) has been employed to explore many other important enzymatic reaction mechanisms.[601,670−674] ONIOM(QM1:QM2) and ONIOM-(QM:MM) schemes have also been used in combination with QM and MD methods to design new enzymes.[675] Glutathione peroxidase (GP_x) is a selenoprotein capable of catalyzing hydrogen peroxide (H_2O_2) reduction (E−Se−H + HOOH → E−Se−OH + HOH). The enzymatic H_2O_2 reduction mechanism was investigated by ONIOM(B3LYP:AMBER) calculations.[601,670] Two key steps, formation of the selenolate anion and the O−O bond cleavage, were calculated to have an overall barrier of about 18 kcal/mol. Also, the overall reaction was computed to be extremely exothermic. As compared to the active-site model, the protein effect on the H_2O_2 reduction is very small, as the active site locates on the surface of the GP_x enzyme.[601,670] An ONIOM study of the catalytic mechanism of the reductive half-reaction of aromatic amine dehydrogenase (AADH) with a tryptamine substrate led to the proposal of a multistep reaction mechanism.[671] A large QM region and electrostatic interactions of the protein played significant roles in the computed barrier.[671] ONIOM(DFT:AMBER) methods (DFT = B3LYP and M06-2X) were employed to investigate the mechanism of hydroxylation and ring-opening of the aromatic 2-methyl-3-hydroxypyridine-5-carboxylic acid (MHPC) substrate catalyzed by 2-methyl-3-hydroxypyridine-5-carboxylic acid oxygenase (MHPCO).[672] The calculated reaction barriers were found to be sensitive to the QM and MM partition: a maximum variation of about 9.5 and 8.4 kcal/mol was observed for the hydroxylation and ring-opening steps, respectively.

The reaction mechanism of formation of the internal aldimine for pyridoxal 5′-phosphate (PLP)-dependent enzymes was studied by ONIOM(M06:B3LYP)//ONIOM-(B3LYP:AM1).[676] Three catalytic steps, the nucleophilic attack of Lys69 to PLP, the carbinolamine formation, and a final dehydration step, were proposed to be involved (Figure 109).

ONIOM(B3LYP:PM6) was used to investigate the reaction mechanism of the cleavage of the headgroup of phosphatidylcholine (PC) to generate phosphatidic acid (PA) and choline in an enzyme from the HKD-containing phospholipase D (PLD) superfamily of *Streptomyces* sp. PMF (PLD$_{PMF}$).[597a] This study found a five-coordinate phosphorane intermediate and supported the associative mechanism for the phosphoryl transfer. The catalytic mechanism of the condensation of

arabinose 5-phosphate (A5P) and phosphoenolpyruvate (PEP) to form 3-deoxy-D-*manno*-octulosonate 8-phosphate (KDO8P) in *A. aeolicus* KDO8P synthase was investigated by ONIOM-(B3LYP/6-31+G(d,p):AMBER)-EE//ONIOM(B3LYP/3-21G:AMBER).[677] The computed results supported the partially concerted pathway with the deprotonated PEP phosphate for the *syn* addition of water to the *si* side of C2^{PEP}, while C3^{PEP} reacted with the *re* side of C1^{A5P}. The overall barrier was estimated to be ∼14 kcal/mol, along with the reaction energy of −38 kcal/mol.[677]

ONIOM(B3LYP:AMBER) was employed to study the protonation states of cysteines in the active site of
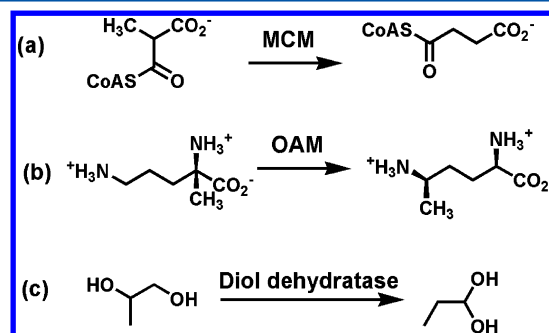
Figure 110. Transformations catalyzed by AdoCbl-dependent enzymes.

thioredoxin.[678] A conserved histidine with a shifted pK_a was suggested to have two catalytic acid−base functions for protein splicing by ONIOM(B3LYP:AMBER).[679] Chlorine kinetic isotope effects (KIE) on the dehalogenation in a haloalkane dehalogenase from *Xanthobacter autotrophicus* GJ10 were calculated by using ONIOM(B1LYP:SE) methods (SE = AM1 and PM3).[680]

9.2.1.2. Metalloproteins: Cobalt-Containing Enzymes. Adenosylcobalamin (AdoCbl, B$_{12}$) is a key cofactor for several enzymes, such as methylmalonyl-CoA mutase (MCM), D-ornithine 4,5-aminomutase (OAM), and diol dehydratase. The AdoCbl coenzyme contains a specific Co−C bond between the Co metal and C5′ of the adenosyl moiety. The Co−C5′ bond cleavage is an essential step, which can promote hydrogen transfer between the substrate and the C5′ radical of the adenosyl moiety to induce the substrate rearrangement.

MCM is an important B$_{12}$-dependent enzyme, which catalyzes a radical-based conversion of methylmalonyl-CoA to succinyl-CoA (Figure 110a). The initial Co−C5′ bond cleavage step in the closed (reactive) and open (unreactive) conformations of MCM enzyme was investigated by using an ONIOM method.[681] In the first ONIOM study, the residues within 15 Å from the cobalt center were included in ONIOM(RI-BP86:AMBER) calculations. For the open conformation of MCM, as with the gas-phase model, the energy increases with cleavage of the Co−C5′ bond. For the reactive conformation of MCM, the Co−C5′ bond cleavage transition state was located for the first time indicating a barrier of about 10 kcal/mol. In addition, the conformation of 5′-deoxyadenosine was found to change during the Co−C5′ bond homolytic cleavage.[681]

The concerted or stepwise mechanism of the bond cleavage and hydrogen transfer in the reactive MCM has been investigated using ONIOM(BP86:AMBER) (Figure 111) with several QM models (containing 74−119 QM atoms).[190]
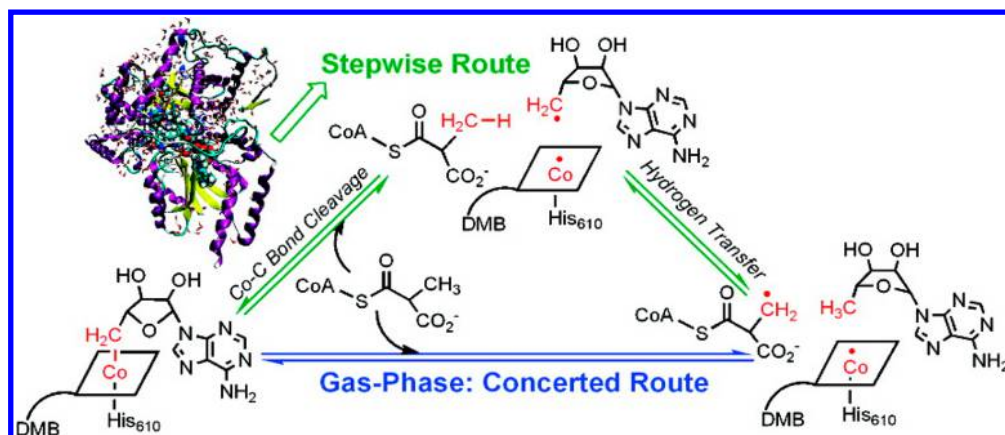
Figure 111. Co−C bond cleavage and hydrogen transfer steps in the transformation of methylmalonyl-CoA to succinyl-CoA by MCM. Reprinted with permission from ref 190. Copyright 2009 American Chemical Society.

This ONIOM study suggested that the protein effect is large, with contributions from the cage effect (∼5 kcal/mol), the geometric distortion of the adenosylcobalamin in the bound state (∼8 kcal/mol for the large model), and the protein environmental effect (∼9 kcal/mol for the large model). In particular, Glu370 and Gln330 were found to play key roles in stabilizing the bond cleavage state. Moreover, the flexible 5′-deoxyadenosyl moiety readily changes to the lowest-energy conformation during the bond cleavage process. In addition, the bond cleavage is concerted with hydrogen transfer in the gas-phase model calculations (Figure 111), but a stepwise pathway was found in the MCM protein. As compared to the active-site model, the hydrogen transfer step in MCM has a lower barrier (∼9−10 kcal/mol), due to the stabilization of the cleavage state and the substrate preorganization.[190]

OAM is another AdoCbl-dependent isomerase, which converts D-ornithine to 2,4-diaminopentanoic acid (Figure 110b). The Co−C5′ bond breaking of AdoCbl in OAM was studied by ONIOM(BP86:AMBER).[682] In the open form of OAM, the protein environment plays a minor role on the Co−C5′ bond rupture, which is similar to that in the gas phase. However, the closed-form OAM protein is considerably active and promotes the Co−C5′ bond cleavage with a barrier of about 11 kcal/mol. The steric and electrostatic effects (∼16 kcal/mol) from the protein were found to be important in the Co−C5′ bond cleavage. The large protein effect on the Co−C5′ bond breaking step catalyzed by OAM is similar to that of MCM.[190,681,682]

The B$_{12}$-dependent diol dehydratase is responsible for the conversion of 1,2-diols to 1,1-diol (Figure 110c). ONIOM(B3LYP:AMBER) calculations were performed to study the OH group migration mechanism catalyzed by this diol dehydratase. The neutral His143 (push effect), the negatively charged Glu170 (pull effect), and the coordinated K$^+$ were found to be crucial in promoting the OH-group migration.[683] As compared to the wild-type diol dehydratase, the higher barrier for the OH-group migration has been found in some mutations of His143 and Glu170.[684]

Methionine synthase (MetH) is a cobalamin-dependent methyltransferase, catalyzing the methyl transfer from methyltetrahydrofolate to the cob(I)alamin to form a six-coordinate CH$_3$-cob(III)alamin intermediate. An ONIOM(BP86:AMBER) method was employed to study the detailed mechanism of the methyl transfer.[685] Two pathways, an S$_N$2-type mechanism (His-off) and an electron-transfer (ET)-based methyl radical

transfer mechanism (His-on), were investigated. Both the S$_N$2-type and the ET-based radical mechanisms were found to be feasible with low activation barriers (∼8−9 kcal/mol).
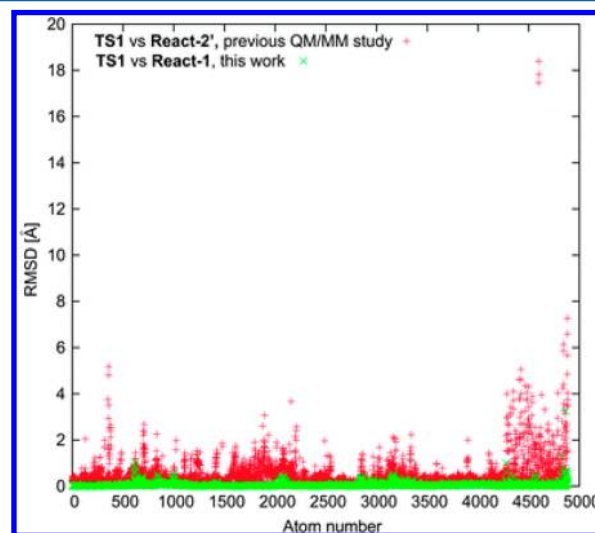
Figure 112. Comparison of RMSD (root-mean-square deviation) of structural parameters between the superimposed transition state (TS1) and reactants (React-2′ or React-1) in tyrosinase. Reprinted with permission from ref 189. Copyright 2011 The Royal Society of Chemistry.

9.2.1.3. Copper-Containing Enzymes. Tyrosinase is a dinuclear copper enzyme, which catalyzes the conversion of tyrosine to dopaquinone with the aid of dioxygen. The enzymatic mechanism was studied by ONIOM(B3LYP:AMBER).[686] A five-step catalytic cycle by tyrosinase was proposed: proton transfer from the phenolic OH group to the peroxy moiety, O−O bond cleavage, formation of a new C−O bond, proton abstraction triggered by His54, and finally electron transfer from one copper center to form dopaquinone. The O−O bond cleavage was computed to be the rate-determining step with a barrier of ∼15 kcal/mol.[686] However, a recent ONIOM(B3LYP:AMBER) study by Siegbahn et al. did not support the above proposal of the low barrier for O−O bond breaking.[189] Their ONIOM calculations suggested that the reactant optimized in the previous study[686] might be a high-energy intermediate, or that the MM part for the reactant and transition state has very different local minima (Figure 112),

which may result in an underestimated barrier for the O−O bond cleavage.

Dopamine β-monooxygenase (DBM) is a dinuclear copper-containing enzyme that catalyzes the transformation of dopamine to norepinephrine, which involves dioxygen. Using the homology modeling approach based on the crystal structure of peptidylglycine α-hydroxylating monooxygenase (PHM) to construct a DBM enzyme structure, ONIOM(B3LYP:AMBER) optimizations were carried out to refine the whole DBM structure.[687] The reactivities of the Cu(II)-superoxo and high-valent Cu(III)-oxo species of DBM toward the dopamine hydroxylation then were investigated using active-site model and ONIOM calculations.[687,688] The hydrogen-abstraction barrier for the triplet Cu(III)-oxo oxidant was computed to be very low (∼5 kcal/mol), whereas a higher barrier was observed for the Cu(II)-superoxo oxidant (∼23 kcal/mol).[688] Therefore, they proposed the triplet Cu(III)-oxo species as a possible oxidant. The protein environment (especially Glu369,
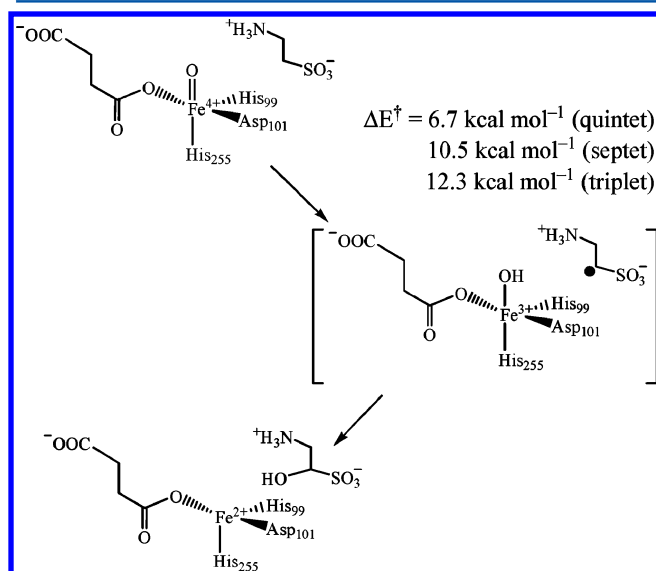
Figure 113. Proposed mechanism of taurine hydroxylation by the iron(IV)−oxo species of TauD. Reprinted with permission from ref 691. Copyright 2008 American Chemical Society.

Glu268, and Tyr494) played important roles in the stereo-specific hydroxylation reaction. The Yoshizawa group also investigated another copper-containing enzyme, particulate methane monooxygenase (pMMO), which is responsible for the conversion of methane to methanol. The reactivity of the monocopper(III)-oxo (triplet and singlet) and dicopper(II,III)-oxo (doublet) species toward methane was computed by B3LYP* and ONIOM(B3LYP*:AMBER).[689]

Galactose oxidase (GO), a mononuclear copper enzyme, catalyzes the radical-based conversion of alcohols to aldehydes coupled with reduction of dioxygen to hydrogen peroxides. An early IMOMM(B3LYP:MM3) calculation with a small QM/MM model (including the backbone link of Tyr495-His496 only in the MM part) was used to study the mechanism of GO.[690]

9.2.1.4. Iron-Containing Enzymes. B3LYP and ONIOM-(B3LYP:UFF) calculations were carried out to study the reaction mechanism of hydroxylation of taurine in nonheme α-ketoglutarate dioxygenase (TauD) enzymes (Figure 113).[691] As compared to the highly polar active site, the effects of the
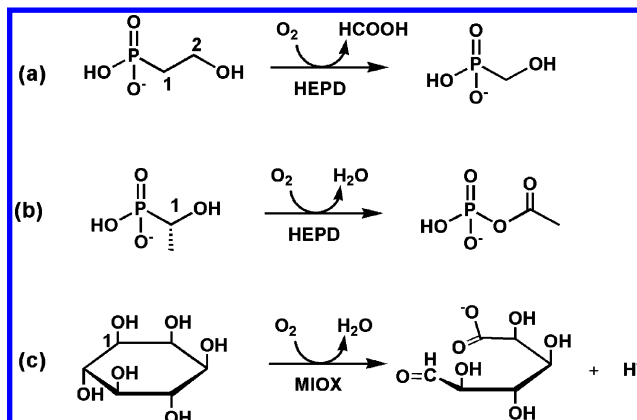
Figure 114. Oxidative-cleavage processes in nonheme HEPD and MIOX enzymes.

protein environment on the structure of the active site and the energetics of different spin states (singlet, triplet, quintet, and septet) were found to be small and very similar to those in the gas phase. The quintet iron(IV)-oxo species was computed to be the ground state, with low-lying septet and triplet excited states. The calculations also showed that neutral His99 and His255 ligands ligated with the iron are important for achieving the correct electronic structures, and the computed reaction barrier of hydrogen atom transfer of taurine by the reactive quintet oxo-iron species was 6.7 kcal/mol.

Hirao et al. have used ONIOM(B3LYP:AMBER) to investigate the mechanisms of two nonheme 2-hydroxyethyl-phosphonate dioxygenase (HEPD)-catalyzed reactions: the conversion of 2-hydroxyethylphosphonate (2-HEP) to hydrox-ymethylphosphonate and formic acid, and that of 1-hydroxyethylphosphonate (1-HEP) to an acetyl phosphate (Figure 114a,b).[692] The ground-state iron(III)-superoxo species in HEPD was suggested to be the septet state, although the stability of the quintet state may be underestimated by the B3LYP method. After the initial hydrogen atom abstraction by the iron(III)-superoxo species, the hydroxyl ligand can migrate to the substrate, followed by the O−O and C−C bond cleavages, and finally C−O bond formation to give hydrox-ymethylphosphonate and formic acid. Although similar reactions and radical intermediates were computationally suggested to be involved in both substrates (2-HEP and 1-HEP), for the reaction with 1-HEP, proton-coupled electron transfer (PCET) on the phosphorus center of the substrate was proposed to occur and promote nucleophilic attack of the acetate oxygen to give an acetyl phosphate.

myo-Inositol oxygenase (MIOX) is a novel nonheme diiron oxygenase, which catalyzes conversion of *myo*-inositol (MI) to D-glucuronate (DG) (Figure 114c). An ONIOM-(B3LYP:AMBER) method was used to study the reaction mechanism of the oxidative conversion of MI.[693] The ground state of the (superoxo)Fe(III)Fe(III) intermediate was computationally suggested to have a doublet side-on O₂ coordination mode (the two iron centers are antiferromagneti-cally coupled, whereas the superoxide ferromagnetically couples with its nearest iron center). This nonheme iron(III)-superoxide intermediate can catalyze C1−H abstraction from MI. Two major effects of the protein environment on the catalytic reaction were observed: the lowering of the barrier of the initial hydrogen abstraction and the prevention of other side-reactions. In addition, the O−O bond cleavage was
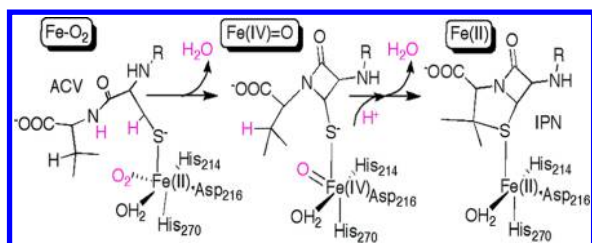
Figure 115. Overall reaction for isopenicillin N synthase (R = L-α-amino-δ-adipoyl). Reprinted with permission from ref 188. Copyright 2009 American Chemical Society.

computed to be the rate-limiting step of the reaction. The bridging hydroxide ligand was found to act as a catalytic base; thus it is not an innocent ligand.

An ONIOM(B3LYP:AMBER) method combined with EDA was carried out to evaluate the protein effect on the initial O_2 binding step in MIOX.[694] Small effects of electrostatic and van der Waals interactions as well as polarization were suggested to promote the O_2 binding step, whereas dispersion-correction (DFT-D)[624] was found to enhance O_2 binding.

Lundberg et al. investigated the reaction mechanism of oxidative conversion of δ-(L-α-aminoadipoyl)-L-cysteinyl-D-valine (ACV) to isopenicillin N (IPN) in a nonheme enzyme isopenicillin N synthase (IPNS) (Figure 115) by using an ONIOM(B3LYP:AMBER) method and the new quadratically coupled QM/MM geometry optimization algorithm (section 2.1.8.2).[55,188] As compared to the active-site model calculations,
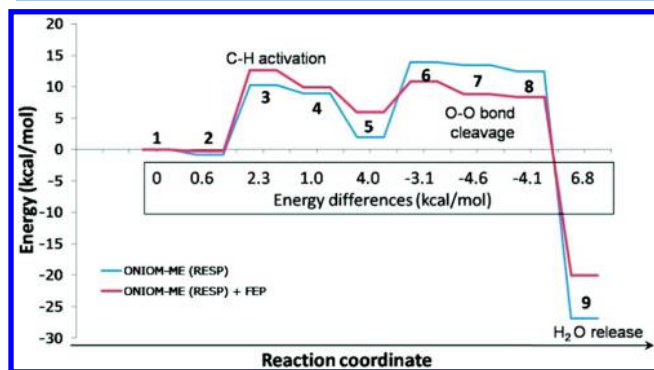
Figure 116. Free-energy profile for the formation of the Fe(IV)−oxo intermediate after dioxygen binding in IPNS. Reprinted with permission from ref 29. Copyright 2011 American Chemical Society.

the protein controls the reactivity to achieve high product specificity and high stereospecificity. For instance, the hydrophobic residues in the active site align the substrate radical precisely for the thiazolidine ring closure and contribute to the product selectivity. A low-energy pathway for the formation of the β-lactam was proposed to be responsible for the heterolytic O−O bond cleavage from the N−H group of the substrate. The protein effect on the transition states was small (>4 kcal/mol).

Subsequently, Kawatsu et al. developed an efficient and approximate ONIOM free-energy method, ONIOM-FE (section 2.3.1.6).[29] Classical MD simulations combined with a free-energy perturbation (FEP) approach were used to include a free-energy correction in the reaction energy determined by the ONIOM(B3LYP:AMBER) geometry optimization method.[188] They applied the ONIOM-FE (or QM:[MM-FEP]) method to eight different reaction steps in IPNS. The effect of protein dynamics was important in the C−

H bond activation and heterolytic O−O bond cleavage steps (Figure 116), due to charge transfer involved in these two steps. The barrier for the O−O bond cleavage step was corrected by several kcal/mol. The protein dynamical contributions were separated into the geometrical effect and the statistical (entropic) effect resulting from the protein fluctuations.

An ONIOM(B3LYP:MM) (MM = Dreiding and CHARMM) ADMP method (section 2.3.1.5) was used to study the effect of the active-site dynamical fluctuations on the key hydrogen abstraction step of the oxidation of linoleic acid in soybean lipoxygenase-1 (SLO-1).[167] The effect of the active-site fluctuation and flexibility was found to play a key role in maintaining the electrostatic interactions, and it affected the hydrogen abstraction step.

B3LYP and ONIOM(B3LYP:AMBER) calculations were performed to study the mechanism of heme metabolism by heme oxygenase (HO).[695] They found that a bridging water molecule and its hydrogen-bond network in the active site play key roles in lowering the barrier (∼14 kcal/mol for the active-site model) and the regioselectivity, as they lead to reduced distortion of the porphyrin in the transition state.

ONIOM(B3LYP:UFF) calculations were carried out to study the reaction mechanism of sulfoxidation of dimethyl sulfide in two cytochrome P450 isozymes (P450$_{CAM}$ and P450$_{BM3}$).[696] The reactivity of two proposed intermediates, iron(IV)-oxo (Cpd I) and iron(III)-hydroperoxo (Cpd 0), for the sulfoxidation reaction of dimethyl sulfide was compared. Cpd 0 was shown to be a sluggish oxidant for the sulfoxidation reaction by the ONIOM calculations. The true oxidant, Cpd I, reacts with dimethyl sulfide via only a quartet state (single-state reactivity).

The reaction mechanism of oxidation of (2′S)-nicotine by the reactive iron-oxo species (Cpd I) in human cytochrome P450 2A6 was investigated by ONIOM(B3LYP:AMBER) calculations to elucidate the reason for the preferential hydrogen abstraction at the 5′-carbon position rather than the N-methyl carbon position of the substrate.[697] This study showed that the selectivity of the rate-limiting hydrogen abstraction is not determined by geometric factors of the active site, but by the lower barrier for the carbon 5′ position of the substrate.

Tryptophan 2,3-dioxygenase (TDO) and indoleamine 2,3-dioxygenase (IDO) are special heme dioxygenases that catalyze oxidative cleavage of L-Trp. Although they were discovered more than 40 years ago, the reaction mechanism in TDO and IDO remained unclear.[698] On the basis of recent crystal structures and mutagenesis studies, two new mechanisms were proposed.[699] However, the active-site model calculations (B3LYP) by Chung et al. did not support the newly proposed concerted electrophilic addition with proton transfer and the Criegee-type rearrangement.[700] Instead, two new dioxygen activation pathways were found: (a) direct electrophilic addition of Fe(II)-dioxygen to C2 or C3 of the indole, and (b) direct radical addition of Fe(III)-superoxide[701] to C2 of the indole.[700] Formation of the dioxetane intermediates or the homolytic O−O bond cleavage followed by oxo attack was found in the two competitive pathways. Later, ONIOM-(B3LYP:AMBER) calculations were performed by using the protein structure of bacterial TDO (xcTDO).[702] A new mechanism was proposed consisting of an unusual direct radical addition to the C2 position, homolytic O−O cleavage concerted with ring-closure to give the epoxide and ferryl-oxo
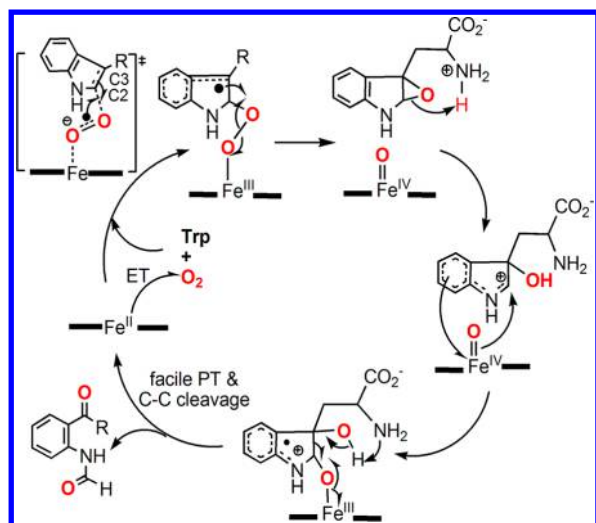
Figure 117. New mechanism of oxidative cleavage of L-tryptophan in TDO. Reprinted with permission from ref 702. Copyright 2010 American Chemical Society.

(Cpd II) intermediates, acid-catalyzed ring-opening of the epoxide, and finally oxo attack and C−C bond cleavage concerted with back proton transfer (Figure 117).[702] This mechanism is mostly supported by the recent experiments.[703] As compared to the reaction in the gas phase, the protein effects were found to lower the barrier for the formation of the Cpd II intermediate by substrate preorganization, and to prevent Cpd II from undergoing side reactions.

Very recently, Kubas et al. reported kinetics and thermodynamics of O_2 binding in the di-iron site of [FeFe]-hydrogenases.[704] These enzymes have the highest reactivity for H_2 formation, but they are extremely sensitive to oxygen. Free energy profiles for O_2 binding in *Clostridium pasteurianum* (*Cp*) and *Desulfovibrio desulfuricans* (*Dd*) were estimated by ONIOM(QM:MM) calculations. The range-separated DFT method CAM-B3LYP was reparameterized against results obtained from the high-level NEVPT2 method, and then used as the QM method for the ONIOM calculations. Free-energy barriers of 12.9 and 13.5 kcal/mol were estimated for *Cp* and *Dd*, respectively. The calculated barriers are in agreement with the observed inactivation rates. According to the ONIOM(QM:MM) results, the proximal [Fe_4S_4] cluster and protein environment stabilize the di-iron site and promote O_2 binding. Therefore, they proposed that mutation of several residues close to the [Fe_4S_4] cluster could reduce the O_2 binding ability.

The structures and energies of catalytically active (Ni−SI and Ni−R) and inactive states (Ni−A and Ni−B) of Ni−Fe hydrogenases were studied using an active-site model of the protein with the BP86 and B3LYP methods, and a larger model including the protein environment with an ONIOM-(DFT:AMBER) method.[705] The ONIOM-optimized Ni−Fe bond distance was more consistent with that of the X-ray crystal structure than those derived from the active-site model calculations. The catalytically active state of Ni−SI was found to be protonated (Ni−SI$_{II}$), not nonprotonated (Ni−SI$_I$). Moreover, H_2 binding to the Ni metal was found to be favored, rather than to the Fe center in Ni−SI$_{II}$. A low-spin state for Ni−SI$_{II}$ was suggested to be the ground state with the BP86 functional. The mechanism of H_2 cleavage in Ni−Fe hydrogenase was examined with an active-site model (137 atoms) using B3LYP and with two truncated protein models (137 and 363 atoms) using ONIOM(B3LYP:AMBER).[706] This study found that the barrier for oxidative addition of H_2 to the Ni(I) metal was 3.4 kcal/mol lower than that of the heterolytic cleavage. The larger ONIOM system with 363 atoms was found to be more reliable than the system with 137 atoms in the ONIOM calculations, as overestimation of the QM polarization effect by the MM part was observed in the smaller ONIOM system.

9.2.1.5. Magnesium-Containing Enzymes. Hepatitis delta virus (HDV) ribozyme is a small noncoding RNA in HDV, which undergoes self-cleavage of the backbone of the ribozyme. First, ONIOM(HF:AMBER) calculations were performed to search the possible binding positions of a Mg^{2+} ion, and to then select three starting structural models (from 13 initial structures) with various inner-shell coordination models for the Mg^{2+} ion.[707] Next, ONIOM(DFT:AMBER) (DFT = BLYP and MPW1K) optimizations and potential energy surface scans were carried out to investigate the detailed reaction mechanism. For the structural model with the hexacoordinated Mg^{2+} ion (Figure 118), a concerted pathway was found to have a low barrier of ~20 kcal/mol, in which the cytosine 75 (C75) and Mg^{2+} ion function as the general base and general acid catalysts, respectively.[707] By contrast, the barrier of the uncatalyzed reaction is much higher (~35 kcal/mol).

Phosphate transfer and hydrolysis are important in many biological systems.[708] Smith et al. investigated the mechanism of a phosphate transfer from ATP to the ribose 5′-hydroxyl of cytidine and uridine in the human uridine-cytidine kinase 2 (UCK2).[709] The mechanistic pathway of the phosphate transfer, which is concerted with a proton transfer from the 5′-hydroxyl group to a neighboring Asp62 (a catalytic base), was supported by ONIOM(B3LYP:AMBER)-EE results with a barrier of 15.1 kcal/mol, which is close to the experimental value (17.5 kcal/mol).
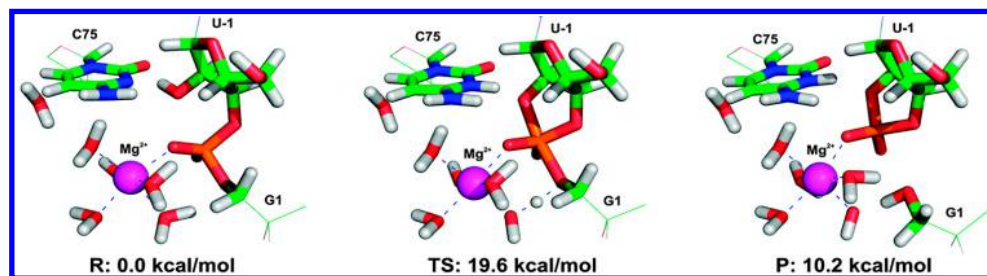
Figure 118. Calculated structures and energies for the corresponding precursor (R), transition state (TS), and product (P) for the most favorable pathway of self-cleavage in HDV ribozyme. Reprinted in part with permission from ref 707. Copyright 2008 American Chemical Society.
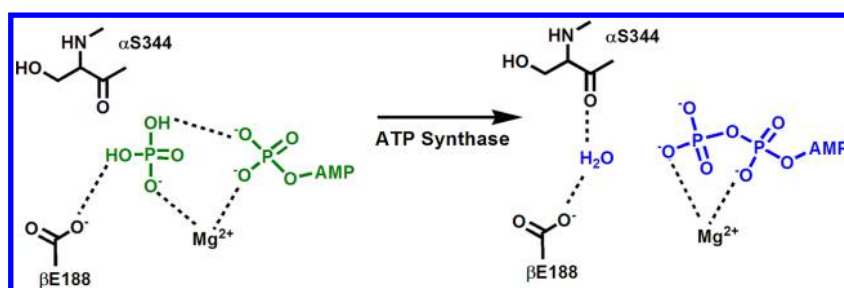
Figure 119. Proposed reaction pathway for ATP synthesis (ADP + H$_2$PO$_4^-$ → ATP + H$_2$O). Adapted with permission from ref 711. Copyright 2011 National Academy of Sciences.
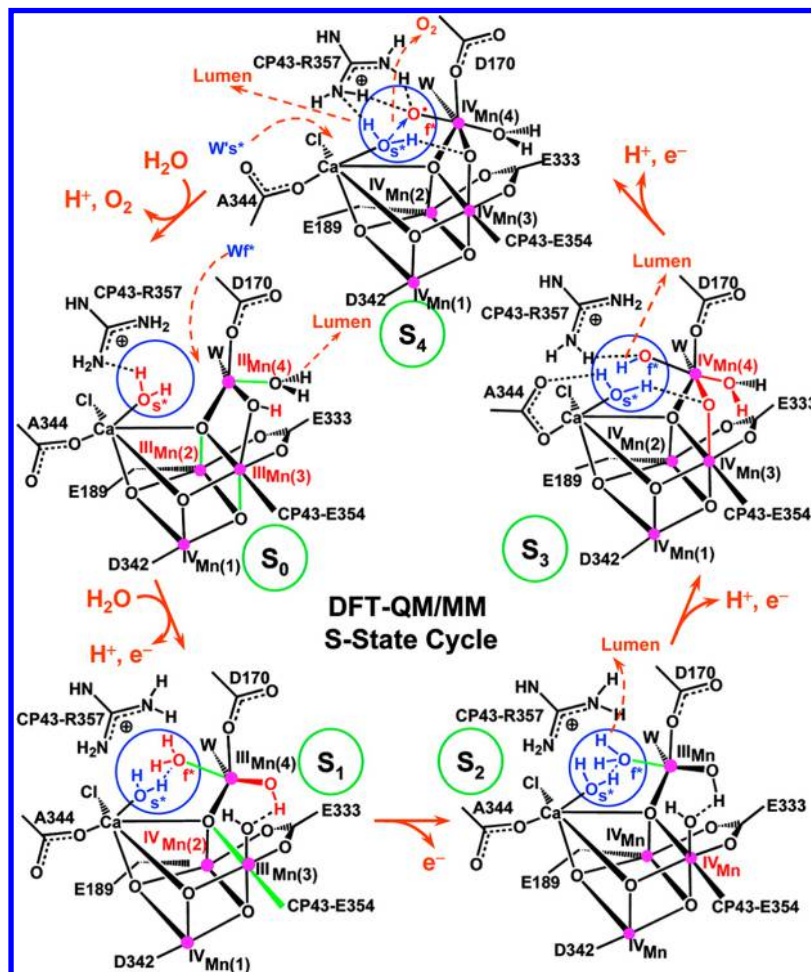
Figure 120. Proposed catalytic cycle of water splitting in photosystem II. Reprinted with permission from ref 714. Copyright 2008 American Chemical Society.
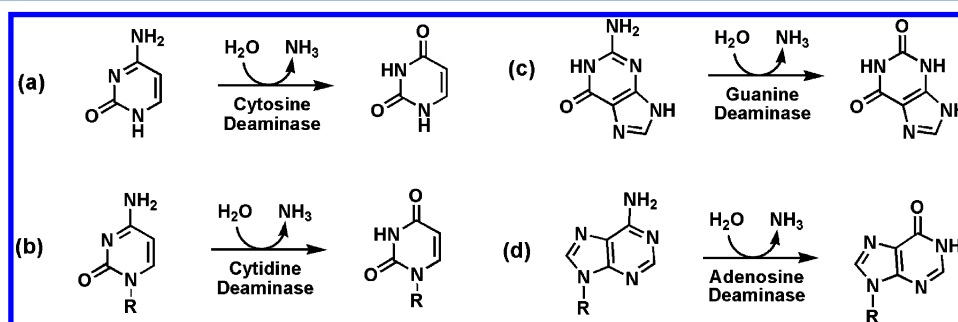
Figure 121. Deamination reactions in (a) cytosine, (b) cytidine, (c) guanine, and (d) adenosine deaminases.

ATP synthesis is a very important biological reaction in living organisms. Therefore, the enzymatic mechanism of ATP synthase has been an important subject for experimental and theoretical studies.[708a,710] The detailed reaction pathway of ATP synthesis (Figure 119) also has been investigated by ONIOM(B3LYP:AMBER). According to the calculated results, the reaction is initiated by double proton transfer from $H_2PO_4^-$ followed by reaction with ADP to form ATP and H_2O. Mg^{2+} and the residues αS344 and βE188 play crucial roles in promoting these steps. In addition, the activation barrier of the reverse process (i.e., hydrolysis of ATP) was found to be increased in the tight binding site, which suggests that the protein conformation favors ATP synthesis.[711] Recently, the same group performed ONIOM calculations to further reveal significant effects of the protein environment that lower the barrier of ATP hydrolysis in the loose binding site of ATP synthase, as compared to that in the tight binding site ($\sim$1 Å-scale movement of the binding site).[712]

Recently, an ONIOM(DFT:AMBER) (DFT = B3LYP and MPWB1K) study was employed to study the mechanism of hydrolysis of *myo*-inositol-1-phosphate (Ins(1)P) to form *myo*-inositol (MI) and inorganic phosphate in *myo*-inositol monophosphatase (IMPase).[713] Mg^{2+} ion, a cofactor of IMPase, was proposed to be critical for catalyzing the hydrolysis reaction. This ONIOM work supported the presence of two Mg^{2+} ions in the active site, with one phosphorus oxygen atom of the substrate functioning as a general acid−base catalyst.

9.2.1.6. Manganese-Containing Enzymes. The Mn and Ca cluster [Mn_4CaO_4] of photosystem II (PSII) is very important for oxygen evolution during photosynthesis. Sproviero et al. reported their ONIOM(B3LYP:AMBER)//ONIOM-(HF:AMBER) calculations to elucidate the challenging and important catalytic mechanism of water splitting in the PSII (Figure 120).[714] The ONIOM-optimized structures of this oxygen-evolving complex (OEC) in the S_0−S_4 states were shown to be comparable to the available experimental data. The proposed mechanism involves coordination of water substrates with Mn(4) and Ca, followed by deprotonation of the water molecule ligated with Mn(4) to form a reactive Mn(IV)-oxyl radical and finally nucleophilic attack of the oxyl radical by the Ca-coordinated water molecule to generate O_2 (Figure 120).[714]

9.2.1.7. Zinc-Containing Enzymes. Cytosine, cytidine, guanine, and adenosine deaminases are zinc-containing metalloenzymes, and play important roles in the activation process of anticancer drugs and catabolism (Figure 121). Matsubara et al. developed and applied an ONIOM BOMD method (section 2.3.1.1) to study the dynamics of cytosine and cytidine deaminases (Figure 121a,b). They found that the thermal motion and perturbation of the protein environment could easily break the Zn−O bond and release the product (uracil or uridine). The C−N bond cleavage to release NH_3 molecule in the deamination reactions was suggested to be the rate-determining step.[156,588a]

In addition, ONIOM(B3LYP:PM3) calculations were carried out to study the reaction mechanism of cytosine deamination in yeast cytosine deaminase (yCD).[715] The proposed mechanism involves the Zn-bound hydroxide attacking the carbon center, promoting C−N bond cleavage. The last and rate-determining step is the oxygen exchange.[715] The mechanism of the Zn−O bond cleavage in yCD was further explored by ONIOM calculations combined with classical simulations (section 2.3.1.6), which allowed relaxation of the surrounding protein and some key residues in the active site during the reaction

process.[172] The ONIOM calculations estimated a low activation barrier of 3 kcal/mol for the Zn−O bond cleavage in yCD. The electrostatic interaction of Glu64 with Zn was found to promote the Zn−O bond breaking. The same group also investigated the mechanism of the deamination of guanine to xanthine in guanine deaminase (GD, Figure 121c) by means of ONIOM(B3LYP:AM1) and MD simulations.[716] Similar to the deamination in yCD, the proposed reaction mechanism for GD involves proton transfers, nucleophilic attack of the Zn-bound hydroxide to the carbon center, C−N bond cleavage, and finally Zn−O bond cleavage to give xanthine. The C−N bond breaking step was found to be the rate-determining step with a barrier of $\sim$9 kcal/mol. Glu55 and Asp114 were suggested to play key roles in proton shuttling in the guanine deamination reaction.[716]

Wu et al. carried out ONIOM(DFT:AMBER) calculations to understand the catalytic mechanism of the adenosine deamination reaction in adenosine deaminase (AD, Figure 121d).[717] As in the cases of other deaminases, Glu217 was suggested to be the catalytic base to abstract one proton from the zinc-bound water molecule, and the deamination step was found to be the rate-determining step with a barrier of $\sim$11 kcal/mol in AD.

Carboxypeptidase A (CPA) is also a zinc-dependent protease, in which the zinc ion plays a key role in the enzymatic reaction. In a study of an irreversible inactivation of CPA, ONIOM(HF:AMBER) calculations showed that it may be caused by the zinc ion promoting a barrierless S_N2 reaction to form a covalent bond between Glu270 and 2-benzyl-3-iodopropanoate inhibitor in the active site.[718] The matrix metalloproteinases (MMPs) are also zinc-dependent enzymes. The inhibition mechanisms involving (4-phenoxyphenylsulfonyl)methylthiirane (SB-3CT) and its analogues in MMP-2 and MMP-3 have been studied by using ONIOM(B3LYP:AMBER) and ONIOM(B3LYP:MNDO) calculations, respectively.[26,719,720] One glutamate (Glu404 in MMP-2 and Glu202 in MMP-3) was found to function as a catalytic base, abstracting a proton from the inhibitor to trigger the opening of the three-membered ring in MMP-2, and abstracting a proton from the zinc-bound water in MMP-3. In addition, the catalytic mechanism of peptide deformylase was investigated using ONIOM(PBE1PBE:AMBER) calculations.[721] The proposed mechanism of deformylation in peptide deformylase involves the rate-determining nucleophilic addition of the metal (Zn^{2+}, Ni^{2+}, and Fe^{2+})-bound water or hydroxide to the carbonyl carbon, followed by proton transfer, and finally C−N bond cleavage to release the product. A ONIOM-(B3LYP:AMBER) method was also used to identify the second bridging ligand of metal ions (Zn^{2+} and Mg^{2+}) in the active site of cyclic nucleotide phosphodiesterases (PDEs). A hydroxide ion was suggested to be the bridging ligand, rather than a water molecule.[722]

In addition, zinc has a central role in the domain responsible for the binding and activation of homocysteine (Hcy) in MetH. The mechanism of the zinc coordination exchange remains unclear: both associative and dissociative pathways have been proposed. ONIOM(B3LYP:AMBER) calculations support the dissociative and barrierless mechanism in MetH, in which the Zn−O(Asn234) bond is cleaved before formation of the Zn−S(Hcy) bond. A large protein effect on the zinc coordination exchange has been found in MetH, which favors the ligation of the Hcy substrate.[723]
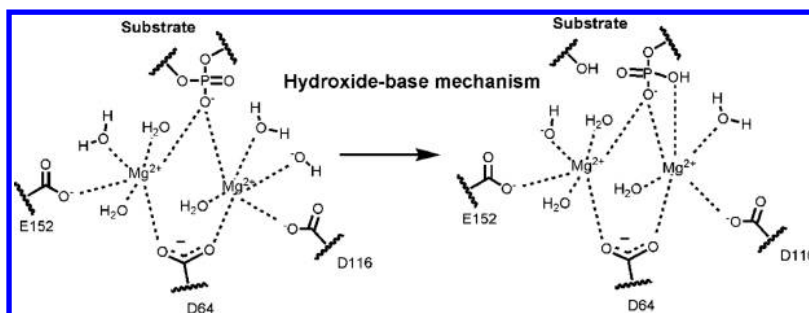
Figure 122. Proposed mechanism for phosphodiester bond hydrolysis (left, reactant; right, product) in human immunodeficiency virus (HIV-1) integrase. Adapted with permission from ref 731. Copyright 2012 American Chemical Society.

9.2.2. Nucleic Acids. In addition to ONIOM applications to reaction mechanisms in proteins, the ONIOM method has also been applied to study reactions involving DNA and RNA. A review article on theoretical methods and applications to RNA catalysis has been published.[724] Herein, we briefly outline some of the ONIOM studies on the reactions in DNA.

Ribonucleotide reductase (RNR) is a very important enzyme, which catalyzes conversion of ribonucleotides to deoxyribonucleotides in DNA synthesis. An ONIOM method has been used to study the first and second steps of the catalytic cycle of class I RNR.[725,726] For the proposed first step in RNR, a Cys439 radical abstracts a hydrogen atom from C3′ of the ribonucleotide. Ser436-Ile442, the side chain of Cys225, and the substrate (ribose ring) were included in ONIOM-(B3LYP:AM1) calculation.[725] This study suggested that stabilization from the enzyme−substrate interactions is counterbalanced by the conformational energy. Therefore, the effect of the enzyme on the overall barrier and reaction energy for the first step is small. The same research group also carried out three-layer ONIOM(B3LYP:AM1:CHARMM) calculations to study the mechanism of the second step.[726] Their calculations suggested that the proton abstraction of the C3′−OH by Glu441 is concerted with the elimination of one water molecule from the C2′−OH by a proton transfer from the nearby Cys225. However, the environmental effect was found to be insignificant. Also, the reaction barrier for the second step of the enzymatic reaction was found to be similar to the active-site model.[726] Therefore, the role of the biological environment might be to protect the reactive radical in the active site from attack by the solvent.[725,726]

Proton transfers in DNA base pairs are important in many biological processes. Multiple proton transfers in DNA base pairs coordinated to cisplatin were studied by an ONIOM-(mPW1PW91:UFF) method.[727] The ONIOM calculations showed that single proton transfer can take place in a model with four base pairs, and the product was calculated to be less stable than the reactant (before proton transfer) by ∼3 kcal/mol. In addition, the effect of cisplatin on DNA structures (the tautomeric equilibrium in guanine−cytosine (GC) base pairs) was recently studied by an ONIOM(M06-2X:UFF) method.[728] This study suggested that the Pt−DNA complex can induce a proton transfer in the GC base pair, and may lead to permanent mutation of the cisplatin−DNA system.[728] In another study, the electron-attachment-induced proton transfer in G:C•− (QM part) in the B-form DNA trimer, d(5′-GGG-3′)·d(3′-CCC-5′) (called a (dG:dC)₃ model), was investigated by an ONIOM(B3LYP:PM3) method.[729] For comparison, the calculations were also carried out using a model without the sugar−phosphate backbone (called a (G:C)₃ model). This

study suggested that the sugar−phosphate backbone and counterions have very minor effects on the proton-transfer process in G:C•−, and the electrostatic interaction with the neighboring G:C base pairs can increase the proton-transfer barrier. On the other hand, hydration significantly lowers the barrier and stabilizes the proton-transfer product.[729]

Human alkyladenine DNA glycosylase (AAG) catalyzes the cleavage of the N-glycosidic bond in 1,N⁶-ethenoadenine (εA), N³-methyladenine (3MeA), and adenine (A) nucleotides. These reactions help repair some of the alkylated and deaminated purines. The catalytic reaction mechanism of the glycosidic bond cleavage in AAG was studied by ONIOM-(M06-2X:AMBER) to obtain a potential energy surface (PES).[730] The ONIOM results showed that the reaction of the neutral εA or cationic 3MeA both follow a concerted (A_ND_N) pathway for the hydrolytic glycosidic bond cleavage. The DNA−protein $\pi-\pi$ interactions and hydrogen bonding in the active site decrease the free energy of activation for εA (87.3 kJ/mol) and 3MeA (57.9 kJ/mol) in AAG. In comparison, the excision of adenine occurs via a stepwise pathway (i.e., the glycosidic bond cleavage followed by an nucleophilic attack of a water molecule) with a higher energy barrier, possibly due to the loss of the hydrogen bond with Tyr127 and poor reorientation of the Glu125 base and water nucleophile.[730]

Recently, the mechanism of the 3′-end processing reaction in human immunodeficiency virus (HIV-1) integrase (INT) with a ssDNA GCAGT substrate was investigated by ONIOM-(MPWB1K:AMBER)//ONIOM(B3LYP:AMBER) calculations.[731] Three possible mechanisms (aspartate-base, phosphate-base, and hydroxide-base) were computationally investigated. This ONIOM study did not support the aspartate-base and phosphate-base mechanisms, due to their computed high barriers of ∼36 kcal/mol. The most feasible mechanism of hydrolyzing the DNA substrate was found to be the hydroxide-base mechanism (Figure 122). The calculated free energy of activation of this hydrolysis pathway was ∼15 kcal/mol, which is in agreement with the experimental observation.[731]

DNA polymerase β (pol β) also plays an important role in DNA repair and replication. The reaction mechanism of the nucleotidyl transfer to the sugar acceptor was studied by ONIOM(B3LYP:AMBER) to obtain a PES.[732] Proton transfer from O3′ of the terminal primer to Asp256 (acting as a general base) was computed to be nearly barrierless. The subsequent nucleophilic attack of O3′ on the α-phosphorus (P_α) of dNTP had a computed barrier of ∼14−21 kcal/mol. EDA showed that the electrostatic interactions from the surrounding environment greatly stabilize the transition state. Two such stabilizing residues, Arg149 and Arg183, also play important roles in the

nucleotide binding and stabilizing the transition state structure.[732] Very recently, the same research group carried out ONIOM(B3LYP:AMBER) calculations to study the mechanism of the nucleotidyl transfer in the pol β enzyme and its D256E mutant.[733] One goal was to elucidate the key role of Asp256 in the activation of O3′. In the wild-type pol β enzyme, the O3′ proton transfer was suggested to easily occur. The concerted O3′−P$_\alpha$ bond formation and P$_\alpha$−O bond cleavage had a low barrier (~14 kcal/mol). Although the proton of O3′ can transfer to Glu256, the proton-transfer process was found to be very slow, and the bond forming/breaking process had a high barrier of ~21 kcal/mol. This slow reaction in the D256E mutant was attributed to the reorganization of the active-site residues (especially Arg254). Therefore, Asp256 was proposed to be a key residue in the pol β enzymatic catalysis that favors the O3′ proton transfer and activation.[733]
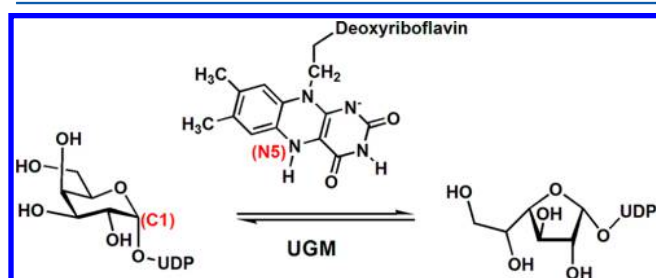
Figure 123. Interconversion of UDP-Gal*p* and UDP-Gal*f* catalyzed by UGM.

9.2.3. Carbohydrates. *Escherichia coli* (lacZ) β-galactosidase catalyzes hydrolysis and transglycosylation reactions. The mechanism of the hydrolysis and transglycosylation with a lactose substrate in the β-galactosidase was studied by ONIOM(BB1K:AMBER)//ONIOM(B3LYP:AMBER).[734] The magnesium ion was proposed to play a crucial role in lowering the activation barrier (by 14.9 kcal/mol) of the first step of the glycosidic bond cleavage of the lactose molecule leading to formation of the galactosyl-enzyme intermediate. In the subsequent hydrolysis step, a water molecule attacks the galactosyl-enzyme intermediate, and the calculated barrier and reaction energy are 15.5 and −9.2 kcal/mol, respectively. For the transglycosylation reactions in the second step, formation of the β(1−6) glycosidic linkage was computed to be more thermodynamically favorable, with a lower reaction energy (~−9 kcal/mol). The enzyme microenvironment was found to provide a large catalytic effect by stabilizing the transition state more than the reactants.[734]

A flavin-containing UDP-galactopyranose (UDP-Gal*p*) mutase (UGM) catalyzes an interconversion of UDP-Gal*p* and UDP-galactofuranose (UDP-Gal*f*) (Figure 123). ONIOM-(B3LYP:AMBER)-EE//ONIOM(B3LYP:AMBER)-ME calculations were performed to elucidate the mechanism of the conversion of UDP-Gal*p* to UDP-Gal*f* in UGM.[735] The completely reduced form of the flavin was suggested to be required in the reaction. The proposed reaction mechanism is complicated, involving a nucleophilic attack of N5$_{FAD}$ of the flavin on C1 of the substrate, O−C1 bond breaking of the substrate, N5$_{FAD}$−H proton transfer to trigger the ring-opening, many tautomerizatons, formation of a furanose ring, and nucleophilic attack on C1 by one phosphate oxygen of the substrate concerted with C1−N5 glycosidic bond breakage,

together with proton transfer back to the N5$_{FAD}$ center. The results elucidated the important role of the flavin cofactor. The environment was found to lower the overall barrier by 20.8 kJ/mol, rendering the reaction highly exergonic.[735]

Trichoderma reesei Cel7B is an endoglucanase that catalyzes the *p*-nitrophenyl lactoside (PNPL) hydrolysis by glycosylation
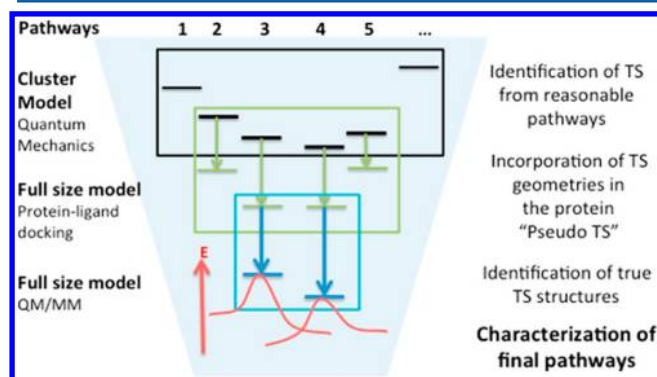
Figure 124. Integrated multilevel computational approach to construct the active site of an artificial imine reductase. Reprinted with permission from ref 738. Copyright 2014 American Chemical Society.

and deglycosylation. ONIOM(B3PW91:AM1) calculations were carried out to investigate the catalytic mechanism of Cel7B.[736] The nucleophilic attack and the breakage of the glycosidic bond in the glycosylation and deglycosylation steps were found to be concerted. The glycosylation step was suggested to be the rate-determining step, with an activation barrier of ~19 kcal/mol.[736] In addition, the reactivity of several mutants was investigated and found to be decreased as compared to that of wild-type Cel7B.

9.2.4. Artificial Enzymes. Incorporation of a synthetic molecule or artificial cofactor into the active site of an artificial enzyme with good catalytic activity attracts much attention. Recently, Robles et al. developed a protocol combining docking and ONIOM(QM:MM) methods to study possible structures and energies of the synthetic cofactor bound to two artificial enzymes.[737,738] In one case, an ONIOM(PBE:AMBER) method was applied to the reaction mechanism of cyclic imine reduction in an artificial imine reductase [Cp*Ir(Biot-*p*-L)Cl]⊂S112A.[738] By means of docking several "pseudo transition states" into the protein, the artificial imine reductase active site was constructed (Figure 124). The ONIOM method was then used to locate the true transition states. The protein interactions and hydrophobic environment were found to decrease the activation barrier by ~10 kcal/mol. In the lowest-energy transition state, Lys121 stabilizes the 1-methyl-6,7-dimethoxy-3,4-dihydroisoquinoline substrate through hydrogen-bonding and C−H⋯π interactions. In addition, the protein environment (the second coordination sphere) was found to be responsible for the enantioselectivity of the asymmetric hydrogenation of the cyclic imines.[738]

Ke et al. carried out ONIOM(B3LYP:AMBER) calculations to investigate the mechanism of phenylacetylene (PA) polymerization catalyzed by an artificial enzyme consisting of rhodium complexes in apo-ferritin (Rh(nbd)·*apo*-Fr) by using a single ferritin subunit as the model.[739] This study suggested that among several active site models, active site D is best for the polymerization. The reaction was predicted to occur in the active site D via a Rh^I-insertion mechanism. A specific "hydrophobic region" near the 4-fold channel was suggested
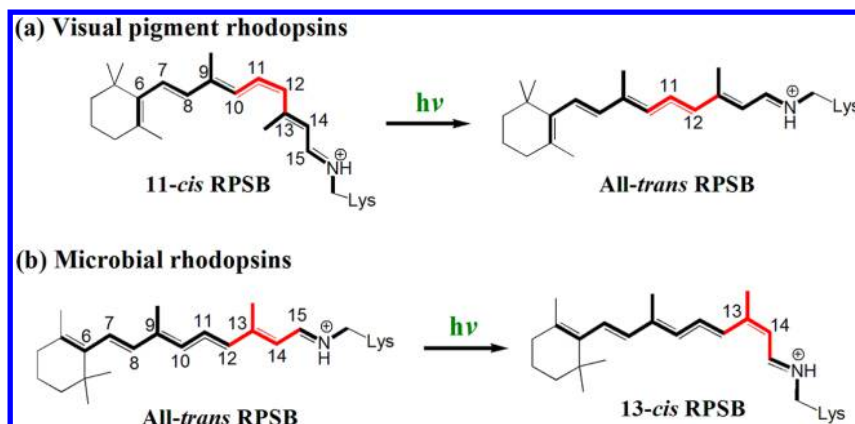
Figure 125. Light-induced photoisomerization reactions in (a) visual pigments and (b) microbial rhodopsins.

to facilitate the accumulation, coordination, and insertion of PA for polymerization.

Petrova et al. carried out classical MD and ONIOM(M06-2X:AMBER) calculations to investigate the origin of an enantioselective intramolecular Friedel–Crafts reaction involving a supramolecular Cu/DNA catalyst L-Cu(II)-R/d-(CAAAAATTTTTG)$_2$ with 28 conformers.[740] The computed binding affinity of pro-S conformations of L-Cu(II)-R to DNA was proposed to promote the formation of the (S)-product, as the conformations are structurally more similar to the C–C bond formation transition state and would require less energy for deformation and conformational changes.

9.3. Applications to Photobiology

Photobiological systems absorb the energy of light to induce many crucial reactions involving electronically excited states. These reactions, including photosynthesis in plants, DNA repairing, and light-induced signal transduction, can proceed through pathways that are different from those of ground-state biochemical reactions. However, investigations of photophysical and photochemical processes in photobiological systems are very challenging, partly due to the fact that electronically excited states cannot be described by MM methods (albeit MMVB and eFF have been developed for studying excited states[741]) and calculations for QM methods are very demanding. This section summarizes some applications of the ONIOM method to photobiological systems.

9.3.1. Rhodopsins. Visual pigments and microbial rhodopsins are seven-helix transmembrane proteins. However, these two types of rhodopsin proteins have different structures and different chromophore conformations (11-*cis* and all-*trans* retinal protonated Schiff base (RPSB), respectively; see Figure 125).

9.3.1.1. Spectral Tuning. The spectroscopic properties of rhodopsins are crucial to their functions. The spectral shift of the chromophore in the protein is a key issue, and its protein effects (electrostatic controlling, polarization effect, and/or steric interaction) have been investigated extensively.

An ONIOM(QM:MM) method has been used to compute absorption energies and ^{1}H/^{13}C NMR spectra of the chromophores in the proteins to understand the origin of the color tuning.[742,743] In addition, ONIOM(QM1:QM2:MM) calculations were performed to understand the effects of the protonation state of Glu181 in the visual pigment rhodopsin. The ONIOM results demonstrated that the neutral or anionic Glu181 can give similar structures, excitation energies, and NMR spectra for the dark-state rhodopsin.[69] Moreover, the
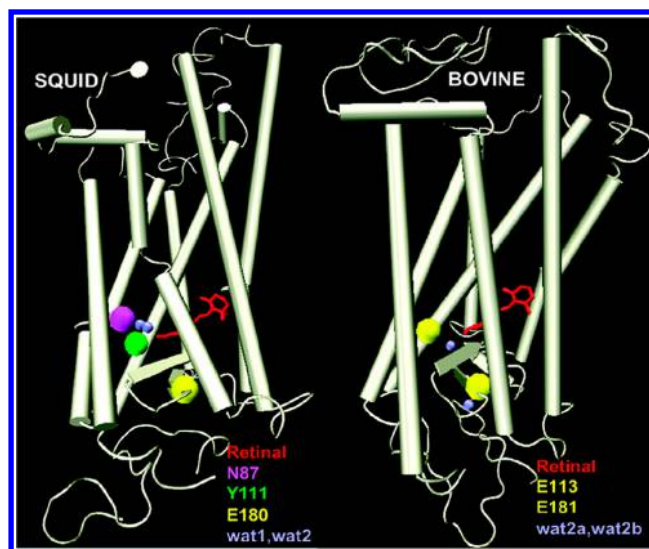
Figure 126. Protein structures of squid (invertebrate) and bovine (vertebrate) rhodopsins. Reprinted with permission from ref 748. Copyright 2011 American Chemical Society.

more accurate SAC-CI method combined with ONIOM-(QM:MM) calculations was performed to further analyze and understand the protein environmental effects (by including the larger size of the residues surrounding the RPSB chromophore).[744]

9.3.1.2. Visual Pigment Rhodopsins. The visual pigment rhodopsin (Rh) is a G-protein-coupled receptor (GPCR), which contains the 11-*cis* RPSB chromophore (Figure 125a). On the basis of the crystal structure of bovine Rh, Altun et al. have investigated absorption energies and spectral tuning in bovine Rh and its mutants (Figure 126).[745,746] According to ONIOM(QM:AMBER) calculations, the B3LYP functional was found to be better than BLYP in terms of the structures and the computed absorption energies (QM = TD-B3LYP). In addition, the electronic polarization of the bovine Rh protein is important for obtaining the reliable geometry of the chromophore, and the calculated absorption energy (503 nm) agrees well with the experimental value (500 nm).[745] Using the reliable B3LYP-optimized structures, higher-level QM methods (e.g., SORCI+Q, MRCISD+Q, and MR-DDCI2+Q) were applied to calculate the absorption energies of the retinal in the gas phase and in the bovine Rh protein.[746] As to the origin of the spectral shift, the important counterion Glu113 in bovine
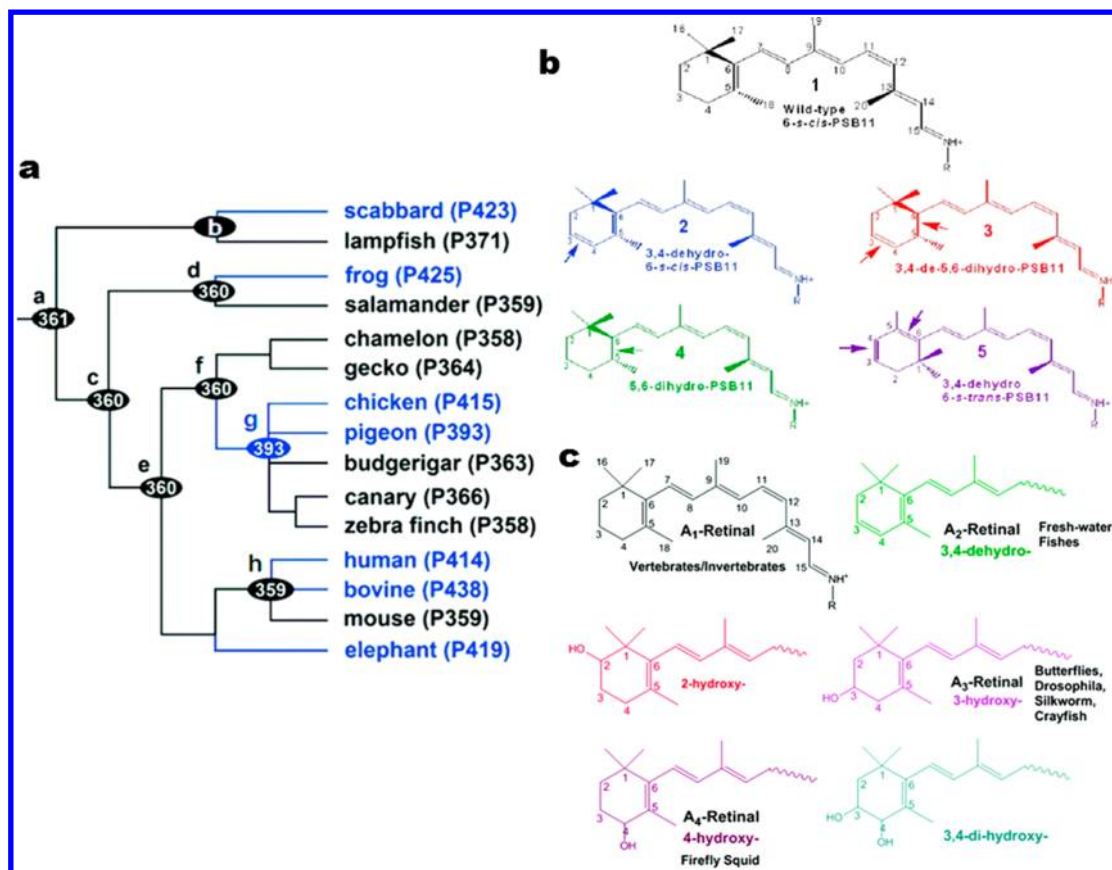
Figure 127. (a) An evolutionary tree of short wavelength-sensitive pigments. (b) The dehydro and dihydro β-ionone retinal analogues in squid and bovine Rhs. (c) The A₁-, A₂-, A₃-, A₄-, 2-hydroxy-, and 3,4-dihydroxy-retinals. Adapted with permission from refs 748, 751, and 754. Copyright 2010 and 2011 American Chemical Society.

Rh is responsible for the shifted absorption energy. The other neighboring charged residues individually can also affect the absorption energy. Apart from ONIOM geometry optimization, various protein conformations can be obtained from different snapshots of MD simulations. The snapshots then can be used to evaluate the absorption or emission energies. For instance, DFTB,[152] a semiempirical method, can be used for DFTB/MM MD simulations to sample initial protein conformations.[747]

On the basis of the crystal structure of bovine Rh (Figure 126), unknown structures of the human and mouse visual pigments were constructed by the homology modeling approach. Their spectroscopic properties then were investigated by ONIOM(QM:MM).[749] Single- and multireference methods, such as TD-B3LYP, RI-CC2, MRCISD+Q, SORCI+Q, and DDCI2+Q, were used as the QM method. According to this ONIOM(QM:MM) study, the ultraviolet (UV)-sensitive mouse pigment (with an absorption maximum of 359 nm) has a deprotonated Schiff-base chromophore, whereas the violet-sensitive human pigment (with an absorption maximum of 414 nm) has a protonated chromophore. The polarization effect of the protein environment leads to an increased bond-length alternation (BLA) of the 11-*cis* RPSB in the human visual pigment, which significantly induces the blue shift in the absorption energy from 500 nm in the bovine Rh to 414 nm in the human pigment. The counterion Glu113 also influences the absorption energy of the protonated Schiff base, but not the deprotonated Schiff base.[749] Interestingly, their ONIOM(TD-B3LYP:AMBER)//ONIOM(B3LYP:AMBER) study on the UV-sensitive and violet-sensitive fish pigments showed that the conversion between the deprotonated and protonated forms of the Schiff base is induced by deleting Phe86 and stabilized by the altered hydrogen-bond network around the chromophore.[750] In addition, the hydrogen-bond network has been shown to determine the protonation state of the retinal Schiff base and thus regulate the UV or violet sensitivity of visual pigments in vertebrates (Figure 127a).[751]

As in bovine Rh, squid Rh has the 11-*cis* RPSB chromophore. Sekharan et al. have investigated the protein structure (especially water molecules close to the chromophore in the active site, Figure 126) and the spectra of squid Rh by using ONIOM(SORCI+Q:AMBER)//ONIOM-(B3LYP:AMBER).[752] Glu180 in squid Rh was regarded as the key counterion, which had strong electrostatic interactions with the 11-*cis* retinal chromophore, and played a crucial role in the spectral shift from the gas phase to the protein by ~100 nm.[752] In addition, several 11-*cis* retinal analogues in squid (invertebrate) and bovine (vertebrate) Rhs have been further studied by using the same ONIOM method.[753,754] The study of the dehydro and dihydro β-ionone ring of the 11-*cis* retinal analogues in squid and bovine Rhs (Figure 127b) provided more insight into the chromophore–protein interactions and the characteristic properties of the binding site (squid Rh, flexible; bovine Rh, rigid). Absorption energies of the modified 11-*cis* retinal chromophores in different environments were calculated for salamander Rh, in which the π-conjugation is expanded from **1** to **2** in Figure 127b, leading to a red shift of ~20 nm from squid or bovine Rh to salamander Rh.[754] On the basis of the ONIOM-optimized structures, stabilities, and

absorption energies of the 7-*cis*, 9-*cis*, 11-*cis*, and 13-*cis* retinal in bovine and squid Rhs, Sekharan et al. further explained why the 11-*cis* retinal occurs in nature.[755] In addition, the A_1-, A_2- (3,4-dehydro-), A_3- (3-hydroxy-), A_4-(4-hydroxy-), 2-hydroxy-, and 3,4-dihydroxy-retinals in squid and bovine Rhs (Figure 127c) were comparatively investigated by ONIOM(SORCI+Q:AMBER)//ONIOM(B3LYP:AMBER). Relative to the A_1-pigments, the A_3- and A_4-pigments showed a blue shift of the absorption energy because of the increased BLA of the hydroxyl retinal, whereas the A_2-pigments exhibited a red-shifted absorption energy due to the extended π-conjugation of the retinal chromophore. According to a spectral-tuning study in small white butterflies, the blue-sensitive (PrB) and violet-sensitive (PrV) pigments were also theoretically obtained by mutating two key sites (116 and 185), which altered the hydrogen-bond network.[748] When studying the monkey and bovine visual pigments, an OH site-specific rule was proposed: interactions of the dipolar residues near the Schiff base and β-ionone can lead to the blue shift and the red shift in the absorption energy, respectively.[756] Also, the protein structure of mouse melanopsin was theoretically constructed by the homology modeling approach (based on the crystal structure of squid Rh) and mutation of several residues. The absorption energies were evaluated by an ONIOM(SORCI+Q:AMBER)//ONIOM(B3LYP:AMBER) method.[757] These systematic ONIOM studies furthered our understanding of the retinal chromophore and its analogues.

In addition to the spectroscopic studies on Rhs, the energy storage and the optical shifts in bovine and squid bath-orhodopsins were calculated by ONIOM(QM:AMBER) methods (QM = B3LYP for the storage, and QM = SORCI+Q for the optics).[758] For the flexible binding site in squid bathorhodopsin, the energy storage (~27 kcal/mol) was found to decrease by ~16 kcal/mol with the relaxation of the nearby protein environment (4 Å within the chromophore). In comparison, for the more rigid binding site in bovine bathorhodopsin, the energy storage (~26 kcal/mol, in an agreement with the previous ONIOM(B3LYP:AMBER) work[743a]) decreased by ~8 kcal/mol with relaxation of the nearby residues. As for the optical shift in bathorhodopsin, it is mainly due to the interaction between the retinal chromophore and the counterion (Glu113 in bovine bathorhodopsin and Glu180 in squid bathorhodopsin).[758]

Very recently, ONIOM(QM:MM)-PE was developed and applied to the geometry optimization of Rh.[115a] The MM protein part was divided into the polarizable and nonpolarizable MM regions. By including the mutual polarization between the QM and MM parts, a minor increase in the BLA of the conjugation bonds (i.e., more localized) of the 11-*cis* retinal chromophore was observed: 0.008 and 0.010 Å for B3LYP and CAM-B3LYP as the QM method, respectively.

9.3.1.3. Microbial Rhodopsins. One of the key microbial rhodopsins, bacteriorhodopsin (bR), is a light-driven proton pump that contains the all-*trans* RPSB chromophore in the dark state (Figure 125b). The structure and spectra of bR have attracted a great deal of interest from experimental and theoretical researchers. An ONIOM(QM:MM) method has been used to determine the structure and absorption energies of bR.[28] By comparing HF and B3LYP as the QM method within an ONIOM scheme with an AMBER force field for the MM part, the B3LYP method was found to be more reliable, giving good bond lengths and torsion angles for the all-*trans* chromophore in bR. The electrostatic interaction between the
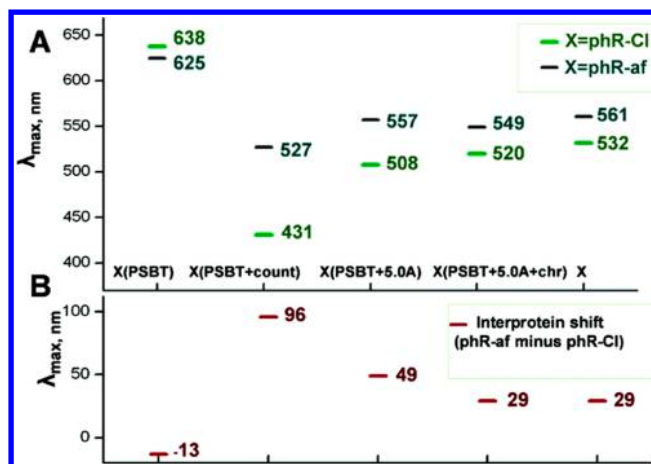
Figure 128. (A) Absorption maxima (λ_{max}) of phR-Cl and phR-af. (B) The interprotein shifts. Reprinted with permission from ref 759. Copyright 2012 American Chemical Society.

all-*trans* RPSB and protein was suggested to be not very critical for decreasing the absorption energy from the solvent to the bR protein.[28]

Halorhodopsin is another microbial rhodopsin, which functions as a light-driven chloride ion pump. Ryazantsev et al. studied the absorption and spectral tuning in halorhodopsin (phR-Cl, chloride-ion-bound; and phR-af, anion-free, Figure 128) by an ONIOM(SORCI+Q:AMBER)//ONIOM-(B3LYP:AMBER) method.[759] This study showed that the spectral shifts in phR-Cl and phR-af are not only due to the electrostatic interaction between the all-*trans* RPSB chromophore and the chloride ion, but also a protein conformational change with alteration of the hydrogen-bond network induced by the presence/absence of the chloride ion.[759] Another related work also discussed the color tuning in halorhodopsin by considering the absence of chloride ion, its replacement by N_3^- or NO_3^-, and mutation of several key residues along the path of the chloride ion transport. Again, the structural reorganization of the protein, together with the change of the hydrogen-bond network and BLA of the chromophore, was found to influence the spectroscopic properties of the all-*trans* RPSB chromophore in halorhodopsin.[760]

9.3.1.4. Photoisomerization Processes. In addition to the spectral tuning mechanism in rhodopsin proteins, photo-isomerization and photodynamics in Rh have also been investigated by ONIOM(QM:MM)-like or ONIOM-(QM:MM) methods.

For the visual pigment Rh, an ultrafast 11-*cis* → all-*trans* photoisomerization process occurs upon the absorption of light (Figure 125a) with a high quantum yield, activating the G-protein and triggering signal transduction. In addition, the 9-*cis* RPSB was also found embedded in the same opsin environ-ment (isorhodopsin, isoRh), in which case the 9-*cis* → all-*trans* photoisomerization is slower, and has a lower quantum yield.

An ONIOM(CASSCF(6e,6o):AMBER) study has shown that the PES of photoisomerization of the 11-*cis* RPSB to the all-*trans* RPSB in Rh is downhill.[761] The study also suggested that from the Franck–Condon (FC) region the ultrafast photoisomerization process occurs via rotation of the 11-*cis* RPSB along the −C11=C12− dihedral angle by ~90° (accessing a crossing funnel of S_0 and S_1). The motion of the retinal can be constrained in the limited protein cavity with the aid of the simultaneous torsion of the −C9=C10− dihedral
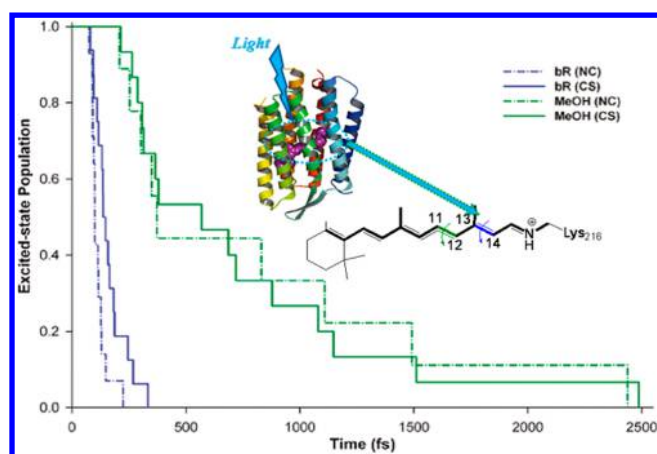
Figure 129. Excited-state population for photoisomerization in bR and methanol (MeOH) via NC (nonadiabatic crossing) and CS (crossing seam) transitions. Adapted with permission from ref 160b. Copyright 2011 American Chemical Society.

angle. In addition, the photoisomerization pathway and photodynamics of the 11-*cis* RPSB in Rh and the 9-*cis* RPSB in isoRh were investigated by ONIOM(QM:MM)-like calculations and MD simulations.[157a,162a,b,762,763] The same protein environment has different steric interactions from the 11-*cis* and 9-*cis* RPSB chromophores, which lead to different photochemical isomerization processes.[157a,162a,b,763]

For bR, a photocycle involving proton transfer and protein conformational changes can be triggered by the all-*trans* → 13-*cis* photoisomerization (Figure 125b), which is ultrafast and very efficient. In comparison, the photoisomerization of the all-*trans* RPSB in methanol solution is much slower and is not efficient, as it produces various photoproducts. Li et al. used ONIOM(B3LYP:AMBER) and nonadiabatic (NA) ONIOM-(CASSCF(12e,12o):AMBER) MD simulations to explore the primary event of the photoinduced isomerization process of all-*trans* RPSB in bR and in methanol solution (Figure 129).[160b] The interactions between the all-*trans* RPSB chromophore and the bR protein were found to confine the photoisomerization to the specific C13=C14 bond (suppressing the rotation of the other bonds by the nearby residues), inducing the unidirectional isomerization. The protein cavity constrains the asynchronous crankshaft motion of the RPSB chromophore. At the S_1-S_0 conical intersection, the electrostatic and polarization interactions between the twisting chromophore and protein (significantly from Asp85 and Asp212) are very large, and decrease the energy gap between S_1 and S_0 by ~16 kcal/mol. In addition, the hydrogen-out-of-plane (HOOP) mode plays an important role around the crossing region. In the absence of the protein matrix or in homogeneous methanol solution, the photoisomerization of the all-*trans* RPSB is not along the C13=C14 bond, but mainly around the C11=C12 bond. Also, the photoisomerization is not efficient and not unidirectional. These ONIOM results indicated that the bR protein efficiently induces the ultrafast all-*trans* → 13-*cis* photoisomerization process.[160b]

9.3.2. Fluorescent Proteins. The photophysical and photochemical properties of green fluorescent protein (GFP) and its related fluorescent protein systems have attracted much attention and are widely used for bioimaging. Herein, we only review some ONIOM applications to fluorescent proteins.

9.3.2.1. Structures and Spectroscopic Properties. An ONIOM report has shown that the β-barrel of GFP can rigidly restrain and stabilize the chromophore through hydrogen bonding.[764] Thus, this is responsible for the enhanced fluorescence of the anionic GFP chromophore. In addition, the quenching process of GFP compressed by force was studied by an ONIOM(CASSCF:AM1) method.[765]

To obtain accurate absorption energies of the GFP chromophore in proteins, the popular ONIOM(QM:MM) method was chosen to optimize the GFP protein and its mutants. The QM region included the chromophore only or the chromophore along with its nearby key residues. Then, the absorption energies and spectral tuning were computed by using INDO/S-CIS, TD-DFT, CASPT2, or SAC-CI as the QM method in the ONIOM calculations.[593d,766,767] For instance, the protein-induced red shift (0.23 eV) of the absorption energy was calculated by the ONIOM(TD-B3LYP:AMBER)-CPCM-X method.[593d]

A new reversibly photoswitchable GFP-like protein Dronpa has been extensively investigated by ONIOM(QM:MM) calculations (Figure 130), where TD-B3LYP, CASSCF, CASPT2, and SAC-CI methods were used for the QM methods. The high-level CASPT2 and SAC-CI calculated absorption (N_{trans}, 3.18−3.24 eV; and A_{cis}, 2.42−2.71 eV) and emission (N_{trans}, 2.12−2.84 eV; and A_{cis}, 2.08−2.42 eV) energies of the neutral *trans* (N_{trans}) and anionic *cis* (A_{cis}) chromophores in Dronpa were in good agreement with the
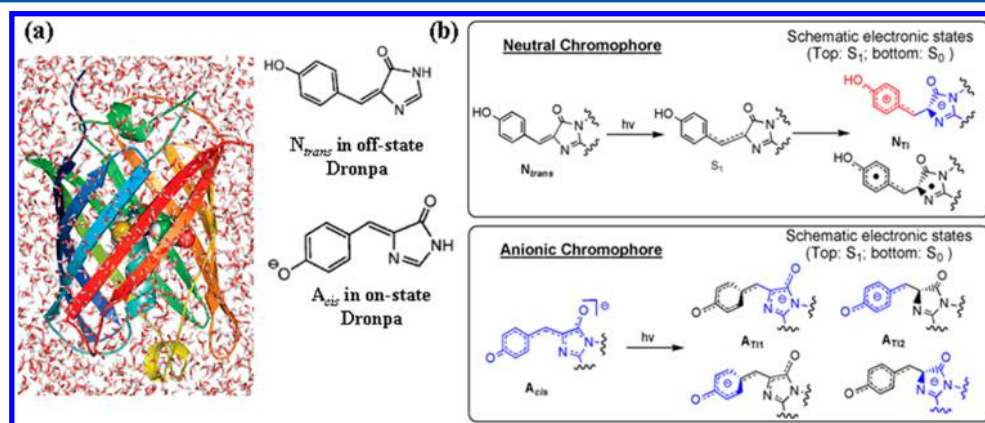
Figure 130. (a) The protein structure and N_{trans}/A_{cis} chromophores of Dronpa. (b) Schematic representation of electronic structures of the chromophores during the photoisomerization. Adapted with permission from ref 768. Copyright 2010 American Chemical Society.

experimental values.[768] The N_{trans} and A_{cis} forms were proposed to be in the nonfluorescent (off) and fluorescent (on) states, respectively. In addition, a very large red-shift of the emission (∼0.6 eV) was observed for the N_{trans} chromophore in off-state Dronpa.

Recently, the vibrational frequencies of GFP were calculated by an ONIOM(B3LYP:AMBER) method. Relative to the bare GFP chromophore, the computed vibrational modes of the chromophore in the protein can reproduce the experimental results.[43c] Therefore, the effect of the protein environment on the vibrational modes of the chromophore can be interpreted and compared.

9.3.2.2. Ground- and Excited-State Reactions. The mechanism of formation of the GFP chromophore in the wild-type GFP protein was investigated by ONIOM-
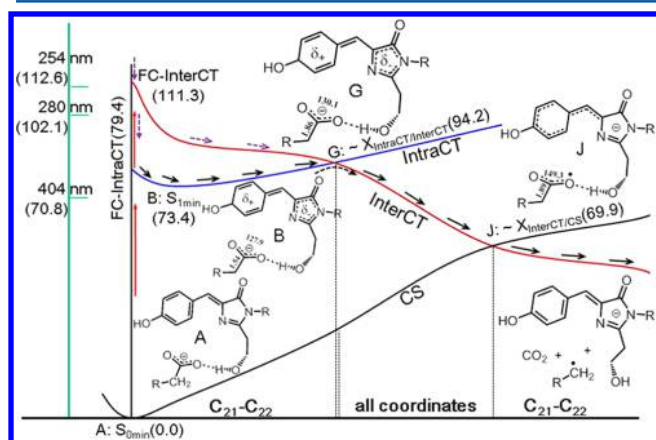

Figure 131. Schematic representation of photoinduced decarboxylation in PA-GFP. Reprinted with permission from ref 771. Copyright 2013 American Chemical Society.

(B3LYP:AMBER) calculations.[769] These ONIOM calculations found a very high-energy barrier for the deprotonation of the α-carbon of Tyr66. Moreover, a barrierless *trans−cis* isomerization was found to occur after the formation of the acylimine in the DsRed chromophore by an ONIOM(B3LYP:AMBER) method.[770]

Photoactivatable (PA) GFP, a new class of fluorescent proteins in which the intensity of fluorescence is dramatically enhanced (∼100-fold) due to light-induced decarboxylation, has attracted much scientific interest. Ding et al. employed an ONIOM(CASPT2:AMBER)//ONIOM(CASSCF-(10e,7o):AMBER) method to investigate the reaction mechanism of the photoinduced decarboxylation in PA-GFP.[771] The ONIOM calculations suggested that the decarboxylation process starts from the first intraCT excited state (intraCT state), and then proceeds along an interCT state after the first crossing $X_{intraCT/interCT}$ (or an approximate transition state) with a barrier of ∼12 kcal/mol (the rate-determining step for the entire decarboxylation process) (Figure 131). Furthermore, the subsequent step is barrierless, reaching the closed-shell (CS) ground state through a crossing of interCT and CS states. Electrostatic and van der Waals interactions were suggested to be important in stabilizing the intraCT and interCT states.[771] This ONIOM study supported the proposed Kolbe pathway, which may be a common mechanism for the irreversible photoinduced decarboxylation in other fluorescent proteins.

A novel photoconversion fluorescent protein, Kaede, can irreversibly alter the fluorescence color from green to red by irradiation with UV light. The mechanism for the green-to-red conversion pathway has been under debate for a long time. To understand the spectral tuning and conversion mechanisms, the absorption energies and the green-to-red conversion mechanisms were studied by ONIOM(QM:AMBER) (QM = B3LYP for the mechanisms; QM = SAC-CI and CASPT2 for the absorptions).[772] The ONIOM calculations supported the stepwise E_1 mechanism and proposed a new E_1cb mechanism (but not the proposed concerted E_2 pathway) for the formation of the red chromophore.[772]

In addition to the above ONIOM(QM:MM) calculations and the new proposed mechanism involving photoisomerization coupled with excited-state proton transfer (ESPT, Figure 130),[768] Li et al. also developed and applied nonadiabatic ONIOM(CASSCF(6e,6o):AMBER)-EE MD simulations (section 2.3.1.2) to study photodynamics of the reversible photoswitching in Dronpa.[160a] The photoinduced ultrafast *trans−cis* isomerization was observed for the N_{trans} chromophore in the off-state protein. The on-state protein can restrain the A_{cis} chromophore to its planar conformation for fluorescence, whereas a fast decay was found to occur in the H193T mutation. According to these extensive investigations, the different protein environments around the chromophore play a crucial role for photoisomerization, fluorescence, and decays.[160a]

9.3.3. Photoactive Yellow Protein. Photoactive yellow protein (PYP) is a well-studied photosensor, both experimentally and theoretically. By the absorption of blue light, the anionic PYP chromophore (*p*-coumaric acid, *p*CA) undergoes *trans−cis* isomerization, which triggers the conformational changes of the protein and produces different photocycle intermediates.

The ground-state isomerization of the *p*CA chromophore in the PYP protein was first investigated by an ONIOM-(DFT:PM3) method to obtain the well-refined structures.[773] In addition, the PYP protein effect on the *trans-cis* photoisomerization of *p*CA chromophore was investigated by an IMOMM(CASSCF(2e,2o):AMBER) method.[774] By comparing the isomerization of the *p*CA chromophore in the protein and in the gas phase, the large chromophore−protein interactions were found to be a major driving force that induces the unidirectional and bond-selective *trans−cis* photoisomerization of the *p*CA chromophore.

Recently, an ONIOM(B3LYP:AMBER) method was employed to simulate the near-infrared (NIR) Raman optical activity (ROA) spectra of a locked *p*CA analogue in the PYP protein.[775] As compared to the small active-site model results, the ONIOM calculations reproduced the ROA spectra (within ±10 cm⁻¹ error).[775] Also, these ONIOM calculations were used to assign vibrational modes, demonstrate the structural information on the locked *p*CA chromophore, and predict an out-of-plane distortion of the *p*CA analogue in the PYP protein.

Another key issue in PYP is the hydrogen-bond network around the *p*CA chromophore. A low-barrier hydrogen bond between *p*CA and Glu46 together with a deprotonated Arg52 was found by ONIOM(QM:AMBER) (QM = B3LYP and MP2).[776] However, the calculated absorption energy of *p*CA was found to be similar to that with the neutral Glu46, anionic *p*CA, and a cationic Arg52 in PYP.

9.3.4. Nucleic Acids. In DNA, the absorption of UV light by TpT and TpC results in the formation of cyclobutane-pyrimidine dimers (CPD) and (6−4) lesions. By the absorption of light at 320 nm, the (6−4) lesions can rearrange to form
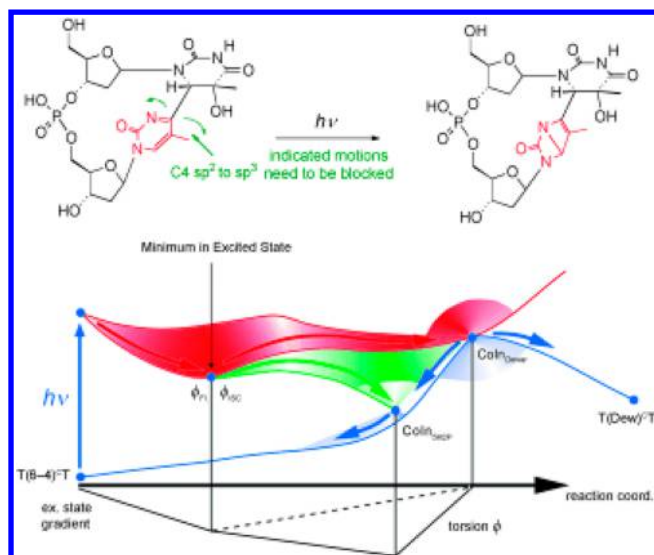
Figure 132. Proposed mechanism of Dewar rearrangement. Reprinted with permission from ref 777. Copyright 2012 Wiley-VCH Verlag GmbH & Co. KGaA.

Dewar lesions (Figure 132). ONIOM(CASPT2:HF)// ONIOM(CASSCF(12e,9o):HF) calculations and nonadiabatic ONIOM(QM1:QM2) MD simulations were applied to study the UV-induced mechanism of Dewar rearrangement from the T(6−4)T dinucleotides to the T(Dew)T lesion.[777] This ONIOM study also suggested that the presence of the DNA backbone leads to a lowest-energy conical intersection (biradical CoIn$_{Dewar}$), and controls the formation of the Dewar lesion (Figure 132). In comparison, the 5-methyl-2-pyrimidone (5M2P) and the (6−4) dinucleotides with the open backbone reach the ground state through another conical intersection (CoIn$_{5M2P}$) without forming the Dewar lesion. These theoretical calculations support the high quantum yield of the Dewar lesion formation controlled by the DNA backbone and give a detailed description of the mechanism.[777]

In addition, ONIOM(MP2:HF) calculations were carried out to explore the repair mechanism of thymine dimer (T═T) in the DNA fragment including the T═T moiety and 8-oxo-7,8-dihydroguanine (OG).[778] According to the proposed mechanism, absorption of light excites the OG:X (X = A or C) pair to give OG*:X. One electron then transfers from OG*:X to T═T to form OG$^+$:X and T−T$^-$, followed by carbon−carbon bond cleavage to form T···T$^-$. Finally, two thymine sites are generated in a process that competes with back electron transfer from T−T$^-$ to OG$^+$:X.[778]

9.3.5. Miscellaneous. The ONIOM method has also been applied to study photophysical and photochemical properties of other photobiological systems (e.g., the light-harvesting complex II and peridinin-chlorophyll *a*-protein).[779,780]

In bioluminescent systems, the luminescence of firefly luciferase[781] was investigated by the ONIOM-like scheme using the SAC-CI method combined with CIS method.[782] The keto form of the firefly oxyluciferin shows red chemiluminescence in solution and yellow-green bioluminescence in firefly luciferase. The origin of the blue shift was proposed to be the electrostatic effect of the protein environment.

In photosynthetic systems, quinones play a crucial role in electron-transfer processes. In the reaction center of *Rhodobacter sphaeroides* and the photosystem II, the spin-density distribution of the semiquinone Q$_A$ anion radical was investigated by an ONIOM(B3LYP:UFF) method.[783] The computed spin-density distribution was found to be very sensitive to the hydrogen-bonding interactions in the active site. In addition, hyperfine couplings calculated by ONIOM-(B3LYP:UFF) were comparable to the experimental data.[783] Also, for ubiquinone at the Q$_A$ site in the photosynthetic reaction centers, ONIOM(B3LYP:AMBER) calculations successfully reproduced the experimental FTIR spectra, which suggested that the calculations should include the protein environment to obtain an accurate FTIR difference spectra.[784] Furthermore, for phylloquinone in the photosystem I and the PsaA-L722T mutant, the structure, spin-density distribution, and methyl hyperfine coupling tensors were calculated by ONIOM(B3LYP:AMBER). In the PsaA-L722T mutant, the hydrogen bonding between the carbonyl oxygen of the phylloquinone and the OH of threonine leads to an increase in the 2-methyl hyperfine couplings.[785] The same research
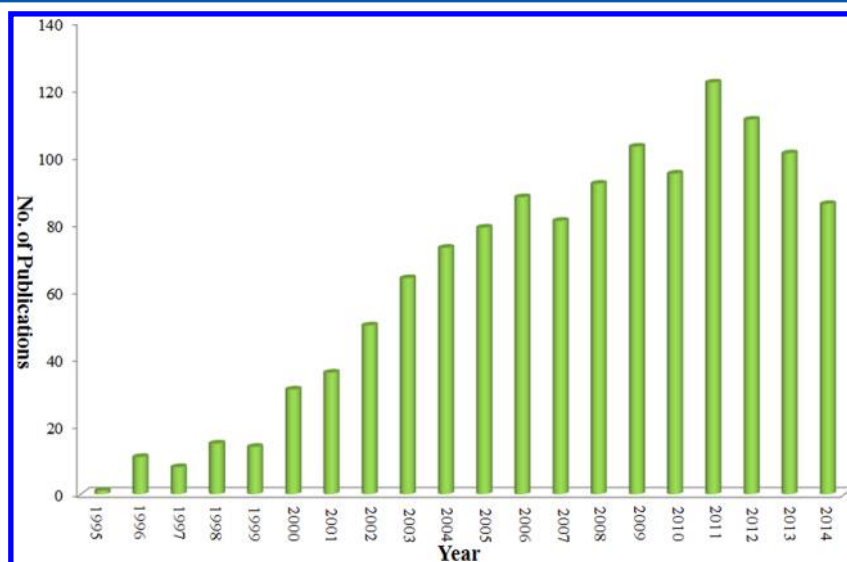
Figure 133. Annual number of published papers: a result of survey through ISI's Web of Science from 1995 to 2014 by using "ONIOM", "IMOMM", or "IMOMO" as keywords.

group also gave a detailed investigation on the FTIR difference spectra of the neutral ubiquinone in the photosynthetic reaction centers by using ONIOM(B3LYP:AMBER).[786]

The absorption spectrum of a tyrosine chromophore in the isolated state and in protein was studied by an ONIOM(TD-B3LYP:AMBER) method.[787] The protein environment and conformations were suggested to tune the UV spectrum of tyrosine (260−280 nm). Another UV-light absorbing amino acid is tryptophan, which is sensitive to different environments. Very recently, the absorption/emission spectra of tryptophan in UVR8 and the UV-B light-induced dissociation mechanism of the UVR8 homodimer have been investigated by Li et al. through ONIOM(QM:AMBER) calculations with various high-level QM methods (e.g., SAC-CI and MS-CASPT2).[788] The ONIOM(QM:MM) results suggested that W285 is the key chromophore, whereas W233 may sense the UV-B light and be responsible for exciton coupling. Several key charged residues play important roles in the red shift of the spectra of tryptophan in UVR8. In the ^1L_a excited state, the electrostatic repulsion and the electron and/or proton transfer in the active site may result in the loss of key salt bridges and trigger the dimer dissociation.

In addition, ONIOM(HF/6-31+G(d):HF/6-31G(d)) and ONIOM(LC-BLYP/6-31+G(d):HF/6-31G(d)) methods have recently been used to investigate the nature of the hyperpolarizability (β) of a collagen triple helix (PPG10).[789] The ONIOM calculations proposed that the amide group was attributed to the hyperpolarizability β of the collagen. Also, the reliability of the ONIOM calculated β values has been shown to be determined by a reasonable combination of QM methods with different basis sets in the two-layer ONIOM schemes. This study demonstrates that the ONIOM method can be an efficient method to study nonlinear optical response of complex systems.

10. CONCLUSIONS

In this Review, at first the theoretical foundation of the ONIOM method (since the proposal of the first version in 1995) as well as numerous improvements and alternative approaches have been reviewed. A comprehensive review on applications to a very wide variety of chemical, biological, and material problems has also been presented, including organic systems, inorganic compounds and homogeneous catalysis, heterogeneous catalysis, nanomaterials, excited states, solution chemistry, and biological macromolecules. The many successful ONIOM applications in these systems demonstrate the power and versatility of the unique multilayer multilevel ONIOM method, which has fundamental conceptual differences from the generic two-layer QM/MM method. We have witnessed that, as time goes by, the yearly number of publications relating to "ONIOM", "IMOMM", or "IMOMO" methods has increased (in total 1261 records found through ISI's Web of Science from 1995 to 2014, Figure 133) as the ONIOM method has become increasingly popular.

Despite the advances and speedup made for quantum chemical calculations, it is not very practical, and perhaps even not so meaningful, to use high-level quantum chemistry to treat all atoms in a complex, large molecular system. Simulations of chemistry, biology, and material science are nowadays dominated by even more complex molecules. The use of hybrid or multiscale methods that combine different levels of theoretical methods to different parts of the whole system will only become more important in the future. In this respect, ONIOM's flexibility in how it combines different levels of

theory is a very important factor that satisfies the need for going beyond a simple QM/MM combination.

We want to add a word of warning on the blind use of the ONIOM models. In reviewing published papers, we found that many papers adopt the ONIOM models and methods without estimating errors. As discussed in detail in section 2.1.2, the error caused by ONIOM approximation relative to the high-level target calculation of the real system can be evaluated by the S-value test. The role of the low-level calculation is to correctly reproduce the effect of difference in the high level going from the small model system to the real system. Depending on the choice of the ONIOM "model" system and
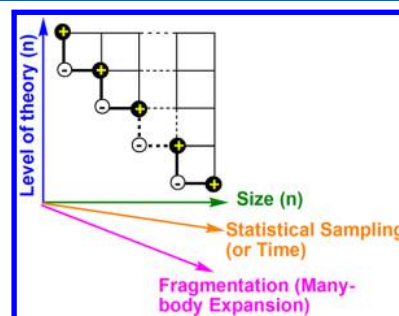
Figure 134. Schematic "dimensions" of the ONIOM method development and applications to more realistic simulations of complex systems.

the "low-level" method, the error can be very large, and the wrong conclusions can be obtained. It is strongly recommended that users perform the S-value test to evaluate the error expected for their choice of model and level, if the high-level calculation for the real system is feasible.

It is hoped that this Review will serve not only as an overview of previous studies using ONIOM, but also as a guide for new directions in ONIOM method developments and applications. With development of new or faster computational methods and powerful computational capabilities (e.g., GPU and distributed computing[790]), we are very optimistic that the ONIOM method will be able to simulate even more realistic and challenging complex chemical, biological, and material systems (e.g., larger QM models, accurate QM methods, larger real systems, and/or a combination with statistical mechanics methods, Figure 134), and could ultimately drive computational design of emerging and useful biological (e.g., health-related) and material (e.g., electronic and energy-related) systems.[675b,791]

AUTHOR INFORMATION

Corresponding Author

*Tel.: +81-75-711-7843. E-mail: morokuma@fukui.kyoto-u.ac.jp.

Notes

Biographies

(Oscar) Lung Wa Chung received his B.Sc. and Ph.D. degrees under the supervision of Prof. Yun-Dong Wu at Hong Kong University of Science and Technology in 2000 and 2006, respectively. He then joined a new group of Prof. Keiji Morokuma at Fukui Institute for Fundamental Chemistry (FIFC), Kyoto University, as a postdoctoral fellow. He sadly gave up a postdoctoral offer from Prof. Martin Karplus in 2012, since he started to look for an independent position. In 2013, he started his tenure-track faculty position at South University of Science and Technology of China. He is very proud to follow four of the best computational chemistry families. His research interests focus on simulations of complex chemical, biochemical, and biophysical processes.

W. M. C. Sameera was awarded a B.Sc. from the University of Sri Jayewardenepura. In 2009, he was awarded a Ph.D. from the University of Glasgow under the supervision of Prof. John E. McGrady. He then moved to Prof. McGrady's group at the University of Oxford as an EPSRC postdoctoral fellow. From 2011 to 2013, he was a postdoctoral fellow in the group of Prof. Feliu Maseras (ICIQ). In 2013, he was awarded a Marie Curie research fellowship to collaborate with Prof. Gunnar Nyman at the University of Gothenburg. Currently, he is a Japan Society for the Promotion of Science postdoctoral fellow in Prof. Keiji Morokuma's group. His research interest focuses on QM/MM method developments and applications.

Romain Ramozzi graduated with degrees in theoretical and organic chemistry from the Ecole Normale Supérieure de Cachan (ENS de Cachan) and Ecole Polytechnique (France) in 2010. He received his Ph.D. in 2013 from the Ecole Normale Supérieure de Lyon (ENS de Lyon, France) under the supervision of Dr. Paul Fleurat-Lessard, Dr. Laurence Grimaud, and Prof. Laurent El Kaïm. In 2013, he received a Japan Society for the Promotion of Science Postdoctoral Fellowship to work in the group of Prof. Keiji Morokuma at the FIFC, Kyoto University. His research focuses on mechanistic studies of organo- and organometallic-catalyzed reactions.

Alister Page received degrees in chemistry and mathematics from The University of Newcastle, Australia, in 2005, and a Ph.D. in 2008 under the supervision of Prof. Ellak I. von Nagy-Felsobuki. Between 2009–2012, he undertook a Fukui Fellowship in the group of Prof. Keiji Morokuma at the FIFC, Kyoto University. In 2012 he was awarded a University Fellowship at The University of Newcastle, and has been a lecturer in physical chemistry at Newcastle since 2013. His research centers on using computational chemistry to understand carbon nanotube and graphene self-assembly, and structure and dynamics in ionic liquids.

Miho Hatanaka studied chemistry at Keio University in Japan, and she wrote her Ph.D. thesis under the supervision of Prof. Satoshi Yabushita for theoretical chemistry and received her Ph.D. from Keio University in 2011. Since 2011 she has worked as a postdoctoral fellow in the group of Prof. Keiji Morokuma at the FIFC, Kyoto University. Her research focuses on the computational chemistry to understand the mechanism of reactions catalyzed by flexible compounds and emission and quenching process of lanthanide complexes.

Galina Petrova studied chemistry at Sofia University, Bulgaria, and received her Ph.D. there under the supervision of Prof. Georgi Vayssilov (Sofia University, Bulgaria) and in cooperation with Prof. Notker Rösch (Technical University Munich, Germany). She worked as a postdoctoral researcher in the group of Prof. Keiji Morokuma at the FIFC, Kyoto University, from 2011 until 2014 and received a Japan Society for the Promotion of Science Postdoctoral Fellowship in 2012. Her research is focused on homo- and heterogeneous catalysis and asymmetric reactions.

Travis Harris studied chemistry at Willamette University, and received his Ph.D. at Montana State University in 2011 under the guidance of

Prof. Robert Szilagyi. He received a Japan Society for the Promotion of Science Postdoctoral Fellowship to work in the group of Prof. Keiji Morokuma at the FIFC, Kyoto University, in 2012, where he continued his computational studies of bioinorganic and organo-metallic systems until 2014. Currently, he is a visiting assistant professor at SUNY Oswego.
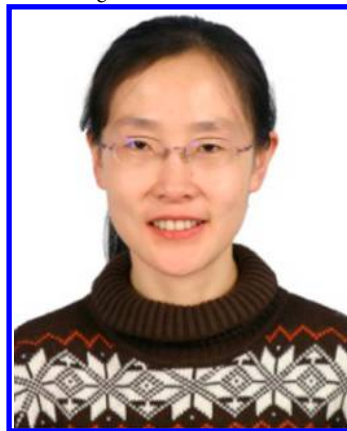
Xin Li studied chemistry and received her Ph.D. degree under Prof. Zhong-Zhi Yang from Liaoning Normal University in 2005. From 2005 to 2007, she worked as a postdoctoral fellow in Peking University with Prof. Zhi-Xiang Yu. From 2007 to 2011, she worked at the FIFC, Kyoto University, as a postdoctoral fellow in the group of Prof. Keiji Morokuma. Since 2012, she has been Associate Professor and was awarded a 100 talents grant at Dalian Institute of Chemical Physics, Chinese Academy of Sciences. Her research focuses on developing efficient simulation methods and understanding mechanisms of enzymatic reactions and photochemical and photobiological processes.
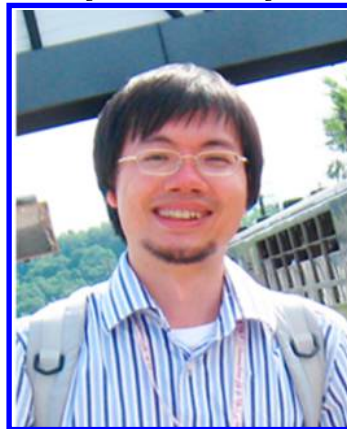
Zhuofeng Ke obtained his B.Sc. (chemistry), M.Sc. (polymer science with Prof. Qing Wu), and Ph.D. (physical chemistry with Prof. Cunyuan Zhao) degrees at Sun Yat-sen University. From 2007 to 2008, he worked with Prof. Weston Borden and Prof. Thomas Cundari at University of North Texas/CASCaM. He then worked as an FIFC fellow with Prof. Keiji Morokuma at the FIFC, Kyoto University, from 2009 to 2012. He joined the faculty of Sun Yat-sen University in 2012. His current research is focused on novel molecular transformation mechanisms in complex chemical or biological systems and their applications in synthesis and energy.

Fengyi Liu studied chemistry at Hebei Normal University, China, and received his Ph.D. degree in chemistry in 2005 from Beijing University of Chemical Technology under the supervision of Prof. Shijun Zheng. From 2007 to 2009, he worked as a postdoctoral researcher with Prof. Roland Lindh at Lund University, Sweden, and then worked in the group of Prof. Keiji Morokuma at the FIFC, Kyoto University, Japan. Since 2013 he has been a professor at Shaanxi Normal University, Xi'an, China. His research focuses on computational photochemistry and photophysics.

Hai-Bei Li studied chemistry at the University of Science and Technology of China (USTC), and she received her Ph.D. degree in chemistry in 2010 under the supervision of Prof. Jinlong Yang and Prof. Shanxi Tian at USTC. From 2010 to 2013, she worked as a postdoctoral fellow in the group of Prof. Morokuma at the FIFC, Kyoto University, focusing on the growth mechanism of nanocarbon materials. Currently, she works at the School of Ocean in Shandong University, Weihai. Her research focuses on the reaction mechanism of organo- and organometallic-catalyzed reactions.

Lina Ding studied chemistry at Zhengzhou University in China, and received her Ph.D. for physical chemistry with Prof. Weihai Fang from Beijing Normal University in 2010. From 2010 to 2013, she worked as a postdoctoral fellow in the group of Prof. Keiji Morokuma at the FIFC, Kyoto University. She is currently an associate professor at the School of Pharmaceutical Sciences, Zhengzhou University, China. Her research focuses on the mechanistic investigation of photochemistry, photobiology, and catalysis by computational chemistry, and drug design and discovery by integrated computational−experimental studies.

Keiji Morokuma finished his Ph.D. at Kyoto University in 1963 under Prof. Kenichi Fukui and did his postdoc with Prof. Martin Karplus; he is proud to have two Nobel Laureates as supervisors. After being Professor at the University of Rochester, Institute for Molecular Science, and Emory University, since 2006 he has been at the FIFC, Kyoto University. He has worked on method developments and applications to many chemical problems.

ACKNOWLEDGMENTS

ABBREVIATIONS AND GLOSSARY

ADDF	anharmonic downward distortion following
ADMP	atom-centered density matrix propagation
AFIR	artificial force induced reaction
AM1	austin model 1 method
AMBER	assisted model building with energy refinement force fields or program
AO	atomic orbital
ASC	apparent surface charge

B1LYP	a one-parameter hybrid functional with Becke exchange and Lee–Yang–Parr correlation functionals
B3LYP	a three-parameter hybrid functional with Becke exchange and 20% HF exchange combined with Lee–Yang–Parr correlation functionals
B3LYP*	a modified B3LYP functional with 15% HF exchange
B3P86	a three-parameter hybrid functional with Becke exchange and Perdew nonlocal correlation functionals
B3PW91	a three-parameter hybrid functional with Becke exchange and Perdew–Wang correlation functionals
BB1K	a one-parameter hybrid-meta functional with Becke exchange and correlation functionals parametrized for kinetics
BHandH (or BH&H)	a hybrid half-and-half functional with Lee–Yang–Parr correlation as well as 50% HF exchange functionals
BHandHLYP (or BH&HLYP)	a hybrid half-and-half functional with Lee–Yang–Parr correlation and Becke exchange as well as 50% HF exchange functionals
BLYP	a functional with Becke exchange and Lee–Yang–Parr correlation functionals
BP86	a pure functional with Becke exchange and Perdew 86 correlation functionals
CAM-B3LYP	coulomb attenuation method (long-range correction) for B3LYP functional
CASSCF	complete active space self-consistent field method
CASPT2	complete active space second-order perturbation theory method
CBS	complete basis set
CC2	second-order approximate coupled-cluster method
ccCA	correlation consistent composite approach
CCSD(T)	coupled cluster with singles and doubles excitations augmented with perturbative triples correction method
CHARMM	chemistry at Harvard macromolecular mechanics force fields or program
CIP	classical interatomic potentials
CIS	configuration interaction with single-excitation method
CM	continuum model
COSMO	conductor-like screening model
CPCM	conductor-like polarizable continuum model
DDCI2+Q	difference-dedicated configuration interaction with 2 degrees of freedom method with a Davidson correction
(TD-)DFT(-D)	(time-dependent) density functional theory method (including an empirical dispersion correction)
DFTB(-D)	density functional-based tight binding (including dispersion correction)
ECP	effective core potential
EDA	energy decomposition analysis
EE	electronic embedding
EOM-CCSD	equation-of-motion coupled-cluster method for single- and double-excitations method
ESP	electrostatic potential
EVB	empirical valence bond method
FEP	free energy perturbation
FMO	fragment molecular orbital
GIAO	gauge invariant atomic orbital method
Gn	Gaussian-n method
GRRM	global reaction root mapping
(R/RO/U/TD-)HF	(restricted/open-shell/unrestricted/time-dependent) Hartree–Fock method
HOMO	the highest occupied molecular orbital
IMOHC	integrated molecular orbital with harmonic cap method
IMOMM	integrated molecular orbital + molecular mechanics method
IMOMO	integrated molecular orbital + molecular orbital method
INDO	intermediate neglect of differential overlap
IRC	intrinsic reaction coordinate
LA	link atom (hydrogen usually)
LAC	link atom connection
LAH	link atom host
LSDA	local spin density approximation functional
LMP2	MP2 method using local orbital approximation
LUMO	the lowest occupied molecular orbital
M05-2X	a hybrid functional developed in Minnesota with 52% HF exchange
M06/M06-2X/M06-HF/M06-L	the 06 family of Minnesota functionals

M08	a functional of the 08 family of Minnesota functionals	QCISD(T)	quadratic configuration interaction with single- and double-excitation and perturbative triplet correction method
MBE	many-body expansion		
MC	Monte Carlo method	QM	quantum mechanics
(BO/CP)MD	(Born−Oppenheimer/Car−Parrinello) molecular dynamics	PBC	periodic boundary conditions
		PBE	Perdew−Burke−Ernzerhof exchange-correlation (pure) functional
ME	mechanical embedding		
MESP	molecular electrostatic potential	PBE1PBE	a hybrid functional with Perdew−Burke−Ernzerhof exchange-correlation functional
MEUC	mechanical embedding with updated charge		
MFEP	minimum free-energy path	PBEP86	a functional with Perdew−Burke−Ernzerhof exchange functional and Perdew 86 correlation functionals
MM	molecular mechanic(s)		
MM2/MM3	molecular mechanic 2/3		
MNDO	modified neglect of diatomic overlap method		
MO	molecular orbital	PCM	polarizable continuum model
(RO)MPn	(restricted open-shell) nth-order Møller−Plesset perturbation method	PE	polarized embedding
		PES	potential energy surface
		PIMD	path integral molecular dynamic
MPW1K	a hybrid functional with modified Perdew−Wang exchange and correlation functionals	PM3/PM6	parametric method 3/6
		PPP	Pariser−Parr−Pople semiempirical method
mPW1PW91	a one-parameter hybrid functional with modified Perdew−Wang exchange and Becke correlation functionals	PW91PW91	Perdew−Wang exchange and correlation functional
		QWAIMD	quantum wavepacket ab initio molecular dynamics method
MPWB1K	a hybrid-meta functional with modified Perdew−Wang exchange and Becke correlation functionals	RISM	reference interaction site model
MPWLYP	a parameterized functional with modified Perdew−Wang exchange and Lee−Yang−Parr correlation functionals	RM1	recife model 1 (a reparameterization of the AM1 method)
		RRKM	Rice−Ramsperger−Kassel−Marcus theory
		SAC−CI	symmetry-adapted-cluster configuration interaction method
MRCISD+Q	multireference configuration interaction with single- and double-excitation method with a Davidson correction		
		SCF	self-consistent field method
		SE	semiempirical methods
MSX (or MECI)	minimum crossing point (or minimum energy conical intersection)	SORCI+Q	spectroscopy oriented configuration interaction method with a Davidson correction
NEB	nudged elastic band		
NEVPT2	N-electron valence state second-order perturbation theory	SVWN	Slater exchange functional and Vosko, Wilk, and Nusair correlation function
		TIP3P	transferable intermolecular potential with three-sites model
ONIOM	our own n-layered integrated molecular orbital and molecular mechanics methods		
		TS(s)	transition state(s)
		UFF	universal force field
ONIOM-CT	an ONIOM method for charge transfer between the two layers	ωB97X-D	Head-Gordon and co-worker long-range corrected hybrid functional based on Becke 97 functional including empirical dispersion correction
ONIOM-XS	an adaptive ONIOM method for the exchange or extension of solvent molecules		
		Wn	Weizmann-n methods
OPLS	optimized potential for liquid simulations	ZPE	zero-point energy

REFERENCES

(1) Honig, B.; Karplus, M. *Nature* **1971**, *229*, 558.

(2) (a) Pariser, R.; Parr, R. G. *J. Chem. Phys.* **1953**, *21*, 767. (b) Pople, J. A. *Trans. Faraday Soc.* **1953**, *49*, 1375.

(3) (a) Warshel, A.; Karplus, M. *J. Am. Chem. Soc.* **1972**, *94*, 5612. (b) Warshel, A.; Karplus, M. *J. Am. Chem. Soc.* **1974**, *96*, 5677.

(4) Warshel, A.; Levitt, M. *J. Mol. Biol.* **1976**, *103*, 227.

(5) (a) Karplus, M. *Angew. Chem., Int. Ed.* **2014**, *38*, 9992. (b) Levitt, M. *Angew. Chem., Int. Ed.* **2014**, *38*, 10006. (c) Warshel, A. *Angew. Chem., Int. Ed.* **2014**, *38*, 10020.

(6) (a) Senn, H. M.; Thiel, W. *Angew. Chem., Int. Ed.* **2009**, *48*, 1198. (b) Senn, H. M.; Thiel, W. In *Atomistic Approaches in Modern Biology: From Quantum Chemistry to Molecular Simulations*; Reiher, M., Ed.; Springer: New York, 2007; Vol. *268*.

(7) Cornell, W. D.; Cieplak, P.; Bayly, C. I.; Gould, I. R.; Merz, K. M.; Ferguson, D. M.; Spellmeyer, D. C.; Fox, T.; Caldwell, J. W.; Kollman, P. A. *J. Am. Chem. Soc.* **1995**, *117*, 5179.

(8) (a) Lonsdale, R.; Harvey, J. N.; Mulholland, A. J. *Chem. Soc. Rev.* **2012**, *41*, 3025. (b) Wallrapp, F. H.; Guallar, V. *WIREs Comput. Mol. Sci.* **2011**, *1*, 315. (c) Hu, H.; Yang, W. *Annu. Rev. Phys. Chem.* **2008**, *59*, 573. (d) Ramos, M. J.; Fernandes, P. A. *Acc. Chem. Res.* **2008**, *41*, 689. (e) Lin, H.; Truhlar, D. G. *Theor. Chem. Acc.* **2007**, *117*, 185. (f) Vreven, T.; Byun, K. S.; Komáromi, I.; Dapprich, S.; Montgomery, J. A., Jr.; Morokuma, K.; Frisch, M. J. *J. Chem. Theory Comput.* **2006**, *2*, 815. (g) Friesner, R. A.; Guallar, V. *Annu. Rev. Phys. Chem.* **2005**, *56*, 389. (h) Gao, J.; Truhlar, D. G. *Annu. Rev. Phys. Chem.* **2002**, *53*, 467. (i) Monard, G.; Merz, K. M. *Acc. Chem. Res.* **1999**, *32*, 904. (j) Gao, J. *Acc. Chem. Res.* **1996**, *29*, 298.

(9) (a) Vreven, T.; Morokuma, K. *Annu. Rep. Comput. Chem.* **2006**, *2*, 35. (b) Chung, L. W.; Hirao, H.; Li, X.; Morokuma, K. *WIREs Comput. Mol. Sci.* **2012**, *2*, 327. (c) Li, X.; Chung, L. W.; Morokuma, K. In *Computational Methods for Large Systems: Electronic Structure Approaches for Biotechnology and Nanotechnology*; Reimers, J. R., Ed.; John Wiley & Sons, Inc.: Hoboken, NJ, 2011. (d) Chung, L. W.; Li, X.; Morokuma, K. In *Quantum Biochemistry*; Matta, C. F., Ed.; Wiley-VCH Verlag GmbH & Co. KGaA: Weinheim, 2010. (e) Lundberg, M.; Morokuma, A. In *Multi-scale Quantum Models for Biocatalysis*; Lee, T.-S., York, D. M., Eds.; Springer: Netherlands, 2009; Vol. 7. (f) Morokuma, K. *Bull. Korean Chem. Soc.* **2003**, *24*, 797. (g) Morokuma, K. *Philos. Trans. R. Soc., A* **2002**, *360*, 1149. (h) Morokuma, K.; Musaev, D. G.; Vreven, T.; Basch, H.; Torrent, M.; Khoroshun, D. V. *IBM J. Res. Dev.* **2001**, *45*, 367.

(10) Maseras, F.; Morokuma, K. *J. Comput. Chem.* **1995**, *16*, 1170.

(11) Matsubara, T.; Sieber, S.; Morokuma, K. *Int. J. Quantum Chem.* **1996**, *60*, 1101.

(12) Matsubara, T.; Maseras, F.; Koga, N.; Morokuma, K. *J. Phys. Chem.* **1996**, *100*, 2573.

(13) Humbel, S.; Sieber, S.; Morokuma, K. *J. Chem. Phys.* **1996**, *105*, 1959.

(14) Vreven, T.; Morokuma, K. *J. Phys. Chem. A* **2002**, *106*, 6167.

(15) Vreven, T.; Morokuma, K. *J. Comput. Chem.* **2000**, *21*, 1419.

(16) Morokuma, K.; Wang, Q.; Vreven, T. *J. Chem. Theory Comput.* **2006**, *2*, 1317.

(17) Svensson, M.; Humbel, S.; Froese, R. D. J.; Matsubara, T.; Sieber, S.; Morokuma, K. *J. Phys. Chem.* **1996**, *100*, 19357.

(18) Sokkar, P.; Boulanger, E.; Thiel, W.; Sanchez-Garcia, E. *J. Chem. Theory Comput.* **2015**, DOI: 10.1021/ct500956u.

(19) Frisch, M. J.; Trucks, G. W.; Schlegel, H. B.; Scuseria, G. E.; Robb, M. A.; Cheeseman, J. R.; Scalmani, G.; Barone, V.; Mennucci, B.; Petersson, G. A.; Nakatsuji, H.; Caricato, M.; Li, X.; Hratchian, H. P.; Izmaylov, A. F.; Bloino, J.; Zheng, G.; Sonnenberg, J. L.; Hada, M.; Ehara, M.; Toyota, K.; Fukuda, R.; Hasegawa, J.; Ishida, M.; Nakajima, T.; Honda, Y.; Kitao, O.; Nakai, H.; Vreven, T.; Montgomery, J. A., Jr.; Peralta, J. E.; Ogliaro, F.; Bearpark, M. J.; Heyd, J.; Brothers, E. N.; Kudin, K. N.; Staroverov, V. N.; Kobayashi, R.; Normand, J.; Raghavachari, K.; Rendell, A. P.; Burant, J. C.; Iyengar, S. S.; Tomasi, J.; Cossi, M.; Rega, N.; Millam, N. J.; Klene, M.; Knox, J. E.; Cross, J. B.; Bakken, V.; Adamo, C.; Jaramillo, J.; Gomperts, R.; Stratmann, R. E.; Yazyev, O.; Austin, A. J.; Cammi, R.; Pomelli, C.;
Ochterski, J. W.; Martin, R. L.; Morokuma, K.; Zakrzewski, V. G.; Voth, G. A.; Salvador, P.; Dannenberg, J. J.; Dapprich, S.; Daniels, A. D.; Farkas, Ö.; Foresman, J. B.; Ortiz, J. V.; Cioslowski, J.; Fox, D. J. *Gaussian 09*, revision D.01; Gaussian, Inc.: Wallingford, CT, 2009.

(20) (a) Curtiss, L. A.; Redfern, P. C.; Raghavachari, K. *WIREs Comput. Mol. Sci.* **2011**, *1*, 810. (b) Pople, J. A.; Head-Gordon, M.; Fox, D. J.; Raghavachari, K.; Curtiss, L. A. *J. Chem. Phys.* **1989**, *90*, 5622. (c) Curtiss, L. A.; Raghavachari, K.; Trucks, G. W.; Pople, J. A. *J. Chem. Phys.* **1991**, *94*, 7221. (d) Curtiss, L. A.; Raghavachari, K.; Redfern, P. C.; Rassolov, V.; Pople, J. A. *J. Chem. Phys.* **1998**, *109*, 7764. (e) Curtiss, L. A.; Redfern, P. C.; Raghavachari, K. *J. Chem. Phys.* **2007**, *126*, 084108.

(21) Bakowies, D.; Thiel, W. *J. Phys. Chem.* **1996**, *100*, 10580.

(22) Weiner, S. J.; Singh, U. C.; Kollman, P. A. *J. Am. Chem. Soc.* **1985**, *107*, 2219.

(23) Dapprich, S.; Komáromi, I.; Byun, K. S.; Morokuma, K.; Frisch, M. J. *J. Mol. Struct. (THEOCHEM)* **1999**, *461*, 1.

(24) Pettitt, B. M.; Karplus, M. *J. Am. Chem. Soc.* **1985**, *107*, 1166.

(25) Clemente, F. R.; Vreven, T.; Frisch, M. J. In *Quantum Biochemistry*; Matta, C. F., Ed.; Wiley-VCH Verlag GmbH & Co. KGaA: Weinheim, 2010.

(26) Tao, P.; Fisher, J. F.; Shi, Q.; Vreven, T.; Mobashery, S.; Schlegel, H. B. *Biochemistry* **2009**, *48*, 9839.

(27) (a) Chirlian, L. E.; Francl, M. M. *J. Comput. Chem.* **1987**, *8*, 894. (b) Besler, B. H.; Merz, K. M.; Kollman, P. A. *J. Comput. Chem.* **1990**, *11*, 431.

(28) Vreven, T.; Morokuma, K. *Theor. Chem. Acc.* **2003**, *109*, 125.

(29) Kawatsu, T.; Lundberg, M.; Morokuma, K. *J. Chem. Theory Comput.* **2011**, *7*, 390.

(30) Kuhn, B.; Kollman, P. A. *J. Am. Chem. Soc.* **2000**, *122*, 2586.

(31) Hayashi, S.; Ohmine, I. *J. Phys. Chem. B* **2000**, *104*, 10678.

(32) Sherwood, P.; de Vries, A. H.; Guest, M. F.; Schreckenbach, G.; Catlow, C. R. A.; French, S. A.; Sokol, A. A.; Bromley, S. T.; Thiel, W.; Turner, A. J.; Billeter, S.; Terstegen, F.; Thiel, S.; Kendrick, J.; Rogers, S. C.; Casci, J.; Watson, M.; King, F.; Karlsen, E.; Sjøvoll, M.; Fahmi, A.; Schäfer, A.; Lennartz, C. *J. Mol. Struct. (THEOCHEM)* **2003**, *632*, 1.

(33) Zhang, Y.; Lin, H.; Truhlar, D. G. *J. Chem. Theory Comput.* **2007**, *3*, 1378.

(34) Das, D.; Eurenius, K. P.; Billings, E. M.; Sherwood, P.; Chatfield, D. C.; Hodoščcek, M.; Brooks, B. R. *J. Chem. Phys.* **2002**, *117*, 10534.

(35) Eichinger, M.; Tavan, P.; Hutter, J.; Parrinello, M. *J. Chem. Phys.* **1999**, *110*, 10452.

(36) König, P. H.; Hoffmann, M.; Frauenheim, T.; Cui, Q. *J. Phys. Chem. B* **2005**, *109*, 9082.

(37) Morokuma, K.; Pedersen, L. *J. Chem. Phys.* **1968**, *48*, 3275.

(38) (a) Singh, U. C.; Kollman, P. A. *J. Comput. Chem.* **1986**, *7*, 718. (b) Field, M. J.; Bash, P. A.; Karplus, M. *J. Comput. Chem.* **1990**, *11*, 700.

(39) Corchado, J. C.; Truhlar, D. G. *J. Phys. Chem. A* **1998**, *102*, 1895.

(40) Eichler, U.; Kölmel, C. M.; Sauer, J. *J. Comput. Chem.* **1997**, *18*, 463.

(41) Koga, N.; Morokuma, K. *Chem. Phys. Lett.* **1990**, *172*, 243.

(42) Zheng, G.; Lundberg, M.; Jakowski, J.; Vreven, T.; Frisch, M. J.; Morokuma, K. *Int. J. Quantum Chem.* **2009**, *109*, 1841.

(43) (a) Ando, K.; Morokuma, K. *Theor. Chem. Acc.* **2011**, *130*, 323. (b) Lu, X.; Tian, F.; Wang, N.; Zhang, Q. *Org. Lett.* **2002**, *4*, 4313. (c) Thompson, L. M.; Lasoroski, A.; Champion, P. M.; Sage, J. T.; Frisch, M. J.; van Thor, J. J.; Bearpark, M. J. *J. Chem. Theory Comput.* **2014**, *10*, 751. (d) Treesuwan, W.; Hirao, H.; Morokuma, K.; Hannongbua, S. *J. Mol. Model.* **2012**, *18*, 2227.

(44) Karadakov, P. B.; Morokuma, K. *Chem. Phys. Lett.* **2000**, *317*, 589.

(45) (a) Pawlak, T.; Trzeciak-Karlikowska, K.; Czernek, J.; Ciesielski, W.; Potrzebowski, M. J. *J. Phys. Chem. B* **2012**, *116*, 1974. (b) Uzunova, E. L.; Mikosch, H.; Hafner, J. *J. Mol. Struct. (THEOCHEM)* **2009**, *912*, 88. (c) Paluch, P.; Potrzebowski, M. J. *Solid State Nucl. Magn. Reson.* **2009**, *36*, 103. (d) Zheng, A.; Liu, S.-B.; Deng, F. *J. Comput. Chem.* **2009**, *30*, 222. (e) Fördös, E.; Ungvári, N.; Kégl, T.; Párkányi, L.;

Szalontai, G.; Ungváry, F. *Inorg. Chim. Acta* **2008**, *361*, 1832. (f) Zheng, A.; Zhang, H.; Lu, X.; Liu, S.-B.; Deng, F. *J. Phys. Chem. B* **2008**, *112*, 4496. (g) Zuccaccia, D.; Bellachioma, G.; Cardaci, G.; Ciancaleoni, G.; Zuccaccia, C.; Clot, E.; Macchioni, A. *Organometallics* **2007**, *26*, 3930. (h) Lomas, J. S.; Cordier, C.; Adenier, A.; Maurel, F.; Vaissermann, J. *J. Phys. Org. Chem.* **2007**, *20*, 410. (i) Jansang, B.; Nanok, T.; Limtrakul, J. *J. Phys. Chem. B* **2006**, *110*, 12626. (j) Zheng, A.; Chen, L.; Yang, J.; Zhang, M.; Su, Y.; Yue, Y.; Ye, C.; Deng, F. *J. Phys. Chem. B* **2005**, *109*, 24273. (k) Zheng, A.; Yang, M.; Yue, Y.; Ye, C.; Deng, F. *Chem. Phys. Lett.* **2004**, *399*, 172. (l) Sillar, K.; Burk, P. *J. Phys. Chem. B* **2004**, *108*, 9893. (m) Clot, E.; Eisenstein, O.; Dubé, T.; Faller, J. W.; Crabtree, R. H. *Organometallics* **2002**, *21*, 575. (n) Qi, X.-J.; Fu, Y.; Liu, L.; Guo, Q.-X. *Organometallics* **2007**, *26*, 4197. (o) Mennucci, B.; Martínez, J. M.; Tomasi, J. *J. Phys. Chem. A* **2001**, *105*, 7287. (p) Shaghaghi, H.; Ebrahimi, H. P.; Panah, N. B.; Tafazzoli, M. *Solid State Nucl. Magn. Reson.* **2013**, *51−52*, 31. (q) Rickard, G. A.; Karadakov, P. B.; Webb, G. A.; Morokuma, K. *J. Phys. Chem. A* **2003**, *107*, 292. (r) Vailikhit, V.; Treesuwan, W.; Hannongbua, S. *J. Mol. Struct. (THEOCHEM)* **2007**, *806*, 99.

(46) Ananikov, V. P.; Musaev, D. G.; Morokuma, K. *J. Mol. Catal. A: Chem.* **2010**, *324*, 104.

(47) (a) Morokuma, K. *Acc. Chem. Res.* **1977**, *10*, 294. (b) Kitaura, K.; Morokuma, K. *Int. J. Quantum Chem.* **1976**, *10*, 325.

(48) Hirao, H. *Chem. Lett.* **2011**, *40*, 1179.

(49) Schlegel, H. B. *WIREs Comput. Mol. Sci.* **2011**, *1*, 790.

(50) (a) Eckert, J.; Kubas, G. J.; Hall, J. H.; Hay, P. J.; Boyle, C. M. *J. Am. Chem. Soc.* **1990**, *112*, 2324. (b) Maseras, F.; Koga, N.; Morokuma, K. *Organometallics* **1994**, *13*, 4008. (c) Kawamura-Kuribayashi, H.; Koga, N.; Morokuma, K. *J. Am. Chem. Soc.* **1992**, *114*, 8687.

(51) Aqvist, J.; Warshel, A. *Chem. Rev.* **1993**, *93*, 2523.

(52) Eksterowicz, J. E.; Houk, K. N. *Chem. Rev.* **1993**, *93*, 2439.

(53) (a) Vreven, T.; Morokuma, K.; Farkas, O.; Schlegel, H. B.; Frisch, M. J. *J. Comput. Chem.* **2003**, *24*, 760. (b) Schlegel, H. B. *J. Comput. Chem.* **2003**, *24*, 1514.

(54) (a) Kästner, J.; Thiel, S.; Senn, H. M.; Sherwood, P.; Thiel, W. *J. Chem. Theory Comput.* **2007**, *3*, 1064. (b) Melaccio, F.; Olivucci, M.; Lindh, R.; Ferré, N. *Int. J. Quantum Chem.* **2011**, *111*, 3339. (c) Prat-Resina, X.; Bofill, J. M.; González-Lafont, A.; Lluch, J. M. *Int. J. Quantum Chem.* **2004**, *98*, 367. (d) Rokob, T. A.; Rulíšek, L. *J. Comput. Chem.* **2012**, *33*, 1197. (e) Martí, S.; Moliner, V.; Tuñón, I. *J. Chem. Theory Comput.* **2005**, *1*, 1008.

(55) Vreven, T.; Frisch, M. J.; Kudin, K. N.; Schlegel, H. B.; Morokuma, K. *Mol. Phys.* **2006**, *104*, 701.

(56) Chan, B.; Deng, J.; Radom, L. *J. Chem. Theory Comput.* **2011**, *7*, 112.

(57) (a) Martin, J. M. L.; de Oliveira, G. *J. Chem. Phys.* **1999**, *111*, 1843. (b) Boese, A. D.; Oren, M.; Atasoylu, O.; Martin, J. M. L.; Kállay, M.; Gauss, J. *J. Chem. Phys.* **2004**, *120*, 4129. (c) Karton, A.; Rabinovich, E.; Martin, J. M. L.; Ruscic, B. *J. Chem. Phys.* **2006**, *125*, 144108.

(58) (a) Ochterski, J. W.; Petersson, G. A.; Montgomery, J. A. *J. Chem. Phys.* **1996**, *104*, 2598. (b) Montgomery, J. A.; Frisch, M. J.; Ochterski, J. W.; Petersson, G. A. *J. Chem. Phys.* **1999**, *110*, 2822. (c) Wood, G. P. F.; Radom, L.; Petersson, G. A.; Barnes, E. C.; Frisch, M. J.; Montgomery, J. A. *J. Chem. Phys.* **2006**, *125*, 094106.

(59) Bearpark, M. J.; Ogliaro, F.; Vreven, T.; Boggio-Pasqua, M.; Frisch, M. J.; Larkin, S. M.; Morrison, M.; Robb, M. A. *J. Photochem. Photobiol., A* **2007**, *190*, 207.

(60) Froese, R. D. J.; Humbel, S.; Svensson, M.; Morokuma, K. *J. Phys. Chem. A* **1997**, *101*, 227.

(61) (a) Kerdcharoen, T.; Morokuma, K. *Chem. Phys. Lett.* **2002**, *355*, 257. (b) Kerdcharoen, T.; Morokuma, K. *J. Chem. Phys.* **2003**, *118*, 8856.

(62) Tasaki, K.; Mcdonald, S.; Brady, J. W. *J. Comput. Chem.* **1993**, *14*, 278.

(63) (a) Kerdcharoen, T.; Liedl, K. R.; Rode, B. M. *Chem. Phys.* **1996**, *211*, 313. (b) Tongraar, A.; Liedl, K. R.; Rode, B. M. *J. Phys. Chem. A*

1998, *102*, 10340. (c) Tongraar, A.; Liedl, K. R.; Rode, B. M. *Chem. Phys. Lett.* **1998**, *286*, 56.

(64) (a) Miertuš, S.; Scrocco, E.; Tomasi, J. *Chem. Phys.* **1981**, *55*, 117. (b) Miertus, S.; Tomasi, J. *Chem. Phys.* **1982**, *65*, 239. (c) Tomasi, J.; Mennucci, B.; Cancès, E. *J. Mol. Struct. (THEOCHEM)* **1999**, *464*, 211. (d) Tomasi, J.; Mennucci, B.; Cammi, R. *Chem. Rev.* **2005**, *105*, 2999. (e) Tomasi, J. *Theor. Chem. Acc.* **2004**, *112*, 184.

(65) Cancès, E.; Mennucci, B.; Tomasi, J. *J. Chem. Phys.* **1997**, *107*, 3032.

(66) (a) Mo, S. J.; Vreven, T.; Mennucci, B.; Morokuma, K.; Tomasi, J. *Theor. Chem. Acc.* **2004**, *111*, 154. (b) Vreven, T.; Mennucci, B.; da Silva, C. O.; Morokuma, K.; Tomasi, J. *J. Chem. Phys.* **2001**, *115*, 62.

(67) (a) Bearpark, M. J.; Larkin, S. M.; Vreven, T. *J. Phys. Chem. A* **2008**, *112*, 7286. (b) Ruiz-Barragan, S.; Morokuma, K.; Blancafort, L. *J. Chem. Theory Comput.* **2015**, DOI: 10.1021/acs.jctc.5b00004.

(68) Vreven, T.; Morokuma, K. *J. Chem. Phys.* **2000**, *113*, 2969.

(69) Hall, K. F.; Vreven, T.; Frisch, M. J.; Bearpark, M. J. *J. Mol. Biol.* **2008**, *383*, 106.

(70) Woo, T. K.; Cavallo, L.; Ziegler, T. *Theor. Chem. Acc.* **1998**, *100*, 307.

(71) (a) Woodcock, H. L.; Miller, B. T.; Hodošček, M.; Okur, A.; Larkin, J. D.; Ponder, J. W.; Brooks, B. R. *J. Chem. Theory Comput.* **2011**, *7*, 1208. (b) Zhu, X.; Lopes, P. E. M.; MacKerell, A. D., Jr. *WIREs Comput. Mol. Sci.* **2012**, *2*, 167.

(72) Altoè, P.; Stenta, M.; Bottoni, A.; Garavelli, M. In *Computational Methods in Science and Engineering Vol. 1: Theory and Computation: Old Problems and New Challenges*; Maroulis, G., Simos, T. E., Eds.; Greece, 2007; Vol. 963.

(73) Ryde, U.; Olsson, M. H. M. *Int. J. Quantum Chem.* **2001**, *81*, 335.

(74) (a) Van der Spoel, D.; Lindahl, E.; Hess, B.; Groenhof, G.; Mark, A. E.; Berendsen, H. J. C. *J. Comput. Chem.* **2005**, *26*, 1701. (b) van der Spoel, D.; Hess, B. *WIREs Comput. Mol. Sci.* **2011**, *1*, 710.

(75) Valiev, M.; Bylaska, E. J.; Govind, N.; Kowalski, K.; Straatsma, T. P.; Van Dam, H. J. J.; Wang, D.; Nieplocha, J.; Apra, E.; Windus, T. L.; de Jong, W. *Comput. Phys. Commun.* **2010**, *181*, 1477.

(76) Kerdcharoen, T.; Birkenheuer, U.; Krüger, S.; Woiterski, A.; Rösch, N. *Theor. Chem. Acc.* **2003**, *109*, 285.

(77) Krylov, A. I.; Gill, P. M. W. *WIREs Comput. Mol. Sci.* **2013**, *3*, 317.

(78) Lin, H.; Truhlar, D. G. *J. Phys. Chem. A* **2005**, *109*, 3991.

(79) Sauer, J.; Sierka, M. *J. Comput. Chem.* **2000**, *21*, 1470.

(80) Shluger, A. L.; Gale, J. D. *Phys. Rev. B* **1996**, *54*, 962.

(81) (a) Kochman, M. A.; Bil, A.; Morrison, C. A. *Phys. Chem. Chem. Phys.* **2013**, *15*, 10803. (b) Kochman, M. A.; Morrison, C. A. *J. Chem. Theory Comput.* **2013**, *9*, 1182.

(82) Shoemaker, J. R.; Burggraf, L. W.; Gordon, M. S. *J. Phys. Chem. A* **1999**, *103*, 3245.

(83) Khare, R.; Mielke, S. L.; Schatz, G. C.; Belytschko, T. *Comput. Methods Appl. Mech. Eng.* **2008**, *197*, 3190.

(84) (a) Byun, Y.; Mo, Y.; Gao, J. *J. Am. Chem. Soc.* **2001**, *123*, 3974. (b) Martí, S.; Moliner, V.; Tuñón, M.; Williams, I. H. *J. Phys. Chem. B* **2005**, *109*, 3707.

(85) Meyer, J.; Reuter, K. *Angew. Chem., Int. Ed.* **2014**, *53*, 4721.

(86) Wesolowski, T. A.; Warshel, A. *J. Phys. Chem.* **1993**, *97*, 8050.

(87) Wesolowski, T. A.; Weber, J. *Chem. Phys. Lett.* **1996**, *248*, 71.

(88) (a) Govind, N.; Wang, Y. A.; Carter, E. A. *J. Chem. Phys.* **1999**, *110*, 7677. (b) Huang, P.; Carter, E. A. *Annu. Rev. Phys. Chem.* **2008**, *59*, 261. (c) Klüner, T.; Govind, N.; Wang, Y. A.; Carter, E. A. *J. Chem. Phys.* **2002**, *116*, 42. (d) Libisch, F.; Huang, C.; Carter, E. A. *Acc. Chem. Res.* **2014**, *47*, 2768. (e) Neugebauer, J. *ChemPhysChem* **2009**, *10*, 3148. (f) Jacob, C. R.; Neugebauer, J. *WIREs Comput. Mol. Sci.* **2013**, *4*, 325.

(89) Cui, Q.; Guo, H.; Karplus, M. *J. Chem. Phys.* **2002**, *117*, 5617.

(90) Yang, W.; Lee, T.-S. *J. Chem. Phys.* **1995**, *103*, 5674.

(91) Gogonea, V.; Westerhoff, L. M.; Merz, K. M. *J. Chem. Phys.* **2000**, *113*, 5604.

(92) Wanko, M.; Hoffmann, M.; Frauenheim, T.; Elstner, M. *J. Phys. Chem. B* **2008**, *112*, 11462.

(93) Trajbl, M.; Hong, G.; Warshel, A. *J. Phys. Chem. B* **2002**, *106*, 13333.

(94) Mayhall, N. J.; Raghavachari, K. *J. Chem. Theory Comput.* **2010**, *6*, 3131.

(95) Jose, K. V. J.; Raghavachari, K. *J. Chem. Theory Comput.* **2014**, *10*, 4351.

(96) (a) Zhang, Y.; Lin, H. *J. Chem. Theory Comput.* **2008**, *4*, 414. (b) Zhang, Y.; Lin, H. *Theor. Chem. Acc.* **2010**, *126*, 315. (c) Bersuker, I. B.; Leong, M. K.; Boggs, J. E.; Pearlman, R. S. *Int. J. Quantum Chem.* **1997**, *63*, 1051.

(97) (a) Zhang, Y.; Lee, T.-S.; Yang, W. *J. Chem. Phys.* **1999**, *110*, 46. (b) Zhang, Y. *J. Chem. Phys.* **2005**, *122*, 024114. (c) Chaudret, R.; Parks, J. M.; Yang, W. *J. Chem. Phys.* **2013**, *138*, 045102. (d) Parks, J. M.; Hu, H.; Cohen, A. J.; Yang, W. *J. Chem. Phys.* **2008**, *129*, 154106.

(98) Lewin, J. L.; Cramer, C. J. *J. Phys. Chem. A* **2008**, *112*, 12754.

(99) Gamoke, B. C.; Das, U.; Hratchian, H. P.; Raghavachari, K. *J. Chem. Phys.* **2013**, *139*, 164708.

(100) Wang, B.; Truhlar, D. G. *J. Chem. Theory Comput.* **2010**, *6*, 359.

(101) Nasluzov, V. A.; Ivanova, E. A.; Shor, A. M.; Vayssilov, G. N.; Birkenheuer, U.; Rösch, N. *J. Phys. Chem. B* **2003**, *107*, 2228.

(102) Xiao, C.; Zhang, Y. *J. Chem. Phys.* **2007**, *127*, 124102.

(103) Antes, I.; Thiel, W. *J. Phys. Chem. A* **1999**, *103*, 9290.

(104) (a) Alary, F.; Heully, J. L.; Poteau, R.; Maron, L.; Trinquier, G.; Daudey, J. P. *J. Am. Chem. Soc.* **2003**, *125*, 11051. (b) Poteau, R.; Ortega, I.; Alary, F.; Solis, A. R.; Barthelat, J. C.; Daudey, J. P. *J. Phys. Chem. A* **2001**, *105*, 198. (c) Alary, F.; Poteau, R.; Heully, J. L.; Barthelat, J. C.; Daudey, J. P. *Theor. Chem. Acc.* **2000**, *104*, 174.

(105) (a) DiLabio, G. A.; Hurley, M. M.; Christiansen, P. A. *J. Chem. Phys.* **2002**, *116*, 9578. (b) Moon, S.; Christiansen, P. A.; DiLabio, G. A. *J. Chem. Phys.* **2004**, *120*, 9080. (c) DiLabio, G. A.; Wolkow, R. A.; Johnson, E. R. *J. Chem. Phys.* **2005**, *122*, 044708.

(106) Slavíček, P.; Martínez, T. J. *J. Chem. Phys.* **2006**, *124*, 084107.

(107) Ohnishi, Y.-y.; Nakao, Y.; Sato, H.; Sakaki, S. *J. Phys. Chem. A* **2008**, *112*, 1946.

(108) Nakamura, Y.; Takahashi, N.; Okamoto, M.; Uda, T.; Ohno, T. *J. Comput. Phys.* **2007**, *225*, 1985.

(109) (a) Ferré, N.; Assfeld, X.; Rivail, J. L. *J. Comput. Chem.* **2002**, *23*, 610. (b) Monard, G.; Loos, M.; Théry, V.; Baka, K.; Rivail, J. L. *Int. J. Quantum Chem.* **1996**, *58*, 153. (c) Théry, V.; Rinaldi, D.; Rivail, J. L.; Maigret, B.; Ferenczy, G. G. *J. Comput. Chem.* **1994**, *15*, 269.

(110) (a) Gao, J.; Amara, P.; Alhambra, C.; Field, M. J. *J. Phys. Chem. A* **1998**, *102*, 4714. (b) Pu, J.; Gao, J.; Truhlar, D. G. *J. Phys. Chem. A* **2004**, *108*, 632. (c) Pu, J.; Gao, J.; Truhlar, D. G. *J. Phys. Chem. A* **2004**, *108*, 5454.

(111) (a) Murphy, R. B.; Philipp, D. M.; Friesner, R. A. *Chem. Phys. Lett.* **2000**, *321*, 113. (b) Philipp, D. M.; Friesner, R. A. *J. Comput. Chem.* **1999**, *20*, 1468.

(112) Sun, Q.; Chan, G. K.-L. *J. Chem. Theory Comput.* **2014**, *10*, 3784.

(113) Gomes, A. S. P.; Jacob, C. R. *Annu. Rep. Prog. Chem., Sect. C: Phys. Chem.* **2012**, *108*, 222.

(114) (a) Hratchian, H. P.; Krukau, A. V.; Parandekar, P. V.; Frisch, M. J.; Raghavachari, K. *J. Chem. Phys.* **2011**, *135*, 014105. (b) Labat, F.; Ciofini, I.; Hratchian, H. P.; Frisch, M.; Raghavachari, K.; Adamo, C. *J. Am. Chem. Soc.* **2009**, *131*, 14290. (c) Mayhall, N. J.; Raghavachari, K.; Hratchian, H. P. *J. Chem. Phys.* **2010**, *132*, 114107. (d) Hratchian, H. P.; Parandekar, P. V.; Raghavachari, K.; Frisch, M. J.; Vreven, T. *J. Chem. Phys.* **2008**, *128*, 034107. (e) Parandekar, P. V.; Hratchian, H. P.; Raghavachari, K. *J. Chem. Phys.* **2008**, *129*, 145101.

(115) (a) Caprasecca, S.; Jurinovich, S.; Viani, L.; Curutchet, C.; Mennucci, B. *J. Chem. Theory Comput.* **2014**, *10*, 1588. (b) Li, Q.; Mennucci, B.; Robb, M. A.; Blancafort, L.; Curutchet, C. *J. Chem. Theory Comput.* **2015**, DOI: 10.1021/ct5010388.

(116) (a) Geerke, D. P.; Thiel, S.; Thiel, W.; van Gunsteren, W. F. *J. Chem. Theory Comput.* **2007**, *3*, 1499. (b) Boulanger, E.; Thiel, W. *J. Chem. Theory Comput.* **2014**, *10*, 1795.

(117) (a) Thompson, M. A. *J. Phys. Chem.* **1996**, *100*, 14492. (b) Illingworth, C. J. R.; Gooding, S. R.; Winn, P. J.; Jones, G. A.; Ferenczy, G. G.; Reynolds, C. A. *J. Phys. Chem. A* **2006**, *110*, 6487.

(c) Lipparini, F.; Cappelli, C.; Scalmani, G.; De Mitri, N.; Barone, V. *J. Chem. Theory Comput.* **2012**, *8*, 4270. (d) Bryce, R. A.; Vincent, M. A.; Malcolm, N. O. J.; Hillier, I. H.; Burton, N. A. *J. Chem. Phys.* **1998**, *109*, 3077. (e) Lu, Z.; Zhang, Y. *J. Chem. Theory Comput.* **2008**, *4*, 1237.

(118) Zhang, Y.; Liu, H.; Yang, W. *J. Chem. Phys.* **2000**, *112*, 3483.

(119) Liang, W.; Chapman, C. T.; Frisch, M. J.; Li, X. *J. Chem. Theory Comput.* **2010**, *6*, 3352.

(120) Fukui, K. *Acc. Chem. Res.* **1981**, *14*, 363.

(121) Hratchian, H. P.; Frisch, M. J. *J. Chem. Phys.* **2011**, *134*, 204103.

(122) Polyak, I.; Boulanger, E.; Sen, K.; Thiel, W. *Phys. Chem. Chem. Phys.* **2013**, *15*, 14188.

(123) Tao, P.; Hodošcek, M.; Larkin, J. D.; Shao, Y.; Brooks, B. R. *J. Chem. Theory Comput.* **2012**, *8*, 5035.

(124) Maeda, S.; Ohno, K.; Morokuma, K. *Phys. Chem. Chem. Phys.* **2013**, *15*, 3683.

(125) (a) Maeda, S.; Ohno, K.; Morokuma, K. *J. Phys. Chem. A* **2009**, *113*, 1704. (b) Maeda, S.; Ohno, K.; Morokuma, K. *J. Chem. Theory Comput.* **2010**, *6*, 1538.

(126) (a) Ohno, K.; Maeda, S. *Chem. Phys. Lett.* **2004**, *384*, 277. (b) Maeda, S.; Ohno, K. *J. Phys. Chem. A* **2005**, *109*, 5742. (c) Ohno, K.; Maeda, S. *J. Phys. Chem. A* **2006**, *110*, 8933.

(127) (a) Maeda, S.; Morokuma, K. *J. Chem. Phys.* **2010**, *132*, 241102. (b) Maeda, S.; Morokuma, K. *J. Chem. Theory Comput.* **2011**, *7*, 2335.

(128) (a) Maeda, S.; Ohno, K. *J. Phys. Chem. A* **2007**, *111*, 13168. (b) Maeda, S.; Ohno, K. *J. Am. Chem. Soc.* **2008**, *130*, 17228. (c) Ohno, K.; Maeda, S. *J. Mol. Catal. A: Chem.* **2010**, *324*, 133.

(129) Maeda, S.; Ohno, K.; Morokuma, K. *J. Chem. Theory Comput.* **2009**, *5*, 2734.

(130) Maeda, S.; Abe, E.; Hatanaka, M.; Taketsugu, T.; Morokuma, K. *J. Chem. Theory Comput.* **2012**, *8*, 5058.

(131) Uematsu, R.; Maeda, S.; Taketsugu, T. *Chem.—Asian J.* **2014**, *9*, 305.

(132) Li, M.-J.; Liu, L.; Fu, Y.; Guo, Q.-X. *J. Phys. Chem. B* **2005**, *109*, 13818.

(133) Li, M.-J.; Liu, L.; Fu, Y.; Guo, Q.-X. *J. Mol. Struct. (THEOCHEM)* **2007**, *815*, 1.

(134) Li, M.-J.; Liu, L.; Wei, K.; Fu, Y.; Guo, Q.-X. *J. Phys. Chem. B* **2006**, *110*, 13582.

(135) Chong, S.-S.; Fu, Y.; Liu, L.; Guo, Q.-X. *J. Phys. Chem. A* **2007**, *111*, 13112.

(136) Li, M.-J.; Fu, Y.; Wang, H.-J.; Li, Y.-Q.; Liu, L.; Guo, Q.-X. *Acta Chim. Sin.* **2007**, *65*, 1243.

(137) Li, Z.; Wang, C.; Fu, Y.; Guo, Q.-X.; Liu, L. *J. Org. Chem.* **2008**, *73*, 6127.

(138) Fu, Y.; Wang, H.-J.; Chong, S.-S.; Guo, Q.-X.; Liu, L. *J. Org. Chem.* **2009**, *74*, 810.

(139) Shi, J.; Huang, X.-Y.; Wang, H.-J.; Fu, Y. *J. Chem. Inf. Model.* **2012**, *52*, 63.

(140) Gilbert, T. M. *J. Comput. Chem.* **2011**, *32*, 1493.

(141) Gille, A. L.; Gilbert, T. M. *J. Chem. Theory Comput.* **2008**, *4*, 1681.

(142) Das, S. R.; Williams, T. G.; Drummond, M. L.; Wilson, A. K. *J. Phys. Chem. A* **2010**, *114*, 9394.

(143) Riojas, A. G.; John, J. R.; Williams, T. G.; Wilson, A. K. *J. Comput. Chem.* **2012**, *33*, 2590.

(144) Oyedepo, G. A.; Wilson, A. K. *ChemPhysChem* **2011**, *12*, 3320.

(145) Vreven, T.; Thompson, L. M.; Larkin, S. M.; Kirker, I.; Bearpark, M. J. *J. Chem. Theory Comput.* **2012**, *8*, 4907.

(146) Frisch, M.; Head-Gordon, M.; Pople, J. *Chem. Phys.* **1990**, *141*, 189.

(147) da Silva, C. O.; Mennucci, B. *J. Chem. Theory Comput.* **2007**, *3*, 62.

(148) Ditchfie, R. *Mol. Phys.* **1974**, *27*, 789.

(149) Caricato, M.; Vreven, T.; Trucks, G. W.; Frisch, M. J. *J. Chem. Phys.* **2010**, *133*, 054104.

(150) Caricato, M.; Vreven, T.; Trucks, G. W.; Frisch, M. J. *J. Chem. Theory Comput.* **2011**, *7*, 180.

(151) (a) Vangunsteren, W. F.; Berendsen, H. J. C. *Angew. Chem., Int. Ed. Engl.* **1990**, *29*, 992. (b) Adcock, S. A.; McCammon, J. A. *Chem. Rev.* **2006**, *106*, 1589.

(152) Gaus, M.; Cui, Q.; Elstner, M. *WIREs Comput. Mol. Sci.* **2014**, *4*, 49.

(153) Riccardi, D.; Schaefer, P.; Yang, Y.; Yu, H.; Ghosh, N.; Prat-Resina, X.; Konig, P.; Li, G.; Xu, D.; Guo, H.; Elstner, M.; Cui, Q. *J. Phys. Chem. B* **2006**, *110*, 6458.

(154) Dewar, M. J. S.; Zoebisch, E. G.; Healy, E. F.; Stewart, J. J. P. *J. Am. Chem. Soc.* **1985**, *107*, 3902.

(155) (a) Virshup, A. M.; Punwong, C.; Pogorelov, T. V.; Lindquist, B. A.; Ko, C.; Martínez, T. J. *J. Phys. Chem. B* **2009**, *113*, 3280. (b) Thiel, W. *WIREs Comput. Mol. Sci.* **2014**, *4*, 145. (c) Lan, Z.; Fabiano, E.; Thiel, W. *J. Phys. Chem. B* **2009**, *113*, 3548. (d) Lu, Y.; Lan, Z.; Thiel, W. *Angew. Chem., Int. Ed.* **2011**, *50*, 6864.

(156) (a) Matsubara, T.; Dupuis, M.; Aida, M. *J. Phys. Chem. B* **2007**, *111*, 9965. (b) Matsubara, T.; Dupuis, M.; Aida, M. *J. Comput. Chem.* **2008**, *29*, 458.

(157) (a) Chung, W. C.; Nanbu, S.; Ishida, T. *J. Phys. Chem. B* **2012**, *116*, 8009. (b) Ishida, T.; Nanbu, S.; Nakamura, H. *J. Phys. Chem. A* **2009**, *113*, 4356.

(158) Groenhof, G.; Bouxin-Cademartory, M.; Hess, B.; De Visser, S. P.; Berendsen, H. J. C.; Olivucci, M.; Mark, A. E.; Robb, M. A. *J. Am. Chem. Soc.* **2004**, *126*, 4228.

(159) (a) Tully, J. C. *J. Chem. Phys.* **1990**, *93*, 1061. (b) Hammes-Schiffer, S.; Tully, J. C. *J. Chem. Phys.* **1994**, *101*, 4657. (c) Warshel, A.; Chu, Z. T. *J. Phys. Chem. B* **2001**, *105*, 9857. (d) Lasorne, B.; Worth, G. A.; Robb, M. A. *WIREs Comput. Mol. Sci.* **2011**, *1*, 460. (e) Ben-Nun, M.; Quenneville, J.; Martínez, T. J. *J. Phys. Chem. A* **2000**, *104*, 5161.

(160) (a) Li, X.; Chung, L. W.; Mizuno, H.; Miyawaki, A.; Morokuma, K. *J. Phys. Chem. Lett.* **2010**, *1*, 3328. (b) Li, X.; Chung, L. W.; Morokuma, K. *J. Chem. Theory Comput.* **2011**, *7*, 2694.

(161) Fingerhut, B. P.; Oesterling, S.; Haiser, K.; Heil, K.; Glas, A.; Schreier, W. J.; Zinth, W.; Carell, T.; de Vivie-Riedle, R. *J. Chem. Phys.* **2012**, *136*, 204307.

(162) (a) Hayashi, S.; Taikhorshid, E.; Schulten, K. *Biophys. J.* **2009**, *96*, 403. (b) Polli, D.; Altoè, P.; Weingart, O.; Spillane, K. M.; Manzoni, C.; Brida, D.; Tomasello, G.; Orlandi, G.; Kukura, P.; Mathies, R. A.; Garavelli, M.; Cerullo, G. *Nature* **2010**, *467*, 440.

(163) (a) Bulo, R. E.; Ensing, B.; Sikkema, J.; Visscher, L. *J. Chem. Theory Comput.* **2009**, *5*, 2212. (b) Heyden, A.; Lin, H.; Truhlar, D. G. *J. Phys. Chem. B* **2007**, *111*, 2231. (c) Park, K.; Götz, A. W.; Walker, R. C.; Paesani, F. *J. Chem. Theory Comput.* **2012**, *8*, 2868. (d) Pezeshki, S.; Lin, H. *J. Chem. Theory Comput.* **2011**, *7*, 3625. (e) Takenaka, N.; Kitamura, Y.; Koyano, Y.; Nagaoka, M. *Chem. Phys. Lett.* **2012**, *524*, 56.

(164) (a) Sumner, I.; Iyengar, S. S. *J. Chem. Phys.* **2008**, *129*, 054109. (b) Sumner, I.; Iyengar, S. S. *J. Phys. Chem. A* **2007**, *111*, 10313.

(165) (a) Rega, N.; Iyengar, S. S.; Voth, G. A.; Schlegel, H. B.; Vreven, T.; Frisch, M. J. *J. Phys. Chem. B* **2004**, *108*, 4210. (b) Schlegel, H. B.; Millam, J. M.; Iyengar, S. S.; Voth, G. A.; Daniels, A. D.; Scuseria, G. E.; Frisch, M. J. *J. Chem. Phys.* **2001**, *114*, 9758.

(166) Car, R.; Parrinello, M. *Phys. Rev. Lett.* **1985**, *55*, 2471.

(167) Phatak, P.; Sumner, I.; Iyengar, S. S. *J. Phys. Chem. B* **2012**, *116*, 10145.

(168) (a) Beveridge, D. L.; Dicapua, F. M. *Annu. Rev. Biophys. Biophys. Chem.* **1989**, *18*, 431. (b) Kollman, P. *Chem. Rev.* **1993**, *93*, 2395. (c) Dror, R. O.; Dirks, R. M.; Grossman, J. P.; Xu, H.; Shaw, D. E. *Annu. Rev. Biophys.* **2012**, *41*, 429. (d) Gao, J.; Ma, S.; Major, D. T.; Nam, K.; Pu, J.; Truhlar, D. G. *Chem. Rev.* **2006**, *106*, 3188. (e) Hu, H.; Yang, W. *J. Mol. Struct. (THEOCHEM)* **2009**, *898*, 17. (f) Hou, G.; Cui, Q. *J. Am. Chem. Soc.* **2013**, *135*, 10457.

(169) Klähn, M.; Braun-Sand, S.; Rosta, E.; Warshel, A. *J. Phys. Chem. B* **2005**, *109*, 15645.

(170) Bentzien, J.; Muller, R. P.; Florián, J.; Warshel, A. *J. Phys. Chem. B* **1998**, *102*, 2293.

(171) (a) Gonzalezlafont, A.; Truong, T. N.; Truhlar, D. G. *J. Phys. Chem.* **1991**, *95*, 4618. (b) Doron, D.; Major, D. T.; Kohen, A.; Thiel, W.; Wu, X. *J. Chem. Theory Comput.* **2011**, *7*, 3420. (c) Cui, Q.; Karplus, M. *J. Am. Chem. Soc.* **2001**, *123*, 2284.

(172) Yao, L.; Yan, H.; Cukier, R. I. *J. Phys. Chem. B* **2006**, *110*, 26320.

(173) Chandrasekhar, J.; Smith, S. F.; Jorgensen, W. L. *J. Am. Chem. Soc.* **1985**, *107*, 154.

(174) (a) Rod, T. H.; Ryde, U. *J. Chem. Theory Comput.* **2005**, *1*, 1240. (b) Kästner, J.; Senn, H. M.; Thiel, S.; Otte, N.; Thiel, W. *J. Chem. Theory Comput.* **2006**, *2*, 452. (c) Heimdal, J.; Ryde, U. *Phys. Chem. Chem. Phys.* **2012**, *14*, 12592.

(175) Okuyama-Yoshida, N.; Nagaoka, M.; Yamabe, T. *Int. J. Quantum Chem.* **1998**, *70*, 95.

(176) (a) Hu, H.; Lu, Z.; Yang, W. *J. Chem. Theory Comput.* **2007**, *3*, 390. (b) Hu, H.; Lu, Z.; Parks, J. M.; Burger, S. K.; Yang, W. *J. Chem. Phys.* **2008**, *128*, 034105.

(177) (a) Kosugi, T.; Hayashi, S. *J. Chem. Theory Comput.* **2012**, *8*, 322. (b) Bohner, M. U.; Kästner, J. *J. Chem. Phys.* **2012**, *137*, 034105.

(178) (a) Hankins, D.; Moskowit, J. W.; Stilling, F. H. *J. Chem. Phys.* **1970**, *53*, 4544. (b) Elrod, M. J.; Saykally, R. J. *Chem. Rev.* **1994**, *94*, 1975.

(179) (a) Yang, W. *Phys. Rev. Lett.* **1991**, *66*, 1438. (b) Day, P. N.; Jensen, J. H.; Gordon, M. S.; Webb, S. P.; Stevens, W. J.; Krauss, M.; Garmer, D.; Basch, H.; Cohen, D. *J. Chem. Phys.* **1996**, *105*, 1968. (c) Gordon, M. S.; Freitag, M. A.; Bandyopadhyay, P.; Jensen, J. H.; Kairys, V.; Stevens, W. J. *J. Phys. Chem. A* **2001**, *105*, 293. (d) Gordon, M. S.; Fedorov, D. G.; Pruitt, S. R.; Slipchenko, L. V. *Chem. Rev.* **2012**, *112*, 632. (e) Fedorov, D. G.; Kitaura, K. *J. Phys. Chem. A* **2007**, *111*, 6904. (f) Pruitt, S. R.; Bertoni, C.; Brorsen, K. R.; Gordon, M. S. *Acc. Chem. Res.* **2014**, *47*, 2786. (g) Richard, R. M.; Lao, K. U.; Herbert, J. M. *Acc. Chem. Res.* **2014**, *47*, 2828. (h) Ji, C.; Mei, Y. *Acc. Chem. Res.* **2014**, *47*, 2795. (i) Merz, K. M. *Acc. Chem. Res.* **2014**, *47*, 2804. (j) Beran, G. J. O.; Hirata, S. *Phys. Chem. Chem. Phys.* **2012**, *14*, 7559. (k) Li, S.; Li, W.; Ma, J. *Acc. Chem. Res.* **2014**, *47*, 2712. (l) Sahu, N.; Gadre, S. R. *Acc. Chem. Res.* **2014**, *47*, 2739. (m) Wang, B.; Yang, K. R.; Xu, X.; Isegawa, M.; Leverentz, H. R.; Truhlar, D. G. *Acc. Chem. Res.* **2014**, *47*, 2731. (n) He, X.; Zhu, T.; Wang, X.; Liu, J.; Zhang, J. Z. H. *Acc. Chem. Res.* **2014**, *47*, 2748. (o) Zhang, D. W.; Zhang, J. Z. H. *J. Chem. Phys.* **2003**, *119*, 3599. (p) Li, S.; Li, W.; Fang, T. *J. Am. Chem. Soc.* **2005**, *127*, 7215. (q) Collins, M. A.; Deev, V. A. *J. Chem. Phys.* **2006**, *125*, 104104. (r) Babu, K.; Gadre, S. R. *J. Comput. Chem.* **2003**, *24*, 484. (s) Deev, V.; Collins, M. A. *J. Chem. Phys.* **2005**, *122*, 154102. (t) Kitaura, K.; Ikeo, E.; Asada, T.; Nakano, T.; Uebayasi, M. *Chem. Phys. Lett.* **1999**, *313*, 701. (u) Gao, J. *J. Phys. Chem. B* **1997**, *101*, 657. (v) Xie, W.; Gao, J. *J. Chem. Theory Comput.* **2007**, *3*, 1890. (w) Collins, M. A.; Cvitkovic, M. W.; Bettens, R. P. A. *Acc. Chem. Res.* **2014**, *47*, 2776.

(180) (a) Hopkins, B. W.; Tschumper, G. S. *J. Comput. Chem.* **2003**, *24*, 1563. (b) Hopkins, B. W.; Tschumper, G. S. *Chem. Phys. Lett.* **2005**, *407*, 362. (c) Hopkins, B. W.; Tschumper, G. S. *Mol. Phys.* **2005**, *103*, 309. (d) Tschumper, G. S. *Chem. Phys. Lett.* **2006**, *427*, 185. (e) Elsohly, A. M.; Shaw, C. L.; Guice, M. E.; Smith, B. D.; Tschumper, G. S. *Mol. Phys.* **2007**, *105*, 2777. (f) Bates, D. M.; Smith, J. R.; Janowski, T.; Tschumper, G. S. *J. Chem. Phys.* **2011**, *135*, 044123. (g) Bates, D. M.; Smith, J. R.; Tschumper, G. S. *J. Chem. Theory Comput.* **2011**, *7*, 2753. (h) Howard, J. C.; Tschumper, G. S. *J. Chem. Phys.* **2013**, *139*, 184113. (i) Asada, N.; Fedorov, D. G.; Kitaura, K.; Nakanishi, I.; Merz, K. M. *J. Phys. Chem. Lett.* **2012**, *3*, 2604. (j) Guo, W.; Wu, A.; Xu, X. *Chem. Phys. Lett.* **2010**, *498*, 203. (k) Saha, A.; Raghavachari, K. *J. Chem. Theory Comput.* **2014**, *10*, 58. (l) Mayhall, N. J.; Raghavachari, K. *J. Chem. Theory Comput.* **2011**, *7*, 1336. (m) Mayhall, N. J.; Raghavachari, K. *J. Chem. Theory Comput.* **2012**, *8*, 2669. (n) Gascon, J. A.; Leung, S. S. F.; Batista, E. R.; Batista, V. S. *J. Chem. Theory Comput.* **2006**, *2*, 175. (o) He, X.; Wang, B.; Merz, K. M. *J. Phys. Chem. B* **2009**, *113*, 10380.

(181) Guo, W.; Wu, A.; Zhang, I. Y.; Xu, X. *J. Comput. Chem.* **2012**, *33*, 2142.

(182) (a) Goedecker, S. *Rev. Mod. Phys.* **1999**, *71*, 1085. (b) Strain, M. C.; Scuseria, G. E.; Frisch, M. J. *Science* **1996**, *271*, 51. (c) Scuseria, G. E. *J. Phys. Chem. A* **1999**, *103*, 4782. (d) Kussmann, J.; Beer, M.; Ochsenfeld, C. *WIREs Comput. Mol. Sci.* **2013**, *3*, 614.

(183) (a) Friesner, R. A.; Murphy, R. B.; Beachy, M. D.; Ringnalda, M. N.; Pollard, W. T.; Dunietz, B. D.; Cao, Y. *J. Phys. Chem. A* **1999**, *103*, 1913. (b) Saebo, S.; Pulay, P. *Annu. Rev. Phys. Chem.* **1993**, *44*, 213. (c) Hampel, C.; Werner, H. J. *J. Chem. Phys.* **1996**, *104*, 6286. (d) Schütz, M.; Hetzer, G.; Werner, H. J. *J. Chem. Phys.* **1999**, *111*, 5691. (e) Schütz, M.; Werner, H. J. *J. Chem. Phys.* **2001**, *114*, 661. (f) Neese, F.; Hansen, A.; Liakos, D. G. *J. Chem. Phys.* **2009**, *131*, 064103.

(184) (a) Klopper, W.; Manby, F. R.; Ten-No, S.; Valeev, E. F. *Int. Rev. Phys. Chem.* **2006**, *25*, 427. (b) Hättig, C.; Klopper, W.; Köhn, A.; Tew, D. P. *Chem. Rev.* **2012**, *112*, 4. (c) Kutzelnigg, W.; Klopper, W. *J. Chem. Phys.* **1991**, *94*, 1985.

(185) (a) Sproviero, E. M.; Newcomer, M. B.; Gascón, J. A.; Batista, E. R.; Brudvig, G. W.; Batista, V. S. *Photosynth. Res.* **2009**, *102*, 455. (b) Menikarachchi, L. C.; Gascón, J. A. *J. Mol. Model.* **2008**, *14*, 479.

(186) Tao, P.; Schlegel, H. B. *J. Comput. Chem.* **2010**, *31*, 2363.

(187) (a) Eurenius, K. P.; Chatfield, D. C.; Brooks, B. R.; Hodošček, M. *Int. J. Quantum Chem.* **1996**, *60*, 1189. (b) Altun, A.; Shaik, S.; Thiel, W. *J. Comput. Chem.* **2006**, *27*, 1324. (c) Zheng, J.; Altun, A.; Thiel, W. *J. Comput. Chem.* **2007**, *28*, 2147. (d) Altun, A.; Guallar, V.; Friesner, R. A.; Shaik, S.; Thiel, W. *J. Am. Chem. Soc.* **2006**, *128*, 3924. (e) Zhang, Y.; Kua, J.; McCammon, J. A. *J. Phys. Chem. B* **2003**, *107*, 4459.

(188) Lundberg, M.; Kawatsu, T.; Vreven, T.; Frisch, M. J.; Morokuma, K. *J. Chem. Theory Comput.* **2009**, *5*, 222.

(189) Siegbahn, P. E. M.; Borowski, T. *Faraday Discuss.* **2011**, *148*, 109.

(190) Li, X.; Chung, L. W.; Paneth, P.; Morokuma, K. *J. Am. Chem. Soc.* **2009**, *131*, 5115.

(191) Goldfuss, B.; Rominger, F. *Tetrahedron* **2000**, *56*, 881.

(192) Alpagut, Y.; Goldfuss, B.; Neudörfl, J. M. *Beilstein J. Org. Chem.* **2008**, *4*, 25.

(193) (a) Wieczorek, R.; Dannenberg, J. J. *J. Am. Chem. Soc.* **2005**, *127*, 17216. (b) Wieczorek, R.; Dannenberg, J. J. *J. Am. Chem. Soc.* **2005**, *127*, 14534.

(194) Vreven, T.; Morokuma, K. *J. Chem. Phys.* **1999**, *111*, 8799.

(195) (a) Froese, R. D. J.; Morokuma, K. *Chem. Phys. Lett.* **1999**, *305*, 419. (b) Froese, R. D. J.; Morokuma, K. *J. Phys. Chem. A* **1999**, *103*, 4580. (c) Borisenko, K. B.; Rankin, D. W. H. *Dalton Trans.* **2005**, 2382. (d) Espinosa-García, J. *Chem. Phys. Lett.* **2003**, *377*, 607.

(196) Nam, P. C.; Chandra, A. K.; Nguyen, M. T. *Chem. Phys. Lett.* **2013**, *555*, 44.

(197) (a) Remko, M.; von der Lieth, C.-W. *Biorg. Med. Chem.* **2004**, *12*, 5395. (b) Remko, M. *J. Phys. Chem. A* **2003**, *107*, 720.

(198) Remko, M.; Walsh, O. A.; Graham Richards, W. *Phys. Chem. Chem. Phys.* **2001**, *3*, 901.

(199) Remko, M.; Lyne, P. D.; Graham Richards, W. *Phys. Chem. Chem. Phys.* **2000**, *2*, 2511.

(200) Remko, M.; Walsh, O. A.; Richards, W. G. *J. Phys. Chem. A* **2001**, *105*, 6926.

(201) Remko, M. *J. Phys. Chem. A* **2002**, *106*, 5005.

(202) (a) Plaza, A.; Piacente, S.; Perrone, A.; Hamed, A.; Pizza, C.; Bifulco, G. *Tetrahedron* **2004**, *60*, 12201. (b) Tafazzoli, M.; Ghiasi, M. *Carbohydr. Polym.* **2009**, *78*, 10.

(203) Rickard, G. A.; Karadakov, P. B.; Webb, G. A.; Morokuma, K. *J. Phys. Chem. A* **2002**, *107*, 292.

(204) (a) Leyton, P.; Brunet, J.; Silva, V.; Paipa, C.; Castillo, M. V.; Brandan, S. A. *Spectrochim. Acta, Part A* **2012**, *88*, 162. (b) Namazian, M.; Coote, M. L. *J. Phys. Chem. A* **2007**, *111*, 7227.

(205) (a) Hodgson, J. L.; Namazian, M.; Bottle, S. E.; Coote, M. L. *J. Phys. Chem. A* **2007**, *111*, 13595. (b) Blinco, J. P.; Hodgson, J. L.; Morrow, B. L.; Walker, J. P.; Will, M. L.; Coote, J. D.; Bottle, S. E. *J. Org. Chem.* **2008**, *73*, 6763.

(206) Svensson, M.; Humbel, S.; Morokuma, K. *J. Chem. Phys.* **1996**, *105*, 3654.

(207) Re, S.; Morokuma, K. *Theor. Chem. Acc.* **2004**, *112*, 59.

(208) Borisov, Y. A.; Arcia, E. E.; Mielke, S. L.; Garrett, B. C.; Dunning, T. H. *J. Phys. Chem. A* **2001**, *105*, 7724.

(209) Mo, S. J.; Vreven, T.; Mennucci, B.; Morokuma, K.; Tomasi, J. *Theor. Chem. Acc.* **2004**, *111*, 154.

(210) Re, S.; Morokuma, K. *J. Phys. Chem. A* **2001**, *105*, 7185.

(211) McClement, C. S.; Smiles, S. *J. Chem. Soc.* **1937**, 1016.

(212) Musaev, D. G.; Galloway, A. L.; Menger, F. M. *J. Mol. Struct. (THEOCHEM)* **2004**, *679*, 45.

(213) Chéron, N.; Jacquemin, D.; Fleurat-Lessard, P. *Phys. Chem. Chem. Phys.* **2012**, *14*, 7170.

(214) Chéron, N.; El Kaïm, L.; Grimaud, L.; Fleurat-Lessard, P. *Chem.—Eur. J.* **2011**, *17*, 14929.

(215) (a) Fabian, J.; Krebs, A.; Schönemann, D.; Schaefer, W. *J. Org. Chem.* **2000**, *65*, 8940. (b) Bakalova, S. M.; Kaneti, J. *J. Phys. Chem. A* **2008**, *112*, 13006.

(216) Torrente, S.; Noya, B.; Branchadell, V.; Alonso, R. *J. Org. Chem.* **2003**, *68*, 4772.

(217) Larkin, S. M.; Vreven, T.; Bearpark, M. J.; Morokuma, K. *Can. J. Chem.* **2009**, *87*, 872.

(218) Paquette, L. A.; Reddy, Y. R.; Vayner, G.; Houk, K. N. *J. Am. Chem. Soc.* **2000**, *122*, 10788.

(219) (a) Feldgus, S.; Shields, G. C. *Chem. Phys. Lett.* **2001**, *347*, 505. (b) Tuttle, T.; Kraka, E.; Cremer, D. *J. Am. Chem. Soc.* **2005**, *127*, 9469.

(220) Izgorodina, E. I.; Brittain, D. R. B.; Hodgson, J. L.; Krenske, E. H.; Lin, C. Y.; Namazian, M.; Coote, M. L. *J. Phys. Chem. A* **2007**, *111*, 10754.

(221) (a) Kyne, S. H.; Lin, C. Y.; Ryu, I.; Coote, M. L.; Schiesser, C. H. *Chem. Commun.* **2010**, *46*, 6521. (b) Lin, C. Y.; Hodgson, J. L.; Namazian, M.; Coote, M. L. *J. Phys. Chem. A* **2009**, *113*, 3690.

(222) Shi, J.; Chong, S.-S.; Fu, Y.; Guo, Q.-X.; Liu, L. *J. Org. Chem.* **2008**, *73*, 974.

(223) (a) Espinosa-Garcia, J. *J. Phys. Chem. A* **2003**, *107*, 1618. (b) Espinosa-Garcia, J. *Phys. Chem. Chem. Phys.* **2002**, *4*, 1807.

(224) (a) Li, Q. S.; Zhao, Q.; Zhang, S. *J. Phys. Chem. A* **2004**, *108*, 6430. (b) Montoya, A.; Mondragon, F.; Truong, T. N. *Carbon* **2002**, *40*, 1863. (c) Truong, T. N.; Truong, T.-T. T. *Chem. Phys. Lett.* **1999**, *314*, 529.

(225) Shi, J.; Zhang, M.; Fu, Y.; Liu, L.; Guo, Q.-X. *Tetrahedron* **2007**, *63*, 12681.

(226) Cerón-Carrasco, J. P.; Jacquemin, D. *RSC Adv.* **2012**, *2*, 11867.

(227) Remko, M.; T, V. D. P.; Swart, M. *Struct. Chem.* **2003**, *14*, 271.

(228) (a) Xu, L.; Sang, P.; Zou, J.-W.; Xu, M.-B.; Li, X.-M.; Yu, Q.-S. *Chem. Phys. Lett.* **2011**, *509*, 175. (b) Hopkins, B. W.; Tschumper, G. S. *Int. J. Quantum Chem.* **2004**, *96*, 294.

(229) Kim, Y. K.; Lee, H. N.; Singh, N. J.; Choi, H. J.; Xue, J. Y.; Kim, K. S.; Yoon, J.; Hyun, M. H. *J. Org. Chem.* **2008**, *73*, 301.

(230) (a) Piyaauksornsak, S.; Tangthongkul, T.; Wanbayor, R.; Wanno, B.; Ruangpornvisuti, V. *Struct. Chem.* **2009**, *20*, 767. (b) Ruangpornvisuti, V. *J. Mol. Struct. (THEOCHEM)* **2004**, *686*, 47.

(231) Ruangpornvisuti, V.; Wanno, B. *J. Mol. Model.* **2007**, *13*, 65.

(232) (a) Shi, J.-h.; Ding, Z.-j.; Hu, Y. *J. Mol. Model.* **2012**, *18*, 803. (b) Shi, J.-h.; Hu, Y.; Ding, Z.-j. *Comput. Theor. Chem.* **2011**, *973*, 62. (c) Huang, M.-J.; Quan, Z.; Liu, Y.-M. *Int. J. Quantum Chem.* **2009**, *109*, 81. (d) Blenke, C.; Da Silva, V. J.; Junqueira, G. M. A.; De Almeida, W. B.; Dos Santos, H. F. *J. Mol. Struct. (THEOCHEM)* **2007**, *809*, 95.

(233) Borosky, G. L.; Laali, K. K. *J. Phys. Org. Chem.* **2010**, *23*, 810.

(234) Pliego, J. R., Jr. *Phys. Chem. Chem. Phys.* **2011**, *13*, 779.

(235) (a) Pliego, J. R.; Piló-Veloso, D. *J. Phys. Chem. B* **2007**, *111*, 1752. (b) Pliego, J. R., Jr. *Org. Biomol. Chem.* **2006**, *4*, 1667.

(236) Balcells, D.; Ujaque, G.; Fernández, I.; Khiar, N.; Maserasa, F. *Adv. Synth. Catal.* **2007**, *349*, 2103.

(237) (a) Simòn, L.; Goodman, J. M. *J. Org. Chem.* **2010**, *75*, 589. (b) Simòn, L.; Goodman, J. M. *J. Am. Chem. Soc.* **2009**, *131*, 4070. (c) Simòn, L.; Goodman, J. M. *J. Org. Chem.* **2011**, *76*, 1775. (d) Simòn, L.; Goodman, J. M. *J. Am. Chem. Soc.* **2008**, *130*, 8741.

(238) Marcelli, T.; Hammar, P.; Himo, F. *Adv. Synth. Catal.* **2009**, *351*, 525.

(239) Shibata, Y.; Yamanaka, M. *J. Org. Chem.* **2013**, *78*, 3731.

(240) Hirata, T.; Yamanaka, M. *Chem.—Asian J.* **2011**, *6*, 510.

(241) Fu, A.; Meng, W.; Li, H.; Nie, J.; Ma, J.-A. *Org. Biomol. Chem.* **2014**, *12*, 1908.

(242) Li, N.; Chen, X.-H.; Song, J.; Luo, S.-W.; Fan, W.; Gong, L.-Z. *J. Am. Chem. Soc.* **2009**, *131*, 15301.

(243) Shi, F.-Q.; Song, B.-A. *Org. Biomol. Chem.* **2009**, *7*, 1292.

(244) Grayson, M. N.; Pellegrinet, S. C.; Goodman, J. M. *J. Am. Chem. Soc.* **2012**, *134*, 2716.

(245) Mori, K.; Ichikawa, Y.; Kobayashi, M.; Shibata, Y.; Yamanaka, M.; Akiyama, T. *J. Am. Chem. Soc.* **2013**, *135*, 3964.

(246) Mori, K.; Katoh, T.; Suzuki, T.; Noji, T.; Yamanaka, M.; Akiyama, T. *Angew. Chem., Int. Ed.* **2009**, *48*, 9652.

(247) Yamanaka, M.; Hoshino, M.; Katoh, T.; Mori, K.; Akiyama, T. *Eur. J. Org. Chem.* **2012**, *2012*, 4508.

(248) Desai, A. A.; Wulff, W. D. *J. Am. Chem. Soc.* **2010**, *132*, 13100.

(249) Zhang, X.; Du, H.; Wang, Z.; Wu, Y.-D.; Ding, K. *J. Org. Chem.* **2006**, *71*, 2962.

(250) Anderson, C. D.; Dudding, T.; Gordillo, R.; Houk, K. N. *Org. Lett.* **2008**, *10*, 2749.

(251) Akakura, M.; Kawasaki, M.; Yamamoto, H. *Eur. J. Org. Chem.* **2008**, *2008*, 4245.

(252) Simòn, L.; Goodman, J. M. *J. Am. Chem. Soc.* **2012**, *134*, 16869.

(253) Díaz, J.; Goodman, J. M. *Tetrahedron* **2010**, *66*, 8021.

(254) Shinisha, C. B.; Sunoj, R. B. *Org. Biomol. Chem.* **2008**, *6*, 3921.

(255) Corey, E. J.; Bakshi, R. K.; Shibata, S. *J. Am. Chem. Soc.* **1987**, *109*, 5551.

(256) Korenaga, T.; Nomura, K.; Onoue, K.; Sakai, T. *Chem. Commun.* **2010**, *46*, 8624.

(257) Su, Z.; Lee, H. W.; Kim, C. K. *Eur. J. Org. Chem.* **2013**, *2013*, 1706.

(258) Li, W.; Huang, D.; Lv, Y. *Org. Biomol. Chem.* **2013**, *11*, 7497.

(259) Dogo-Isonagie, C.; Bekele, T.; France, S.; Wolfer, J.; Weatherwax, A.; Taggi, A. E.; Paull, D. H.; Dudding, T.; Lectka, T. *Eur. J. Org. Chem.* **2007**, *2007*, 1091.

(260) Petrova, G. P.; Li, H.-B.; Maruoka, K.; Morokuma, K. *J. Phys. Chem. B* **2014**, *118*, 5154.

(261) Tang, K.; Wang, J.; Hou, Q.; Cheng, X.; Liu, Y. *Tetrahedron: Asymmetry* **2011**, *22*, 942.

(262) Dudding, T.; Houk, K. N. *Proc. Natl. Acad. Sci. U.S.A.* **2004**, *101*, 5770.

(263) Kheirabadi, M.; Çelebi-Ölçüm, N.; Parker, M. F.; Zhao, Q.; Kiss, G.; Houk, K. N.; Schafmeister, C. E. *J. Am. Chem. Soc.* **2012**, *134*, 18345.

(264) Simòn, L.; Goodman, J. M. *Org. Biomol. Chem.* **2009**, *7*, 483.

(265) Sengupta, A.; Sunoj, R. B. *J. Org. Chem.* **2012**, *77*, 10525.

(266) Lu, N.; Chen, D.; Mi, S.; Zhang, G.; Zhang, H. *Int. J. Quantum Chem.* **2011**, *111*, 4206.

(267) (a) Chaffey-Millar, H.; Stenzel, M. H.; Davis, T. P.; Coote, M. L.; Barner-Kowollik, C. *Macromolecules* **2006**, *39*, 6406. (b) Coote, M. L.; Krenske, E. H.; Izgorodina, E. I. *Macromol. Rapid Commun.* **2006**, *27*, 473. (c) Klumperman, B.; van den Dungen, E. T. A.; Heuts, J. P. A.; Monteiro, M. J. *Macromol. Rapid Commun.* **2010**, *31*, 1846. (d) Coote, M. L. *Macromol. Theory Simul.* **2009**, *18*, 388.

(268) Coote, M. L. *J. Phys. Chem. A* **2005**, *109*, 1230.

(269) Izgorodina, E. I.; Coote, M. L. *J. Phys. Chem. A* **2006**, *110*, 2486.

(270) Coote, M. L.; Izgorodina, E. I.; Cavigliasso, G. E.; Roth, M.; Busch, M.; Barner-Kowollik, C. *Macromolecules* **2006**, *39*, 4585.

(271) Izgorodina, E. I.; Coote, M. L. *Macromol. Theory Simul.* **2006**, *15*, 394.

(272) Nebhani, L.; Sinnwell, S.; Lin, C. Y.; Coote, M. L.; Stenzel, M. H.; Barner-Kowollik, C. *J. Polym. Sci., Part A: Polym. Chem.* **2009**, *47*, 6053.

(273) Hodgson, J. L.; Roskop, L. B.; Gordon, M. S.; Lin, C. Y.; Coote, M. L. *J. Phys. Chem. A* **2010**, *114*, 10458.

(274) Megiel, E.; Kaim, A. *J. Polym. Sci., Part A: Polym. Chem.* **2008**, *46*, 1165.

(275) Izgorodina, E. I.; Coote, M. L. *Chem. Phys.* **2006**, *324*, 96.

(276) Falvello, L. R.; Ginés, J. C.; Carbó, J. J.; Lledós, A.; Navarro, R.; Soler, T.; Urriolabeitia, E. P. *Inorg. Chem.* **2006**, *45*, 6803.

(277) (a) Ujaque, G.; Cooper, A. C.; Maseras, F.; Eisenstein, O.; Caulton, I. G. *J. Am. Chem. Soc.* **1998**, *120*, 361. (b) Ujaque, G.; Maseras, F.; Eisenstein, O.; Liable-Sands, L.; Rheingold, A. L.; Yao, W.; Crabtree, R. H. *New J. Chem.* **1998**, *22*, 1493. (c) Maseras, F.; Eisenstein, O. *New J. Chem.* **1998**, *22*, 5. (d) Ogasawara, M.; Maseras, F.; Gallego-Planas, N.; Kawamura, K.; Ito, K.; Toyota, K.; Streib, W. E.; Komiya, S.; Eisenstein, O.; Caulton, K. G. *Organometallics* **1997**, *16*, 1979. (e) Barea, G.; Lledós, A.; Maseras, F.; Jean, Y. *Inorg. Chem.* **1998**, *37*, 3321. (f) Christmann, U.; Pantazis, D. A.; Benet-Buchholz, J.; McGrady, J. E.; Maseras, F.; Vilar, R. *J. Am. Chem. Soc.* **2006**, *128*, 6376. (g) Yandulov, D. V.; Caulton, K. G.; Belkova, N. V.; Shubina, E. S.; Epstein, L. M.; Khoroshun, D. V.; Musaev, D. G.; Morokuma, K. *J. Am. Chem. Soc.* **1998**, *120*, 12553.

(278) Gusev, D. G.; Lough, A. J. *Organometallics* **2002**, *21*, 5091.

(279) Mohr, M.; McNamara, J. P.; Wang, H.; Rajeev, S. A.; Ge, J.; Morgado, C. A.; Hillier, I. H. *Faraday Discuss.* **2003**, *124*, 413.

(280) Iordanov, T. D. *J. Mol. Struct. (THEOCHEM)* **2008**, *850*, 152.

(281) Li, Z.; Liu, L.; Fu, Y.; Guo, Q.-X. *J. Mol. Struct. (THEOCHEM)* **2005**, *757*, 69.

(282) (a) Tsai, Y.-C.; Lu, D.-Y.; Lin, Y.-M.; Hwang, J.-K.; Yu, J.-S. K. *Chem. Commun.* **2007**, 4125. (b) McKee, M. L.; Hill, W. E. *J. Phys. Chem. A* **2002**, *106*, 6201.

(283) Clot, E.; Eisenstein, O. *Struct. Bonding (Berlin, Ger.)* **2004**, *113*, 1.

(284) Jaffart, J.; Mathieu, R.; Etienne, M.; McGrady, J. E.; Eisenstein, O.; Maseras, F. *Chem. Commun.* **1998**, 2011.

(285) Jaffart, J.; Etienne, M.; Maseras, F.; McGrady, J. E.; Eisenstein, O. *J. Am. Chem. Soc.* **2001**, *123*, 6000.

(286) Cooper, A. C.; Clot, E.; Huffman, J. C.; Streib, W. E.; Maseras, F.; Eisenstein, O.; Caulton, K. G. *J. Am. Chem. Soc.* **1999**, *121*, 97.

(287) Balcells, D.; Carbó, J. J.; Maseras, F.; Eisenstein, O. *Organometallics* **2004**, *23*, 6008.

(288) Solans-Monfort, X.; Clot, E.; Copéret, C.; Eisenstein, O. *Organometallics* **2005**, *24*, 1586.

(289) Moores, A.; Mézailles, N.; Ricard, L.; Jean, Y.; le Floch, P. *Organometallics* **2004**, *23*, 2870.

(290) (a) Mora, G.; Deschamps, B.; van Zutphen, S.; Le Goff, X. F.; Ricard, L.; Le Floch, P. *Organometallics* **2007**, *26*, 1846. (b) Ison, E. A.; Cameron, T. M.; Abboud, K. A.; Boncella, J. M. *Organometallics* **2004**, *23*, 4070.

(291) Barea, G.; Maseras, F.; Jean, Y.; Lledós, A. *Inorg. Chem.* **1996**, *35*, 6401.

(292) Ujaque, G.; Maseras, F.; Lledós, A. *Theor. Chim. Acta* **1996**, *94*, 67.

(293) Vyboishchikov, S. F.; Nikonov, G. I. *Organometallics* **2007**, *26*, 4160.

(294) Woo, T. K.; Pioda, G.; Rothlisberger, U.; Togni, A. *Organometallics* **2000**, *19*, 2144.

(295) Clark, M.; Cramer, R. D.; Vanopdenbosch, N. *J. Comput. Chem.* **1989**, *10*, 982.

(296) Hutter, J.; Ballone, P.; Bernasconi, M.; Focher, P.; Fois, E.; Goedecker, S.; Parrinello, M.; Tuckerman, M.; *CPMD*; Max-Planck-Institut für Festkörperforschung: Stuttgart, Germany, and IBM Zürich Research Laboratory, 1998.

(297) Doman, T. N.; Landis, C. R.; Bosnich, B. *J. Am. Chem. Soc.* **1992**, *114*, 7264.

(298) Macchioni, A. *Chem. Rev.* **2005**, *105*, 2039.

(299) (a) Gruet, K.; Clot, E.; Eisenstein, O.; Lee, D. H.; Patel, B.; Macchioni, A.; Crabtree, R. H. *New J. Chem.* **2003**, *27*, 80. (b) Kovacevic, A.; Grundemann, S.; Miecznikowski, J. R.; Clot, E.; Eisenstein, O.; Crabtree, R. H. *Chem. Commun.* **2002**, 2580. (c) Macchioni, A.; Zuccaccia, C.; Clot, E.; Gruet, K.; Crabtree, R. H. *Organometallics* **2001**, *20*, 2367.

(300) Kitagawa, Y.; Yasuda, N.; Hatake, H.; Saito, T.; Kataoka, Y.; Matsui, T.; Kawakami, T.; Yamanaka, S.; Okumura, M.; Yamaguch, K. *Int. J. Quantum Chem.* **2013**, *113*, 290.

(301) Kitagawa, Y.; Saito, T.; Ito, M.; Shoji, M.; Koizumi, K.; Yamanaka, S.; Kawakami, T.; Okumura, M.; Yamaguchi, K. *Chem. Phys. Lett.* **2007**, *442*, 445.

(302) Noyori, R.; Kitamura, M.; Ohkuma, T. *Proc. Natl. Acad. Sci. U.S.A.* **2004**, *101*, 5356.

(303) Perrin, L.; Maron, L.; Eisenstein, O.; Lappert, M. F. *New J. Chem.* **2003**, *27*, 121.

(304) Hitchcock, P. B.; Lappert, M. F.; Smith, R. G.; Bartlett, R. A.; Power, P. P. *J. Chem. Soc., Chem. Commun.* **1988**, 1007.

(305) Perrin, L.; Maron, L.; Eisenstein, O. *Faraday Discuss.* **2003**, *124*, 25.

(306) Goldfuss, B.; Steigelmann, M.; Rominger, F.; Urtel, H. *Chem.—Eur. J.* **2001**, *7*, 4456.

(307) Eisenstein, O.; Hitchcock, P. B.; Khvostov, A. V.; Lappert, M. F.; Maron, L.; Perrin, L.; Protchenko, A. V. *J. Am. Chem. Soc.* **2003**, *125*, 10790.

(308) Fleurat-Lessard, P.; Volatron, F. *Inorg. Chem.* **2000**, *39*, 1849.

(309) Girasolo, M. A.; Di Salvo, C.; Schillaci, D.; Barone, G.; Silvestri, A.; Ruisi, G. *J. Organomet. Chem.* **2005**, *690*, 4773.

(310) Kwon, O.; McKee, M. L. *J. Phys. Chem. A* **2001**, *105*, 10133.

(311) Goldfuss, B.; Loschmann, T.; Rominger, F. *Chem.—Eur. J.* **2001**, *7*, 2028.

(312) (a) Matczak, P. *Comput. Theor. Chem.* **2013**, *1013*, 7. (b) Matczak, P. *Cent. Eur. J. Chem.* **2013**, *11*, 1257.

(313) Suresh, C. H. *Inorg. Chem.* **2006**, *45*, 4982.

(314) (a) Suresh, C. H.; Koga, N. *Inorg. Chem.* **2002**, *41*, 1573. (b) Kuhl, O. *Coord. Chem. Rev.* **2005**, *249*, 693.

(315) Mathew, J.; Thomas, T.; Suresh, C. H. *Inorg. Chem.* **2007**, *46*, 10800.

(316) Goldfuss, B.; Eisentrager, F. *Aust. J. Chem.* **2000**, *53*, 209.

(317) Ashkenazi, N.; Vigalok, A.; Parthiban, S.; Ben-David, Y.; Shimon, L. J. W.; Martin, J. M. L.; Milstein, D. *J. Am. Chem. Soc.* **2000**, *122*, 8797.

(318) Al-Ibadi, M. A. M.; Duckett, S. B.; McGrady, J. E. *Dalton Trans.* **2012**, *41*, 4618.

(319) Blazina, D.; Duckett, S. B.; Dyson, P. J.; Johnson, B. F. G.; Lohman, J. A. B.; Sleigh, C. J. *J. Am. Chem. Soc.* **2001**, *123*, 9760.

(320) Qi, X.-J.; Liu, L.; Fu, Y.; Guo, Q-X. *Organometallics* **2006**, *25*, 5879.

(321) Kovacs, G.; Papai, I. *Organometallics* **2006**, *25*, 820.

(322) Ivanov, S. A.; Arachchige, I.; Aikens, C. M. *J. Phys. Chem. A* **2011**, *115*, 8017.

(323) Cavallo, L.; Woo, T. K.; Ziegler, T. *Can. J. Chem.* **1998**, *76*, 1457.

(324) Durfey, B. L.; Gilbert, T. M. *Inorg. Chem.* **2011**, *50*, 7871.

(325) Wang, K.; Luo, G.; Hong, J.; Zhou, X.; Weng, L.; Luo, Y.; Zhang, L. *Angew. Chem., Int. Ed.* **2014**, *53*, 1053.

(326) Perrin, L.; Maron, L.; Eisenstein, O. *New J. Chem.* **2004**, *28*, 1255.

(327) Maron, L.; Werkema, E. L.; Perrin, L.; Eisenstein, O.; Andersen, R. A. *J. Am. Chem. Soc.* **2004**, *127*, 279.

(328) Stephan, D. W. In *Topics in Current Chem.: Frustrated Lewis Pairs I*; Stephan, D. W., Erker, G., Eds.; Springer Press: New York, 2013.

(329) Menard, G.; Gilbert, T. M.; Hatnean, J. A.; Kraft, A.; Krossing, I.; Stephan, D. W. *Organometallics* **2013**, *32*, 4416.

(330) Gilbert, T. M. *Dalton Trans.* **2012**, *41*, 9046.

(331) Chase, P. A.; Gille, A. L.; Gilbert, T. M.; Stephan, D. W. *Dalton Trans.* **2009**, 7179.

(332) Geier, S. J.; Gille, A. L.; Gilbert, T. M.; Stephan, D. W. *Inorg. Chem.* **2009**, *48*, 10466.

(333) Geier, S. J.; Gilbert, T. M.; Stephan, D. W. *Inorg. Chem.* **2011**, *50*, 336.

(334) Dutmer, B. C.; Gilbert, T. M. *Organometallics* **2011**, *30*, 778.

(335) Curtiss, L. A.; Redfern, P. C.; Raghavachari, K.; Rassolov, V.; Pople, J. A. *J. Chem. Phys.* **1999**, *110*, 4703.

(336) (a) Li, W.; Qin, S.; Su, Z.; Yang, H.; Hu, C. *Organometallics* **2011**, *30*, 2095. (b) Li, W.; Qin, S.; Su, Z.; Hu, C.; Feng, X. *Comput. Theor. Chem.* **2012**, *989*, 44.

(337) Lobachevsky, S.; Schiesser, C. H.; Lin, C. Y.; Coote, M. L. *J. Phys. Chem. A* **2008**, *112*, 13622.

(338) Henry, D. J.; Sullivan, M. B.; Radom, L. *J. Chem. Phys.* **2003**, *118*, 4849.

(339) (a) Koga, N.; Morokuma, K. *Chem. Rev.* **1991**, *91*, 823. (b) Torrent, M.; Sola, M.; Frenking, G. *Chem. Rev.* **2000**, *100*, 439. (c) Cramer, C. J.; Truhlar, D. G. *Phys. Chem. Chem. Phys.* **2009**, *11*, 10757. (d) Sameera, W. M. C.; Maseras, F. *WIREs Comput. Mol. Sci.* **2012**, *2*, 375.

(340) Koga, N.; Daniel, C.; Han, J.; Fu, X. Y.; Morokuma, K. *J. Am. Chem. Soc.* **1987**, *109*, 3455.

(341) Ananikov, V. P.; Szilagyi, R.; Morokuma, K.; Musaev, D. G. *Organometallics* **2005**, *24*, 1938.

(342) Li, Z.; Jiang, Y. Y.; Yeagley, A. A.; Bour, J. P.; Liu, L.; Chruma, J. J.; Fu, Y. *Chem.—Eur. J.* **2012**, *18*, 14527.

(343) (a) Braga, A. A. C.; Morgon, N. H.; Ujaque, G.; Maseras, F. *J. Am. Chem. Soc.* **2005**, *127*, 9298. (b) Braga, A. A. C.; Ujaque, G.; Maseras, F. *Organometallics* **2006**, *25*, 3647.

(344) Besora, M.; Braga, A. A. C.; Ujaque, G.; Maseras, F.; Lledó, A. *Theor. Chem. Acc.* **2011**, *128*, 639.

(345) (a) Ishikawa, A.; Nakao, Y.; Sato, H.; Sakaki, S. *Dalton Trans.* **2010**, *39*, 3279. (b) Mollar, C.; Besora, M.; Maseras, F.; Asensio, G.; Medio-Simon, M. *Chem.—Eur. J.* **2010**, *16*, 13390. (c) Ananikov, V. P.; Musaev, D. G.; Morokuma, K. *Eur. J. Inorg. Chem.* **2007**, 5390. (d) Fujihara, T.; Yoshida, S.; Ohta, H.; Tsuji, Y. *Angew. Chem., Int. Ed.* **2008**, *47*, 8310.

(346) Li, Z.; Fu, Y.; Zhang, S.-L.; Guo, Q.-X.; Liu, L. *Chem.—Asian J.* **2010**, *5*, 1475.

(347) (a) Altman, R. A.; Hyde, A. M.; Huang, X.; Buchwald, S. L. *J. Am. Chem. Soc.* **2008**, *130*, 9613. (b) Kozuch, S.; Shaik, S. *J. Mol. Catal. A: Chem.* **2010**, *324*, 120. (c) Liu, Q.; Lan, Y.; Liu, J.; Li, G.; Wu, Y. D.; Lei, A. W. *J. Am. Chem. Soc.* **2009**, *131*, 10201.

(348) (a) Dobereiner, G. E.; Nova, A.; Schley, N. D.; Hazari, N.; Miller, S. J.; Eisenstein, O.; Crabtree, R. H. *J. Am. Chem. Soc.* **2011**, *133*, 7547. (b) Donoghue, P. J.; Helquist, P.; Wiest, O. *J. Org. Chem.* **2007**, *72*, 839. (c) Feldgus, S.; Landis, C. R. *Organometallics* **2001**, *20*, 2374.

(349) (a) Adlhart, C.; Chen, P. *Angew. Chem., Int. Ed.* **2002**, *41*, 4484. (b) Goumans, T. P. M.; Ehlers, A. W.; Lammertsma, K. *Organometallics* **2005**, *24*, 3200.

(350) Aguado-Ullate, S.; Saureu, S.; Guasch, L.; Carbó, J. J. *Chem.—Eur. J.* **2012**, *18*, 995.

(351) (a) Daura-Oller, E.; Segarra, A. M.; Poblet, J. M.; Claver, C.; Fernández, E.; Bo, C. *J. Org. Chem.* **2004**, *69*, 2669. (b) Carbió, J. J.; Maseras, F.; Bo, C.; van Leeuwen, P. W. N. M. *J. Am. Chem. Soc.* **2001**, *123*, 7630. (c) Zuidema, E.; Escorihuela, L.; Eichelsheim, T.; Carbó, J. J.; Bo, C.; Kamer, P. C. J.; Van Leeuwen, P. W. N. M. *Chem.—Eur. J.* **2008**, *14*, 1843. (d) Cid, J.; Carbó, J. J.; Fernández, E. *Chem.—Eur. J.* **2012**, *18*, 12794.

(352) Sundermann, A.; Uzan, O.; Martin, J. M. L. *Organometallics* **2001**, *20*, 1783.

(353) Muñoz-Molina, J. M.; Sameera, W. M. C.; Álvarez, E.; Maseras, F.; Belderrain, T. R.; Pérez, P. J. *Inorg. Chem.* **2011**, *50*, 2458.

(354) Dang, L.; Lin, Z.; Marder, T. B. *Organometallics* **2008**, *27*, 4443.

(355) Takagi, N.; Sakaki, S. *J. Am. Chem. Soc.* **2013**, *135*, 8955.

(356) Hicks, J. D.; Hyde, A. M.; Cuezva, A. M.; Buchwald, S. L. *J. Am. Chem. Soc.* **2009**, *131*, 16720.

(357) (a) Le Paih, J.; Monnier, F.; Dérien, S.; Dixneuf, P. H.; Clot, E.; Eisenstein, O. *J. Am. Chem. Soc.* **2003**, *125*, 11964. (b) Goldfuss, B.; Steigelmann, M.; Khan, S. I.; Houk, K. N. *J. Org. Chem.* **2000**, *65*, 77. (c) Goldfuss, B.; Steigelmann, M.; Rominger, F. *Eur. J. Org. Chem.* **2000**, 1785. (d) Dachs, A.; Osuna, S.; Roglans, A.; Solà, M. *Organometallics* **2010**, *29*, 562. (e) Rao, W.; Koh, M. J.; Li, D.; Hirao, H.; Chan, P. W. H. *J. Am. Chem. Soc.* **2013**, *135*, 7926. (f) Yamamoto, Y. *Adv. Synth. Catal.* **2010**, *352*, 478. (g) Normand, A.

T.; Hawkest, K. J.; Clernentt, N. D.; Cavell, K. J.; Yates, B. F. *Organometallics* **2007**, *26*, 5352. (h) Martín-Rodríguez, M.; Nájera, C.; Sansano, J. M.; de Cózar, A.; Cossío, F. P. *Chem.—Eur. J.* **2011**, *17*, 14224.

(358) Mori, S.; Vreven, T.; Morokuma, K. *Chem.—Asian J.* **2006**, *1*, 391.

(359) (a) Ujaque, G.; Maseras, F.; Lledós, A. *J. Am. Chem. Soc.* **1999**, *121*, 1317. (b) Ujaque, G.; Maseras, F.; Lledós, A. *J. Org. Chem.* **1997**, *62*, 7892.

(360) Balcells, D.; Maseras, F.; Ujaque, G. *J. Am. Chem. Soc.* **2005**, *127*, 3624.

(361) Feldgus, S.; Landis, C. R. *J. Am. Chem. Soc.* **2000**, *122*, 12714.

(362) García, J. I.; Jiménez-Osés, G.; Martínez-Merino, V.; Mayoral, J. A.; Pires, E.; Villalba, I. *Chem.—Eur. J.* **2007**, *13*, 4064.

(363) Donoghue, P. J.; Helquist, P.; Norrby, P. O.; Wiest, O. *J. Chem. Theory Comput.* **2008**, *4*, 1313.

(364) Fjermestad, T.; Pericàs, M. A.; Maseras, F. *J. Mol. Catal. A: Chem.* **2010**, *324*, 127.

(365) (a) García, J. I.; Jiménez-Osés, G.; Mayoral, J. A. *Chem.—Eur. J.* **2011**, *17*, 529. (b) Cornejo, A.; Fraile, J. M.; García, J. I.; Gil, M. J.; Martínez-Merino, V.; Mayoral, J. A.; Salvatella, L. *Angew. Chem., Int. Ed.* **2005**, *44*, 458. (c) Fraile, J. M.; García, J. I.; Jiménez-Osés, G.; Mayoral, J. A.; Roldan, M. *Organometallics* **2008**, *27*, 2246.

(366) (a) Deng, W.; Vreven, T.; Frisch, M. J.; Wiberg, K. B. *J. Mol. Struct. (THEOCHEM)* **2006**, *775*, 93. (b) García-Cuadrado, D.; de Mendoza, P.; Braga, A. A. C.; Maseras, F.; Echavarren, A. M. *J. Am. Chem. Soc.* **2007**, *129*, 6880.

(367) Ben-Ari, E.; Cohen, R.; Gandelman, M.; Shimon, L. J. W.; Martin, J. M. L.; Milstein, D. *Organometallics* **2006**, *25*, 3190.

(368) Schoenebeck, F.; Houk, K. N. *J. Am. Chem. Soc.* **2010**, *132*, 2496.

(369) Decker, S. A.; Cundari, T. R. *J. Organomet. Chem.* **2001**, *635*, 132.

(370) Rossin, A.; Kovacs, G.; Ujaque, G.; Lledós, A.; Joo, F. *Organometallics* **2006**, *25*, 5010.

(371) Yang, Z.; Yu, H.; Fu, Y. *Chem.—Eur. J.* **2013**, *19*, 12093.

(372) Doux, M.; Ricard, L.; Le Floch, P.; Jean, Y. *Organometallics* **2006**, *25*, 1101.

(373) Rudolph, J.; Bolm, C.; Norrby, P. O. *J. Am. Chem. Soc.* **2005**, *127*, 1548.

(374) (a) Su, Z.; Li, W.; Wang, J.; Hu, C.; Feng, X. *Chem.—Eur. J.* **2013**, *19*, 1637. (b) Su, Z.; Qin, S.; Hu, C.; Feng, X. *Chem.—Eur. J.* **2010**, *16*, 4359.

(375) García, J. I.; Jiménez-Osés, G.; López-Sánchez, B.; Mayoral, J. A.; Vélez, A. *Dalton Trans.* **2010**, *39*, 2098.

(376) Gourlaouen, C.; Ujaque, G.; Lledós, A.; Medio-Simon, M.; Asensio, G.; Maseras, F. *J. Org. Chem.* **2009**, *74*, 4049.

(377) Cowley, R. E.; Eckert, N. A.; Vaddadi, S.; Figg, T. M.; Cundari, T. R.; Holland, P. L. *J. Am. Chem. Soc.* **2011**, *133*, 9796.

(378) Sundermann, A.; Uzan, O.; Milstein, D.; Martin, J. M. L. *J. Am. Chem. Soc.* **2000**, *122*, 7095.

(379) Rivilla, I.; Sameera, W. M. C.; Álvarez, E.; Díaz-Requejo, M. M.; Maseras, F.; Pérez, P. J. *Dalton Trans.* **2013**, *42*, 4132.

(380) (a) McGuinness, D. S.; Cavell, K. J.; Yates, B. F.; Skelton, B. W.; White, A. H. *J. Am. Chem. Soc.* **2001**, *123*, 8317. (b) Christian, G. J.; Llobet, A.; Maseras, F. *Inorg. Chem.* **2010**, *49*, 5977. (c) McGuinness, D. S.; Saendig, N.; Yates, B. F.; Cavell, K. J. *J. Am. Chem. Soc.* **2001**, *123*, 4029. (d) Hruszkewycz, D. P.; Wu, J.; Green, J. C.; Hazari, N.; Schmeier, T. J. *Organometallics* **2012**, *31*, 470. (e) Alcaraz, G.; Helmstedt, U.; Clot, E.; Vendier, L.; Sabo-Etienne, S. *J. Am. Chem. Soc.* **2008**, *130*, 12878. (f) Yandulov, D. V.; Tran, N. T. *J. Am. Chem. Soc.* **2007**, *129*, 1342. (g) Gans-Eichler, T.; Gudat, D.; Nieger, M. *Angew. Chem., Int. Ed.* **2002**, *41*, 1888. (h) Ariafard, A.; Lin, Z. *Organometallics* **2006**, *25*, 4030. (i) Luo, Y.; Hou, Z. *Organometallics* **2007**, *26*, 2941. (j) Ghosh, R.; Zhang, X.; Achord, P.; Emge, T. J.; Krogh-Jespersen, K.; Goldman, A. S. *J. Am. Chem. Soc.* **2007**, *129*, 853. (k) Cowley, R. E.; DeYonker, N. J.; Eckert, N. A.; Cundari, T. R.; DeBeer, S.; Bill, E.; Ottenwaelder, X.; Flaschenriem, C.; Holland, P. L. *Inorg. Chem.* **2010**, *49*, 6172. (l) Sola, E.; García-Camprubí, A.; Andrés, J. L.; Martín, M.;

Plou, P. *J. Am. Chem. Soc.* **2010**, *132*, 9111. (m) Ison, E. A.; Ortiz, C. O.; Abboud, K.; Boncella, J. M. *Organometallics* **2005**, *24*, 6310. (n) Morao, I.; Tai, Z.; Hillier, I. H.; Burton, N. A. *J. Mol. Struct. (THEOCHEM)* **2003**, *632*, 277. (o) Ward, B. D.; Orde, G.; Clot, E.; Cowley, A. R.; Gade, L. H.; Mountford, P. *Organometallics* **2004**, *23*, 4444. (p) Urtel, H.; Bikzhanova, G. A.; Grotjahn, D. B.; Hofmann, P. *Organometallics* **2001**, *20*, 3938. (q) Appelhans, L. N.; Zuccaccia, D.; Kovacevic, A.; Chianese, A. R.; Miecznikowski, J. R.; Macchioni, A.; Clot, E.; Eisenstein, O.; Crabtree, R. H. *J. Am. Chem. Soc.* **2005**, *127*, 16299. (r) Maron, L.; Werkema, E. L.; Perrin, L.; Eisenstein, O.; Andersen, R. A. *J. Am. Chem. Soc.* **2005**, *127*, 279. (s) Moyer, B. A.; Thompson, M. S.; Meyer, T. J. *J. Am. Chem. Soc.* **1980**, *102*, 2310. (t) Eckert, N. A.; Vaddadi, S.; Stoian, S.; Lachicotte, R. J.; Cundari, T. R.; Holland, P. L. *Angew. Chem., Int. Ed.* **2006**, *45*, 6868. (u) Macgregor, S. A.; Wondimagegn, T. *Organometallics* **2007**, *26*, 1143. (v) Slattery, J. M.; Fish, C.; Green, M.; Hooper, T. N.; Jeffery, J. C.; Kilby, R. J.; Lynam, J. M.; McGrady, J. E.; Pantazis, D. A.; Russell, C. A.; Willans, C. E. *Chem.—Eur. J.* **2007**, *13*, 6967.

(381) Vanka, K.; Xu, Z.; Ziegler, T. *Organometallics* **2004**, *23*, 2900.

(382) Vyboishchikov, S. F.; Musaev, D. G.; Froese, R. D. J.; Morokuma, K. *Organometallics* **2001**, *20*, 309.

(383) (a) Xu, Z.; Vanka, K.; Firman, T.; Michalak, A.; Zurek, E.; Zhu, C.; Ziegler, T. *Organometallics* **2002**, *21*, 2444. (b) Vanka, K.; Xu, Z.; Ziegler, T. *Can. J. Chem.* **2003**, *81*, 1413.

(384) Wondimagegn, T.; Vanka, K.; Xu, Z.; Ziegler, T. *Organometallics* **2004**, *23*, 2651.

(385) (a) Xu, Z.; Vanka, K.; Ziegler, T. *Organometallics* **2004**, *23*, 104. (b) Vanka, K.; Xu, Z.; Ziegler, T. *Organometallics* **2005**, *24*, 419. (c) Wondimagegn, T.; Xu, Z.; Vanka, K.; Ziegler, T. *Organometallics* **2005**, *24*, 2076. (d) Ziegler, T.; Vanka, K.; Xu, Z. *C. R. Chim.* **2005**, *8*, 1552. (e) Martínez, S.; Ramos, J.; Cruz, V. L.; Martínez-Salazar, J. *Polymer* **2006**, *47*, 883.

(386) Yang, S.-Y.; Ziegler, T. *Organometallics* **2006**, *25*, 887.

(387) Rowley, C. N.; Woo, T. K. *Organometallics* **2011**, *30*, 2071.

(388) Talarico, G.; Busico, V.; Cavallo, L. *Organometallics* **2004**, *23*, 5989.

(389) Pilmé, J.; Busico, V.; Cossi, M.; Talarico, G. *J. Organomet. Chem.* **2007**, *692*, 4227.

(390) Champouret, Y.; MacLeod, K. C.; Baisch, U.; Patrick, B. O.; Smith, K. M.; Poli, R. *Organometallics* **2010**, *29*, 167.

(391) Yoshida, T.; Koga, N.; Morokuma, K. *Organometallics* **1996**, *15*, 766.

(392) Mercandelli, P.; Sironi, A.; Resconi, L.; Camurati, I. *J. Organomet. Chem.* **2007**, *692*, 4784.

(393) Longo, P.; Grisi, F.; Guerra, G.; Cavallo, L. *Macromolecules* **2000**, *33*, 4647.

(394) Longo, P.; Pragliola, S.; Milano, G.; Guerra, G. *J. Am. Chem. Soc.* **2003**, *125*, 4799.

(395) Wang, D.; Tomasi, S.; Razavi, A.; Ziegler, T. *Organometallics* **2008**, *27*, 2861.

(396) Luo, Y.; Luo, Y.; Qu, J.; Hou, Z. *Organometallics* **2011**, *30*, 2908.

(397) Zhong, L.; Lee, M.-Y.; Liu, Z.; Wanglee, Y.-J.; Liu, B.; Scott, S. L. *J. Catal.* **2012**, *293*, 1.

(398) (a) Froese, R. D. J.; Musaev, D. G.; Morokuma, K. *J. Am. Chem. Soc.* **1998**, *120*, 1581. (b) Musaev, D. G.; Froese, R. D. J.; Morokuma, K. *Organometallics* **1998**, *17*, 1850.

(399) Musaev, D. G.; Morokuma, K. *Top. Catal.* **1999**, *7*, 107.

(400) Woo, T. K.; Blochl, P. E.; Ziegler, T. *J. Phys. Chem. A* **2000**, *104*, 121.

(401) Chan, M. S. W.; Deng, L.; Ziegler, T. *Organometallics* **2000**, *19*, 2741.

(402) Khoroshun, D. V.; Musaev, D. G.; Vreven, T.; Morokuma, K. *Organometallics* **2001**, *20*, 2007.

(403) Collins, S.; Ziegler, T. *Organometallics* **2007**, *26*, 6612.

(404) Urtel, H.; Meier, C.; Rominger, F.; Hofmann, P. *Organometallics* **2010**, *29*, 5496.

(405) Ferreira, D. A. C.; Morais, S. F. D.; Meneghetti, S. M. P.; Meneghetti, M. R. *J. Mol. Catal. A: Chem.* **2012**, *363*, 1.

(406) Milano, G.; Guerra, G.; Pellecchia, C.; Cavallo, L. *Organometallics* **2000**, *19*, 1343.

(407) Ke, Z. F.; Abe, S.; Ueno, T.; Morokuma, K. *J. Am. Chem. Soc.* **2011**, *133*, 7926.

(408) Ramos, J.; Cruz, V.; Muñoz-Escalona, A.; Martínez-Salazar, J. *Polymer* **2001**, *42*, 8019.

(409) Nozaki, K.; Sato, N.; Tonomura, Y.; Yasutomi, M.; Takaya, H.; Hiyama, T.; Matsubara, T.; Koga, N. *J. Am. Chem. Soc.* **1997**, *119*, 12779.

(410) Nozaki, K.; Komaki, H.; Kawashima, Y.; Hiyama, T.; Matsubara, T. *J. Am. Chem. Soc.* **2001**, *123*, 534.

(411) Ramos, J.; Cruz, V.; Muñoz-Escalona, A.; Martínez-Salazar, J. *Polymer* **2002**, *43*, 3635.

(412) Szabo, M. J.; Jordan, R. F.; Michalak, A.; Piers, W. E.; Weiss, T.; Yang, S.-Y.; Ziegler, T. *Organometallics* **2004**, *23*, 5565.

(413) Wu, G.-P.; Ren, W.-M.; Luo, Y.; Li, B.; Zhang, W.-Z.; Lu, X.-B. *J. Am. Chem. Soc.* **2012**, *134*, 5682.

(414) Papayannis, D. K.; Kosmas, A. M. *J. Mol. Struct. (THEOCHEM)* **2010**, *957*, 47.

(415) Solans-Monfort, X.; Sodupe, M.; Branchadell, V.; Sauer, J.; Orlando, R.; Ugliengo, P. *J. Phys. Chem. B* **2005**, *109*, 3539.

(416) Fermann, J. T.; Moniz, T.; Kiowski, O.; McIntire, T. J.; Auerbach, S. M.; Vreven, T.; Frisch, M. J. *J. Chem. Theory Comput.* **2005**, *1*, 1232.

(417) (a) Li, Y.; Guo, W.; Fan, W.; Yuan, S.; Li, J.; Wang, J.; Jiao, H.; Tatsumi, T. *J. Mol. Catal. A: Chem.* **2011**, *338*, 24. (b) Li, Y.; Guo, W.; Yuan, S.; Fan, W.; Wang, J.; Jiao, H. *J. Mol. Struct. (THEOCHEM)* **2009**, *916*, 53.

(418) Rappé, A. K.; Casewit, C. J.; Colwell, K. S.; Goddard, W. A., III; Skiff, W. M. *J. Am. Chem. Soc.* **1992**, *114*, 10024.

(419) (a) Boekfa, B.; Pantu, P.; Limtrakul, J. *J. Mol. Struct.* **2008**, *889*, 81. (b) Pantu, P.; Boekfa, B.; Limtrakul, J. *J. Mol. Catal. A: Chem.* **2007**, *277*, 171. (c) Stefanovich, E. V.; Truong, T. N. *J. Phys. Chem. B* **1998**, *102*, 3018.

(420) Li, Y.; Guo, W.; Fan, W.; Qin, Z.; Wang, J. *Chin. J. Catal.* **2010**, *31*, 1419.

(421) Maihom, T.; Boekfa, B.; Sirijaraensre, J.; Nanok, T.; Probst, M.; Limtrakul, J. *J. Phys. Chem. C* **2009**, *113*, 6654.

(422) Chu, Z.-K.; Fu, G.; Guo, W.; Xu, X. *J. Phys. Chem. C* **2011**, *115*, 14754.

(423) (a) Boekfa, B.; Choomwattana, S.; Khongpracha, P.; Limtrakul, J. *Langmuir* **2009**, *25*, 12990. (b) Maihom, T.; Namuangruk, S.; Nanok, T.; Limtrakul, J. *J. Phys. Chem. C* **2008**, *112*, 12914. (c) Sirijaraensre, J.; Limtrakul, J. *Struct. Chem.* **2013**, *24*, 1307. (d) Vollmer, J. M.; Stefanovich, E. V.; Truong, T. N. *J. Phys. Chem. B* **1999**, *103*, 9415.

(424) Ganesh, V.; Dongare, R. K.; Balanarayan, P.; Gadre, S. R. *J. Chem. Phys.* **2006**, *125*, 104109.

(425) Shor, A. M.; Shor, E. A. I.; Nasluzov, V. A.; Vayssilov, G. N.; Rösch, N. *J. Chem. Theory Comput.* **2007**, *3*, 2290.

(426) (a) Uzunova, E. L.; Mikosch, H. *ACS Catal.* **2013**, *3*, 2759. (b) Uzunova, E. L.; Mikosch, H. *Microporous Mesoporous Mater.* **2013**, *177*, 113. (c) Uzunova, E. L.; Mikosch, H.; St Nikolov, G. *Int. J. Quantum Chem.* **2013**, *113*, 723. (d) Van der Mynsbrugge, J.; Hemelsoet, K.; Vandichel, M.; Waroquier, M.; Van Speybroeck, V. *J. Phys. Chem. C* **2012**, *116*, 5499.

(427) (a) Erbetta, D.; Ricci, D.; Pacchioni, G. *J. Chem. Phys.* **2000**, *113*, 10744. (b) Ricci, D.; Pacchioni, G.; Szymanski, M. A.; Shluger, A. L.; Stoneham, A. M. *Phys. Rev. B* **2001**, *64*, 2241041.

(428) Atoguchi, T.; Yao, S. *J. Mol. Catal. A: Chem.* **2003**, *191*, 281.

(429) Li, Y.; Liu, H.; Zhu, J.; He, P.; Wang, P.; Tian, H. *Microporous Mesoporous Mater.* **2011**, *142*, 621.

(430) (a) Knozinger, H.; Huber, S. *J. Chem. Soc., Faraday Trans.* **1998**, *94*, 2047. (b) Hadjiivanov, K. I.; Vayssilov, G. N. In *Advances in Catalysis*; Gates, B. C., Knozinger, H., Eds.; Elsevier: New York, 2002; Vol. 47. (c) Lavalley, J. C. *Catal. Today* **1996**, *27*, 377. (d) Lercher, J. A.; Gründling, C.; Eder-Mirth, G. *Catal. Today* **1996**, *27*, 353.

(431) Yang, G.; Zhou, L.; Han, X. *J. Mol. Catal. A: Chem.* **2012**, *363*, 371.

(432) Kalita, B.; Deka, R. C. *Catal. Lett.* **2010**, *140*, 205.

(433) (a) Griffe, B.; Brito, J. L.; Sierraalta, A. *J. Mol. Catal. A: Chem.* **2010**, *315*, 28. (b) Griffe, B.; Sierraalta, A.; Brito, J. L. *Int. J. Quantum Chem.* **2010**, *110*, 2573.

(434) Sierraalta, A.; Añez, R.; Ehrmann, E. *J. Mol. Catal. A: Chem.* **2007**, *271*, 185.

(435) Sierraalta, A.; Diaz, L.; Añez, R. *J. Mol. Catal. A: Chem.* **2012**, *363*, 380.

(436) Sierraalta, A.; Añez, R.; Diaz, L.; Gomperts, R. *J. Phys. Chem. A* **2010**, *114*, 6870.

(437) Sung, C.-Y.; Broadbelt, L. J.; Snurr, R. Q. *J. Phys. Chem. C* **2009**, *113*, 15643.

(438) Fang, H.; Zheng, A.; Xu, J.; Li, S.; Chu, Y.; Chen, L.; Deng, F. *J. Phys. Chem. C* **2011**, *115*, 7429.

(439) Tang, H.-R.; Fan, K.-N. *Chem. Phys. Lett.* **2000**, *330*, 509.

(440) Roggero, I.; Civalleri, B.; Ugliengo, P. *Chem. Phys. Lett.* **2001**, *341*, 625.

(441) Tunega, D.; Haberhauer, G.; Gerzabek, M. H.; Lischka, H. *Langmuir* **2002**, *18*, 139.

(442) Martins, J. B. L.; Longo, E.; Salmon, O. D. R.; Espinoza, V. A. A.; Taft, C. A. *Chem. Phys. Lett.* **2004**, *400*, 481.

(443) Mendoza-Huizar, L. H.; Palomar-Pardave, M.; Robles, J. *J. Mol. Struct. (THEOCHEM)* **2004**, *679*, 187.

(444) Ugliengo, P.; Damin, A. *Chem. Phys. Lett.* **2002**, *366*, 683.

(445) Anez, R.; Sierraalta, A.; Martorell, G. *J. Mol. Struct. (THEOCHEM)* **2009**, *900*, 59.

(446) Chu, Y.; Han, B.; Zheng, A.; Deng, F. *J. Phys. Chem. C* **2012**, *116*, 12687.

(447) (a) Li, L.-L.; Janik, J. M.; Nie, X.-W.; Song, C.-S.; Guo, X.-W. *Acta Phys. Chem. Sin.* **2013**, *29*, 1467. (b) Nie, X.; Janik, M. J.; Guo, X.; Liu, X.; Song, C. *Catal. Today* **2011**, *165*, 120. (c) Nie, X.; Janik, M. J.; Guo, X.; Song, C. *J. Phys. Chem. C* **2012**, *116*, 4071.

(448) (a) Li, Y.-F.; Zhu, J.-Q.; Liu, H.; He, P.; Wang, P.; Tian, H.-P. *Bull. Korean Chem. Soc.* **2011**, *32*, 1851. (b) Nie, X.; Janik, M. J.; Guo, X.; Song, C. *Phys. Chem. Chem. Phys.* **2012**, *14*, 16644. (c) Wattanakit, C.; Nokbin, S.; Boekfa, B.; Pantu, P.; Limtrakul, J. *J. Phys. Chem. C* **2012**, *116*, 5654.

(449) Guo, Y.-H.; Pu, M.; Chen, B.-H.; Cao, F. *Appl. Catal., A* **2013**, *455*, 65.

(450) (a) Chong, S. X.; Wahab, H. A.; Abdallah, H. H. *Comput. Mater. Sci.* **2012**, *55*, 217. (b) Däumer, D.; Räuchle, K.; Reschetilowski, W. *ChemCatChem* **2012**, *4*, 802. (c) Sun, Y.; Han, S. *J. Mol. Model.* **2013**, *19*, 5407. (d) Vaitheeswaran, S.; Green, S. K.; Dauenhauer, P.; Auerbach, S. M. *ACS Catal.* **2013**, *3*, 2012. (e) Chu, Y.; Han, B.; Zheng, A.; Deng, F. *J. Phys. Chem. C* **2013**, *117*, 2194.

(451) Jansen, A.; Ruangpornvisuti, V. *J. Mol. Catal. A: Chem.* **2012**, *363*, 171.

(452) Erdogan, R.; Onal, I. *Int. J. Quantum Chem.* **2011**, *111*, 2149.

(453) Sierka, M.; Sauer, J. *J. Phys. Chem. B* **2001**, *105*, 1603.

(454) Kalita, B.; Deka, R. C. *J. Phys. Chem. C* **2009**, *113*, 16070.

(455) Meeprasert, J.; Jungsuttiwong, S.; Truong, T. N.; Namuangruk, S. *J. Mol. Graphics* **2013**, *43*, 31.

(456) Chu, C. Q.; Zhao, H. T.; Qi, Y. Y.; Xin, F. *J. Mol. Model.* **2013**, *19*, 2217.

(457) Fu, H.; Xie, S.; Fu, A.; Ye, T. *Comput. Theor. Chem.* **2012**, *982*, 51.

(458) Sangthong, W.; Probst, M.; Limtrakul, J. *J. Mol. Struct.* **2005**, *748*, 119.

(459) (a) Handzlik, J. *Int. J. Quantum Chem.* **2007**, *107*, 2111. (b) Handzlik, J. *J. Phys. Chem. C* **2007**, *111*, 9337.

(460) Martins, J. B. L.; Taft, C. A.; Longo, E.; de Castro, E. A. S.; da Cunha, W. F.; Politi, J. R. S.; Gargano, R. *Int. J. Quantum Chem.* **2012**, *112*, 3223.

(461) Halls, M. D.; Raghavachari, K. *J. Phys. Chem. A* **2004**, *108*, 2982.

(462) Liu, Y.; Su, K.; Wang, X.; Wang, Y.; Zeng, Q.; Cheng, L.; Zhang, L. *Chem. Phys. Lett.* **2010**, *501*, 87.

(463) Jiang, G. P.; Polanyi, J. C.; Rogers, D. *Surf. Sci.* **2003**, *544*, 147.

(464) (a) Hou, X.-J.; Li, H. *J. Phys. Chem. C* **2010**, *114*, 13501. (b) Pianwanit, A.; Kritayakornupong, C.; Vongachariya, A.; Selphusit, N.; Ploymeerusmee, T.; Remsungnen, T.; Nuntasri, D.; Fritzsche, S.; Hannongbua, S. *Chem. Phys.* **2008**, *349*, 77.

(465) Ariyageadsakul, P.; Kritayakornupong, C. *e-J. Surf. Sci. Nanotechnol.* **2012**, *10*, 203.

(466) Braga, C. F.; Longo, R. L. *J. Mol. Struct. (THEOCHEM)* **2005**, *716*, 33.

(467) Cortese, R.; Duca, D. *Phys. Chem. Chem. Phys.* **2011**, *13*, 15995.

(468) Choomwattana, S.; Maihom, T.; Khongpracha, P.; Probst, M.; Limtrakul, J. *J. Phys. Chem. C* **2008**, *112*, 10855.

(469) Yadnum, S.; Choomwattana, S.; Khongpracha, P.; Sirijaraensre, J.; Limtrakul, J. *ChemPhysChem* **2013**, *14*, 923.

(470) Yu, M.-F.; Lourie, O.; Dyer, M. J.; Moloni, K.; Kelly, T. F.; Ruoff, R. S. *Science* **2000**, *287*, 637.

(471) Cong, H.-P.; Ren, X.-C.; Wang, P.; Yu, S.-H. *Sci. Rep.* **2012**, *2*, 613.

(472) Novoselov, K. S.; Geim, A. K.; Morozov, S. V.; Jiang, D.; Zhang, Y.; Dubonos, S. V.; Grivorieva, L. V.; Firsov, A. A. *Science* **2004**, *306*, 666.

(473) Kataura, H.; Kumazawa, Y.; Maniwa, Y.; Umezu, I.; Suzuki, S.; Ohtsuka, Y.; Achiba, Y. *Synth. Met.* **1999**, *103*, 2555.

(474) (a) Dresselhaus, M. S.; Dresselhaus, G.; Eklund, P. C. *Science of Fullerenes and Carbon Nanotubes*; Academic Press Inc.: San Diego, CA, 1996. (b) Reed, C. A.; Bolskar, R. D. *Chem. Rev.* **2000**, *100*, 1075. (c) Bühl, M.; Hirsch, A. *Chem. Rev.* **2001**, *101*, 1153. (d) Lu, X.; Chen, Z. *Chem. Rev.* **2005**, *105*, 3643. (e) Diederich, F.; Gomez-Lopez, M. *Chem. Soc. Rev.* **1999**, *28*, 263. (f) Diederich, F.; Kessinger, R. *Acc. Chem. Res.* **1999**, *32*, 537. (g) Martín, N.; Sánchez, L.; Illescas, B.; Pérez, I. *Chem. Rev.* **1998**, *98*, 2527. (h) Hirsch, A. *The Chemistry of the Fullerenes*; Wiley-VCH Verlag GmbH & Co. KGaA: Weinheim, 2002.

(475) Froese, R. D. J.; Morokuma, K. *Chem. Phys. Lett.* **1999**, *305*, 419.

(476) (a) Arbogast, J. W.; Darmanyan, A. P.; Foote, C. S.; Diederich, F. N.; Whetten, R. L.; Rubin, Y.; Alvarez, M. M.; Anz, S. J. *J. Phys. Chem.* **1991**, *95*, 11. (b) Zeng, Y.; Biczok, L.; Linschitz, H. *J. Phys. Chem.* **1992**, *96*, 5237. (c) Sauve, G.; Kamat, P. V.; Thomas, K. G.; Thomas, K. J.; Das, S.; George, M. V. *J. Phys. Chem.* **1996**, *100*, 2117.

(477) (a) Izquierdo, M.; Osuna, S.; Filippone, S.; Martin-Domenech, A.; Solà, M.; Martin, N. *Eur. J. Org. Chem.* **2009**, 6231. (b) Osuna, S.; Morera, J.; Cases, M.; Morokuma, K.; Sola, M. *J. Phys. Chem. A* **2009**, *113*, 9721. (c) Osuna, S.; Swart, M.; Sola, M. *J. Phys. Chem. A* **2011**, *115*, 3491.

(478) Lu, X.; Zhang, L.; Xu, X.; Wang, N.; Zhang, Q. *J. Phys. Chem. B* **2002**, *106*, 2136.

(479) Castillo, A.; Lee, L.; Greer, A. *J. Phys. Org. Chem.* **2012**, *25*, 42.

(480) Liu, L. V.; Tian, W. Q.; Wang, Y. A. *J. Phys. Chem. B* **2006**, *110*, 13037.

(481) Dillon, A. C.; Jones, K. M.; Bekkedahl, T. A.; Kiang, C. H.; Bethune, D. S.; Heben, M. J. *Nature* **1997**, *386*, 377.

(482) Collins, P. G.; Bradley, K.; Ishigami, M.; Zettl, A. *Science* **2000**, *287*, 1801.

(483) (a) Bauschlicher, C. W. *Chem. Phys. Lett.* **2000**, *322*, 237. (b) Bauschlicher, C. W. *Nano Lett.* **2001**, *1*, 223. (c) Bauschlicher, C. W.; So, C. R. *Nano Lett.* **2002**, *2*, 337.

(484) Ng, T. Y.; Ren, Y. X.; Liew, K. M. *Int. J. Hydrogen Energy* **2010**, *35*, 4543.

(485) Yang, F. H.; Lachawiec, A. J.; Yang, R. T. *J. Phys. Chem. B* **2006**, *110*, 6236.

(486) Kar, T.; Akdim, B.; Duan, X.; Pachter, R. *Chem. Phys. Lett.* **2004**, *392*, 176.

(487) Walch, S. P. *Chem. Phys. Lett.* **2003**, *374*, 501.

(488) Lu, X.; Yuan, Q.; Zhang, Q. *Org. Lett.* **2003**, *5*, 3527.

(489) Irle, S.; Mews, A.; Morokuma, K. *J. Phys. Chem. A* **2002**, *106*, 11973.

(490) Chapleski, R.; Morris, J. R.; Troya, D. *Phys. Chem. Chem. Phys.* **2014**, *16*, 5977.

(491) Yim, W. L.; Liu, Z. F. *Chem. Phys. Lett.* **2004**, *398*, 297.

(492) (a) Ikeda, A.; Kameno, Y.; Nakao, Y.; Sato, H.; Sakaki, S. *J. Organomet. Chem.* **2007**, *692*, 299. (b) Irle, S.; Rubin, Y.; Morokuma, K. *J. Phys. Chem. A* **2002**, *106*, 680. (c) Rogachev, A. Y.; Sevryugina, Y.; Filatov, A. S.; Petrukhina, M. A. *Dalton Trans.* **2007**, 3871.

(493) Lu, X.; Tian, F.; Zhang, Q. R. *J. Phys. Chem. B* **2003**, *107*, 8388.

(494) Lu, X.; Tian, F.; Feng, Y.; Xu, X.; Wang, N.; Zhang, Q. *Nano Lett.* **2002**, *2*, 1325.

(495) Yuan, Y.; Chen, P.; Ren, X.; Wang, H. *ChemPhysChem* **2012**, *13*, 741.

(496) (a) Osuna, S.; Houk, K. N. *Chem.—Eur. J.* **2009**, *15*, 13219. (b) Lu, X.; Tian, F.; Xu, X.; Wang, N.; Zhang, Q. *J. Am. Chem. Soc.* **2003**, *125*, 10459. (c) Yang, T.; Zhao, X.; Nagase, S. *J. Comput. Chem.* **2013**, *34*, 2223.

(497) Filippone, S.; Barroso, M. I.; Martín-Domenech, A.; Osuna, S.; Solà, M.; Martín, N. *Chem.—Eur. J.* **2008**, *14*, 5198.

(498) Izquierdo, M.; Osuna, S.; Filippone, S.; Martin-Domenech, A.; Solà, M.; Martin, N. *J. Org. Chem.* **2009**, *74*, 1480.

(499) (a) Basiuk, V. A.; Basiuk, E. V.; Saniger-Blesa, J. M. *Nano Lett.* **2001**, *1*, 657. (b) Basiuk, V. A. *Nano Lett.* **2002**, *2*, 835. (c) Kar, T.; Akdim, B.; Duan, X.; Pachter, R. *Chem. Phys. Lett.* **2006**, *423*, 126. (d) Kar, T.; Scheiner, S.; Patnaik, S. S.; Bettinger, H. F.; Roy, A. K. *J. Phys. Chem. C* **2010**, *114*, 20955.

(500) (a) Basiuk, V. A. *J. Phys. Chem. B* **2003**, *107*, 8890. (b) Basiuk, V. A. *J. Comput. Theor. Nanosci.* **2004**, *1*, 378. (c) Basiuk, V. A. *J. Nanosci. Nanotechnol.* **2004**, *4*, 1095.

(501) Petsalakis, I. D.; Pagona, G.; Theodorakopoulos, G.; Tagmatarchis, N.; Yudasaka, M.; Iijima, S. *Chem. Phys. Lett.* **2006**, *429*, 194.

(502) Cao, Y.; Houk, K. N. *J. Mater. Chem.* **2011**, *21*, 1503.

(503) Wanno, B.; Du, A. J.; Ruangpornvisuti, V.; Smith, S. C. *Chem. Phys. Lett.* **2007**, *436*, 218.

(504) Chakrapani, N.; Zhang, Y. M.; Nayak, S. K.; Moore, J. A.; Carroll, D. L.; Choi, Y. Y.; Ajayan, P. M. *J. Phys. Chem. B* **2003**, *107*, 9308.

(505) Chen, R. J.; Zhang, Y.; Wang, D.; Dai, H. *J. Am. Chem. Soc.* **2001**, *123*, 3838.

(506) Zheng, M.; Jagota, A.; Semke, E. D.; Diner, B. A.; McLean, R. S.; Lustig, S. R.; Richardson, R. E.; Tassi, N. G. *Nat. Mater.* **2003**, *2*, 338.

(507) Dabbagh, H. A.; Zamani, M.; Mortaji, H. *J. Iran. Chem. Soc.* **2012**, *9*, 205.

(508) Lopez-Martinez, E. I.; Rodriguez-Valdez, L. M.; Flores-Holguin, N.; Marquez-Lucero, A.; Glossman-Mitnik, D. *J. Comput. Chem.* **2009**, *30*, 1027.

(509) Trzaskowski, B.; Adamowicz, L.; Beck, W.; Muralidharan, K.; Deymier, P. A. *Chem. Phys. Lett.* **2014**, *595–596*, 6.

(510) Tetasang, S.; Keawwangchai, S.; Wanno, B.; Ruangpornvisuti, V. *Struct. Chem.* **2012**, *23*, 7.

(511) (a) Lee, V. S.; Nimmanpipug, P.; Aruksakunwong, O.; Promsri, S.; Sompornpisut, P.; Hannongbua, S. *J. Mol. Graphics* **2007**, *26*, 558. (b) Promsri, S.; Chuichay, P.; Sanghiran, V.; Parasuk, V.; Hannongbua, S. *J. Mol. Struct. (THEOCHEM)* **2005**, *715*, 47.

(512) Shukla, M. K.; Leszczynski, J. *Chem. Phys. Lett.* **2009**, *469*, 207.

(513) Riley, K. E.; Hobza, P. *Acc. Chem. Res.* **2012**, *46*, 927.

(514) Xu, S.; Irle, S.; Musaev, A. G.; Lin, M. C. *J. Phys. Chem. A* **2005**, *109*, 9563.

(515) Kar, T.; Bettinger, H. F.; Scheiner, S.; Roy, A. K. *J. Phys. Chem. C* **2008**, *112*, 20070.

(516) (a) Xu, S. C.; Irle, S.; Musaev, D. G.; Lin, M. C. *J. Phys. Chem. C* **2007**, *111*, 1355. (b) Zhanpeisov, N. U.; Zhidomirov, G. M.; Fukumura, H. *J. Phys. Chem. C* **2009**, *113*, 6118. (c) Fomina, L.; Reyes, A.; Guadarrama, P.; Fomine, S. *Int. J. Quantum Chem.* **2004**, *97*, 679.

(517) Ellison, M. D.; Good, A. P.; Kinnaman, C. S.; Padgett, N. E. *J. Phys. Chem. B* **2005**, *109*, 10640.

(518) Wanbayor, R.; Ruangpornvisuti, V. *Chem. Phys. Lett.* **2007**, *441*, 127.

(519) Fomina, L.; Reyes, A.; Fomine, S. *Int. J. Quantum Chem.* **2002**, *89*, 477.

(520) (a) Xu, Y.-J.; Li, J.-Q. *Chem. Phys. Lett.* **2005**, *412*, 439. (b) Walch, S. P. *Chem. Phys. Lett.* **2003**, *373*, 422.

(521) (a) Ricca, A.; Bauschlicher, C. W.; Maiti, A. *Phys. Rev. B* **2003**, *68*, 035433. (b) Ricca, A.; Drocco, J. A. *Chem. Phys. Lett.* **2002**, *362*, 217.

(522) Wang, L.; Yi, C.; Zou, H.; Gan, H.; Xu, J.; Xu, W. *Mol. Phys.* **2011**, *109*, 1841.

(523) Xu, S. C.; Irle, S.; Musaev, D. G.; Lin, M. C. *J. Phys. Chem. B* **2006**, *110*, 21135.

(524) Liu, L. V.; Tian, W. Q.; Wang, Y. A. *J. Phys. Chem. B* **2006**, *110*, 1999.

(525) Rosi, M.; Bauschlicher, C. W., Jr. *Chem. Phys. Lett.* **2007**, *437*, 99.

(526) (a) Pan, X.; Bao, X. *Acc. Chem. Res.* **2011**, *44*, 553. (b) Pan, X.; Fan, Z.; Chen, W.; Ding, Y.; Luo, H.; Bao, X. *Nat. Mater.* **2007**, *6*, 507. (c) Halls, M. D.; Schlegel, H. B. *J. Phys. Chem. B* **2002**, *106*, 1921.

(527) Chaban, V. V.; Prezhdo, V. V.; Prezhdo, O. V. *ACS Nano* **2012**, *6*, 2766.

(528) Garcia, G.; Ciofini, I.; Fernandez-Gomez, M.; Adamo, C. *J. Phys. Chem. Lett.* **2013**, *4*, 1239.

(529) Kazachkin, D. V.; Nishimura, Y.; Witek, H. A.; Irle, S.; Borguet, E. *J. Am. Chem. Soc.* **2011**, *133*, 8191.

(530) Wang, L.; Yi, C.; Zou, H.; Gan, H.; Xu, J.; Xu, W. *J. Mol. Model.* **2011**, *17*, 2751.

(531) Wang, W.; Wang, D.; Zhang, Y.; Ji, B.; Tian, A. *J. Chem. Phys.* **2011**, *134*, 054317.

(532) Ellison, M. D.; Morris, S. T.; Sender, M. R.; Brigham, J.; Padgett, N. E. *J. Phys. Chem. C* **2007**, *111*, 18127.

(533) Tzeli, D.; Theodorakopoulos, G.; Petsalakis, I. D.; Ajami, D.; Rebek, J. *J. Am. Chem. Soc.* **2011**, *133*, 16977.

(534) Wang, L.; Wu, J.; Yi, C.; Zou, H.; Gan, H.; Li, S. *Comput. Theor. Chem.* **2012**, *982*, 66.

(535) Wang, L.; Yi, C.; Zou, H.; Xu, J.; Xu, W. *Acta Phys. Chem. Sin.* **2010**, *26*, 149.

(536) Wang, L.; Yi, C.; Zou, H.; Xu, J.; Xu, W. *Mater. Chem. Phys.* **2011**, *127*, 232.

(537) Wang, L.; Zou, H.; Yi, C.; Xu, J.; Xu, W. *J. Nanosci. Nanotechnol.* **2011**, *11*, 3298.

(538) (a) Wang, L.; Yi, C.; Zou, H.; Xu, J.; Xu, W. *Chem. Phys.* **2010**, *367*, 120. (b) Wang, L.; Xu, J.; Yi, C.; Zou, H.; Xu, W. *J. Mol. Struct. (THEOCHEM)* **2010**, *940*, 76.

(539) Trzaskowski, B.; Adamowicz, L. *Theor. Chem. Acc.* **2009**, *124*, 95.

(540) Basiuk, E. V.; Basiuk, V. A.; Banuelos, J. G.; Saniger-Blesa, J. M.; Pokrovskiy, V. A.; Gromovoy, T. Y.; Mischanchuk, A. V.; Mischanchuk, B. G. *J. Phys. Chem. B* **2002**, *106*, 1588.

(541) Ahmadi, A.; Beheshtian, J.; Kamfiroozi, M. *J. Mol. Model.* **2012**, *18*, 1729.

(542) Li, F.; Xia, Y.; Zhao, M.; Liu, X.; Huang, B.; Ji, Y.; Song, C. *Phys. Lett. A* **2006**, *357*, 369.

(543) Choi, H.; Park, Y. C.; Kim, Y.-H.; Lee, Y. S. *J. Am. Chem. Soc.* **2011**, *133*, 2084.

(544) Ahmadi, A.; Kamfiroozi, M.; Beheshtian, J.; Hadipour, N. L. *Struct. Chem.* **2011**, *22*, 1261.

(545) Cardelino, B. H.; Cardelino, C. A. *J. Phys. Chem. C* **2009**, *113*, 21765.

(546) Cardelino, B. H.; Cardelino, C. A. *J. Phys. Chem. C* **2011**, *115*, 9090.

(547) Barraza-Jimenez, D.; Galvan, D. H.; Posada-Amarillas, A.; Flores-Hidalgo, M. A.; Glossman-Mitnik, D.; Jose-Yacaman, M. *J. Mol. Model.* **2012**, *18*, 4885.

(548) Prasomsri, T.; Shi, D.; Resasco, D. E. *Chem. Phys. Lett.* **2010**, *497*, 103.

(549) Banerjee, S.; Montgomery, J. A.; Gascón, J. A. *J. Mater. Sci.* **2012**, *47*, 7686.

(550) Froese, R. D. J.; Morokuma, K. *Chem. Phys. Lett.* **1996**, *263*, 393.

(551) Caricato, M.; Vreven, T.; Trucks, G. W.; Frisch, M. J.; Wiberg, K. B. *J. Chem. Phys.* **2009**, *131*, 134105.

(552) Zhang, R.-B.; Ai, X.-C.; Zhang, X.-K.; Zhang, Q.-Y. *J. Mol. Struct. (THEOCHEM)* **2004**, *680*, 21.

(553) Tossell, J. A. *Geochem. Trans.* **2003**, *4*, 28.

(554) (a) Pedone, A.; Bloino, J.; Monti, S.; Prampolini, G.; Barone, V. *Phys. Chem. Chem. Phys.* **2010**, *12*, 1000. (b) Barone, V.; Bloino, J.; Monti, S.; Pedone, A.; Prampolini, G. *Phys. Chem. Chem. Phys.* **2011**, *13*, 2160.

(555) García, G.; Ciofini, I.; Fernández-Gómez, M.; Adamo, C. *J. Phys. Chem. Lett.* **2013**, *4*, 1239.

(556) Wang, L.-F.; Chen, J.-W.; Chen, J.-W. *Mater. Chem. Phys.* **2012**, *136*, 151.

(557) Tzeli, D.; Theodorakopoulos, G.; Petsalakis, I. D.; Ajami, D.; Rebek, J. *J. Am. Chem. Soc.* **2012**, *134*, 4346.

(558) Velardez, G. F.; Lemke, H. T.; Breiby, D. W.; Nielsen, M. M.; Møller, K. B.; Henriksen, N. E. *J. Phys. Chem. A* **2008**, *112*, 8179.

(559) Yang, S.-Y.; Zhao, L.; Duan, Y.-A.; Geng, Y.; Su, Z.-M. *Theor. Chem. Acc.* **2013**, *132*, 1377.

(560) Mutai, T.; Sawatani, H.; Shida, T.; Shono, H.; Araki, K. *J. Org. Chem.* **2013**, *78*, 2482.

(561) Labat, F.; Ciofini, I.; Hratchian, H. P.; Frisch, M. J.; Raghavachari, K.; Adamo, C. *J. Phys. Chem. C* **2011**, *115*, 4297.

(562) Li, M.-C.; Hayashi, M.; Lin, S.-H. *J. Phys. Chem. A* **2011**, *115*, 14531.

(563) Peng, Q.; Yi, Y.; Shuai, Z.; Shao, J. *J. Am. Chem. Soc.* **2007**, *129*, 9333.

(564) Li, Q.; Blancafort, L. *Chem. Commun.* **2013**, *49*, 5966.

(565) (a) Guo, Y.; Greenfield, M.; Bernstein, E. R. *J. Chem. Phys.* **2005**, *122*, 244310. (b) Guo, Y.; Greenfield, M.; Bhattacharya, A.; Bernstein, E. R. *J. Chem. Phys.* **2007**, *127*, 154301. (c) Im, H.-S.; Bernstein, E. R. *J. Chem. Phys.* **2000**, *113*, 7911.

(566) Bhattacharya, A.; Bernstein, E. R. *J. Phys. Chem. A* **2011**, *115*, 4135.

(567) Yu, Z.; Bernstein, E. R. *J. Chem. Phys.* **2011**, *135*, 154305.

(568) Prager, S.; Burghardt, I.; Dreuw, A. *J. Phys. Chem. A* **2014**, *118*, 1339.

(569) (a) Douhal, A.; Fiebig, T.; Chachisvilis, M.; Zewail, A. H. *J. Phys. Chem. A* **1998**, *102*, 1657. (b) Milewski, M.; Augustyniak, W.; Maciejewski, A. *J. Phys. Chem. A* **1998**, *102*, 7427. (c) Grabner, G.; Rechthaler, K.; Mayer, B.; Köhler, G.; Rotkiewicz, K. *J. Phys. Chem. A* **2000**, *104*, 1365. (d) Nau, W. M.; Zhang, X. *J. Am. Chem. Soc.* **1999**, *121*, 8022. (e) Douhal, A.; Amat-Guerri, F.; Acuña, A. U. *Angew. Chem., Int. Ed.* **1997**, *36*, 1514.

(570) (a) Casadesús, R.; Moreno, M.; Lluch, J. M. *Chem. Phys. Lett.* **2002**, *356*, 423. (b) Casadesús, R.; Moreno, M.; Lluch, J. M. *J. Photochem. Photobiol., A* **2005**, *173*, 365.

(571) (a) Re, S.; Morokuma, K. *J. Phys. Chem. A* **2001**, *105*, 7185. (b) Re, S.; Morokuma, K. *Theor. Chem. Acc.* **2004**, *112*, 59.

(572) Fukaya, H.; Morokuma, K. *J. Org. Chem.* **2003**, *68*, 8170.

(573) Zhang, H.; Kim, C.-K. *Bull. Korean Chem. Soc.* **2008**, *29*, 2528.

(574) Vailikhit, V.; Holzschuh, W. J.; Hannongbua, S. *J. Mol. Struct. (THEOCHEM)* **2010**, *944*, 173.

(575) Nazarski, R. B. *J. Phys. Org. Chem.* **2009**, *22*, 834.

(576) Lu, S.-I. *J. Mol. Struct. (THEOCHEM)* **2009**, *893*, 84.

(577) Salvador, P.; Asensio, A.; Dannenberg, J. J. *J. Phys. Chem. B* **2007**, *111*, 7462.

(578) Gkionis, K.; Platts, J. A. *Comput. Theor. Chem.* **2012**, *993*, 60.

(579) Sundaresan, N.; Pillai, C. K. S.; Suresh, C. H. *J. Phys. Chem. A* **2006**, *110*, 8826.

(580) Sundaresan, N.; Suresh, C. H. *J. Chem. Theory Comput.* **2007**, *3*, 1172.

(581) Tsuchida, N.; Yamazaki, S.; Yamabe, S. *Org. Biomol. Chem.* **2008**, *6*, 3109.

(582) Yamabe, S.; Mizukami, N.; Tsuchida, N.; Yamazaki, S. *J. Organomet. Chem.* **2008**, *693*, 1335.

(583) Li, W.; Li, S.; Jiang, Y. *J. Phys. Chem. A* **2007**, *111*, 2193.

(584) Li, W. *J. Chem. Phys.* **2013**, *138*, 014106.

(585) Wanprakhon, S.; Tongraar, A.; Kerdcharoen, T. *Chem. Phys. Lett.* **2011**, *517*, 171.

(586) Sripa, P.; Tongraar, A.; Kerdcharoen, T. *J. Phys. Chem. A* **2013**, *117*, 1826.

(587) Thaomola, S.; Tongraar, A.; Kerdcharoen, T. *J. Mol. Liq.* **2012**, *174*, 26.

(588) (a) Matsubara, T.; Dupuis, M.; Aida, M. *Chem. Phys. Lett.* **2007**, *437*, 138. (b) Matsubara, T.; Sugimoto, H.; Aida, M. *Bull. Chem. Soc. Jpn.* **2008**, *81*, 1258. (c) Matsubara, T. *J. Phys. Chem. A* **2009**, *113*, 3227. (d) Sakae, Y.; Matsubara, T.; Aida, M.; Kondo, H.; Masaki, K.; Iefuji, H. *Bull. Chem. Soc. Jpn.* **2009**, *82*, 338. (e) Matsubara, T.; Takahashi, R.; Asai, S. *Bull. Chem. Soc. Jpn.* **2013**, *86*, 243.

(589) Shiga, M.; Tachikawa, M. *Mol. Simul.* **2007**, *33*, 171.

(590) Li, Q.; Gusarov, S.; Evoy, S.; Kovalenko, A. *J. Phys. Chem. B* **2009**, *113*, 9958.

(591) Wu, J.; Albrecht, L.; Boyd, R. J. *J. Phys. Chem. B* **2011**, *115*, 14885.

(592) (a) Matsui, T.; Sato, T.; Shigeta, Y. *Int. J. Quantum Chem.* **2009**, *109*, 2168. (b) Zahariev, T.; Ivanova, A.; Velinova, M.; Tadjer, A. *Chem. Phys.* **2013**, *410*, 1. (c) Talipov, M. R.; Timerghazin, Q. K. *J. Phys. Chem. B* **2013**, *117*, 1827.

(593) (a) Barone, V.; Bloino, J.; Monti, S.; Pedone, A.; Prampolini, G. *Phys. Chem. Chem. Phys.* **2011**, *13*, 2160. (b) Pedone, A.; Prampolini, G.; Monti, S.; Barone, V. *Phys. Chem. Chem. Phys.* **2011**, *13*, 16689. (c) Pedone, A.; Bloino, J.; Barone, V. *J. Phys. Chem. C* **2012**, *116*, 17807. (d) Petrone, A.; Caruso, P.; Tenuta, S.; Rega, N. *Phys. Chem. Chem. Phys.* **2013**, *15*, 20536.

(594) (a) Li, H.; Hains, A. W.; Everts, J. E.; Robertson, A. D.; Jensen, J. H. *J. Phys. Chem. B* **2002**, *106*, 3486. (b) Jensen, J. H.; Li, H.; Robertson, A. D.; Molina, P. A. *J. Phys. Chem. A* **2005**, *109*, 6634.

(595) Barone, V.; De Rienzo, F.; Langella, E.; Menziani, M. C.; Regal, N.; Sola, M. *Proteins* **2006**, *62*, 262.

(596) (a) Li, Y.; Hartke, B. *ChemPhysChem* **2013**, *14*, 2678. (b) Akyuz, M. A.; Erdem, S. S. *J. Neural Transm.* **2013**, *120*, 937.

(597) (a) DeYonker, N. J.; Webster, C. E. *J. Am. Chem. Soc.* **2013**, *135*, 13764. (b) Dourado, D. F. A. R.; Fernandes, P. A.; Ramos, M. J.; Mannervik, B. *Biochemistry* **2013**, *52*, 8069.

(598) (a) Marianski, M.; Dannenberg, J. J. *J. Phys. Chem. B* **2012**, *116*, 1437. (b) Cerón-Carrasco, J. P.; Requena, A.; Jacquemin, D. *Theor. Chem. Acc.* **2012**, *131*, 1188. (c) Gkionis, K.; Mutter, S. T.; Platts, J. A. *RSC Adv.* **2013**, *3*, 4066.

(599) (a) Boggio-Pasqua, M.; Burmeister, C. F.; Robb, M. A.; Groenhof, G. *Phys. Chem. Chem. Phys.* **2012**, *14*, 7912. (b) Marchand, A. P.; Coxon, J. M. *Acc. Chem. Res.* **2002**, *35*, 271.

(600) Prabhakar, R.; Morokuma, K.; Musaev, D. G. *J. Comput. Chem.* **2005**, *26*, 443.

(601) Prabhakar, R.; Musaev, D. G.; Khavrutskii, I. V.; Morokuma, K. *J. Phys. Chem. B* **2004**, *108*, 12643.

(602) Moon, S.; Case, D. A. *J. Comput. Chem.* **2006**, *27*, 825.

(603) Wieczorek, R.; Dannenberg, J. J. *J. Am. Chem. Soc.* **2004**, *126*, 14198.

(604) Plumley, J. A.; Dannenberg, J. J. *J. Am. Chem. Soc.* **2010**, *132*, 1758.

(605) (a) Plumley, J. A.; Dannenberg, J. J. *J. Phys. Chem. B* **2011**, *115*, 10560. (b) Plumley, J. A.; Ali-Torres, J.; Pohl, G.; Dannenberg, J. J. *J. Phys. Chem. B* **2014**, *118*, 3326.

(606) Roy, D.; Dannenberg, J. J. *Chem. Phys. Lett.* **2011**, *512*, 255.

(607) Ali-Torres, J.; Dannenberg, J. J. *J. Phys. Chem. B* **2012**, *116*, 14017.

(608) Roy, D.; Pohl, G.; Ali-Torres, J.; Marianski, M.; Dannenberg, J. J. *Biochemistry* **2012**, *51*, 5387.

(609) Pohl, G.; Asensio, A.; Dannenberg, J. J. *Biochemistry* **2014**, *53*, 617.

(610) Tsai, M.; Xu, Y.; Dannenberg, J. J. *J. Am. Chem. Soc.* **2005**, *127*, 14130.

(611) Wieczorek, R.; Dannenberg, J. J. *J. Phys. Chem. B* **2008**, *112*, 1320.

(612) Alzate-Morales, J. H.; Caballero, J.; Jague, A. V.; Nilo, F. D. G. *J. Chem. Inf. Model.* **2009**, *49*, 886.

(613) Pandey, K. K.; Snyder, J. P.; Liotta, D. C.; Musaev, D. G. *J. Phys. Chem. B* **2010**, *114*, 1127.

(614) Lu, Y.; Wang, Y.; Xu, Z.; Yan, X.; Luo, X.; Jiang, H.; Zhu, W. *J. Phys. Chem. B* **2009**, *113*, 12615.

(615) Lu, Y.; Shi, T.; Wang, Y.; Yang, H.; Yan, X.; Luo, X.; Jiang, H.; Zhu, W. *J. Med. Chem.* **2009**, *52*, 2854.

(616) Zhou, P.; Zou, J.; Tian, F.; Shang, Z. *J. Chem. Inf. Model.* **2009**, *49*, 2344.

(617) Rickard, G. A.; Bergès, J.; Houèe-Levin, C.; Rauk, A. *J. Phys. Chem. B* **2008**, *112*, 5774.

(618) Torrent, M.; Vreven, T.; Musaev, D. G.; Morokuma, K.; Farkas, O.; Schlegel, H. B. *J. Am. Chem. Soc.* **2002**, *124*, 192.

(619) Hoffmann, M.; Khavrutskii, I. V.; Musaev, D. G.; Morokuma, K. *Int. J. Quantum Chem.* **2004**, *99*, 972.

(620) Lundberg, M.; Morokuma, K. *J. Phys. Chem. B* **2007**, *111*, 9380.

(621) Hirao, H.; Morokuma, K. *J. Phys. Chem. Lett.* **2010**, *1*, 901.

(622) Harris, T. V.; Morokuma, K. *Inorg. Chem.* **2013**, *52*, 8551.

(623) (a) Tomchick, D. R.; Phan, P.; Cymborowski, M.; Minor, W.; Holman, T. R. *Biochemistry* **2001**, *40*, 7509. (b) Solomon, E. I.; Zhou, J.; Neese, F.; Pavel, E. G. *Chem. Biol.* **1997**, *4*, 795.

(624) Grimme, S. *WIREs Comput. Mol. Sci.* **2011**, *1*, 211.

(625) Barrett, M. L.; Harvey, I.; Sundararajan, M.; Surendran, R.; Hall, J. F.; Ellis, M. J.; Hough, M. A.; Strange, R. W.; Hillier, I. H.; Hasnain, S. S. *Biochemistry* **2006**, *45*, 2927.

(626) Paraskevopoulos, K.; Sundararajan, M.; Surendran, R.; Hough, M. A.; Eady, R. R.; Hillier, I. H.; Hasnain, S. S. *Dalton Trans.* **2006**, 3067.

(627) Comba, P.; Lledós, A.; Maseras, F.; Remenyi, R. *Inorg. Chim. Acta* **2001**, *324*, 21.

(628) Dalosto, S. D. *J. Phys. Chem. B* **2007**, *111*, 2932.

(629) Datta, S. N.; Sudhamsu, J.; Pandey, A. *J. Phys. Chem. B* **2004**, *108*, 8007.

(630) Barea, G.; Maseras, F.; Lledós, A. *J. Mol. Struct. (THEOCHEM)* **2003**, *632*, 323.

(631) Wu, S.; Liu, S.; Sim, S.; Pedersen, L. G. *J. Phys. Chem. Lett.* **2012**, *3*, 2293.

(632) Pandey, A.; Datta, S. N. *J. Phys. Chem. B* **2005**, *109*, 9066.

(633) Azimi, S.; Rauk, A. *J. Chem. Theory Comput.* **2012**, *8*, 5150.

(634) Chen, K.; Xu, L.; Wiest, O. *J. Org. Chem.* **2013**, *78*, 5051.

(635) Gkionis, K.; Platts, J. A. *J. Biol. Inorg. Chem.* **2009**, *14*, 1165.

(636) Ahmadi, F.; Jamali, N.; Jahangard-Yekta, S.; Jafari, B.; Nouri, S.; Najafi, F.; Rahimi-Nasrabadi, M. *Spectrochim. Acta, Part A* **2011**, *79*, 1004.

(637) Ruiz, R.; García, B.; Ruisi, G.; Silvestri, A.; Barone, G. *J. Mol. Struct. (THEOCHEM)* **2009**, *915*, 86.

(638) Robertazzi, A.; Platts, J. A. *Chem.—Eur. J.* **2006**, *12*, 5747.

(639) Lauria, A.; Bonsignore, R.; Terenzi, A.; Spinello, A.; Giannici, F.; Longo, A.; Almerico, A. M.; Barone, G. *Dalton Trans.* **2014**, *43*, 6108.

(640) Rutledge, L. R.; Wetmore, S. D. *Can. J. Chem.* **2010**, *88*, 815.

(641) Galano, A.; Alvarez-Idaboy, J. R. *Phys. Chem. Chem. Phys.* **2012**, *14*, 12476.

(642) Lipiec, E.; Sekine, R.; Bielecki, J.; Kwiatek, W. M.; Wood, B. R. *Angew. Chem., Int. Ed.* **2014**, *53*, 169.

(643) Ueno-Noto, K.; Hara-Yokoyama, M.; Takano, K. *Bull. Chem. Soc. Jpn.* **2008**, *81*, 1062.

(644) Potamitis, C.; Zervou, M.; Katsiaras, V.; Zoumpoulakis, P.; Durdagi, S.; Papadopoulos, M. G.; Hayes, J. M.; Grdadolnik, S. G.; Kyrikou, I.; Argyropoulos, D.; Vatougia, G.; Mavromoustakos, T. *J. Chem. Inf. Model.* **2009**, *49*, 726.

(645) Świderek, K.; Panczakiewicz, A.; Bujacz, A.; Bujacz, G.; Paneth, P. *J. Phys. Chem. B* **2009**, *113*, 12782.

(646) Kuno, M.; Hannongbua, S.; Morokuma, K. *Chem. Phys. Lett.* **2003**, *380*, 456.

(647) Kuno, M.; Hongkrengkai, R.; Hannongbua, S. *Chem. Phys. Lett.* **2006**, *424*, 172.

(648) Saen-Oon, S.; Kuno, M.; Hannongbua, S. *Proteins* **2005**, *61*, 859.

(649) Kuno, M.; Palangsuntikul, R.; Hannongbua, S. *J. Chem. Inf. Comput. Sci.* **2003**, *43*, 1584.

(650) Saen-oon, S.; Aruksakunwong, O.; Wittayanarakul, K.; Sompornpisut, P.; Hannongbua, S. *J. Mol. Graphics* **2007**, *26*, 720.

(651) Srivab, P.; Hannongbua, S. *ChemMedChem* **2008**, *3*, 803.

(652) Boonsri, P.; Kuno, M.; Hannongbua, S. *MedChemComm* **2011**, *2*, 1181.

(653) Sae-Tang, D.; Kittakoop, P.; Hannongbua, S. *Monatsh. Chem.* **2009**, *140*, 1533.

(654) Prajongtat, P.; Phromyothin, D. S. T.; Hannongbua, S. *J. Mol. Model.* **2013**, *19*, 3165.

(655) Suresh, C. H.; Vargheese, A. M.; Vijayalakshmi, K. P.; Mohan, N.; Koga, N. *J. Comput. Chem.* **2008**, *29*, 1840.

(656) Lu, S.-Y.; Jiang, Y.-J.; Lv, J.; Zou, J.-W.; Wu, T.-X. *J. Comput. Chem.* **2011**, *32*, 1907.

(657) Fong, P.; McNamara, J. P.; Hillier, I. H.; Bryce, R. A. *J. Chem. Inf. Model.* **2009**, *49*, 913.

(658) Raju, R. K.; Burton, N. A.; Hillier, I. H. *Phys. Chem. Chem. Phys.* **2010**, *12*, 7117.

(659) Gleeson, M. P.; Gleeson, D. *J. Chem. Inf. Model.* **2009**, *49*, 1437.

(660) Gleeson, M. P.; Gleeson, D. *J. Chem. Inf. Model.* **2009**, *49*, 670.

(661) Zhan, C.-G.; Gao, D. *Biophys. J.* **2005**, *89*, 3863.

(662) Gao, D.; Zhan, C.-G. *Proteins* **2006**, *62*, 99.

(663) Gesto, D. S.; Cerqueira, N.; Fernandes, P. A.; Ramos, M. J. *J. Am. Chem. Soc.* **2013**, *135*, 7146.

(664) (a) Barman, A.; Prabhakar, R. *J. Mol. Graphics* **2013**, *40*, 1. (b) Barman, A.; Schürer, S.; Prabhakar, R. *Biochemistry* **2011**, *50*, 4337.

(665) Meroueh, S. O.; Fisher, J. F.; Schlegel, H. B.; Mobashery, S. *J. Am. Chem. Soc.* **2005**, *127*, 15397.

(666) Li, J.; Cross, J. B.; Vreven, T.; Meroueh, S. O.; Mobashery, S.; Schlegel, H. B. *Proteins* **2005**, *61*, 246.

(667) Shi, Q.; Meroueh, S. O.; Fisher, J. F.; Mobashery, S. *J. Am. Chem. Soc.* **2008**, *130*, 9293.

(668) Shi, Q.; Meroueh, S. O.; Fisher, J. F.; Mobashery, S. *J. Am. Chem. Soc.* **2011**, *133*, 5274.

(669) My, N. H.; Hirao, H.; Van, D. U.; Morokuma, K. *J. Chem. Inf. Model.* **2011**, *51*, 3226.

(670) Prabhakar, R.; Vreven, T.; Frisch, M. J.; Morokuma, K.; Musaev, D. G. *J. Phys. Chem. B* **2006**, *110*, 13608.

(671) Pang, J.; Scrutton, N. S.; de Visser, S. P.; Sutcliffe, M. J. *Chem. Commun.* **2010**, *46*, 3104.

(672) Tian, B.; Strid, A.; Eriksson, L. A. *J. Phys. Chem. B* **2011**, *115*, 1918.

(673) Passos, O.; Fernandes, P. A.; Ramos, M. J. *J. Phys. Chem. B* **2011**, *115*, 14751.

(674) Haines, B. E.; Steussy, C. N.; Stauffacher, C. V.; Wiest, O. *Biochemistry* **2012**, *51*, 7983.

(675) (a) Kiss, G.; Röthlisberger, D.; Baker, D.; Houk, K. N. *Protein Sci.* **2010**, *19*, 1760. (b) Kiss, G.; Çelebi-Ölçüm, N.; Moretti, R.; Baker, D.; Houk, K. N. *Angew. Chem., Int. Ed.* **2013**, *52*, 5700.

(676) Oliveira, E. F.; Cerqueira, N.; Fernandes, P. A.; Ramos, M. J. *J. Am. Chem. Soc.* **2011**, *133*, 15496.

(677) Tao, P.; Gatti, D. L.; Schlegel, H. B. *Biochemistry* **2009**, *48*, 11706.

(678) Carvalho, A. T. P.; Fernandes, P. A.; Ramos, M. J. *J. Phys. Chem. B* **2006**, *110*, 5758.

(679) Du, Z.; Shemella, P. T.; Liu, Y.; McCallum, S. A.; Pereira, B.; Nayak, S. K.; Belfort, G.; Belfort, M.; Wang, C. *J. Am. Chem. Soc.* **2009**, *131*, 11581.

(680) Lewandowicz, A.; Rudziński, J.; Tronstad, L.; Widersten, M.; Ryberg, P.; Matsson, O.; Paneth, P. *J. Am. Chem. Soc.* **2001**, *123*, 4550.

(681) Kwiecien, R. A.; Khavrutskii, I. V.; Musaev, D. G.; Morokuma, K.; Banerjee, R.; Paneth, P. *J. Am. Chem. Soc.* **2006**, *128*, 1287.

(682) Pang, J.; Li, X.; Morokuma, K.; Scrutton, N. S.; Sutcliffe, M. J. *J. Am. Chem. Soc.* **2012**, *134*, 2367.

(683) Kamachi, T.; Toraya, T.; Yoshizawa, K. *J. Am. Chem. Soc.* **2004**, *126*, 16207.

(684) Kamachi, T.; Toraya, T.; Yoshizawa, K. *Chem.—Eur. J.* **2007**, *13*, 7864.

(685) Kumar, N.; Kozlowski, P. M. *J. Phys. Chem. B* **2013**, *117*, 16044.

(686) Inoue, T.; Shiota, Y.; Yoshizawa, K. *J. Am. Chem. Soc.* **2008**, *130*, 16890.

(687) Kamachi, T.; Kihara, N.; Shiota, Y.; Yoshizawa, K. *Inorg. Chem.* **2005**, *44*, 4226.

(688) Yoshizawa, K.; Kihara, N.; Kamachi, T.; Shiota, Y. *Inorg. Chem.* **2006**, *45*, 3034.

(689) Yoshizawa, K.; Shiota, Y. *J. Am. Chem. Soc.* **2006**, *128*, 9873.

(690) Himo, F.; Eriksson, L. A.; Maseras, F.; Siegbahn, P. E. M. *J. Am. Chem. Soc.* **2000**, *122*, 8031.

(691) Godfrey, E.; Porro, C. S.; de Visser, S. P. *J. Phys. Chem. A* **2008**, *112*, 2464.

(692) Hirao, H.; Morokuma, K. *J. Am. Chem. Soc.* **2011**, *133*, 14550.

(693) Hirao, H.; Morokuma, K. *J. Am. Chem. Soc.* **2009**, *131*, 17206.

(694) Hirao, H. *J. Phys. Chem. B* **2011**, *115*, 11278.

(695) Kamachi, T.; Yoshizawa, K. *J. Am. Chem. Soc.* **2005**, *127*, 10686.

(696) Porro, C. S.; Sutcliffe, M. J.; de Visser, S. P. *J. Phys. Chem. A* **2009**, *113*, 11635.

(697) Kwiecień, R. A.; Le Questel, J. Y.; Lebreton, J.; Delaforge, M.; André, F.; Pihan, E.; Roussel, A.; Fournial, A.; Paneth, P.; Robins, R. J. *J. Phys. Chem. B* **2012**, *116*, 7827.

(698) Yamamoto, S.; Hayaishi, O. *J. Biol. Chem.* **1967**, *242*, 5260.

(699) (a) Zhang, Y.; Kang, S. A.; Mukherjee, T.; Bale, S.; Crane, B. R.; Begley, T. P.; Ealick, S. E. *Biochemistry* **2007**, *46*, 145. (b) Sugimoto, H.; Oda, S. I.; Otsuki, T.; Hino, T.; Yoshida, T.; Shiro, Y. *Proc. Natl. Acad. Sci. U.S.A.* **2006**, *103*, 2611.

(700) Chung, L. W.; Li, X.; Sugimoto, H.; Shiro, Y.; Morokuma, K. *J. Am. Chem. Soc.* **2008**, *130*, 12299.

(701) Chung, L. W.; Li, X.; Hirao, H.; Morokuma, K. *J. Am. Chem. Soc.* **2011**, *133*, 20076.

(702) Chung, L. W.; Li, X.; Sugimoto, H.; Shiro, Y.; Morokuma, K. *J. Am. Chem. Soc.* **2010**, *132*, 11993.

(703) (a) Rafice, S. A.; Chauhan, N.; Efimov, I.; Basran, J.; Raven, E. L. *Biochem. Soc. Trans.* **2009**, *37*, 408. (b) Yanagisawa, S.; Yotsuya, K.; Hashiwaki, Y.; Horitani, M.; Sugimoto, H.; Shiro, Y.; Appelman, E. H.; Ogura, T. *Chem. Lett.* **2010**, *39*, 36. (c) Chauhan, N.; Thackray, S. J.; Rafice, S. A.; Eaton, G.; Lee, M.; Efimov, I.; Basran, J.; Jenkins, P. R.; Mowat, C. G.; Chapman, S. K.; Raven, E. L. *J. Am. Chem. Soc.* **2009**, *131*, 4186. (d) Davydov, R. M.; Chauhan, N.; Thackray, S. J.; Anderson, J. L. R.; Papadopoulou, N. D.; Mowat, C. G.; Chapman, S. K.; Raven, E. L.; Hoffman, B. M. *J. Am. Chem. Soc.* **2010**, *132*, 5494. (e) Lewis-Ballester, A.; Batabyal, D.; Egawa, T.; Lu, C.; Lin, Y.; Marti, M. A.; Capece, L.; Estrin, D. A.; Yeh, S.-R. *Proc. Natl. Acad. Sci. U.S.A.* **2009**, *106*, 17371.

(704) Kubas, A.; De Sancho, D.; Best, R. B.; Blumberger, J. *Angew. Chem., Int. Ed.* **2014**, *53*, 4081.

(705) Jayapal, P.; Sundararajan, M.; Hillier, I. H.; Burton, N. A. *Phys. Chem. Chem. Phys.* **2008**, *10*, 4249.

(706) Lill, S. O. N.; Siegbahn, P. E. M. *Biochemistry* **2009**, *48*, 1056.

(707) Banáš, P.; Rulíšek, L.; Hánošová, V.; Svozil, D.; Walter, N. G.; Šponer, J.; Otyepka, M. *J. Phys. Chem. B* **2008**, *112*, 11177.

(708) (a) Cleland, W. W.; Hengge, A. C. *Chem. Rev.* **2006**, *106*, 3252. (b) Zhou, D.-M.; Taira, K. *Chem. Rev.* **1998**, *98*, 991. (c) Oivanen, M.; Kuusela, S.; Lönnberg, H. *Chem. Rev.* **1998**, *98*, 961. (d) Noodleman, L.; Lovell, T.; Han, W.-G.; Li, J.; Himo, F. *Chem. Rev.* **2004**, *104*, 459. (e) Jackson, M. D.; Denu, J. M. *Chem. Rev.* **2001**, *101*, 2313.

(709) Smith, A. J. T.; Li, Y.; Houk, K. N. *Org. Biomol. Chem.* **2009**, *7*, 2716.

(710) (a) Cross, R. L. *Annu. Rev. Biochem.* **1981**, *50*, 681. (b) Boyer, P. D. *Annu. Rev. Biochem.* **1997**, *66*, 717. (c) Yoshida, M.; Muneyuki, E.; Hisabori, T. *Nat. Rev. Mol. Cell Biol.* **2001**, *2*, 669. (d) Karplus, M.; Kuriyan, J. *Proc. Natl. Acad. Sci. U.S.A.* **2005**, *102*, 6679. (e) Dittrich, M.; Hayashi, S.; Schulten, K. *Biophys. J.* **2004**, *87*, 2954. (f) Gao, Y. Q.; Yang, W.; Karplus, M. *Cell* **2005**, *123*, 195. (g) Böckmann, R. A.; Grubmüller, H. *Nat. Struct. Biol.* **2002**, *9*, 198. (h) Štrajbl, M.; Shurki, A.; Warshel, A. *Proc. Natl. Acad. Sci. U.S.A.* **2003**, *100*, 14834.

(711) Beke-Somfai, T.; Lincoln, P.; Nordén, B. *Proc. Natl. Acad. Sci. U.S.A.* **2011**, *108*, 4828.

(712) Beke-Somfai, T.; Lincoln, P.; Nordén, B. *Proc. Natl. Acad. Sci. U.S.A.* **2013**, *110*, 2117.

(713) Wang, X.; Hirao, H. *J. Phys. Chem. B* **2013**, *117*, 833.

(714) Sproviero, E. M.; Gascón, J. A.; McEvoy, J. P.; Brudvig, G. W.; Batista, V. S. *J. Am. Chem. Soc.* **2008**, *130*, 3428.

(715) Sklenak, S.; Yao, L.; Cukier, R. I.; Yan, H. *J. Am. Chem. Soc.* **2004**, *126*, 14879.

(716) Yao, L.; Cukier, R. I.; Yan, H. *J. Phys. Chem. B* **2007**, *111*, 4200.

(717) Wu, X.-H.; Zou, G.-L.; Quan, J.-M.; Wu, Y.-D. *J. Comput. Chem.* **2010**, *31*, 2238.

(718) Cross, J. B.; Vreven, T.; Meroueh, S. O.; Mobashery, S.; Schlegel, H. B. *J. Phys. Chem. B* **2005**, *109*, 4761.

(719) (a) Tao, P.; Fisher, J. F.; Shi, Q.; Mobashery, S.; Schlegel, H. B. *J. Phys. Chem. B* **2010**, *114*, 1030. (b) Zhou, J.; Tao, P.; Fisher, J. F.; Shi, Q.; Mobashery, S.; Schlegel, H. B. *J. Chem. Theory Comput.* **2010**, *6*, 3580.

(720) Pelmenschikov, V.; Siegbahn, P. E. M. *Inorg. Chem.* **2002**, *41*, 5659.

(721) Wu, X.-H.; Quan, J.-M.; Wu, Y.-D. *J. Phys. Chem. B* **2007**, *111*, 6236.

(722) (a) Xiong, Y.; Lu, H.-T.; Li, Y.; Yang, G.-F.; Zhan, C.-G. *Biophys. J.* **2006**, *91*, 1858. (b) Xiong, Y.; Lu, H.-T.; Zhan, C.-G. *J. Comput. Chem.* **2008**, *29*, 1259.

(723) Abdel-Azeim, S.; Li, X.; Chung, L. W.; Morokuma, K. *J. Comput. Chem.* **2011**, *32*, 3154.

(724) Banáš, P.; Jurečka, P.; Walter, N. G.; Šponer, J.; Otyepka, M. *Methods* **2009**, *49*, 202.

(725) Cerqueira, N.; Fernandes, P. A.; Eriksson, L. A.; Ramos, M. J. *J. Comput. Chem.* **2004**, *25*, 2031.

(726) Cerqueira, N.; Fernandes, P. A.; Eriksson, L. A.; Ramos, M. J. *Biophys. J.* **2006**, *90*, 2109.

(727) Matsui, T.; Shigeta, Y.; Hirao, K. *J. Phys. Chem. B* **2007**, *111*, 1176.

(728) Cerón-Carrasco, J. P.; Jacquemin, D.; Cauët, E. *Phys. Chem. Chem. Phys.* **2012**, *14*, 12457.

(729) Chen, H.-Y.; Kao, C.-L.; Hsu, S. C. N. *J. Am. Chem. Soc.* **2009**, *131*, 15930.

(730) Rutledge, L. R.; Wetmore, S. D. *J. Am. Chem. Soc.* **2011**, *133*, 16258.

(731) Ribeiro, A. J. M.; Ramos, M. J.; Fernandes, P. A. *J. Am. Chem. Soc.* **2012**, *134*, 13436.

(732) Lin, P.; Pedersen, L. C.; Batra, V. K.; Beard, W. A.; Wilson, S. H.; Pedersen, L. G. *Proc. Natl. Acad. Sci. U.S.A.* **2006**, *103*, 13294.

(733) Batra, V. K.; Perera, L.; Lin, P.; Shock, D. D.; Beard, W. A.; Pedersen, L. C.; Pedersen, L. G.; Wilson, S. H. *J. Am. Chem. Soc.* **2013**, *135*, 8078.

(734) Brás, N. F.; Fernandes, P. A.; Ramos, M. J. *J. Chem. Theory Comput.* **2010**, *6*, 421.

(735) Huang, W.; Gauld, J. W. *J. Phys. Chem. B* **2012**, *116*, 14040.

(736) Zhang, Y.; Yan, S.; Yao, L. *J. Phys. Chem. B* **2013**, *117*, 8714.

(737) Robles, V. M.; Ortega-Carrasco, E.; Fuentes, E. G.; Lledós, A.; Marechal, J. D. *Faraday Discuss.* **2011**, *148*, 137.

(738) Robles, V. M.; Vidossich, P.; Lledós, A.; Ward, T. R.; Marechal, J. D. *ACS Catal.* **2014**, *4*, 833.

(739) Ke, Z.; Abe, S.; Ueno, T.; Morokuma, K. *J. Am. Chem. Soc.* **2012**, *134*, 15418.

(740) Petrova, G. P.; Ke, Z.; Park, S.; Sugiyama, H.; Morokuma, K. *Chem. Phys. Lett.* **2014**, *600*, 87.

(741) (a) Bearpark, M. J.; Bernardi, F.; Clifford, S.; Olivucci, M.; Robb, M. A.; Smith, B. R.; Vreven, T. *J. Am. Chem. Soc.* **1996**, *118*, 169. (b) Bernardi, F.; Olivucci, M.; Robb, M. A. *J. Am. Chem. Soc.* **1992**, *114*, 1606. (c) Su, J. T.; Goddard, W. A. *Phys. Rev. Lett.* **2007**, *99*. (d) Bearpark, M. J.; Bernardi, F.; Olivucci, M.; Robb, M. A.; Smith, B. R. *J. Am. Chem. Soc.* **1996**, *118*, 5254.

(742) Altun, A.; Yokoyama, S.; Morokuma, K. *Photochem. Photobiol.* **2008**, *84*, 845.

(743) (a) Gascón, J. A.; Batista, V. S. *Biophys. J.* **2004**, *87*, 2931. (b) Gascón, J. A.; Sproviero, E. M.; Batista, V. S. *J. Chem. Theory Comput.* **2005**, *1*, 674.

(744) Hasegawa, J.; Fujimoto, K. J.; Kawatsu, T. *J. Chem. Theory Comput.* **2012**, *8*, 4452.

(745) Altun, A.; Yokoyama, S.; Morokuma, K. *J. Phys. Chem. B* **2008**, *112*, 6814.

(746) Altun, A.; Yokoyama, S.; Morokuma, K. *J. Phys. Chem. B* **2008**, *112*, 16883.

(747) Hoffmann, M.; Wanko, M.; Strodel, P.; König, P. H.; Frauenheim, T.; Schulten, K.; Thiel, W.; Tajkhorshid, E.; Elstner, M. *J. Am. Chem. Soc.* **2006**, *128*, 10808.

(748) Sekharan, S.; Yokoyama, S.; Morokuma, K. *J. Phys. Chem. B* **2011**, *115*, 15380.

(749) Altun, A.; Yokoyama, S.; Morokuma, K. *J. Phys. Chem. A* **2009**, *113*, 11685.

(750) Tada, T.; Altun, A.; Yokoyama, S. *Proc. Natl. Acad. Sci. U.S.A.* **2009**, *106*, 17457.

(751) Altun, A.; Morokuma, K.; Yokoyama, S. *ACS Chem. Biol.* **2011**, *6*, 775.

(752) Sekharan, S.; Altun, A.; Morokuma, K. *Chem.—Eur. J.* **2010**, *16*, 1744.

(753) Sekharan, S.; Morokuma, K. *J. Phys. Chem. Lett.* **2010**, *1*, 668.

(754) Sekharan, S.; Altun, A.; Morokuma, K. *J. Am. Chem. Soc.* **2010**, *132*, 15856.

(755) Sekharan, S.; Morokuma, K. *J. Am. Chem. Soc.* **2011**, *133*, 19052.

(756) Sekharan, S.; Katayama, K.; Kandori, H.; Morokuma, K. *J. Am. Chem. Soc.* **2012**, *134*, 10706.

(757) Sekharan, S.; Wei, J. N.; Batista, V. S. *J. Am. Chem. Soc.* **2012**, *134*, 19536.

(758) Sekharan, S.; Morokuma, K. *J. Am. Chem. Soc.* **2011**, *133*, 4734.

(759) Ryazantsev, M. N.; Altun, A.; Morokuma, K. *J. Am. Chem. Soc.* **2012**, *134*, 5520.

(760) Pal, R.; Sekharan, S.; Batista, V. S. *J. Am. Chem. Soc.* **2013**, *135*, 9624.

(761) Blomgren, F.; Larsson, S. *J. Phys. Chem. B* **2005**, *109*, 9104.

(762) Tomasello, G.; Olaso-González, G.; Altoè, P.; Stenta, M.; Serrano-Andrés, L.; Merchán, M.; Orlandi, G.; Bottoni, A.; Garavelli, M. *J. Am. Chem. Soc.* **2009**, *131*, 5172.

(763) Polli, D.; Weingart, O.; Brida, D.; Poli, E.; Maiuri, M.; Spillane, K. M.; Bottoni, A.; Kukura, P.; Mathies, R. A.; Cerullo, G.; Garavelli, M. *Angew. Chem., Int. Ed.* **2014**, *53*, 2504.

(764) Patnaik, S. S.; Trohalaki, S.; Pachter, R. *Biopolymers* **2004**, *75*, 441.

(765) Gao, Q.; Tagami, K.; Fujihira, M.; Tsukada, M. *Jpn. J. Appl. Phys., Part 2* **2006**, *45*, L929.

(766) Matsuura, A.; Hayashi, T.; Sato, H.; Takahashi, A.; Sakurai, M. *Chem. Phys. Lett.* **2010**, *484*, 324.

(767) Amat, P.; Nifosì, R. *J. Chem. Theory Comput.* **2013**, *9*, 497.

(768) Li, X.; Chung, L. W.; Mizuno, H.; Miyawaki, A.; Morokuma, K. *J. Phys. Chem. B* **2010**, *114*, 1114.

(769) Ma, Y.; Sun, Q.; Li, Z.; Yu, J.-G.; Smith, S. C. *J. Phys. Chem. B* **2012**, *116*, 1426.

(770) Ren, X.; Xie, D.; Zeng, J. *J. Phys. Chem. A* **2011**, *115*, 10129.

(771) Ding, L.; Chung, L. W.; Morokuma, K. *J. Phys. Chem. B* **2013**, *117*, 1075.

(772) Li, X.; Chung, L. W.; Mizuno, H.; Miyawaki, A.; Morokuma, K. *J. Phys. Chem. B* **2010**, *114*, 16666.

(773) Thompson, M. J.; Bashford, D.; Noodleman, L.; Getzoff, E. D. *J. Am. Chem. Soc.* **2003**, *125*, 8186.

(774) Yamada, A.; Ishikura, T.; Yamato, T. *Proteins* **2004**, *55*, 1063.

(775) Kubota, K.; Shingae, T.; Foster, N. D.; Kumauchi, M.; Hoff, W. D.; Unno, M. *J. Phys. Chem. Lett.* **2013**, *4*, 3031.

(776) Hirano, K.; Sato, H. *Chem. Phys.* **2013**, *419*, 163.

(777) Haiser, K.; Fingerhut, B. P.; Heil, K.; Glas, A.; Herzog, T. T.; Pilles, B. M.; Schreier, W. J.; Zinth, W.; de Vivie-Riedle, R.; Carell, T. *Angew. Chem., Int. Ed.* **2012**, *51*, 408.

(778) Anusiewicz, I.; Świerszcz, I.; Skurski, P.; Simons, J. *J. Phys. Chem. A* **2013**, *117*, 1240.

(779) Kröner, D.; Götze, J. P. *J. Photochem. Photobiol., B* **2012**, *109*, 12.

(780) Di Valentin, M.; Tait, C. E.; Salvadori, E.; Orian, L.; Polimeno, A.; Carbonera, D. *Biochim. Biophys. Acta* **2014**, *1837*, 85.

(781) Chung, L. W.; Hayashi, S.; Lundberg, M.; Nakatsu, T.; Kato, H.; Morokuma, K. *J. Am. Chem. Soc.* **2008**, *130*, 12880.

(782) Nakatani, N.; Hasegawa, J. Y.; Nakatsuji, H. *J. Am. Chem. Soc.* **2007**, *129*, 8756.

(783) (a) Lin, T.-J.; O'Malley, P. J. *J. Mol. Struct. (THEOCHEM)* **2008**, *870*, 31. (b) Lin, T.-J.; O'Malley, P. J. *J. Phys. Chem. B* **2011**, *115*, 4227.

(784) Lamichhane, H. P.; Hastings, G. *Proc. Natl. Acad. Sci. U.S.A.* **2011**, *108*, 10526.

(785) Mula, S.; McConnell, M. D.; Ching, A.; Zhao, N.; Gordon, H. L.; Hastings, G.; Redding, K. E.; van der Est, A. *J. Phys. Chem. B* **2012**, *116*, 14008.

(786) Zhao, N.; Hastings, G. *J. Phys. Chem. B* **2013**, *117*, 8705.

(787) Bellina, B.; Compagnon, I.; Joly, L.; Albrieux, F.; Allouche, A. R.; Bertorelle, F.; Lemoine, J.; Antoine, R.; Dugourd, P. *Int. J. Mass Spectrom.* **2010**, *297*, 36.

(788) Li, X.; Chung, L. W.; Morokuma, K.; Li, G. *J. Chem. Theory Comput.* **2014**, *10*, 3319.

(789) de Wergifosse, M.; de Ruyck, J.; Champagne, B. *J. Phys. Chem. C* **2014**, *118*, 8595.

(790) (a) Hachmann, J.; Olivares-Amaya, R.; Atahan-Evrenk, S.; Amador-Bedolla, C.; Sánchez-Carrera, R. S.; Gold-Parker, A.; Vogt, L.; Brockway, A. M.; Aspuru-Guzik, A. *J. Phys. Chem. Lett.* **2011**, *2*, 2241. (b) Pande, V. S.; Baker, I.; Chapman, J.; Elmer, S. P.; Khaliq, S.; Larson, S. M.; Rhee, Y. M.; Shirts, M. R.; Snow, C. D.; Sorin, E. J.; Zagrovic, B. *Biopolymers* **2003**, *68*, 91. (c) Snow, C. D.; Nguyen, N.; Pande, V. S.; Gruebele, M. *Nature* **2002**, *420*, 102.

(791) (a) Tinberg, C. E.; Khare, S. D.; Dou, J.; Doyle, L.; Nelson, J. W.; Schena, A.; Jankowski, W.; Kalodimos, C. G.; Johnsson, K.; Stoddard, B. L.; Baker, D. *Nature* **2013**, *501*, 212. (b) Curtarolo, S.; Hart, G. L. W.; Nardelli, M. B.; Mingo, N.; Sanvito, S.; Levy, O. *Nat. Mater.* **2013**, *12*, 191. (c) Grigoryan, G.; Kim, Y. H.; Acharya, R.; Axelrod, K.; Jain, R. M.; Willis, L.; Drndic, M.; Kikkawa, J. M.; DeGrado, W. F. *Science* **2011**, *332*, 1071. (d) Farha, O. K.; Yazaydin, A. O.; Eryazici, I.; Malliakas, C. D.; Hauser, B. G.; Kanatzidis, M. G.; Nguyen, S. T.; Snurr, R. Q.; Hupp, J. T. *Nat. Chem.* **2010**, *2*, 944.